

Novel Methods for Molecular and Ionic Liquids

From Fundamentals to Applications as
Electrolytes

Dissertation

zur

Erlangung des Doktorgrades (Dr. rer. nat.)

der

Mathematisch-Naturwissenschaftlichen Fakultät

der

Rheinischen Friedrich-Wilhelms-Universität Bonn

vorgelegt von

Johannes Carl Maria Ingenmey

aus

Mechernich

Bonn, 2021

Angefertigt mit Genehmigung der Mathematisch-Naturwissenschaftlichen Fakultät
der
Rheinischen Friedrich-Wilhelms-Universität Bonn

Promotionskommission

Betreuerin/Erstgutachterin: Prof. Dr. Barbara Kirchner

Zweitgutachter: Prof. Dr. Thomas Bredow

Tag der Promotion: 15.07.2021

Erscheinungsjahr: 2021

Doch am dritten Tag im Felsgesteine
hat ein Zöllner Brecht den Weg verwehrt,
»Kostbarkeiten zu verzollen?« »Keine!«
Und der Knabe, der den Ochsen führte,
sprach: »Er hat gelehrt!«
Und so war auch das geklärt.

Der Zöllner in einer heiteren Regung
fragte noch: »Hat er denn was rausgekriegt?«
»Dass das weiche Wasser in Bewegung
mit der Zeit den harten Stein besiegt.
Du verstehst, das Harte unterliegt!«

C. F. Ingenmey, „Bertolt Brecht“

Statement of Authorship

I, Johannes Carl Maria Ingenmey, hereby declare that I am the sole author of this thesis. The ideas and work of others, whether published or unpublished, have been fully acknowledged and referenced in my thesis.

Bonn, April 20, 2021

Publications

Parts of this thesis have already been published in peer-reviewed journals:

1. **J. Ingenmey**, M. von Domaros, B. Kirchner, “Predicting Miscibility of Binary Liquids from Small Cluster QCE Calculations”, *J. Chem. Phys.*, **2017**, *146* (15), 154502, doi:10.1063/1.4980032.
2. **J. Ingenmey**, M. von Domaros, E. Perlt, S. P. Verevkin, B. Kirchner, “Thermodynamics and Proton Activities of Protic Ionic Liquids with Quantum Cluster Equilibrium Theory”, *J. Chem. Phys.*, **2018**, *148* (19), 193822, doi:10.1063/1.5010791.
3. **J. Ingenmey**, S. Gehrke, B. Kirchner, “How to Harvest Grotthuss Diffusion in Protic Ionic Liquid Electrolyte Systems”, *ChemSusChem*, **2018**, *11* (12), 1900–1910, doi:10.1002/cssc.201800436.
4. **J. Ingenmey**, J. Blasius, G. Marchelli, A. Riegel, B. Kirchner, “A Cluster Approach for Activity Coefficients: General Theory and Implementation”, *J. Chem. Eng. Data*, **2019**, *64* (1), 255–261, doi:10.1021/acs.jced.8b00779.
5. J. Blasius, **J. Ingenmey**, E. Perlt, M. von Domaros, O. Hollóczki, B. Kirchner, “Predicting Mole-Fraction-Dependent Dissociation for Weak Acids”, *Angew. Chem. Int. Ed.*, **2019**, *58* (10), 3212–3216 doi:10.1002/anie.201811839; “Dissoziation schwacher Säuren über den gesamten Molenbruchbereich”, *Angew. Chem.*, **2019**, *131* (10), 3245–3249, doi:10.1002/ange.201811839.
6. **J. Ingenmey**, O. Hollóczki, B. Kirchner, “Ion Pairing in Ionic Liquids”, in *Encyclopedia of Ionic Liquids*, ed. S. Zhang, Springer, Singapore, **2021**, doi:10.1007/978-981-10-6739-6_63-1.
7. I. Weber, **J. Ingenmey**, J. Schnaidt, B. Kirchner, and R. J. Behm, “Influence of Complexing Additives on the Reversible Deposition/Dissolution of Magnesium in an Ionic Liquid”, *ChemElectroChem*, **2021**, *8* (2), 390–402, doi:10.1002/celec.202001488.

Further publications (not part of this thesis):

8. M. von Domaros, E. Perlt, **J. Ingenmey**, G. Marchelli, B. Kirchner, “Peacemaker 2: Making Clusters Talk About Binary Mixtures and Neat Liquids”, *SoftwareX*, **2018**, *7*, 356–359, *doi:10.1016/j.softx.2018.11.002*.
9. R. Macchieraldo, **J. Ingenmey**, B. Kirchner, “Understanding the Complex Surface Interplay for Extraction: A Molecular Dynamics Study”, *Chem. Eur. J.*, **2020**, *26 (65)*, 14969, *doi:10.1002/chem.202002744*.
10. G. Marchelli, **J. Ingenmey**, B. Kirchner, “Activity coefficients of binary methanol alcohol mixtures from cluster weighting”, *ChemistryOpen*, **2020**, *9 (7)*, 774–785, *doi:10.1002/open.202000171*.

Danksagung

An dieser Stelle möchte ich meinen Dank ausdrücken für all jene, die mich während der Promotion unterstützt haben. Auch wenn diese Arbeit meinen Namen auf der Titelseite trägt, wäre sie nicht ohne die Unterstützung zahlreicher Menschen entstanden.

Zuallererst möchte ich Prof. Dr. Barbara Kirchner danken für ihre anhaltende Unterstützung und die Möglichkeit, mich in der Forschung frei zu bewegen und zu entwickeln. Insbesondere danke ich ihr auch für ihre Geduld und Verständnis in schwierigen Zeiten und wenn der Bericht erst 3 Uhr Nachts am Tag vor der Abgabe kam.

Besonderer Dank gilt auch Prof. Dr. Thomas Bredow für die freundliche Übernahme des Vorsitzes der Promotionskommission. Ebenso danke ich Prof. Dr. Helmut Baltruschat, der meinen akademischen Werdegang seit der Bachelorarbeit unterstützt hat, und Prof. Dr. Karl Wagner für ihren Beitritt zur Promotionskommission.

Ich danke herzlichst den neuen und alten Mitgliedern des Arbeitskreises und selbstverständlich auch allen Mitarbeitern und Mitarbeiterinnen des Mulliken Centers für die wunderbare Atmosphäre und heitere Zusammenarbeit. Insbesondere danke ich meinen Kollegen und Freunden Gwydyon Marchelli und Lars Esser. Dr. Werner Reckien danke ich besonders für seine beständige Geduld und Hilfsbereitschaft.

Von ganzem Herzen danke ich Annika, die stets für mich da war.

Mein tiefster Dank gilt meiner Schwester Eva, meiner Mutter Reinhild und meinem Vater Kalle, der mir fehlt wie ein Lachen in der Stille.

Abstract

The trend towards sustainable technologies and processes requires the development of suitable solvents and electrolytes. In this regard, next to traditional molecular solvents, ionic liquids (ILs) are regarded as promising candidates. During the last decades, the continually growing interest in these substances gave rise to a wealth of research directed at their use as designer solvents. Enabling the application-driven design of solvents requires a solid understanding of their dynamics and fundamental structure–property relationships. This thesis aims to contribute to this goal and to describe the development and application of various computational methods to research molecular and ionic liquids.

The first part of the thesis focuses on developing and testing the binary Quantum Cluster Equilibrium method as a general and highly efficient approach to model liquids. The bQCE method applies methods of statistical thermodynamics to quantum chemically optimized clusters in order to obtain a cluster-based model of liquids. In Chapters 3 and 4, the bQCE method is applied to a variety of binary solvent mixtures. Their mixing behaviors and thermodynamic functions can be reproduced with minimal computational effort. Based on these results, an approach is developed to calculate activity coefficients of binary mixtures based on cluster distributions. Furthermore, this thesis documents the extension of the bQCE method from binary to general multi-component mixtures, allowing its future application to complex systems such as solute salts in electrolytes.

The second part of the thesis contains three studies on proton transfer equilibria in ionic, pseudo-ionic, and molecular liquids. In Chapter 5, a computational approach to model proton transfer equilibria based on the bQCE method is developed and applied to a range of alkylammonium-based PILs. It is shown that several properties are affected by the reverse proton transfer reaction. An extreme example of that is explored in Chapter 6. Despite its low ionicity, the pseudo-PIL *N*-methylimidazolium acetate features a unexpectedly high proton conductivity. By means of *ab initio* molecular dynamics simulations the underlying mechanism can be explained as a chain transfer reaction resembling Grotthuss diffusion. Based on these results, quantum chemical calculations are performed to find potential candidates for PILs with high proton conductivities. In Chapter 7, the bQCE approach to proton transfer equilibria is applied to aqueous formic acid and acetic acid as case studies. The degree of dissociation can be predicted over the whole mixing range, thus allowing a molecular interpretation of the experimental conductivity maximum in both systems.

The final part of the thesis deals with ion pairing in ILs, which is thought to be a cause for low ionicity. This hypothesis is disputed, however, due to conflicting evidence. Chapter 8 provides a detailed review of experimental and theoretical findings regarding the nature of ion pairing in ILs and extends them by the analysis of ion pair dynamics in 1-butyl-3-methylimidazolium triflate. By the aid of *ab initio* molecular dynamics and static quantum chemistry, it can be shown that ion pairs are short-lived in this system and its ionicity can be explained by charge transfer between anion and cation. In their practical applications, however, ILs are often solvents for other compounds and discussions of ion pairing must involve not only the its constituent ions but also the solutes. Chapter 9 deals with the ion association of magnesium in an IL-based electrolyte. The coordination of the Mg^{2+} cation by the anions of the IL prevents its deposition on the electrode and thus reduces reversibility. In a combined experimental and theoretical study, quantum chemical calculations on ionic clusters show that the 18-crown-6 ether can displace the anions and prevent ion association.

In summary, the thesis aims to explore different theoretical approaches to model liquids and liquid phase phenomena. The presented methods are computationally efficient and can be applied to complex systems. In future studies, they can help to establish structure–property relationships for the rational design of novel solvents and electrolytes.

Zusammenfassung

Die Wende hin zu nachhaltigen Technologien und Prozessen erfordert die Entwicklung geeigneter Lösungsmittel und Elektrolyten. Neben traditionellen molekularen Lösungsmitteln gelten ionische Flüssigkeiten hierbei als vielversprechender Kandidat und wurden in den letzten zwei Jahrzehnten mit zunehmendem Interesse und dem Ziel erforscht, ein anwendungsorientiertes Design neuer Lösungsmittel zu ermöglichen. Hierfür ist ein Verständnis der Dynamik und fundamentalen Struktur-Wirkungsbeziehungen dieser Systeme vonnöten. Die vorliegende Arbeit leistet hierzu wertvolle Beiträge und beschreibt die Entwicklung und Anwendung verschiedener theoretischer Methoden zur Erforschung ionischer und molekularer Flüssigkeiten.

Der erste Teil der Arbeit befasst sich mit der Entwicklung der binären „Quantum Cluster Equilibrium“-Methode (bQCE) als effizienten Ansatz zur Modellierung von Flüssigkeiten. Der bQCE-Ansatz wendet Methoden der statistischen Thermodynamik auf quantenchemisch optimierte Cluster an, um Flüssigkeiten als Gleichgewichtsverteilung von Clustern zu beschreiben. Kapitel 3 und 4 schildern die Anwendung der bQCE-Methode auf eine Reihe binärer Mischungen exemplarischer Lösungsmittel. Mit minimalem rechnerischen Aufwand kann das Mischungsverhalten dieser Systeme vorhergesagt werden. Darauf aufbauend wird eine Methode zur Bestimmung von Aktivitätskoeffizienten in binären Mischungen entwickelt. Darüberhinaus dokumentiert diese Arbeit die Erweiterung der bQCE-Methode von binären zu allgemeinen Multikomponentensystemen und erlaubt damit in Zukunft die Anwendung der Methode auf komplexe Systeme wie etwa in Elektrolyten gelöste Salze.

Der zweite Teil der Arbeit umfasst drei Studien zu Protonentransfer-Gleichgewichten in ionischen, pseudo-ionischen und molekularen Flüssigkeiten. In Kapitel 5 wird ein Ansatz zur Vorhersage des Protonentransfergrades mithilfe der bQCE-Methode entwickelt und an einer Reihe Alkylammonium-basierter protischer ionischer Flüssigkeiten getestet. Es kann gezeigt werden, dass verschiedene Eigenschaften maßgeblich durch das Protonentransfer-Gleichgewicht beeinflusst werden. Ein extremes Beispiel hierfür wird in Kapitel 6 untersucht. Trotz ihrer geringen Ionizität besitzt die protische pseudo-ionische Flüssigkeit *N*-Methylimidazoliumacetat eine unerwartet hohe Protonenleitfähigkeit. Mithilfe von ab initio-Molekulardynamik-Simulationen wird der zugrundeliegende Mechanismus geklärt und gezeigt, dass ein der Grotthuss-Diffusion ähnlicher Kettentransfer von Protonen die hohe Leitfähigkeit ermöglicht. Auf Grundlage dieser Ergebnisse werden eine Reihe quantenchemischer Rechnungen durchgeführt, um potentielle Kandidaten für protische

ionische Flüssigkeiten mit hoher Protonenleitfähigkeit zu finden. In Kapitel 7 wird der bQCE-Ansatz für Protonentransfer-Gleichgewichte auf wässrige Lösungen der Ameisen- und Essigsäure angewandt. Der Dissoziationsgrad kann über den kompletten Mischungsbereich vorhergesagt und der Ursprung des beobachteten Leitfähigkeitsmaximums beider Säuren erklärt werden.

Der abschließende Teil befasst sich mit der Ionenpaarbildung in ionischen Flüssigkeiten, die als Ursache für die häufig beobachtete geringe Ionizität vermutet wird. Diese Hypothese ist jedoch aufgrund gegensätzlicher Forschungsergebnisse umstritten. Kapitel 8 liefert eine detaillierte Übersicht der neusten experimentellen und theoretischen Erkenntnisse und erweitert diese um eine Analyse der Ionenpaarbildung in 1-Butyl-3-methylimidazoliumtriflat. Mithilfe von ab initio-Molekulardynamik kann gezeigt werden, dass Ionenpaare in diesem System nur kurzlebig sind und die Ionizität mit einem Ladungsaustausch zwischen den Anion und Kation erklärt werden kann. Kapitel 9 schließlich befasst sich mit der Ionenassoziation Magnesiums in einem auf einer ionischen Flüssigkeit basierten Elektrolyten. Die Koordination des Mg^{2+} -Kations durch die anwesenden Anionen verhindert die Abscheidung an der Elektrode und verringert so die Reversibilität. Mithilfe quantenchemischer Methoden kann gezeigt werden, dass der 18-Krone-6-Ether die Anionen verdrängt und die Ionenpaarbildung verhindert.

Zusammenfassend werden in der Arbeit verschiedene theoretische Ansätze zur Modellierung von Flüssigkeiten erforscht. Die vorgestellten Methoden sind effizient und können auf komplexe Systeme angewandt werden. Sie können dabei helfen, Struktur-Wirkungsbeziehungen im anwendungsorientierten Design neuer Lösungsmittel und Elektrolyten zu finden.

Contents

1	Introduction	1
1.1	The Quantum Cluster Equilibrium Method	2
1.2	Ionic Liquids	5
1.2.1	Protic Ionic Liquids	7
1.2.2	Ion Pairing and Ionicity	8
1.2.3	Ionic Liquids in Energy Devices	10
1.3	Scope of the Thesis	11
2	Methodology	13
2.1	Classical Force Fields	13
2.2	Static Quantum Chemical Calculations	15
2.3	Quantum Cluster Equilibrium Theory	18
2.3.1	Statistical Thermodynamics	19
2.3.2	Binary Quantum Cluster Equilibrium Theory	20
2.3.3	Multi-Component Systems	25
2.4	Peacemaker 2	29
2.5	Cyclic Voltammetry	32
I	Modeling Organic Solvent Mixtures	35
3	Predicting Miscibility From Small Cluster QCE Calculations	39
3.1	Introduction	40
3.2	Model and Methods	41
3.2.1	The QCE Method	41
3.2.2	Quantum Chemical Method	43
3.2.3	Parameter Optimization and Approximation	44
3.2.4	Cluster Sets	45
3.3	Results and Discussion	49
3.3.1	Pure Components	49
3.3.2	Thermodynamics of Mixing	49
3.3.3	Population Analysis	56
3.4	Conclusion and Outlook	59

4	A Cluster Approach for Activity Coefficients	61
4.1	Introduction	62
4.2	Methods and Computational Details	63
4.2.1	The bQCE Method	63
4.2.2	Activity Coefficients from bQCE	65
4.2.3	Computational Details	66
4.2.4	Cluster Sets	67
4.3	Case Studies	68
4.4	Conclusion	71
II	Proton Transfer Equilibria in Ionic and Molecular Liquids	73
5	Thermodynamics and Proton Activities of Protic ILs with QCE Theory	77
5.1	Introduction	78
5.2	Model and Methods	81
5.2.1	The bQCE Method	81
5.2.2	Computational Details	83
5.2.3	Cluster Sets	84
5.3	Results and Discussion	86
5.3.1	Boiling Points	86
5.3.2	Thermodynamics of Vaporization	89
5.3.3	Proton Activity	94
5.4	Conclusion	98
6	How to Harvest Grotthuss Diffusion in Protic IL Electrolyte Systems	101
6.1	Introduction	103
6.2	Results and Discussion	106
6.2.1	Ionicities From ab initio Molecular Dynamics	107
6.2.2	Insight into the Proton Transfer Mechanisms	109
6.2.3	Suggesting Candidates for Grotthuss Diffusion	116
6.3	Conclusions	121
7	Predicting Mole-Fraction-Dependent Dissociation for Weak Acids	123
7.1	Communication	124
III	Ionicity and Ion Association in Ionic Liquids	131
8	Ion Pairing in Ionic Liquids	135
8.1	What is Ion Pairing?	136

8.2	Understanding Ion Pairing in Ionic Liquids	138
8.2.1	Ionic Liquids at Interfaces	139
8.2.2	Spectroscopy	140
8.2.3	Molecular Dynamics	141
8.2.4	Charge Transfer	143
8.2.5	Protic Ionic Liquids	144
8.2.6	Grotthuss Diffusion	145
8.2.7	Ionic Liquids in Mixtures	146
8.3	Conclusion	148
9	Influence of Complexing Additives on Mg Deposition/Dissolution in an IL	151
9.1	Introduction	152
9.2	Results and Discussion	154
9.2.1	Electrochemical Characterization	154
9.2.2	Simulation	164
9.3	Conclusions	171
9.4	Experimental Section	172
9.4.1	Electrochemical Methods	172
9.4.2	Computational Methods	173
	Conclusion and Outlook	176
	Appendix	184
A	Supporting Information to Chapter 3	185
B	Supporting Information to Chapter 4	189
C	Supporting Information to Chapter 5	193
D	Supporting Information to Chapter 6	199
E	Supporting Information to Chapter 7	207
F	Supporting Information to Chapter 9	213
	Bibliography	225

List of Figures

1.1	QCE cluster populations and thermodynamics of methanol.	3
1.2	Structures and abbreviations of common IL ions.	6
1.3	Walden plot of various protic and aprotic ILs.	9
2.1	Peacemaker 2 program structure	30
2.2	Comparison of different cyclic voltammogram shapes.	32
3.1	Neat and mixed clusters of acetone, acetonitrile, benzene, and water. . . .	46
3.2	Thermodynamic functions of acetone, acetonitrile, benzene, and water. . . .	50
3.3	Calculated and experimental Gibbs energies of mixing of binary mixtures. . .	52
3.4	Optimized QCE parameters of binary mixtures.	53
3.5	Populations of neat and mixed clusters in binary mixtures.	57
4.1	Calculated and experimental Gibbs energies of mixing of binary mixtures. . .	69
5.1	Structural formulas of cations and anions investigated in this work.	79
5.2	Walden plot of alkylammonium PILs.	80
5.3	Ethylammonium nitrate clusters.	85
5.4	bQCE ⁰ phase volume of EAN for different cluster sizes.	87
5.5	bQCE ⁰ isobaric heat capacity of EAN.	88
5.6	Calculated enthalpy of EAN in the gas phase and liquid phase.	90
5.7	Populations of the single ionic and neutral species in EAN's vapor phase. . .	91
5.8	Calculated Gibbs energy of neutral and ionic species in EAN.	92
5.9	Vaporization enthalpy of alkylammonium PILs and their parent amines. . . .	93
5.10	p <i>K</i> _s and Δp <i>K</i> _a values for several PILs.	96
5.11	Temperature dependence of p <i>K</i> _s of EAN and EAFm.	97
5.12	van't Hoff plots of the proton transfer in EAN and EAFm	98
6.1	Radial distribution functions of the O···H*/N···H* hydrogen bonds.	107
6.2	Content of neutral acid molecules in C ₁ Im-HOAc.	108
6.3	MSD of imidazole, acetate, and the active proton in C ₁ Im-HOAc.	109
6.4	Continuous autocorrelation function for the N···H*/O···H* association. . .	110
6.5	Snapshots of simulation B _{ion} showing several proton transfers.	111
6.6	Snapshots of simulation A _{neu} showing several proton transfers.	112

6.7	Snapshots of simulation \mathbf{B}_{mix}	113
6.8	Combined distribution functions of the $\text{O}\cdots\text{H}^*$ and $\text{N}\cdots\text{H}^*$ distance.	114
6.9	Energy profiles of the proton transfer in $\text{C}_1\text{Im-HOAc}$	120
7.1	Neat and mixed clusters of water, formic acid, and acetic acid.	125
7.2	Mole-fraction-dependent acid strength $\text{p}K_{\text{a}}$ of formic and acetic acid.	127
7.3	Mole-fraction-dependent dissociation constant α of formic and acetic acid.	128
7.4	Mole-fraction-dependent ion concentrations in formic and acetic acid.	129
7.5	Mole-fraction-dependent conductivities of formic and acetic acid.	130
8.1	Walden plot of several alyklammonium- and alkylimidazolium-based ILs.	137
8.2	Analyses of ion pairing in $[\text{C}_4\text{C}_1\text{Im}][\text{OTf}]$ by the aid of AIMD and DFT.	142
8.3	Walden plot of various deep eutectic solvents.	147
9.1	CVs recorded on a GC in $\text{BMP-TFSI} + 0.1 \text{ M Mg}(\text{BH}_4)_2 + 0.1 \text{ M } 18\text{c}6$	156
9.2	CVs recorded on GC in BMP-TFSI with different additives.	160
9.3	CVs recorded on Mg in $\text{BMP-TFSI} + 0.1 \text{ M Mg}(\text{BH}_4)_2 + 0.1 \text{ M } 18\text{c}6$	163
9.4	Most stable clusters conformations of Mg^{2+} at different compositions.	164
9.5	Different coordination states of Mg^{2+}	165
9.6	Coordination and binding energies of different Mg^{2+} clusters.	166
9.7	Coordination energies of Mg^{2+} clusters before and after reduction.	169
A.1	Thermodynamic mixing functions of the NMF -water mixture.	185
B.1	Populations of neat and mixed clusters in binary mixtures.	191
D.1	Radial distribution functions of $\text{O}\cdots\text{H}^*$ and $\text{N}\cdots\text{H}^*$ hydrogen bonds.	203
D.2	Continuous autocorrelation function for the $\text{N}\cdots\text{H}^*/\text{O}\cdots\text{H}^*$ association.	204
E.1	Enthalpy and entropy of formic and acetic acid.	209
E.2	Cluster populations in formic and acetic acid.	209
E.3	Populations of neutral and ionic clusters in aqueous acetic acid.	210
E.4	Concentration of neutral and ionic species in aqueous acetic acid.	210
F.1	CVs recorded on a GC electrode in $\text{BMP-TFSI}+0.1 \text{ M Mg}(\text{BH}_4)_2$	214
F.2	CVs on GC in $\text{Mg}^{2+}/\text{Ca}^{2+}$ -containing BMP-TFSI	215
F.3	CVs recorded on GC in $\text{Mg}^{2+}/\text{Ca}^{2+}$ -containing BMP-TFSI	216
F.4	Charge accumulated on GC in in $\text{BMP-TFSI}+0.1 \text{ M Mg}(\text{BH}_4)_2$	217
F.5	Charge accumulated on GC in $\text{BMP-TFSI}+0.1 \text{ M Mg}(\text{BH}_4)_2+0.1 \text{ M } 18\text{c}6$	217
F.6	Charge accumulated on GC in $\text{BMP-TFSI}+0.05 \text{ M Mg}(\text{BH}_4)_2+0.1 \text{ M } 18\text{c}6$	218
F.7	CVs recorded on GC in $0.01 \text{ M Mg}(\text{BH}_4)_2+0.09 \text{ M MgTFSI}_2+0.2 \text{ M } 18\text{c}6$	218
F.8	Mg^{2+} clusters at different compositions.	219

List of Figures

F.9	Representation of the $\text{MgTFSI}_2 + 2$ 18-crown-6 cluster.	220
F.10	Binding energies of the $\text{MgTFSI}_2 + \text{BMP-TFSI}$ cluster.	220
F.11	Binding energies of the $\text{MgTFSI}_2 + 2$ BMP-TFSI cluster.	221
F.12	Binding energies of the $\text{MgTFSI}_2 + 18\text{c6}$ cluster.	221
F.13	Binding energies of the $\text{MgTFSI}_2 + 18\text{-crown-6} + \text{BMP-TFSI}$ cluster.	222
F.14	Binding energies of the $\text{MgTFSI}_2 + 2$ 18-crown-6 cluster.	222
F.15	Spin density distribution of reduced molecules and clusters.	223

List of Tables

3.1	Binding energies of acetone, acetonitrile, benzene, and water clusters. . . .	47
4.1	Calculated and experimental vaporization enthalpies of organic solvents. . .	68
4.2	Calculated and experimental activity coefficients of binary mixtures.	70
5.1	Experimental properties of alkylammonium nitrates and formates.	81
5.2	Calculated and experimental boiling points of alkylammonium PILs.	88
5.3	Calculated and experimental enthalpies of vaporization of alkylammonium nitrates and formates.	92
6.1	Average coordination number of the active proton in C ₁ Im-HOAc.	115
6.2	Gibbs energies of the reverse proton transfer between several anions and cations.	117
9.1	Calculated electron affinities and reduction potentials of Mg ²⁺ , TFSI ⁻ , 18- crown-6, BMP-TFSI and their clusters.	170
A.1	Binding energies of water, NMF, and mixed clusters.	186
B.1	Redlich–Kister coefficients of binary mixtures.	189
B.2	Densities, boiling points, and QCE parameters of binary mixtures.	190
C.1	Vaporization enthalpies and heat capacities of alkylammonium nitrates. . .	193
C.2	Vaporization enthalpies of amines and their nitrates and acetates.	194
C.3	Empirically optimized bQCE(8) parameters.	195
C.4	Comparison of bQCE results for EAN with different quantum chemical methods.	196
C.5	Calculated boiling points of PILs on PBEh-3c and GFN-xTB level.	196
D.1	Composition of the six C ₁ Im-HOAc simulations.	199
D.2	Gibbs energies of the proton transfer between several anions and cations. .	205
E.1	Calculated and experimental vaporization enthalpies of formic and acetic acid.	208
F.1	Electron affinities and reduction potentials of BH ₄ ⁻ and Mg(BH ₄) ₂	219

1 Introduction

The quest for sustainable technologies and processes in industrial and everyday applications¹¹ has without a doubt reached the highest political circles and is recognized by the United Nations as a major goal and responsibility to the global community.¹² Man-induced emissions and pollution are now widely accepted¹³ as a cause for the current shift in global climate,^{14,15} degrading air quality,¹⁶ and the bio-diversity crisis.¹⁷ In light of the growing awareness for their environmental impact, the development of ecologically friendly alternatives to traditional technologies, processes, and sources of energy has received enormous attention and has led to important achievements.¹⁸ For example, renewable energies now cover 27.3% of the global electricity production and their share is continuously increasing.¹⁹ However, significant amounts of the renewable energy output are generated by intermittent sources such as wave power, wind power, and solar power which depend on non-controllable factors like the time of year and weather conditions.¹⁹ The option of long-term energy storage is therefore a vital criterion to their triumph over fossil fuels.²⁰ As was recently shown by becoming a declared goal of the European Green Deal,²¹ this motivates a strong interest in the development of sustainable fuel cell and battery technologies, such as metal-air batteries.^{22–24} Significant efforts were also made in the development of carbon capture technologies, which aim to remove carbon dioxide from industrial waste gases.^{25–27} Industrial emissions also include harmful gases caused by volatile solvents in chemical synthesis and processing.²⁸ The search for alternative reaction media to comply with the principles of Green Chemistry is a major step in the aim for sustainability.¹¹

What is common to these recent advances is the need to develop novel solvent and electrolyte systems. The rational design of state-of-the-art materials for these applications is a challenge that may only be solved by the close collaboration of experimental and computational research. With notable exceptions such as supercritical fluid solvents²⁹ and solid-state electrolytes,³⁰ these systems are usually found in the liquid state. Ionic liquids in particular have received great attention in recent years.³¹ Therefore, computational efforts in enabling the targeted design of solvents and electrolytes should aim to model liquids and liquid phase phenomena in a realistic environment. This is the general aim of this thesis. By developing and employing methods to model liquids, physico-chemical properties fundamental to their application as solvents and electrolytes such as their mixing behavior, vapor pressure, acidity, or electrochemical stability are studied at a microscopic level.

1. Introduction

Many theoretical approaches to model liquids exist. The methods used in this thesis include force-field-based approaches such as classical molecular dynamics (MD) as well as ab initio molecular dynamics (AIMD) and static quantum chemical calculations and will be introduced in more detail in Chapter 2. While often being considered the pinnacle of liquid modeling,³² AIMD simulations are computationally demanding. On the other hand, classical MD simulations require well-optimized force fields, which sometimes may not be available. An alternative approach to modeling liquids that combines statistical thermodynamics and static quantum chemistry exists in the quantum cluster equilibrium (QCE) method and its extension to binary systems (bQCE). In addition to the aforementioned approaches, the bQCE method is fundamental to the works presented in this thesis.

In the following a brief overview of the bQCE method's history so far will be provided. Afterwards, the reader will be introduced to the promising ionic liquids solvent class. The introduction will be completed by outlining the scope this thesis.

1.1 The Quantum Cluster Equilibrium Method

In 1995, Ralf Ludwig and Frank Weinhold began publishing computational studies of hydrogen-bonded liquids based on the quantum cluster equilibrium (QCE) method.³³⁻³⁵ The QCE method was developed by Weinhold, who first published its underlying theory in 1998.³⁶ It combines methods of classical statistical thermodynamics and quantum chemistry to obtain a model of the liquid and the vapor phase that is based on an equilibrium distribution of characteristic molecular clusters. Molecular clusters, as Weinhold describes them, are “distinctive chemical moieties, intermediate between the monomeric species of low-density gases and the fully aggregated limit of condensed phases.”³⁶ Although the liquid and gaseous phase are separate aggregate states with distinct properties under most conditions, the existence of the gas-liquid critical point³⁷ implies a continuous transition path between both states. As the temperature and pressure approach critical conditions, the properties of the liquid and gaseous phase become more similar until their differences vanish, as the system enters the critical state, and no distinction between liquid and gaseous phase can be made. Thus, by simply adjusting the distribution of clusters from small monomeric or dimeric species to larger aggregates, it should be possible to extend a cluster-based model of a dense gas to the liquid phase.³⁶ The QCE procedure therefore assigns populations to a set of quantum chemically calculated clusters, which collectively reproduce liquid phase behavior. From these populations the total partition function of the system can be derived which gives access to thermodynamic quantities such as the enthalpy, entropy, and Gibbs energy. In order to apply this approach to real substances only two van der Waals-like empirical parameters are introduced, accounting for the exclusion volume, i.e., the volume occupied by the molecules themselves, and

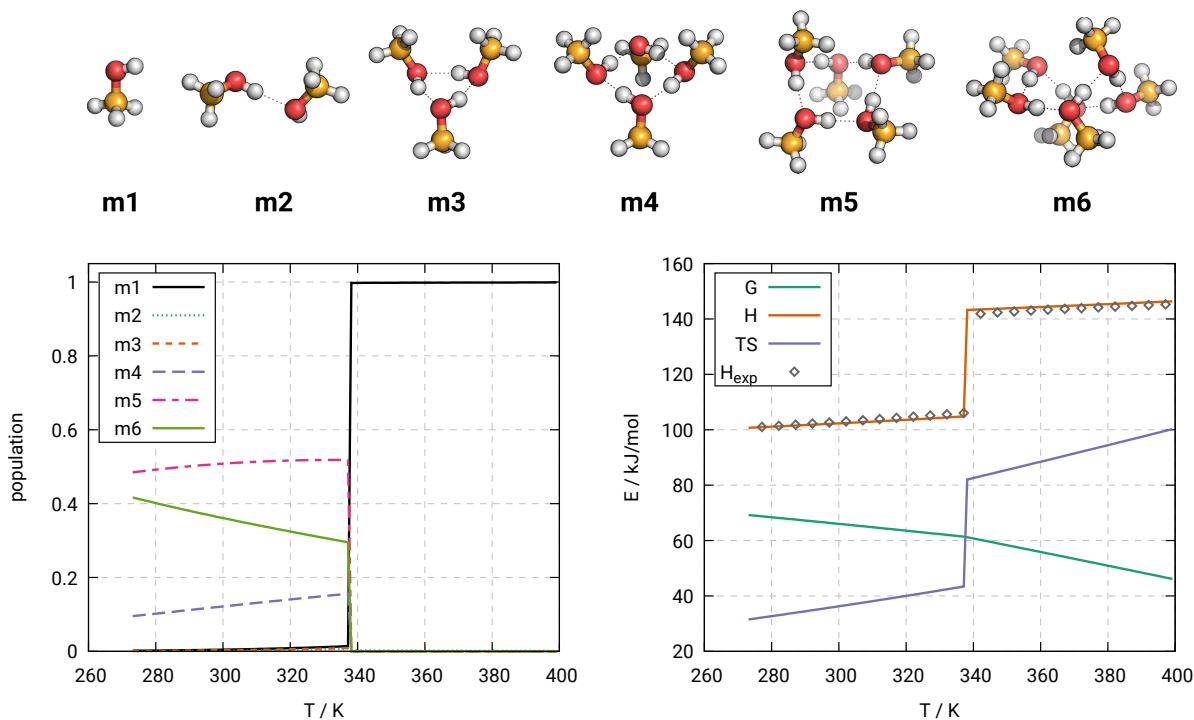


Figure 1.1: Cluster populations (left graph) and thermodynamic functions (right graph) of methanol as obtained from QCE with a minimal cluster set (top). Experimental enthalpy taken from Ref. 46.

the attractive inter-cluster interaction. To illustrate the general concept of the method, Fig. 1.1 shows an example of a simple QCE calculation of methanol based on a minimal cluster set of mainly ring structures. The QCE method finds an equilibrium distribution of clusters that is dominated by pentamers in the liquid range, with significant amounts of tetrameric and hexameric rings, whereas the gas phase is dominated by the monomer with trace amounts of dimers. From these populations, the thermodynamic functions can be calculated in close agreement with experiment. Despite the simple model, the enthalpy of vaporization at the boiling point of methanol is predicted within 3 kJ/mol accuracy. In 2005, the QCE approach was taken up by Barbara Kirchner, who reformulated and updated its theory,³⁸ which marked the first time a definitive and comprehensive version of the QCE theory was available, and released the first publicly available QCE code Peacemaker.^{8,38,39} Following this release, the Kirchner group became the most active in QCE research and extended the method by innovative applications such as the prediction of proton transfer equilibrium constants, which they demonstrated by reproducing the temperature dependence of the ionic product of water with quantitative accuracy,⁴⁰ or a QCE-based cluster-weighting approach for vibrational circular dichroism (VCD) spectra.^{41,42} In 2011, the Kirchner group fundamentally extended the theory to include binary systems in its description.⁴³ This opened up a wide field of potential new applications such as calculating the mixing thermodynamics of binary mixtures.^{1,4,10,43–45}

1. Introduction

Although the formation of extended hydrogen bond networks, such as in water,⁴⁷ seems to put the upper limit n , i.e., the number of molecules that form a cluster, in a range that is unfeasible to ab initio methods, experimental⁴⁸ and theoretical⁴⁹ evidence suggests that quantum chemically accessible clusters could be sufficiently representative of the liquid structure.³⁶ More convincing, however, is perhaps the number of systems that were successfully modeled with the QCE method.^{39,50,51} These include mostly studies of strongly associating hydrogen-bonded liquids such as water,^{38,52–62} alcohols,^{63–69} amides,^{34,35,45,70} hydrogen halides,^{71–74} ammonia,^{75,76} and weak acids.^{5,77,78} A more detailed review of these works may be found in Refs. 50 and 51. More obscure systems that were investigated by the QCE approach are liquid sulfur⁷⁹ and *cis,cis*-cyclotriazane.⁸⁰

At the heart of the QCE approach lies the construction of a set of representative clusters that include all important characteristic binding motifs. Such cluster sets may be based on experimentally observed molecular configurations,⁷⁹ but can also include motifs derived from computational methods^{2,4} or chemical intuition.^{40,55} By assigning populations to each of these clusters, the QCE approach allows the interpretation of structural properties on a molecular level. The cluster weighted total partition function gives access to all thermodynamic functions which can then be attributed to the interplay of different structural motifs. One prominent example of the QCE approach allowing the direct interpretation of a macroscopic property resulting from a structural change was presented by Ralf Ludwig in 2007, when he demonstrated that the inclusion of three-dimensional water clusters, containing tetrahedrally coordinated water molecules, in the QCE model of water reproduced the density anomaly.⁵⁵ Cluster populations not only allow insights into the structural features governing the liquid phase, but can also be used in cluster-weighting approaches to the prediction of NMR shifts,⁸¹ quadrupole coupling constants,⁸² and IR spectra.⁸³

The development of the QCE approach was motivated by the desire to find an alternative to contemporary force-field-based methods that could adequately describe nonpairwise-additive cooperative effects in strongly associating hydrogen-bonded liquids.³⁶ The simple and easily modifiable QCE approach satisfied that ambition as it can sample any number of binding motifs by design and is open to any level of theory. While the size of employed clusters in the QCE approach has no upper bound in principle – and, indeed, water clusters up to the size of 60 molecules have been considered⁵⁶ – their size is usually limited to $n \leq 20$ molecules per cluster. This opens up the possibility of employing high level quantum chemical methods that are computationally too expensive to be used in dynamic liquid simulations in a feasible manner. Several QCE studies focused on testing the effects of employing different levels of theory.^{38,60–63,69–72,78,79} It should be noted here, that the insights gained in these works are not necessarily applicable to the bQCE procedure in its current form, as it has undergone several changes since its conception.^{8,45,84} While it was found that the correct treatment of cooperative effects is more important than dispersion

effects in the modeling of hydrogen-bonded liquids such as water,^{38,50,62} dispersion effects significantly contribute to the interaction energy of compounds with long alkyl-chains such as *n*-butanol⁶⁹ and its constitutional isomers.¹⁰ Systematic comparisons of quantum chemical methods showed that density functional theory (DFT) is capable of producing results of similar quality as methods based on wave function theory.^{38,62,71,72,78} Significant basis set effects were found for correlated methods, where a too small basis set could not adequately model liquid phase behavior.^{38,62,71,72,78}

On the other hand, increasing method and basis set to the highest feasible level of theory does not necessarily result in a better performance of the QCE method.^{71,72} Although since its conception the computational power of scientific computer clusters drastically increased and computationally intensive methods such as AIMD simulations are accessible to a much wider community,^{85,86} the QCE approach still provides a computationally economical alternative method for liquid modeling. It seems self-evident, that the research on sustainable solvents and electrolytes should itself strive for sustainable methodology. Thus, the effort to decrease computational costs is in the spirit of sustainability, but also enables the sampling of a vastly higher number of clusters. In recent years, the low-cost PBEh-3c functional⁸⁷ was established as performing remarkably well in combination with QCE,^{8,40,74} being able to predict the temperature dependence of the ionic product of water with quantitative accuracy.⁴⁰

This thesis focuses on the development of the bQCE method as a highly efficient and general approach to liquid modeling. Section 2.3 documents for future reference the next major extension of the bQCE theory from binary to general multi-component systems, allowing the modeling of mixtures with any number of components. Chapters 3 and 4 describe the application of the method to a range of binary organic solvent mixtures. These include, for the first time, non-polar solvents like benzene and chloroform. By employing low-cost electronic structure methods, the computational effort is reduced to a level that ensures its feasibility when applied to more complex systems such as ionic liquids. Such applications are described in the second part of the thesis. The bQCE method is used to model the proton transfer in protic ionic liquids (Chapter 5) and aqueous acid solutions (Chapter 7), further establishing the its ability to describe such equilibria in different environments.

1.2 Ionic Liquids

In 1888, while investigating the reactions of vinylamine with sulfuric and nitric acid, German chemist Siegmund Gabriel synthesized ethanolammonium nitrate and thus discovered the first member of a vast class of versatile substances that would later be known as ionic liquids (ILs).⁸⁸ Being now widely regarded as one of the major innovations of modern chemistry, it was not until the 1990s that the interest in these substances gained

1. Introduction

momentum that would result in an avalanche of research directed at their properties and applications.^{32,89–92} Ionic liquids are salts that are liquid at moderate temperatures, typically with a melting point below the arbitrary limit of 100 °C. The functional range of ILs covers a wide selection of scientific and industrial fields. Their uses include the application as solvents and co-solutes in synthesis,⁹⁰ catalysis,⁹³ and separation processes,⁹¹ such as liquid-liquid separation.⁹⁴ Furthermore, they find applications as absorbent in carbon capture technology,^{27,95,96} as medium or active agent in pharmaceuticals,⁹² and as electrolyte in modern energy devices,^{97,98} such as metal-ion batteries⁹⁹ or solar cells.¹⁰⁰

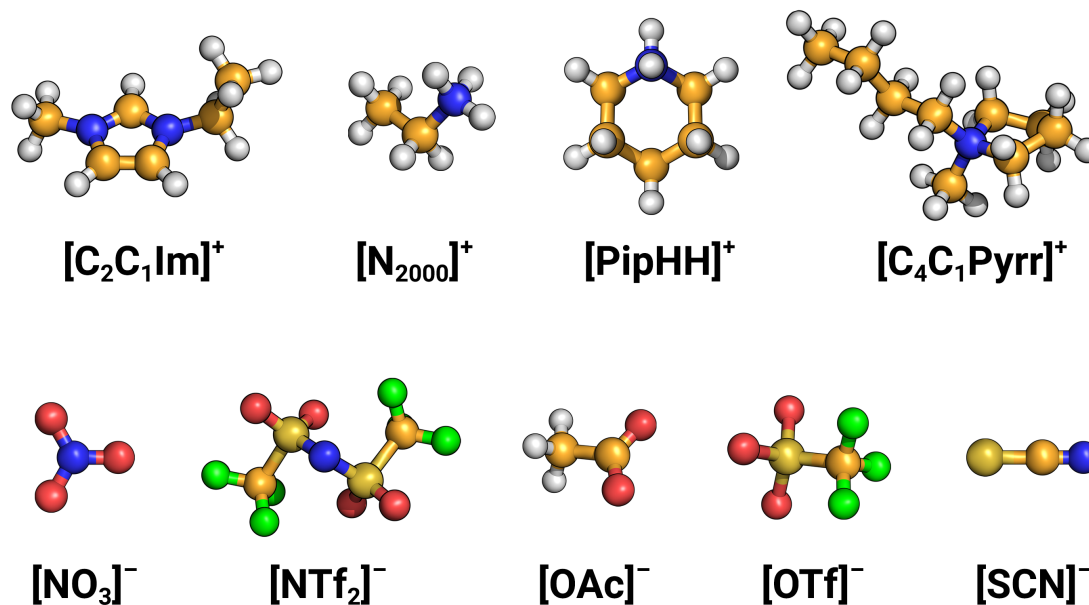


Figure 1.2: Molecular structures and abbreviations of various cations and anions commonly used as components of ionic liquids. White H; orange C; blue N; red O; green F; yellow S.

Simple inorganic salts constituted of monoatomic ions, such as the common salt NaCl, usually have high melting points and the energy required to transfer them to the molten state makes their use in these areas unfeasible. Ionic liquids, on the other hand, melt at moderate temperatures. To enable their liquid state at such low temperatures, ILs usually consist of polyatomic, charge-diffuse ions, often a large organic cation with low symmetry paired with an inorganic anion (see Fig. 1.2).¹⁰¹ Varying combinations of the constituent ions will result in different properties, allowing in principle their targeted design as solvents or material for specific applications. Indeed, the vast number of possible combinations with diverse sets of properties makes any generalization of their characteristics, beyond a few key attributes, an over-simplification. Owing to their ionic nature, all ILs are to some degree ion-conductive.⁹¹ Other than that, many ILs share an almost negligible vapor pressure, a wide liquid range, incombustibility, and good thermal and electrochemical stability.⁸⁹ It was these properties in particular, which sparked the recent interest in their exploration, as, despite often being toxic, their low volatility and thus reduced risk of contaminating the environment renders them promising alternatives to traditional organic

solvents in sustainable technologies and processes. An estimated number of one million possible ion combinations are thought to form ILs.¹⁰² Hence, synthesizing a new ionic liquid is generally not a difficult task. However, not all ionic liquids exhibit desirable properties and an exhaustive search approach to their synthesis is not feasible. Instead, a rational design based on predicting their properties would be preferable and enabling this is a major goal of current research.⁸⁹ Alkyl chain elongation and ion functionalization are common strategies to influence IL behavior by modifying their constituent ions.¹⁰³ In order to fully exploit their potential as tunable “designer solvents”, a strong understanding of their fundamental structure–property relationships is required. Due to the complexity of their intermolecular interactions, this can best be achieved with the aid of computational methods.^{32,89,104}

1.2.1 Protic Ionic Liquids

A special subgroup of the IL solvent class is comprised of those ILs that are formed by a proton transfer reaction between a Brønsted acid and a Brønsted base according to



Although the equilibrium is usually located far on the right, i.e., ionic side of that reaction, the proton has a certain degree of mobility in such materials, leading to their characterization as protic ionic liquids (PILs). They are frequently used in the study of proteins and protein protein folding,^{105,106} as they have shown great potential as both protein stabilizers¹⁰⁷ and additives for protein refolding,¹⁰⁸ tunable by the choice of their constituent ions. The mobility of the proton makes PILs attractive candidates for proton-conducting electrolytes in fuel cells.^{109,110} While their range of properties is similarly variable as in aprotic ILs, their proton conductivity is a common characteristic of PILs. However, a high proton mobility often comes with a low degree of proton transfer and, thus, a certain amount of neutral acid and base species in the liquid phase. In addition to lowering the ionicity by reducing the effective number of charge carriers in the system,¹¹¹ the presence of the neutral parent species has detrimental effects on exactly those properties that are usually desired in ILs, such as their low vapor pressure, vast liquid range, and conductivity.^{112,113} On the other hand, a highly mobile proton could potentially enable particularly high proton conductivities through Grotthuss-like structural diffusion.^{114,115} Yoshizawa et al. suggested the $\Delta\text{p}K_{\text{a}}$ value, which is the difference between the $\text{p}K_{\text{a}}$ values of a PIL’s constituent acid and protonated base

$$\Delta\text{p}K_{\text{a}} = \text{p}K_{\text{a}}(\text{HB}^+) - \text{p}K_{\text{a}}(\text{HA}) \quad (1.2)$$

1. Introduction

as an approximate measure for the degree of proton transfer.¹¹⁶ They could find good correlations between the ΔpK_a value of PILs and some of their properties such as their boiling point, glass transition temperature, and Walden behavior. However, pK_a values are usually measured in aqueous solutions and their applicability to non-aqueous systems is uncertain. The protonated base and deprotonated acid are stabilized in the aqueous phase by a strong hydration shell, but the same stabilization does not occur in PILs. Indeed, it was found that the acidity of carboxylic acids in various alkylimidazolium-based PILs follows the sequence of propanoic > ethanoic > methanoic acid, opposite to their behavior in water.¹¹⁷ To truly understand the proton transfer in PILs, it must be evaluated in the PIL itself. Some experimental efforts to quantify the proton transfer degree on a consistent scale, similar to the pH scale in aqueous solution, were made in the past.^{118–120} Byrne and Angell used the $\delta(N - H)$ proton chemical shift in a range of alkylammonium-based PILs to assess their proton activity.^{105,118} While it was shown that PILs do not necessarily follow the Hofmeister series for protein stability,¹²¹ Byrne and Angell could tune the folding behavior of proteins with remarkable accuracy by adjusting the proton activity as measured by $\delta(N - H)$.^{105,118} However, their approach makes comparison between PILs with different types of cations difficult. Kanzaki et al. used potentiometric methods to directly measure the concentration of neutral species in various PILs.^{122–125} While their results correlate well with ΔpK_a values, their approach was recently criticized¹¹¹ as it is itself based on the assumption that aqueous acid strengths are valid in ILs, which was shown to be not always true,^{117,122} and disregards possible trace amounts of water. Computational investigations of proton transfer equilibria in PILs are sparse and mostly limited to single ion or ion pair calculations to support experimental studies.^{126–129} More ambitious investigations by computational methods could offer valuable insights into the dynamics of the proton transfer reaction in PILs and help establishing structure–property relationships. This is the aim of Chapters 5 and 6, which present approaches to calculate the proton transfer degree in PILs based on bQCE and AIMD, respectively.

1.2.2 Ion Pairing and Ionicity

As stated earlier, the intermolecular interactions of ILs are complex and their study must proceed through close cooperation of experiment and theory. Indeed, even the very nature of their molecular level structure as either mostly neutral ion pairs or relatively independent ions is still subject of debate and a striking example of how different approaches may lead to opposite pictures.^{131–133} Being liquids composed entirely of cations and anions, it is conceivable that oppositely charged ions associate to form neutral aggregates. Speculations about significant ion pairing in ILs first emerged because measured conductivities often undercut expectation.¹³⁰ This is often illustrated in form of the Walden plot,¹³⁴ as

shown in Fig. 1.3. The Walden plot compares the relationship between an molar conductivity of an IL and its viscosity to an ideal reference electrolyte. ILs typically fall somewhere below the ideal reference line and their vertical distance from the reference is sometimes used as an approximate measure of ionicity.^{116,133,135} ILs that fall significantly below the expected value, such as [N₂₀₀₀][OFm] and [HC₁Im][OAc] in Fig. 1.3, are considered subionic.¹¹⁶ The ionicity is defined as the effective ratio of charge carrying species in an IL that contribute to its conductivity. It is calculated as the ratio between the measured conductivity and the expected conductivity based on the ionic self-diffusion coefficients.¹³⁰ Many ILs were found to have low ionicity and various effects are hypothesized to play a role, including ion pairing,^{130,132,136} charge transfer,^{137–139} and ion size effects on diffusion.¹³³ Gebbie et al. proposed a picture of ILs as diluted electrolytes consisting mainly of neutral ion pairs and only a small amount of 0.003% of “free” ions based on direct surface force measurements.^{132,140} They criticized the ion pairing interpretation of the ionicity scale, as it leads to free ion concentrations several orders of magnitude higher than their own estimate. At the same time, the ion pairing interpretation is criticized from the other side as various experimental^{141,142} and computational^{143–145} studies find no evidence for any amount of significant formation of long-lived ion pairs. Finding a conclusive answer to the question of ion pairing in ILs is important as it has some implications on their design and application as electrolytes as solvents in chemical synthesis,³¹ where the formation and stabilization of ions or transition states is a major consideration. Chapter 8 contributes to that aim by reviewing the available experimental and computational evidence and analyzing the dynamics of ion pairing in 1-butyl-3-methylimidazolium triflate. Afterwards, a more application-related situation is considered in Chapter 9, which focuses on the coordination and ion association of Mg²⁺ cations in an IL-based electrolyte (see following section).

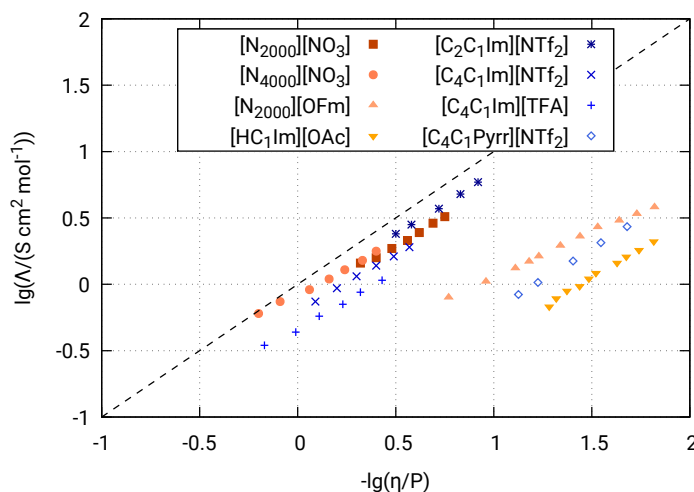


Figure 1.3: Walden plot of various protic¹⁰⁹ (orange) and aprotic¹³⁰ (blue) ILs.

1.2.3 Ionic Liquids in Energy Devices

Due to their inherent conductivity, generally low volatility, and good electrochemical stability, ILs have received significant attention as potential electrolytes and solvents in electrochemical applications, including batteries,^{146,147} super-capacitors,^{148,149} and solar cells.¹⁵⁰ Different battery types have been investigated in combination with ILs as electrolyte materials. Lithium-ion batteries in particular have found widespread use for their high energy density and low self-discharge, allowing their use in mobile devices.²⁰ Commercial lithium-ion batteries use organic electrolytes, which gives rise to some safety concerns especially in high temperature applications such as electric vehicles due to their volatility and flammability.¹⁵¹ Next to solid-state electrolytes, which show promising properties and drastically reduce safety concerns,³⁰ ILs have been investigated as electrolytes in lithium-ion batteries.¹⁴⁷ However, some considerations motivate the research on alternative battery technologies. Renewable energy sources and electric mobility require high long-term energy storage capacity at low mass and volume,²⁰ which may be achieved through metal-air batteries.¹⁵² While lithium-air batteries feature a theoretical energy density that can compete with gasoline,¹⁵³ concerns about the ecological impact of lithium mining and its limited availability drive the research on battery technologies based on more abundant metals.²⁴

Magnesium-air (Mg-O_2) batteries are a promising alternative due to their high volumetric and specific energy density, low cost, and eco-friendliness.¹⁵⁴ In contrast to lithium-ion batteries, the metal-air cell contains a pure metal anode, at which the solute metal dissolves under discharge and deposits during charge. Atmospheric oxygen in the surrounding air serves as active cathode material. However, the realization of a truly rechargeable Mg-O_2 battery is complicated by the formation of insulating MgO and MgO_2 film, the slow kinetics of the oxygen reduction reaction, and unwanted reactions with the electrolyte.^{154,155} Research on rechargeable magnesium-air batteries is sparse but some advances could be achieved in recent years.^{22,155,156} Water saturated trihexyl(tetradecyl)phosphonium chloride ($[\text{P}_{6,6,6,14}][\text{Cl}]$) was tested as an IL-based electrolyte for Mg-O_2 batteries with promising results.¹⁵⁷ The IL forms a semi-passive interfacial layer on the magnesium anode, stabilizing it while still allowing discharge.¹⁵⁸ In general, the tendency of the magnesium anode to form passivating layers through decomposition of the electrolyte is another obstacle to the realization of Mg batteries.¹⁵⁹ Approaches to improve the reversibility of Mg deposition in molecular^{160,161} and ionic^{162,163} often include the addition of chelating^{164,165} or water-scavenging^{166,167} additives. This is also the focus of Chapter 9, in which the positive effects of two additives on the Mg deposition and dissolution reversibility in an IL-based electrolyte are studied in a combined experimental and theoretical investigation.

1.3 Scope of the Thesis

As was illustrated earlier, there is an enormous interest in the design of novel and sustainable solvent media. Ionic liquids are considered a promising candidate to substitute or complement traditional molecular solvents, but the immense variations in their physico-chemical properties necessitate a rigid understanding of their structure–property relationships. While many such relationships could be established in the past by experimental and computational means, their investigation is as vital now as before to enable the rational design of IL-based materials for a specific application. A computational approach to that end must aim to model the liquid phase and liquid phase phenomena in a realistic environment. While many theoretical methods to model the liquid phase exist, developing new approaches can facilitate the study of certain properties and phenomena that are difficult to access with other methods, such as proton transfer equilibria.

Therefore, this thesis will follow two main objectives. The first and more general objective is the study of liquids at the molecular level, using theoretical methods to establish a microscopic interpretation of their macroscopic properties. The focus here will be on ILs, whose properties – especially if compared against the vast range of IL systems yet to discover – remain widely uncharted. The second objective is the development and extension of the bQCE method as an alternative approach to model liquids with quantum chemical methods in a computationally efficient way. Though the QCE method has been thoroughly established for neat protic polar solvents, its binary extension and applicability to other compound classes were tested for only few cases. Therefore, under this second objective the focus will be on traditional molecular solvents, as they are generally more simple and well studied than ILs and thus better suited as case studies.

The first part of the thesis describes the application of the bQCE method to a range of binary organic solvent mixtures in order to test the applicability of the method to these systems and its ability to describe their mixing behavior. The studies presented in this part aim for computational efficiency to ensure feasibility of the approach even when applied to more complex systems such as ILs.

The second part contains three studies on proton transfer equilibria in different systems. These include ionic, molecular, and, bridging the gap between both, pseudo-ionic liquids. The proton transfer equilibrium in PILs has received little attention from theoretical research despite its empirical correlation with many physico-chemical properties. This part presents the first attempts to quantify the proton transfer degree in PILs and pseudo-PILs with theoretical methods.

The third part deals with ionicity and ion association in ILs. First, the concept of ion pairing in neat ILs and its implications for ionicity are discussed. Thereafter, the effect of additives on the coordination sphere of solute Mg^{2+} cations in an IL-based electrolyte is studied to explain their impact on the reversibility of Mg deposition and dissolution.

2 Methodology

2.1 Classical Force Fields

Classical molecular dynamics (MD) describe molecular and atomic motion based on Newton’s laws of motion and provide a computationally efficient method of simulating large systems with thousands of atoms at high speeds. Throughout this thesis, classical MD simulations will be used only as pre-equilibration method for AIMD simulations (Chapter 6) and static quantum chemical calculations (Chapter 9). However, several studies presented in this thesis (Chapters 3–5 and Chapter 7) make use of the genetic global structure optimization algorithm OGOLEM,^{168,169} which relies on the force-field-based description of molecular interactions. Therefore, this section will provide a brief overview of the relevant equations and expressions of a typical force field, but will not cover more involved aspects of MD theory. In this thesis, the generalized AMBER force field¹⁷⁰ (GAFF) and the OPLS-AA force field¹⁷¹ are used, which rely mostly on the same expressions. The following equations are therefore not general to all classical force fields, but are commonly used and describe the force fields used in this thesis.

In a system of N particles, the force field energy $E(r_1, r_2, \dots, r_N)$ is a function of all $3N$ particle coordinates. The analytical expression for the force field contains a set of equations and parameters, that account for different forces acting upon the particles. It may be expressed as a sum of contributions, which describe the energy corresponding to a specific distortion or interaction type of the molecule:

$$E = E_{\text{str}} + E_{\text{bend}} + E_{\text{tors}} + E_{\text{vdw}} + E_{\text{el}}, \quad (2.1)$$

where E_{str} is the bond stretching energy, E_{bend} is the angle bending energy, and E_{tors} is the torsional rotation energy. These can be categorized as bonded interactions. The non-bonded contributions E_{vdw} and E_{el} represent the van der Waals energy and electrostatic interaction energy, respectively.

The bonded interaction potentials are often, and throughout this thesis, treated by harmonic expressions, but more complex descriptions are possible in principle. The harmonic bond stretching energy is calculated as

$$E_{\text{str}} = K_{ij}^r (r_{ij} - r_0)^2, \quad (2.2)$$

2. Methodology

where K_{ij}^r is the force constant corresponding to the bond type between particles i and j , $r_{ij} = |r_i - r_j|$ is the inter-particle distance, and r_0 is the equilibrium bond length. The angle bending energy depends on the angle θ_{ijk} that is formed between the vectors r_{ij} and r_{jk} . It is given by

$$E_{\text{bend}} = K_{ijk}^{\theta} (\theta_{ijk} - \theta_0)^2, \quad (2.3)$$

where K_{ijk}^{θ} is the force constant corresponding to the angle type between particles i , j , and k and θ_0 is the equilibrium angle. The torsional rotation energy depends on the dihedral angle ϕ_{ijkl} between four bonded atoms i , j , k , and l . It is treated differently by GAFF and OPLS-AA:

$$E_{\text{tors}}^{\text{GAFF}} = K_{ijkl}^{\phi} (1 + d \cos(n\phi_{ijkl})) \quad (2.4)$$

$$E_{\text{tors}}^{\text{OPLS}} = \sum_{n=1}^4 \frac{K_{ijkl}^{\phi,n}}{2} (1 + (-1)^n \cos(n\phi_{ijkl})), \quad (2.5)$$

where in the GAFF description K_{ijkl}^{ϕ} is the force constant corresponding to the dihedral type of ϕ_{ijkl} , d is either -1 or 1 , and n is the phase. The OPLS-AA expression allows the summation of up to four dihedral torsion profiles, where $K_{ijkl}^{\phi,n}$ is the force constant corresponding to the n th phase.

The non-bonded interaction energies E_{vdw} and E_{el} are given by the same expressions in both force fields. To describe van der Waals interactions, the Lennard-Jones potential is used ($E_{\text{vdw}} = E_{\text{LJ}}$):

$$E_{\text{LJ}} = 4\epsilon \left[\left(\frac{\sigma_{ij}^{12}}{r_{ij}} \right) - \left(\frac{\sigma_{ij}}{r_{ij}} \right)^6 \right], \quad (2.6)$$

where σ_{ij} is the distance at which E_{LJ} is 0, which is commonly identified as the particle diameter, and ϵ is the depth of the potential energy well. The electrostatic interaction energy E_{el} is given by the Coulomb potential:

$$E_{\text{el}} = \frac{q_i q_j}{4\pi\epsilon_0 r_{ij}}, \quad (2.7)$$

where q_a and q_b are the charges of the interacting particles, r is the inter-particle distance, and ϵ_0 is the vacuum permittivity.

With Eqs. (2.2) to (2.7), the full analytical expression of the force field energy is known as defined by Eq. (2.1). Chapters 3 to 5 and Chapter 7 use the GAFF description in combination with a genetic global minimum structure algorithm as a computationally efficient way to sample thousands of potential cluster geometries. Chapters 6 and 9 use the OPLS-AA force field in molecular dynamics simulations as pre-equilibration for subsequent quantum chemical calculations.

2.2 Static Quantum Chemical Calculations

In 1926, Austrian physicist Erwin Schrödinger postulated an equation that describes the wave function of a quantum-mechanical system and could explain the hydrogen spectral series.¹⁷² The time-independent form of the Schrödinger equation

$$\mathbf{H}\Psi = E\Psi \quad (2.8)$$

is the fundamental expression of quantum chemistry. It states that the energy E of a system described by the wave function Ψ is an eigenvalue of the Hamilton operator \mathbf{H} :

$$\mathbf{H} = \mathbf{T} + \mathbf{V}, \quad (2.9)$$

where \mathbf{T} and \mathbf{V} are the operators of kinetic and potential energy, respectively. Molecules and even atoms are many-particle systems of electrons and nuclei and suitable approximations must be made for all but the most simple systems to allow finding a solution to the Schrödinger equation. The Born–Oppenheimer approximation makes the assumption that, because of their much greater weight and slower movement, nuclei appear stationary in the reference frame of the electron.¹⁷³ This assumption allows a separation of the motion of electrons and nuclei and, thus, calculating only the electronic component Ψ_e of the wave function, which omits the kinetic energy operator of the nuclei \mathbf{T}_n . The electronic Hamilton operator can then be written as

$$\mathbf{H}_e = \mathbf{T}_e + \mathbf{V}_{ne} + \mathbf{V}_{ee} + \mathbf{V}_{nn}, \quad (2.10)$$

where \mathbf{T}_e denotes the electronic kinetic energy operator, \mathbf{V}_{ne} the electron-nucleus interaction operator, \mathbf{V}_{ee} the electron-electron interaction operator, and \mathbf{V}_{nn} the nucleus-nucleus interaction operator. The electron-electron coupling prevents an analytical solution for systems with more than one electron. Strategies of calculating the energy of the electronic system are based on a set of suitable approximations, that allow an approximate solution of the Schrödinger equation. In computational chemistry, these strategies are usually based on wave function theory (WFT), density functional theory (DFT) or a hybrid approach, utilizing both theories.

Methods based on WFT usually use the Hartree–Fock self-consistent-field procedure as a starting point.^{174,175} Within the Hartree–Fock approach the electron-electron interactions are approximated by treating the motion of an electron in the mean-field created by the other electrons. The wave function can then be represented as a single Slater determinant of one-electron wave functions, allowing the approximate evaluation of the electronic energy. Due to the omission of contributions by electron correlation, the Hartree–Fock method underestimates the total electronic energy of the system. So-called post-

2. Methodology

Hartree–Fock methods such as Møller–Plesset perturbation theory (MP), coupled cluster (CC), and configuration interaction (CI) are based on the Hartree–Fock wave function as the ground state and account for electron correlation by introducing additional terms.

In this thesis, strategies to obtain the electronic energy as an approximate solution to the Schrödinger equation are predominantly based on DFT. The DFT approach is based on the proof by Hohenberg and Kohn¹⁷⁶ that the ground-state electronic energy is a functional of and, thus, determined completely by the electron density ρ . In principle, this simplifies the problem drastically, as instead of the $3N$ coordinates required by the wave function of an N -electron system, the electron density is a function of only three coordinates, regardless of the number of electrons. The prime objective of DFT is therefore the determination of the electron density in the system rather than its wave function. With the appropriate functional, the electronic energy and related properties of the system can be obtained directly from the electron density. However, the exact nature of that functional is not known. Therefore, DFT methods use functionals that approximate the unknown exact functional by different approaches.

The basic strategy to obtain the electron density ρ is based on an approach suggested by Kohn and Sham.¹⁷⁷ They constructed a fictive reference system of non-interacting electrons that reproduces the ground-state electronic density of a given system of interacting electrons. The wave function of the non-interacting electrons is represented as a single Slater determinant of N one-electron wave functions $\phi_i(\mathbf{r})$, similar to the Hartree–Fock approach. The electron density is then given by

$$\rho(\mathbf{r}) = \sum_{i=1}^N |\phi_i(\mathbf{r})|^2. \quad (2.11)$$

In analogy to Eq. 2.10 the energy functional $E[\rho]$ can be divided into different contributions to the total energy:

$$E[\rho] = T[\rho] + E_{\text{ne}}[\rho] + E_{\text{ee}}[\rho] \quad (2.12)$$

where $T[\rho]$ is the kinetic energy functional, $E_{\text{ne}}[\rho]$ the nuclei-electron interaction functional, and $E_{\text{ee}}[\rho]$ the electron-electron interaction functional. The electron-electron interaction is further divided into a Coulomb part $J[\rho]$ and an exchange part $K[\rho]$. Evaluation of the kinetic energy of the electronic system $T[\rho]$ is problematic. It is approximated as the kinetic energy of the system of non-interacting electrons $T_S[\rho]$. The difference between the exact kinetic energy and its estimate is fused with the exchange part into the exchange-correlation functional $E_{\text{xc}}[\rho]$. The DFT energy expression can then be written as:

$$E_{\text{DFT}}[\rho] = T_S[\rho] + E_{\text{ne}}[\rho] + J[\rho] + E_{\text{xc}}[\rho]. \quad (2.13)$$

While the explicit expressions for all other terms in Eq. 2.13 are known, this is not the case for $E_{\text{xc}}[\rho]$. The various density functionals used in computational chemistry

(which all approximate the unknown exact functional in Eq. 2.12) can be categorized by their approach to estimate the exchange-correlation contribution. The most common approaches include the local density approximation (LDA), generalized gradient approximation (GGA), and hybrid functionals. LDA functionals are based only on the electron density itself. They assume at any given point that the electron density is homogeneous, i.e., the same everywhere. This typically leads to an underestimation of the exchange energy and overestimation of the correlation energy. A better estimate is achieved by the computationally more demanding GGA functionals (e.g., BP86^{178,179}), which include the density gradient in their description. By including contributions from the Hartree–Fock exchange energy, hybrid functionals (e.g., B3LYP¹⁸⁰) achieve a very accurate description, but are also computationally more demanding than LDA and GGA functionals.

2.3 Quantum Cluster Equilibrium Theory

The underlying theory of the QCE method was first published by Weinhold in 1998³⁶ and later described in more detail by Barbara Kirchner.³⁸ Weinhold describes a cluster as a characteristic configuration of molecules that lies between the limits of an isolated monomer species in the gas phase and the aggregated state in the condensed phase. He argues that the existence of the critical phase, in which the gas phase and liquid phase become indistinguishable, implies that the description of a system as a dense gas of clusters can be seamlessly expanded to the fluid phase by continuously adjusting the cluster distribution to the gradually changing pressure and temperature.

In 2011, the theory was extended to binary liquids by the Kirchner group.⁴³ The introduction of the binary QCE method (bQCE) opened the cluster approach to an enormous number of new possible applications such as the description of protic ionic liquids or molecular mixtures. This thesis will, for the first time, describe the next major extension from binary liquids to general multi-component systems (mQCE). Although this extension introduces a wide variety of new applications, such as mixtures of ionic liquids with organic solvents or with each other, and will hopefully contribute greatly to future studies, it is not part of the works presented in this thesis which are instead based on bQCE theory. Therefore, this chapter will first introduce the reader to the binary form of QCE theory. Afterwards, the extension to general multi-component systems will be documented for future reference.

The bQCE theory will be derived for the canonical ensemble. Therefore, the system is characterized by the particle number N , the volume V , and the temperature T . In the following, all thermodynamic functions are assumed to be functions of these parameters (or a selection thereof), even when not explicitly stated. For the sake of readability the explicit mention of function variables will be omitted, e.g., $Q(N, V, T) = Q$ for the partition function.

2.3.1 Statistical Thermodynamics

For a canonical ensemble with a total number of particles N , volume V , and temperature T the probability of finding the system in a state with energy E_j is given by the Boltzmann factor

$$p_j \propto e^{-\frac{E_j}{k_B T}}, \quad (2.14)$$

where k_B is the Boltzmann constant. The sum of all probabilities p_j must fulfill the condition $\sum_j p_j = 1$. The normalizing constant is then $1/Q$, where Q is called the partition function of the system:

$$Q = \sum_j e^{-\frac{E_j}{k_B T}}. \quad (2.15)$$

The partition function Q is the central quantity of the QCE model. It allows calculation of all thermodynamic state functions of a system. For example, the average energy $\langle E \rangle$ can be derived from the partition function over

$$\langle E \rangle = \sum_j p_j \cdot E_j = \sum_j \frac{e^{-\frac{E_j}{k_B T}}}{Q} \cdot E_j. \quad (2.16)$$

Differentiating $\ln Q$ with respect to the temperature T gives

$$\left(\frac{\partial \ln Q}{\partial T} \right) = \frac{1}{Q} \left(\frac{\partial Q}{\partial T} \right) = \frac{1}{k_B T^2} \sum_j \frac{e^{-\frac{E_j}{k_B T}}}{Q} \cdot E_j. \quad (2.17)$$

From comparing Eqs. (2.16) and (2.17) it is obvious that

$$\langle E \rangle = k_B T^2 \left(\frac{\partial \ln Q}{\partial T} \right). \quad (2.18)$$

All thermodynamic potentials can be calculated from similar expressions. The partition function of a system of indistinguishable particles may be written as

$$Q = \frac{1}{N!} q^N, \quad (2.19)$$

where $q(V, T)$ is the partition function of a single particle.* Assuming that the energy ε of a molecule can be split according to its degrees of freedom

$$\varepsilon = \varepsilon^{\text{trans}} + \varepsilon^{\text{rot}} + \varepsilon^{\text{vib}} + \varepsilon^{\text{elec}}, \quad (2.20)$$

*Equation (2.19) is valid, if the number of particles N is much smaller than the number of possible states with an energy lower than $k_B T$.¹⁸¹ If this condition is met, the system obeys Boltzmann statistics. Fluids at room temperature usually fulfill this criterion.

2. Methodology

we can write the molecular partition function $q(V, T)$ as

$$q = q^{\text{trans}} q^{\text{rot}} q^{\text{vib}} q^{\text{elec}}. \quad (2.21)$$

The particle partition functions of translation, rotation and vibration can be derived from standard expressions for the particle in a box, the rigid rotator, and the harmonic oscillator:

$$q^{\text{trans}} = \frac{V}{\Lambda^3} \quad \text{with} \quad \Lambda = \sqrt{\frac{h^2}{2\pi m k_B T}}, \quad (2.22)$$

$$q^{\text{rot}} = \frac{\pi^{1/2}}{\sigma} \sqrt{\frac{T^3}{\Theta_A^{\text{rot}} \Theta_B^{\text{rot}} \Theta_C^{\text{rot}}}} \quad \text{with} \quad \Theta_j^{\text{rot}} = \frac{h^2}{8\pi^2 I_j k_B}, \quad (2.23)$$

$$q^{\text{vib}} = \prod_{i=1}^{3N-x} \frac{e^{-\Theta_i^{\text{vib}}/2T}}{1 - e^{-\Theta_i^{\text{vib}}/T}} \quad \text{with} \quad \Theta_i^{\text{vib}} = \frac{h\nu_i}{k_B}, \quad (2.24)$$

where h is the Planck constant, m the particle mass, σ the rotational symmetry number, I_j the moment of inertia, $3N - x$ the number of vibrational degrees of freedom, and ν_i the vibrational frequency of the i th normal mode. Assuming that under the applied conditions molecules are in the electronic ground state, the electronic partition function is calculated from the ground state energy $\varepsilon_1^{\text{elec}}$ only:

$$q^{\text{elec}} = g_1 e^{-\frac{\varepsilon_1^{\text{elec}}}{k_B T}}, \quad (2.25)$$

where g_1 is the degeneracy of the ground state.

2.3.2 Binary Quantum Cluster Equilibrium Theory

Equations (2.21)–(2.25) provide all relevant expressions required to build up the bQCE theory. The bQCE method describes the liquid phase as a dense gas of interacting molecular clusters. Within the scope of the bQCE method, a cluster is built up from one or more monomers of one (neat systems) or two (binary systems) components. The cluster gas is assumed to be in thermodynamic equilibrium in which clusters may form and disaggregate. The equilibrium reaction may be expressed as



where A and B are the monomers of components a and b , respectively. In the following, a cluster of the form $A_n B_m$ will be given the general label P_i , where i is an index running from 1 to K , the total number of clusters. The monomers A and B are assigned the

indices 1 and 2, respectively. The equilibrium reaction may then be written in the general form



where n_i^a and n_i^b are the number of monomers of components a and b in the cluster P_i , respectively. It should be noted that this formulation permits the presence of multiple clusters of the same composition, allowing the inclusion of different conformations and interaction motifs at the same cluster size, such as ring and chain structures. The goal is then to find a distribution $\{N_i\}$ of all clusters P_i that, at a given state with volume V , temperature T , and particle number $N^{\text{tot}} = N_1^{\text{tot}} + N_2^{\text{tot}}$, minimizes free energy F of the system:

$$F = -k_B T \ln Q. \quad (2.28)$$

The total partition function Q of a system of molecular clusters is given by

$$Q = \prod_i^L \frac{1}{N_i!} q_i^{N_i}, \quad (2.29)$$

where N_i and q_i are the population and the total cluster partition function of a cluster P_i , respectively, and L is the total number of clusters in the cluster set. Analogous to Eq. (2.21), the cluster partition function is given by

$$q_i = q_i^{\text{trans}} q_i^{\text{rot}} q_i^{\text{vib}} q_i^{\text{elec}}. \quad (2.30)$$

The cluster partition functions of translation, rotation, and vibration are calculated according to Eqs. (2.22)–(2.24). Together with the electronic partition function q_i^{elec} they represent the degrees of freedom of the cluster. The electronic partition function is obtained from the adiabatic interaction energy of the electronic system of the cluster

$$\Delta_{\text{bind}} \varepsilon_i^{\text{elec}} = \varepsilon_i^{\text{elec}} - n_i^a \varepsilon_1^{\text{elec}} - n_i^b \varepsilon_2^{\text{elec}} \quad (2.31)$$

where $\varepsilon_i^{\text{elec}}$ is the electronic ground state energy of the cluster P_i . It is extended by an additional term that introduces the inter-cluster interaction energy in form of an attractive mean-field energy weighted by the phase volume and cluster size. It is then calculated as

$$q_i^{\text{elec}} = \exp \left\{ - \frac{\Delta_{\text{bind}} \varepsilon_i^{\text{elec}} - (n_i^a + n_i^b) \frac{a_{\text{mf}}}{V}}{k_B T} \right\}, \quad (2.32)$$

where, a_{mf} is the empirical mean-field parameter. It has the dimension energy \cdot volume and describes the average inter-cluster interaction.

In addition, since molecular clusters are non-punctiform particles, the volume V in the translational partition function q_i^{trans} requires a correction to account for the cluster vol-

2. Methodology

ume v_i . The combined volume of all clusters in the system is called the exclusion volume V_{ex} and is inaccessible to translation. It is given by

$$\begin{aligned} V_{\text{ex}} &= b_{\text{xv}} \sum_i^L N_i v_i = b_{\text{xv}} \sum_i^L N_i (n_i^a v_1 + n_i^b v_2) \\ &= b_{\text{xv}} (v_1 N_1^{\text{tot}} + v_2 N_2^{\text{tot}}). \end{aligned} \quad (2.33)$$

The proportionality constant b_{xv} is a dimensionless empirical parameter, that is required to correctly scale the particle volume, since cluster volume schemes are often highly sensitive to the choice of atomic radii.⁵² The translational partition function is then extended to

$$q_i^{\text{trans}} = \frac{V - b_{\text{xv}}(v_1 N_1^{\text{tot}} + v_2 N_2^{\text{tot}})}{\Lambda^3}. \quad (2.34)$$

Equations (2.22)–(2.24) and (2.29)–(2.34) provide all necessary expressions to describe the cluster gas. To calculate the partition function and obtain physically meaningful thermodynamic data from it, all independent quantities ($\{N_i\}, V, T$) that characterize the canonical ensemble must be known. Furthermore, the empirical parameters a_{mf} and b_{xv} must be chosen in a sensible way. In practice, they are optimized so that the deviation of bQCE results from an experimental reference, such as density and boiling point, is minimized. The choice and optimization of these parameters is described in more detail in Sec. 2.4. To determine the independent properties, we will first consider the conservation of the particle numbers N_1^{tot} and N_2^{tot} as required by the canonical ensemble:

$$\begin{aligned} N_1^{\text{tot}} + N_2^{\text{tot}} &= \sum_i^L (n_i^a + n_i^b) N_i, \\ 0 &= \sum_i^L \frac{(n_i^a + n_i^b) N_i}{N_1^{\text{tot}} + N_2^{\text{tot}}} - 1 = \sum_i^L \tilde{N}_i - 1. \end{aligned} \quad (2.35)$$

Here, \tilde{N}_i is called the monomer-normalized cluster population, which is the quantity that is depicted in the various population plots presented in later chapters. Equation (2.35) shows that the sum in Eq. (2.33) is constant. Thus, the exclusion volume V_{ex} introduces no population dependency to the cluster partition function q_i^{tot} . Since the system is required to be in thermodynamic equilibrium, an infinitesimal change in the population of a cluster i must not affect the free energy F :

$$0 = \sum_i^L n_i^a \frac{\partial F}{\partial N_1} d\lambda + \sum_i^L n_i^b \frac{\partial F}{\partial N_2} d\lambda - \sum_i^L \frac{\partial F}{\partial N_i} d\lambda. \quad (2.36)$$

Herein, $d\lambda$ is the progress of reaction. Equation (2.36) expresses that any change in the free energy F caused by an infinitesimal number of clusters P_i disaggregating into monomers

of their respective components, must be balanced by an equal change in the free energy caused by an infinitesimal increase in the monomer populations. Equation (2.36) must be fulfilled for any $d\lambda$ and for each cluster i independently. Thus, Eq. (2.36) can be simplified and rearranged to

$$\frac{\partial F}{\partial N_i} = n_i^a \frac{\partial F}{\partial N_1} + n_i^b \frac{\partial F}{\partial N_2}. \quad (2.37)$$

With

$$F = -k_B T \ln Q^{\text{tot}} \quad (2.38)$$

and

$$\ln Q = \ln \left(\prod_i^L \frac{1}{N_i!} q_i^{N_i} \right) = \sum_i^L (N_i \ln q_i - \ln N_i!), \quad (2.39)$$

Equation (2.37) can be rearranged to

$$\begin{aligned} \frac{\partial}{\partial N_i} \sum_i^L (N_i \ln q_i - \ln N_i!) &= n_i^a \left(\frac{\partial}{\partial N_1} \sum_i^L (N_i \ln q_i - \ln N_i!) \right) \\ &+ n_i^b \left(\frac{\partial}{\partial N_2} \sum_i^L (N_i \ln q_i - \ln N_i!) \right) \end{aligned} \quad (2.40)$$

Using the Stirling approximation $\ln(n!) \approx n \cdot \ln(n) - n$, the differentials in Eq. (2.40) can be solved to express the direct relationship between all cluster populations N_i and the monomer populations N_1 and N_2 :

$$\begin{aligned} \ln \frac{q_i}{N_i} &= n_i^a \ln \frac{q_1}{N_1} + n_i^b \ln \frac{q_2}{N_2}, \\ N_i &= q_i \left(\frac{N_1}{q_1} \right)^{n_i^a} \left(\frac{N_2}{q_2} \right)^{n_i^b}. \end{aligned} \quad (2.41)$$

Equation (2.41) reduces the problem of finding the whole set of cluster populations $\{N_i\}$ to a much simpler goal of finding the monomer populations N_1 and N_2 . If the monomer populations are known, the task to find all other cluster populations becomes trivial, as they can be directly calculated from Eq. (2.41). By insertion of Eq. (2.41) into Eq. (2.35), the so called population polynomial³⁹ is obtained:

$$0 = \sum_i^L \frac{n_i^a + n_i^b}{N_1^{\text{tot}} + N_2^{\text{tot}}} \cdot q_i \left(\frac{N_1}{q_1} \right)^{n_i^a} \left(\frac{N_2}{q_2} \right)^{n_i^b} - 1 \quad (2.42)$$

The population polynomial is one of the key equations of the QCE model. The number of unknowns is equal to the number of components in the system. For neat systems ($N_2^{\text{tot}} = 0, n_i^b = 0$) it can be solved directly to find the monomer population N_1 . In the case of binary systems, the emergence of two unknown variables, the monomer populations

2. Methodology

N_1 and N_2 , prevents the direct solution. The conservation of mass is introduced as an additional condition:

$$\begin{aligned} M_1 N_1^{\text{tot}} + M_2 N_2^{\text{tot}} &= \sum_i^L (n_i^a M_1 + n_i^b M_2) N_i, \\ 0 &= \sum_i^L \frac{n_i^a M_1 + n_i^b M_2}{M_1 N_1^{\text{tot}} + M_2 N_2^{\text{tot}}} N_i - 1, \end{aligned} \quad (2.43)$$

where M_1 and M_2 are the molecular masses of the first and second component, respectively. By inserting Eq. (2.41) into Eq. (2.43) we obtain the so-called mass polynomial:

$$0 = \sum_i^L \frac{n_i^a M_1 + n_i^b M_2}{M_1 N_1^{\text{tot}} + M_2 N_2^{\text{tot}}} \cdot q_i \left(\frac{N_1}{q_1} \right)^{n_i^a} \left(\frac{N_2}{q_2} \right)^{n_i^b} - 1. \quad (2.44)$$

From Eqs. (2.42) and (2.44) a non-linear system of equations can be set up and solved numerically. In practice, this is achieved by employing the Newton–Raphson algorithm.¹⁸² For a given volume V , the derived equations allow the calculation of the system partition function Q for any temperature. However, the volume shall be obtained as an intrinsic property that is dependent on the cluster populations. To achieve this, we begin expressing the relationship between the pressure p and the partition function:

$$\begin{aligned} p &= -\frac{\partial F}{\partial V}, \\ 0 &= -p + k_B T \frac{\partial \ln Q}{\partial V}. \end{aligned} \quad (2.45)$$

From Eqs. (2.22)–(2.24) and Eq. (2.32) it is clear that only the electronic and translational partition functions q_i^{elec} and q_i^{trans} depend on the volume. Therefore, if differentiated by the volume, the other partition functions vanish. By inserting Eq. (2.39) and (2.30) into Eq. (2.45) and subsequent rearranging, the so-called volume polynomial is obtained:

$$\begin{aligned} 0 &= -pV^3 + \left(\sum_i^L k_B T N_i + p b_{\text{xv}} (v_1 N_1^{\text{tot}} + v_2 N_2^{\text{tot}}) \right) V^2 \\ &\quad - \left(\sum_i^L N_i (n_i^a + n_i^b) a_{\text{mf}} \right) V \\ &\quad + \sum_i^L N_i (n_1^a + n_2^b) a_{\text{mf}} \cdot b_{\text{xv}} (v_1 N_1^{\text{tot}} + v_2 N_2^{\text{tot}}). \end{aligned} \quad (2.46)$$

To solve the volume polynomial, the cluster populations N_i must be already known. However, the cluster populations can only be obtained for a given volume. To resolve this circular problem, Eqs. (2.42) and (2.46) are solved iteratively. First, the population polynomial is solved for an estimated volume. With the obtained cluster distribution $\{N_i\}$

the volume polynomial can then be solved to obtain a new volume. The difference in the Gibbs energy $|\Delta G|$ is used as convergence criterion. In the case that multiple solutions $(V, \{N_i\})$ exist, the one with the lower Gibbs energy

$$G = -k_B T \ln Q + V k_B T \frac{\partial \ln Q}{\partial V} \quad (2.47)$$

is chosen. Other thermodynamic functions such as the inner energy U , the enthalpy H and the entropy S can be derived from Q by similar expressions:

$$U = k_B T^2 \frac{\partial \ln Q}{\partial T}, \quad (2.48)$$

$$H = U + pV = k_B T^2 \frac{\partial \ln Q}{\partial T} + V k_B T \frac{\partial \ln Q}{\partial V}, \quad (2.49)$$

$$S = \frac{U - F}{T} = k_B T \frac{\partial \ln Q}{\partial T} + k_B \ln Q. \quad (2.50)$$

Furthermore, the isochoric and isobaric heat capacities c_v and c_p can be calculated:

$$c_v = \frac{\partial U}{\partial T} = 2k_B T \frac{\partial \ln Q}{\partial T} + k_B T^2 \frac{\partial^2 \ln Q}{\partial T^2}, \quad (2.51)$$

$$c_p = \frac{\partial U}{\partial T} + p \frac{\partial V}{\partial T} = c_v + p \frac{\partial V}{\partial T}. \quad (2.52)$$

2.3.3 Multi-Component Systems

Based on the theoretic framework described in the previous section, the QCE theory for multi-component systems can be derived in a similar way. The generalization of most equations is straightforward. First, we recall the equilibrium reaction between clusters in a binary system:



In a multi-component system, this equilibrium may be expressed as

$$\sum_c^K n_i^c C \rightleftharpoons P_i, \quad (2.54)$$

where n_i^c is the number of monomers C of the general component c that form the cluster P_i and K is the total number of components. The overall strategy of finding a cluster distribution $\{N_i\}$ for which the Gibbs energy G becomes minimal remains unchanged. Slight adjustments to the expressions for the adiabatic interaction energy

$$\Delta_{\text{bind}} \varepsilon_i^{\text{elec}} = \varepsilon_i^{\text{elec}} - \sum_c n_i^c \varepsilon_c^{\text{elec}} \quad (2.55)$$

2. Methodology

and the exclusion volume

$$\begin{aligned} V_{\text{ex}} &= b_{\text{xv}} \sum_i N_i v_i \\ &= b_{\text{xv}} \sum_c \sum_i N_i (n_c^i v_c) = b_{\text{xv}} \sum_c v_c N_c^{\text{tot}}. \end{aligned} \quad (2.56)$$

are sufficient to obtain the generalized forms of the electronic partition function

$$q_i^{\text{elec}} = \exp \left\{ -\frac{\Delta_{\text{bind}} \varepsilon_i^{\text{elec}} - \sum_c n_c^i \frac{a_{\text{mf}}}{V}}{k_{\text{B}} T} \right\} \quad (2.57)$$

and translational partition function

$$q_i^{\text{trans}} = \frac{V - b_{\text{xv}} \sum_c v_c N_c^{\text{tot}}}{\Lambda^3}, \quad (2.58)$$

respectively. As for binary systems, the canonical ensemble requires that the total particle number N_c^{tot} of each component is conserved:

$$\begin{aligned} \sum_c N_c^{\text{tot}} &= \sum_c \sum_i n_c^i N_i, \\ 0 &= \frac{\sum_c \sum_i n_c^i \cdot N_i}{\sum_c N_c^{\text{tot}}} - 1 = \sum_i \tilde{N}_i - 1. \end{aligned} \quad (2.59)$$

The chemical equilibrium between clusters requires that the change in the free energy F caused by an infinitesimal change in the cluster population N_i is balanced by an equal change caused by an infinitesimal change in the monomer populations N_c :

$$\frac{\partial F}{\partial N_i} = \sum_c n_c^i \frac{\partial F}{\partial N_c}. \quad (2.60)$$

In an analogous number of steps as shown in Eqs. (2.36)–(2.41) for binary systems, this leads to an expression for the direct relationship between the cluster populations N_i and the monomer populations N_c :

$$N_i = q_i \prod_c \left(\frac{N_c}{q_c} \right)^{n_c^i}. \quad (2.61)$$

Equation (2.61) allows the calculation of all cluster populations N_i if the monomer populations N_c are known. By insertion of Eq. (2.61) into Eq. (2.59), the generalized population polynomial is obtained:

$$0 = \sum_c \sum_i \frac{n_c^i}{\sum_c N_c^{\text{tot}}} \cdot \prod_c q_i \left(\frac{N_c}{q_c} \right)^{n_c^i} - 1. \quad (2.62)$$

The number of unknown monomer populations N_c is equal to the number of components K in the system. Therefore, in order to solve Eq. 2.62 for its roots N_c , a set of $K - 1$ additional equations are required. It is this obstacle, that prevented the extension of the QCE theory from binary to multi-component systems. To better illustrate this and introduce step by step the changes made to the theory, we will first consider the case of a neat system, i.e., a system of only one component ($K = 1$). In that case Eq. 2.62 reduces to

$$0 = \sum_i \frac{n_i^a q_1}{N_1^{\text{tot}}} \cdot \left(\frac{N_1}{q_1} \right)^{n_i^a} - 1 \quad (2.63)$$

and can be solved directly to find the root N_1 . In the case of binary systems ($K = 2$), the emergence of two unknown variables N_1 and N_2 , i.e., the monomer populations of the first and second component, prevents the direct solution:

$$0 = \sum_i \frac{n_i^a + n_i^b}{N_1^{\text{tot}} + N_2^{\text{tot}}} \cdot q_i \left(\frac{N_1}{q_1} \right)^{n_i^a} \left(\frac{N_2}{q_2} \right)^{n_i^b} - 1 \quad (2.64)$$

In the original formulation of the bQCE theory in 2011⁴³ and as shown in the previous section, the conservation of mass was introduced as an additional condition:

$$\begin{aligned} M_1 N_1^{\text{tot}} + M_2 N_2^{\text{tot}} &= \sum_i (n_i^a M_1 + n_i^b M_2) N_i, \\ 0 &= \sum_i \frac{n_i^a M_1 + n_i^b M_2}{M_1 N_1^{\text{tot}} + M_2 N_2^{\text{tot}}} N_i - 1, \end{aligned} \quad (2.65)$$

which by insertion of Eq. (2.61) with $K = 2$ leads to the known mass polynomial:

$$0 = \sum_i \frac{n_i^a M_1 + n_i^b M_2}{M_1 N_1^{\text{tot}} + M_2 N_2^{\text{tot}}} \cdot q_i \left(\frac{N_1}{q_1} \right)^{n_i^a} \left(\frac{N_2}{q_2} \right)^{n_i^b} - 1. \quad (2.66)$$

For binary systems, Eqs. (2.64) and (2.66) form a non-linear system of equations and can be solved numerically. Although Eq. (2.66) can easily be extended to ternary or general multi-component systems, this approach requires additional conserved quantities to set up a system of equations that matches the number of components K . One additional conserved property might be found in the total cluster volume V_{ex} . As expressed by Eq. (2.33), in the current bQCE theory all clusters occupy an impenetrable volume v_i . These cluster volumes are assumed to be integer multiples of the monomer volumes v_c . However, this assumption is due to computational efficiency rather than physical reality and may be subject to change in future implementations. Indeed, a more realistic approach that allows individual cluster volumes, thereby reducing Eq. (2.33) to its upper part and making V_{ex} dependent on cluster populations (and, thus, temperature) rather than a

2. Methodology

constant value, is currently under research. An extension to ternary systems based on the conservation of the total cluster volume is therefore not a long term solution.

The key to solving the generalized population polynomial as given by Eq. (2.62) lies in the realization that Eq. (2.65), initially written down to define the conservation of mass, can define the conservation of any general property P , regardless of its physical meaning. Indeed, as long as the condition is fulfilled, that the total mass of all clusters in the system is equal to the total mass of all monomers in the system, the exact values of M_1 and M_2 and their proportion to each other do not affect the solution of the population polynomial. However, the analytical proof for that (and for general systems) is out of the scope of this chapter and will be documented in a future publication. Based on this insight, we can formulate the conservation of a general property P in a multi-component system:

$$\sum_c P_c N_c^{\text{tot}} = \sum_c \sum_i n_i^c P_c N_i \quad (2.67)$$

$$0 = \sum_c \sum_i \frac{n_i^c P_c}{\sum_c P_c N_c^{\text{tot}}} \cdot N_i - 1. \quad (2.68)$$

By insertion of Eq. 2.61 a new form of the population polynomial is obtained:

$$0 = \sum_c \sum_i \frac{n_i^c P_c}{\sum_c P_c N_c^{\text{tot}}} \cdot \prod_c q_i \left(\frac{N_c}{q_c} \right)^{n_i^c} - 1. \quad (2.69)$$

Since P_c is not required to correspond to any real physical property, Eq. (2.69) can be solved for any number of components K by simply creating a number of K sets of linearly independent coefficients $\{P_1, P_2, \dots, P_K\}$. This allows us to create the necessary number of variations of Eq. (2.69) to set up a system of non-linear equations that can be solved by a suitable method.

With a way to solve the generalized population polynomial, the remaining equations for multi-component systems are derived analogously to the bQCE theory. The generalized volume polynomial reads

$$\begin{aligned} 0 = & -pV^3 + \left(\sum_i k_B T N_i + p b_{\text{xv}} \sum_c v_c N_c^{\text{tot}} \right) V^2 \\ & - \left(\sum_c \sum_i n_i^c N_i a_{\text{mf}} \right) V \\ & + \sum_c \sum_i n_i^c N_i a_{\text{mf}} \cdot b_{\text{xv}} \sum_c v_c N_c^{\text{tot}}. \end{aligned} \quad (2.70)$$

and is solved iteratively in turn with the population polynomial until a convergence criterion is met.

2.4 Peacemaker 2

The bQCE calculations presented throughout this thesis are performed with the Kirchner group’s open source Peacemaker 2 code, which is freely available and published under the GNU general Public License.^{8,38,39} It is written in modern Fortran (2003+) and makes no use of external libraries with the exception of Townsend’s varying string module,¹⁸³ which is published under the GNU Lesser General Public License. The code is designed following procedural and modular programming principles⁸ and easily extendable. Peacemaker 2 is currently the only publicly available QCE code and has been used in various studies on aqueous mixtures,^{8,45} organic solvent mixtures^{1,4,10} (including Chapters 3 and 4) and protic ionic liquids² (Chapter 5). It was used to study the ionic product of water⁴⁰ and mole-fraction dependent dissociation of weak acids⁵ (Chapter 7). Recently, it was also employed in the prediction of vibrational circular dichroism spectra.^{41,42}

The general structure of the Peacemaker 2 code and the QCE procedure implemented therein are illustrated in Fig. 2.1 and will be briefly expanded on. The quantum chemically obtained cluster geometries, adiabatic binding energies, and vibrational frequencies are compiled in a so-called cluster set. Environmental conditions such as the temperature range and pressure are defined by the user, together with a general set of instructions, in an input file that is parsed together with the cluster set as input to the Peacemaker 2 program. The empirical parameters a_{mf} and b_{xv} can either be predefined by the user or optimized by stepwise sampling in a rectangular grid defined by the user. This parameter sampling takes place in an outer loop encompassing the QCE main iteration (see Fig. 2.1). Within the QCE main iteration the parameters stay constant. Such an iteration consists of the following steps:

1. An initial estimate V^0 for the phase volume V is calculated based on the ideal gas law.
2. The cluster partition functions q_i are calculated at the current phase volume V and temperature T for all clusters P_i .
3. The cluster distribution $\{N_i\}$ are determined by solving the population polynomial.
4. Using the cluster distribution $\{N_i\}$, a new phase volume V is obtained from the volume polynomial.
5. The relative change in the Gibbs energy ΔG compared to the previous iteration is used as convergence criterion. If $\Delta G > \varepsilon_G$ the iteration returns to Step 2.
6. If multiple solutions $[\{N_i\}, V]$ exist, the one with the lower Gibbs energy G is chosen.

This process is repeated for every temperature in the investigated temperature range, with the change that instead of calculating a new volume estimate based on the ideal

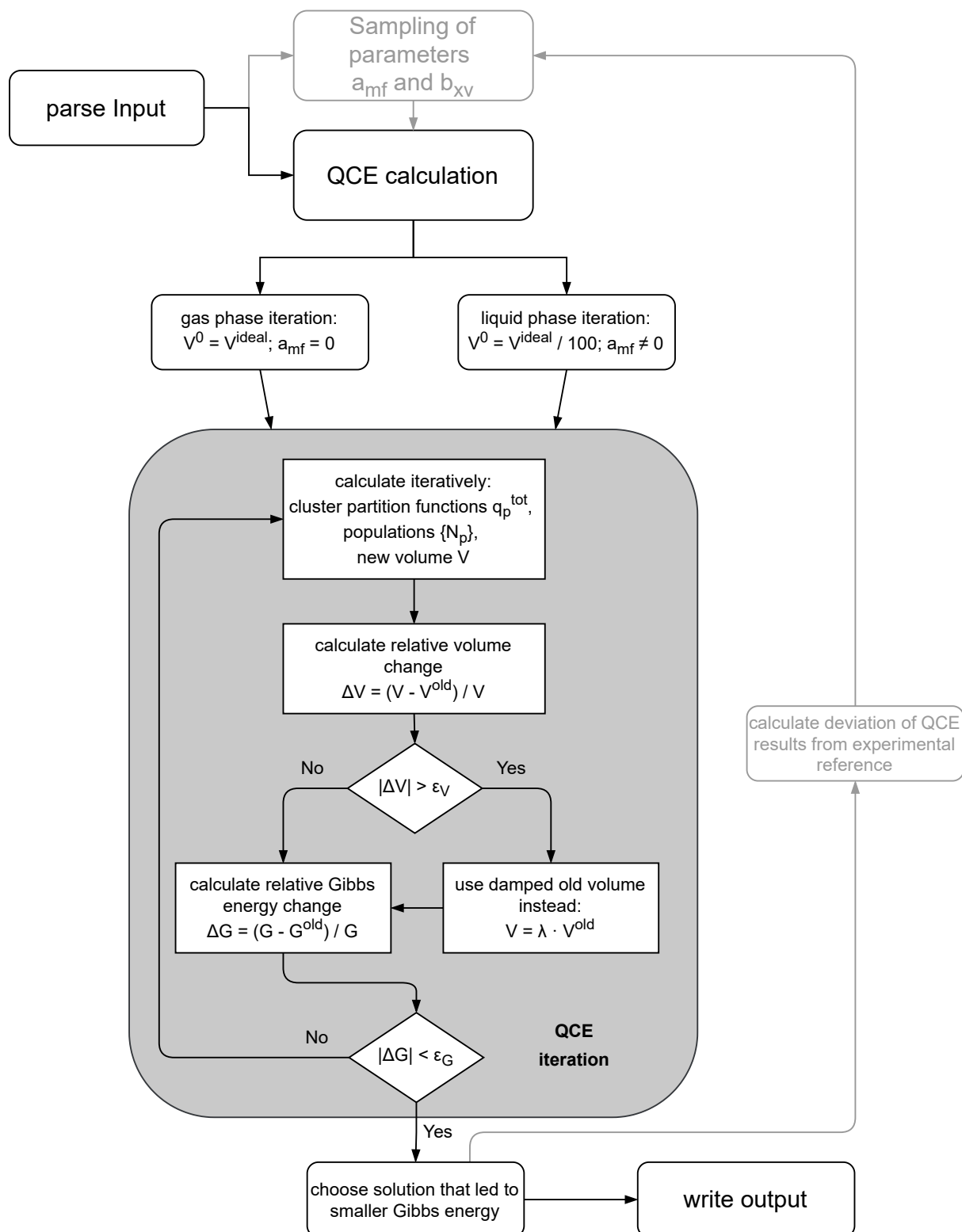


Figure 2.1: Peacemaker 2 program structure, adapted with permission from Refs. 39 and 45.

gas law, the phase volume of the previous temperature is used as initial volume guess. Furthermore, to prevent meta-stable solutions the QCE main iterations is repeated two times at any given temperature.⁴⁵ The so-called gas phase iteration uses the ideal gas volume V^{id} as initial volume guess and sets the mean-field parameter a_{mf} to 0, canceling all inter-cluster interactions. It should be noted here, that this has little to no effect on the gas phase solution as the mean-field contribution vanishes at large volumes (see Eq. (2.32)), but prevents the gas phase iteration from converging towards a condensed phase solution. The liquid phase iteration uses $V^0 = V^{\text{id}}/100$ as initial volume guess and makes no changes to a_{mf} . If both iterations converge, the solution with lower Gibbs energy is chosen. This allows Peacemaker 2 to model realistic first order phase transitions. The population polynomial is solved using the Newton–Raphson algorithm.¹⁸²

If the user provides experimental reference data, Peacemaker 2 will compare the QCE results to the available reference. As experimental input Peacemaker 2 accepts an isobar of the molar volume V , a density ρ at a specific temperature, a boiling point temperature T_{b} , or any combination thereof. Peacemaker 2 will calculate the deviation of the QCE results from the experimental reference according to

$$\text{error} = w_{\rho} \left(\frac{\rho - \rho^{\text{exp}}}{\rho^{\text{exp}}} \right)^2 + w_V \frac{1}{N} \sum_{i=1}^N \left(\frac{V_i - V_i^{\text{exp}}}{V_i^{\text{exp}}} \right)^2 + w_T \left(\frac{T_{\text{b}} - T_{\text{b}}^{\text{exp}}}{T_{\text{b}}^{\text{exp}}} \right)^2, \quad (2.71)$$

where w_{ρ} , w_V , and w_T are weighting parameters for the individual errors of density, isobar, and boiling point, respectively, and N is the number of volumes V_i contained in the isobar. These weighting parameters are 1 by default, but can be set by the user. It should be noted that the error expression was changed during the last years and may be reported differently in later chapters. Equation (C.3) describes the error as it is calculated in the current implementation of Peacemaker 2. During parameter sampling, Peacemaker 2 will use this error as criterion to determine the best pair of empirical parameters a_{mf} and b_{xv} .

2.5 Cyclic Voltammetry

Cyclic voltammetry is an electrochemical measurement method to obtain insights into the different (electro-)chemical processes happening at the electrode–electrolyte interface.¹⁸⁴ In cyclic voltammetry a linearly increasing (or decreasing) potential is applied to the working electrode until a set limit potential is reached and the applied potential decreases (or increases) linearly into the opposite direction. These cycles may be repeated several times to observe changes in the chemical environment of the electrode over time. In the presence of an electrochemically active species, their oxidation or reduction reaction can be observed as a signal in the cyclic voltammogram (CV), which depicts the current measured at the working electrode against the applied potential (see Fig. 2.2). These signals will appear at distinct, substance-specific potentials and can reveal information about the presence of certain species and the electrochemical reactions they participate in. Here, only a very brief overview of the basics of cyclic voltammetry will be provided. A more detailed description may be found in Ref. 184.

If reducible species are present and their reduction potential is within the scanned potential range, the increasingly reducing potential will lead to an initial increase in the cathodic (negative by convention) current during the cathodic scan (from the upper to the lower limit potential), as the reducible species accept electrons (e.g., $\text{Fe}^{3+} + \text{e}^- \rightarrow \text{Fe}^{2+}$) from the working electrode. As the concentration of reducible species close to the electrode depletes, the cathodic current will reach its peak (j_p^{red} in Fig. 2.2) and decrease. During the anodic scan (from the lower to the upper limit potential) an increasingly oxidizing potential is applied to the working electrode. If the redox couple formed by the reducible species and its reduction product is reversible, the re-oxidation of the previously reduced species (e.g., $\text{Fe}^{2+} \rightarrow \text{Fe}^{3+} + \text{e}^-$) will generate an anodic current that will be visible in the CV. In an ideal system of a completely reversible redox couple, the peaks observed during the cathodic and anodic scan will be similar in size and shape (Fig. 2.2a). In the case of

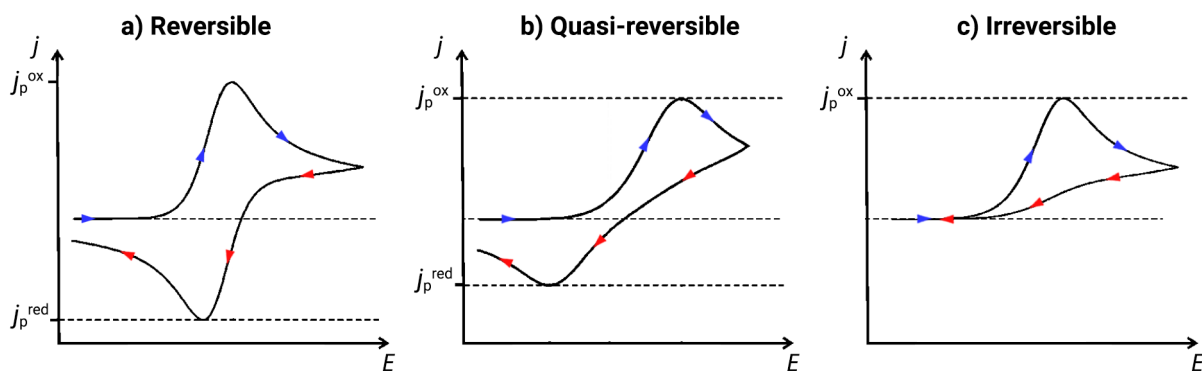


Figure 2.2: Comparison of CV shapes for reversible (a), quasi-reversible (b), and irreversible processes (c). The anodic and cathodic scan directions are indicated by blue and red arrows, respectively. Adapted with permission from Ref. 185.

limited reversibility, the peak currents j_p^{red} and j_p^{ox} observed in the cathodic and anodic scan, respectively, will be recorded at distant potentials and vary in shape and size (see Fig. 2.2b). If the electrochemical reactions observed in either scan are irreversible, e.g., because the reaction product takes part in further reactions, the opposing current signal will be missing during the reverse scan (see Fig. 2.2c). It should be noted, however, that the experimental setup, the scan rate, the electrolyte composition and other factors may also affect the recorded CVs.

Besides the redox reactions of electrochemically active species, the CVs may record additional processes such as reductive or oxidative decomposition reactions of the electrolyte. Such processes are usually irreversible and will often form insulating layers on the electrode surface. The limited accessibility of the electrode will lead to reduced currents recorded in the following cycles.

Part I

Modeling Organic Solvent Mixtures

Summary of Part I

The QCE method presents a highly efficient approach to model liquid thermodynamics based on small, quantum chemically accessible molecular clusters. It has been established as an effective method for a wide variety of substances. In 2011, it was fundamentally extended to binary systems (bQCE), allowing its application to mixtures.⁴³ However, since its conception the bQCE method had only been applied to three well-mixing aqueous mixtures of polar solvents.^{43–45} These studies continued the trend of polar hydrogen-bonded liquids that were the main focus of QCE studies in the past. Although they showed promising results and could reproduce the thermodynamics of mixing of the studied systems with reasonable accuracy, more case studies are required to establish the ability of the bQCE method to model binary mixtures. In addition, a wider variety of substance classes including non-polar and aprotic polar solvents could potentially open the bQCE method to a multitude of new applications.

This part of the thesis presents two studies which apply the bQCE method to a range of binary mixtures of common solvents, including for the first time non-polar solvents. As a secondary goal, these studies aim to minimize the computational effort by choosing highly efficient quantum chemical methods, limiting the cluster size, and optimizing the cluster generation method. An earlier study⁴⁵ on the binary mixture of water and *N*-methylformamide found no significant differences between the high-level CCSD(T)(F12*)/cc-pVDZ-F12 method and DFT results obtained at the B3LYP/def2-TZVPP level of theory, as the mean-field parameter a_{mf} could compensate for systematic energy differences. Based on this insight, although the original motivation of the QCE model was the possibility to apply high-level computational methods to a liquid model, here, the low-cost PBEh-3c¹⁸⁶ composite method and the semi-empirical GFN-xTB¹⁸⁷ are used. Another insight of that study was that the thermodynamics of mixing could be reproduced qualitatively with only small clusters of a maximum size of three molecules to represent mixed interactions.

In Chapter 3, the bQCE method is applied to four binary mixtures of common solvents. These comprise the well-mixing acetonitrile–acetone, benzene–acetone, and water–acetone systems and the hardly miscible water–benzene system. In an effort to reduce computational cost, the PBEh3-c functional is chosen as quantum chemical method. Additionally, the cluster size is restricted to a maximum of three molecules. The Gibbs energy of the neat liquids can be calculated in good agreement with the experimental reference. However, this is partly due to error cancellation as the enthalpy and entropy show greater deviations. By performing QCE calculations at different mole fractions over the whole mixing range, the Gibbs energy of mixing $\Delta_{mix}G$ can be calculated. Despite the considerable restrictions on the quantum chemical method and cluster size, the experimental thermodynamics of mixing are reproduced within a reasonable accuracy of 0.25 kJ/mol for the

two non-aqueous mixtures. Phase separation is correctly predicted for the water–benzene system at all investigated compositions. However, the description of the acetone–water mixture breaks down in the water-rich composition range, for which the bQCE method wrongly predicts phase separation. This is explained by the more complicated dynamics compared to the non-aqueous systems. Larger clusters are required to capture the hydrophobic effect¹⁸⁸ introduced by the interactions of water with the methyl groups of acetone. By interpolating the empirical parameters a_{mf} and b_{xv} between their neat liquid values, an attempt is made to predict the miscibility without any experimental input from the mixed phase. The mixing behavior of all four mixtures can be correctly predicted with the exception of the water-rich benzene–water mixture, for which miscibility is wrongly predicted. The population analysis allows insight into the inner structure of the mixtures in well agreement with experimental observations. Same-species interactions are preferred over mixed interactions in all mixing systems. Unexpectedly, however, the water–benzene mixture shows a high population of mixed clusters. The water–benzene dimer is found necessary to correctly predict phase separation in this system.

Chapter 4 introduces a cluster approach to calculate activity coefficients in binary mixtures based on the bQCE method. Compared to the previous chapter, the maximum cluster size is increased to six molecules. By employing the semi-empirical GFN-xTB method, the computational effort is still reduced drastically, allowing the inclusion of a much greater number of cluster motifs. The excess Gibbs energy of mixing is calculated for an exemplary set of three diverse binary systems. These comprise the acetonitrile–benzene and acetone–chloroform mixtures, which exhibit positive and negative deviations from Raoult’s law, respectively, and the near ideal methanol–ethanol mixture. All three mixtures show good to reasonable agreement with the experimental reference with a maximum deviation of about 0.3 kJ/mol. While the strong association between acetone and chloroform, which leads to a negative $\Delta_{\text{mix}}G^e$, is reproduced correctly in the equimolar mixing range, both the acetone-rich and chloroform-rich regions show the wrong behavior. By fitting the calculated data to Redlich–Kister-type polynomials,¹⁸⁹ an algebraic expression for $\Delta_{\text{mix}}G^e$ can be obtained. Derivation of this expression by the particle number allows the calculation of activity coefficients. The obtained results are generally in good agreement with the experimental activity coefficients but the error increases in the more dilute regions.

Furthermore, the vaporization enthalpies $\Delta_{\text{vap}}H$ of the neat systems are calculated. With the exception of benzene, all systems are in excellent to good agreement with the experimental references with errors of <4 kJ/mol. For benzene, the approach breaks down as the calculated value of 17.1 kJ/mol significantly underestimates the experimental reference value of 33.9 kJ/mol. This is possibly due to a systematic underbinding of π -stacked systems inherent to the GFN-xTB method¹⁸⁷ and may be resolved by a higher order quantum chemical method.

3 Predicting Miscibility of Binary Liquids From Small Cluster QCE Calculations

Johannes Ingenmey,* Michael von Domaros,* and Barbara Kirchner*

Received: January 28, 2017, Published: April 18, 2017

Reprinted (adapted) with permission from

J. Ingenmey, M. von Domaros, and B. Kirchner, *J. Chem. Phys.*, 2017, **146**, 154502.

Copyright © 2018 American Institute of Physics

DOI: 10.1063/1.4980032

Contributions to the manuscript

- Construction of the cluster sets and performing the DFT optimizations
- Running the QCE calculations
- Analyzing and discussing the results
- Providing the figures
- Writing the manuscript

*Mulliken Center for Theoretical Chemistry, Institut für Physikalische und Theoretische Chemie, Rheinische Friedrich-Wilhelms-Universität Bonn, Berlingstraße 4+6, 53115 Bonn, Germany

Abstract The quantum cluster equilibrium method is applied to model binary systems of molecular solvents. We minimize the computational effort as well as the experimental input and present the results obtained for the completely miscible acetonitrile/acetone, benzene/acetone, and water/acetone systems, as well as for the hardly miscible water/benzene system. Only clusters of sizes up to $n = 3$ are applied and these are optimized employing the low-cost functional PBEh-3c. The thermodynamic functions of the pure liquids are in reasonable agreement with experiments. For both non-water containing binary systems, the Gibbs energy of mixing can be reproduced with an accuracy of ≈ 0.25 kJ/mol. Water containing systems are not sufficiently described by small clusters. The empirical mean-field parameter a_{mf} and exclusion volume scaling parameter b_{xv} which depend on the experimental input are approximated by linear interpolation between their neat liquids' reference values. This makes the approach independent from the experimental data of the binary system. Despite the roughness of the approximation as well as the small size of the cluster sets, the approach is able to correctly predict the mixing behavior of all acetone systems. The benzene/water system is correctly predicted to be non-miscible at most mole fractions. A small range at high benzene concentrations ($x > 0.8$) is falsely predicted to be miscible.

3.1 Introduction

The thermodynamics of mixtures is a vast subject that has been extensively investigated by experimental and theoretical means.¹⁹⁰ In order to conduct a chemical process in the solution and, for example, to achieve a sufficient yield of reaction products and process rates, the understanding of and control over process parameters and hence solvent properties are needed.¹⁹¹ Since binary mixtures often exhibit markedly different physico-chemical properties than their neat components, they are of particular importance as solvents in the chemical industry and in laboratories. Many models have been developed to describe liquid phase equilibrium thermodynamics of pure substances and multi-component systems. Relevant examples are the quantum chemistry based COSMO-RS model (conductor like screening model for real solvents)¹⁹² and the group contribution method UNIFAC (universal quasichemical functional-group activity coefficients).¹⁹³

In 1998 Frank Weinhold published the theory about his quantum cluster equilibrium (QCE) method³⁶ which since then has been used in widespread applications to neat liquids.^{38,52,53,55-58,60-72,75-79,81,82,194-196} Later this method was extended by us and successfully applied to binary systems.⁴³⁻⁴⁵ The QCE method employs statistical mechanics to quantum chemically calculated clusters and molecular properties in order to achieve a thermodynamic description of the liquid and vapor phases using partition functions. A strong benefit of the QCE approach is that it provides equilibrium populations of the different clusters included at each phase point. Applied to binary systems this allows

insight into the structural composition of the liquid phase and the importance of different cluster motifs and their dependence on the temperature and compound. It also provides access to thermodynamic excess quantities. One important quantity is the (excess) Gibbs free energy of mixing as it is a measure of phase stability and serves as a criterion for whether a system of a certain composition will spontaneously form a mixture or phase separation will occur. In a recent study,⁴⁵ it has been shown that the QCE approach can provide results for the Gibbs free energy of mixing that lie quantitatively within the correct order of magnitude of experimentally measured results, even when the mixed cluster set comprises small clusters of sizes $n \leq 3$ only, indicating that a complete cluster set may not be necessary, if the employed cluster set is balanced.⁴³ Thus, if combined with a computationally cheap quantum chemical method, QCE could provide a fast, qualitative test for whether two substances mix or not, tremendously facilitating design calculations of solvent mixtures. It is the purpose of this study to investigate this possibility.

As test cases, four binary mixtures of standard solvents are investigated, namely, the well-mixing systems acetonitrile-acetone, benzene-acetone, and water-acetone and the hardly miscible system benzene-water.¹⁹⁷ These systems cover a range from weakly and non-associating to strongly associating liquids, as well as near ideal mixing behavior to phase separation. In an attempt to reduce the computational effort to a minimum and to further investigate the QCE model’s capabilities at small cluster sizes, only clusters of sizes $n \leq 3$ were quantum chemically optimized in density functional theory (DFT) calculations using the low-cost functional PBEh-3c by Grimme et al.¹⁸⁶ This way a computationally inexpensive description of the liquid phase is achieved that is partly ab initio in principle. Furthermore, an attempt is made, to limit the experimental input, that is needed in QCE calculations, to that of the pure substances only, by approximating parameters of the mixed systems. The central quantity of interest in this study is the Gibbs free energy of mixing. Thus the main goal is the correct prediction of miscibility for the model systems.

3.2 Model and Methods

3.2.1 The QCE Method

Detailed derivations of the QCE theory have been described in several earlier works^{36,38} as have the extension of the model to binary systems^{43,45} and the implementation of the Peacemaker program package.^{39,43,45} Hence, this section shall provide only a short overview of the QCE theory. The QCE model describes liquid phases as a gas consisting of weakly interacting, distinct particles, so-called clusters, built up from one (neat substance) or two (binary mixture) monomers. The cluster gas is assumed to be in thermodynamic

3. Predicting Miscibility From Small Cluster QCE Calculations

equilibrium; hence, the QCE cluster equilibrium reaction mechanism for a binary system can be written as



where $i(\varphi)$ and $j(\varphi)$ denote the number of monomers of each component C_1 and C_2 that build up the cluster φ . From Eq. (3.1) the QCE model for a pure substance is recovered when $j(\varphi) = 0$. The overall goal in the QCE approach is to find the set of particle numbers $\{N_\varphi\}$ for each cluster φ that minimizes the free energy A at a given volume V , temperature T , and total number of monomers $N^{\text{tot}} = N_1^{\text{tot}} + N_2^{\text{tot}}$. To calculate thermodynamic quantities like the free energy A from these particle numbers, the partition function Q^{tot} is needed,

$$A(\{N_\varphi\}, V, T) = -k_B T \ln Q^{\text{tot}}(\{N_\varphi\}, V, T), \quad (3.2)$$

which is given by

$$Q^{\text{tot}}(\{N_\varphi\}, V, T) = \sum_{\varphi=1}^N \frac{1}{N_\varphi!} [q_\varphi^{\text{tot}}(V, T)]^{N_\varphi}, \quad (3.3)$$

where $q_\varphi^{\text{tot}}(V, T)$ is a single particle partition function, which is given by

$$q_\varphi^{\text{tot}}(V, T) = q_\varphi^{\text{rot}}(T) q_\varphi^{\text{vib}}(T) q_\varphi^{\text{trans}}(V, T) q_\varphi^{\text{elec}}(T). \quad (3.4)$$

Here, $q_\varphi^{\text{rot}}(T)$, $q_\varphi^{\text{vib}}(T)$, and $q_\varphi^{\text{trans}}(V, T)$ are the rotational, vibrational, and translational partition functions, calculated from standard equations for the rigid rotor, harmonic oscillator, and particle in a box, respectively. Together with the electronic cluster partition function $q_\varphi^{\text{elec}}(V, T)$ they represent the different degrees of freedom for each particle φ . A correction needs to be made for the volume V in the translational partition function, accounting for non-punctiform particles with volume v_φ . The exclusion volume V_{ex} , which is subtracted from the phase volume V , is given by

$$V_{\text{ex}} = b_{\text{xv}} \sum_{\varphi=1}^N N_\varphi v_\varphi. \quad (3.5)$$

The proportionality constant b_{xv} is an empirical parameter ensuring appropriate volume scaling, since cluster volumes v_φ are often sensitive to the choice of atomic radii.⁵² The electronic cluster partition function $q_\varphi^{\text{elec}}(V, T)$ is calculated from the ground state energy $\epsilon_\varphi^{\text{elec}}$ of the electronic system and extended by a term accounting for interactions between clusters in the form of a volume and cluster size dependent mean-field-type attractive energy. It is given by

$$q_\varphi^{\text{elec}}(V, T) = \exp \left\{ - \frac{\epsilon_\varphi^{\text{elec}} - [i(\varphi) + j(\varphi)] \frac{a_{\text{mf}}}{V}}{k_B T} \right\}, \quad (3.6)$$

where k_B represents the Boltzmann constant, and the mean-field parameter a_{mf} is the second empirical correction parameter incorporated into the QCE model. Both parameters are chosen in a way so as to minimize the deviation of the QCE results from experimental data such as densities and temperatures of phase transition. From the partition function Q^{tot} , all thermodynamic properties can be calculated. However, all independent variables ($\{N_\varphi\}, V, T$) need to be known. At a given temperature, the particle numbers $\{N_\varphi\}$ and the volume V are obtained in an iterative process where the difference in free energy $|\Delta A|$ is used as a convergence criterion. The volume V is restricted by the requirement to be in accordance with an externally applied pressure

$$p = k_B T \left(\frac{\partial \ln Q^{\text{tot}}}{\partial V} \right)_{T, \{N_\varphi\}}. \quad (3.7)$$

If several combinations of V and $\{N_\varphi\}$ exist that fulfill this condition, then the solution with the lowest Gibbs energy,

$$\begin{aligned} G &= -k_B T \ln Q^{\text{tot}} + V k_B T \left(\frac{\partial \ln Q^{\text{tot}}}{\partial V} \right)_{T, \{N_\varphi\}} \\ &= A + pV, \end{aligned} \quad (3.8)$$

is chosen, which is the central thermodynamic quantity of interest in this work.

3.2.2 Quantum Chemical Method

Geometry optimizations and frequency analyses were performed on all structures using DFT with the ORCA program package.¹⁹⁸ All calculations were performed employing the low-cost PBEh-3c functional by Grimme¹⁸⁶ which uses a modified def2-SV(P) basis set termed as def2-mSV(P). The method, which was newly implemented in ORCA, involves a geometrical counterpoise (gCP) correction¹⁹⁹ in order to deal with the intermolecular as well as intramolecular basis set superposition error (BSSE). Furthermore, the London dispersion energy is accounted for by Grimme’s empirical dispersion correction D3.^{87,200} Tight SCF convergence criteria were applied in each geometry optimization. Harmonic frequencies were calculated as analytical derivatives of the energy gradient.

QCE calculations were performed with the Peacemaker 2.4 program package³⁹ which has successfully been used to describe binary mixtures previously.^{43–45} All calculations were performed at a fixed pressure of 101.325 kPa and temperature ranging from 273.15 to 400 K. Cluster volumes were calculated employing GEPO93’s solvent excluding surface algorithm²⁰¹ with van der Waals radii taken from Bondi’s compilation.²⁰²

3.2.3 Parameter Optimization and Approximation

The empirical parameters a_{mf} and b_{xv} were sampled on a rectangular grid evenly distributed between 0.0 and 2.0. Note that the mean-field parameter a_{mf} has the dimension energy and volume and is specified in $\text{J m}^3/\text{mol}$ and the exclusion volume scaling parameter b_{xv} is dimensionless. In the sampling process, using the boiling point T_{b} of the resulting isobar and the density ρ at a specified temperature, the pair of parameters is determined, that minimizes the deviation from the respective experimental values according to

$$\frac{|T_{\text{b}} - T_{\text{b}}^{\text{exp}}|}{T_{\text{b}}^{\text{exp}}} + \frac{|\rho - \rho^{\text{exp}}|}{\rho^{\text{exp}}}. \quad (3.9)$$

When treating binary systems, experimental data of the mixture, which is often rare, are needed over the whole composition range for the purpose of parameter sampling. Therefore, it is of particular interest to test the QCE model's predictive capabilities with little experimental input. Whereas mixtures of even simple solvents are often sparsely investigated, physical properties of pure substances are readily available in most cases. Thus, it would be convenient if thermodynamic quantities of mixtures could be predicted, using the QCE method, from an experimentally backed up description of the pure substances only. The empirical parameters a_{mf} and b_{xv} must then be guessed over the whole composition range where no data are available. As a first approximation, in this work both parameters are chosen by linear interpolation between their values for the pure substances with the aid of the mole fraction x ,

$$a_{\text{mf}}(x) = x \cdot a_{\text{mf}}(1) + a_{\text{mf}}(2) \cdot (1 - x). \quad (3.10)$$

The exclusion volume scaling parameter b_{xv} is chosen in an analogous way. Combining Eqs. (3.6) and (3.10), the cluster interaction part of Eq. (3.6) can be written as

$$u_{\varphi}^{\text{int}} = - \left(i(\varphi) \cdot a_{\text{mf}}(1) \frac{x_1}{V} + j(\varphi) \cdot a_{\text{mf}}(2) \frac{x_2}{V} + i(\varphi) \cdot a_{\text{mf}}(2) \frac{x_2}{V} + j(\varphi) \cdot a_{\text{mf}}(1) \frac{x_1}{V} \right). \quad (3.11)$$

The obtained data from this approach are compared to results from fully sampled QCE calculations and to experimental data in Sec. 3.3.2. It is noteworthy that in Ref. 36 Weinhold proposes a different way to treat binary systems without experimental data from the mixture by approximating the empirical parameters. While b_{xv} is chosen according

to Eq. (3.10), a_{mf} is varied within the calculation. The cluster interaction in Weinhold’s approach is calculated as

$$u_{\varphi}^{\text{int}} = - \sum_i \sum_j i(\varphi) a_{\text{mf}}(i, j) \frac{x_j}{V}, \quad (3.12)$$

where x_j is the mole fraction of component C_j and $a_{\text{mf}}(i, j)$ are additional “off-diagonal” parameters for each pair of components C_i and C_j , which are evaluated as the geometric mean of the pure component parameters $a_{\text{mf}}(i, i)$,

$$a_{\text{mf}}(i, j) = [a_{\text{mf}}(i, i)a_{\text{mf}}(j, j)]^{1/2}. \quad (3.13)$$

In a binary system Eq. (3.12) dissolves to

$$u_{\varphi}^{\text{int}} = - \left(i(\varphi) \cdot a_{\text{mf}}(1, 1) \frac{x_1}{V} + j(\varphi) \cdot a_{\text{mf}}(2, 2) \frac{x_2}{V} + a_{\text{mf}}(1, 2) \left(i(\varphi) \cdot \frac{x_2}{V} + j(\varphi) \cdot \frac{x_1}{V} \right) \right). \quad (3.14)$$

Equations (3.10)–(3.14) reduce properly to the corresponding one-component equations in the limit $x_j = 1$. In Weinhold’s proposed approach, the interaction between mixed clusters is treated differently from those between neat ones (note the difference in the latter parts of Eqs. (3.11) and (3.14)). However, the approach is not implemented yet and will not be a part of the recent study.

3.2.4 Cluster Sets

As has been demonstrated before,^{39,43} the construction of the cluster set is a crucial step in the application of the QCE model. It has been shown^{43,45} that a cluster set does not necessarily need to be large but should include important structural motifs that characterize the investigated system. In this work, cluster sets were constructed by only using small clusters of sizes up to $n = 3$.

Starting structures for the geometry optimizations were taken from the literature, if the system had been previously investigated or constructed by chemical intuition and the motivation to describe different structure motifs. Additional structures were obtained by running a global energy minimization for each cluster size with the aid of a genetic structure optimization at a classical force field level of theory. For this purpose the OGOLEM framework,^{168,169} the AMBER 2016 molecular dynamics package,²⁰³ and the generalized AMBER force field (GAFF),¹⁷⁰ implemented therein, were used, using default settings. Of course, there is no guarantee that the global minimum obtained at the force field level corresponds to the global minimum of the DFT potential energy surface. Furthermore, in the present approach the importance of energetically more unfavorable

3. Predicting Miscibility From Small Cluster QCE Calculations

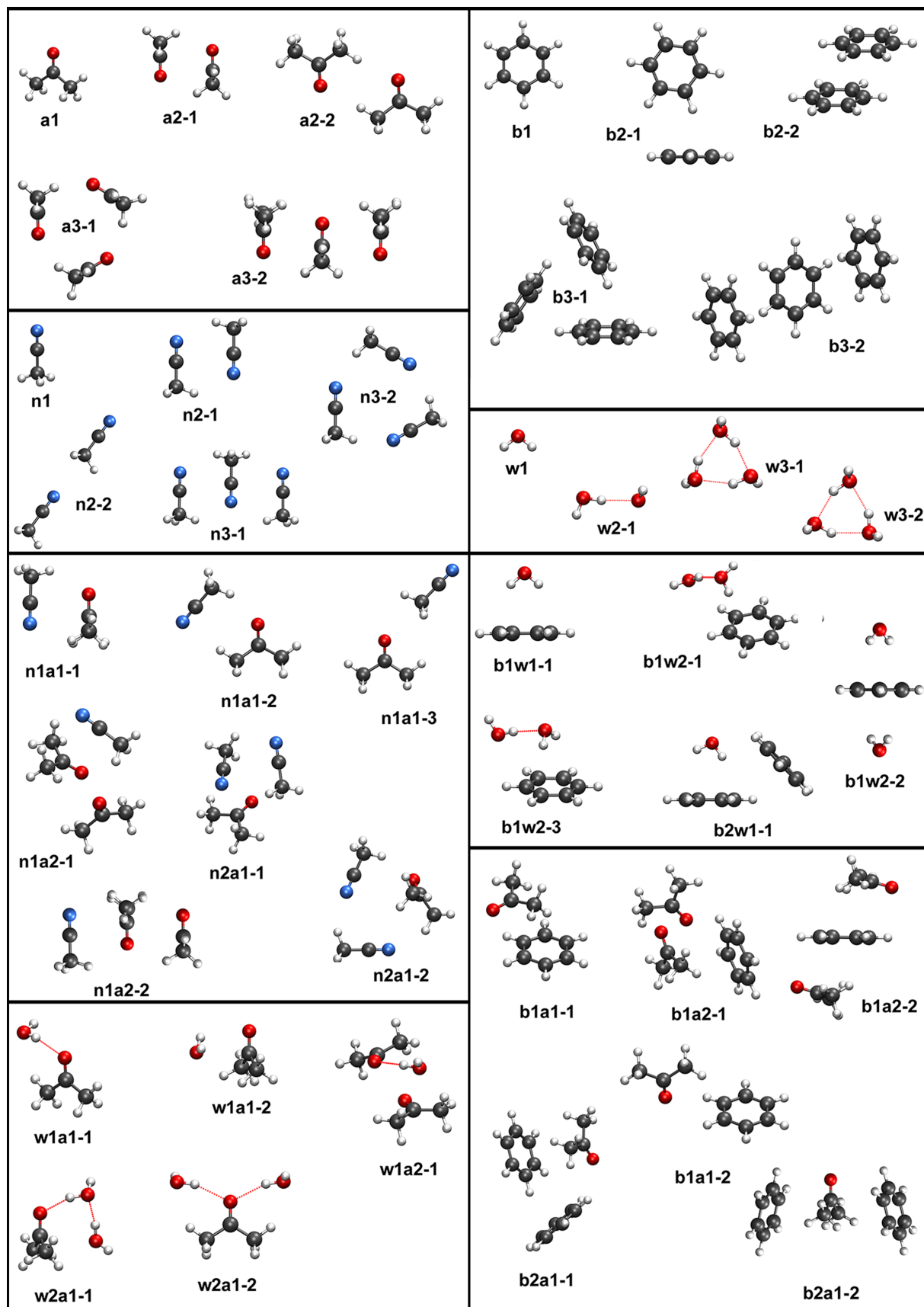


Figure 3.1: All neat and mixed clusters used in the QCE calculations of this work. Their geometries can be obtained upon request.

Table 3.1: Binding energies $\Delta_{\text{bind}}E$ in kJ/mol at the PBEh-3c/def2-mSV(P) level of theory for all clusters used in the QCE calculations.

Acetone		Acetonitrile		Benzene		Water	
a1	0.0	n1	0.0	b1	0.0	w1	0.0
a2-1	-26.7	n2-1	-26.2	b2-1	-12.2	w2	-25.2
a2-2	-17.7	n2-2	-13.9	b2-2	-11.2	w3-1	-78.3
a3-1	-52.6	n3-1	-49.0	b3-1	-37.1	w3-2	-71.8
a3-2	-51.4	n3-2	-51.5	b3-2	-23.7		
Water / Acetone		Acetonitrile / Acetone		Benzene / Acetone		Benzene / Water	
w1a1-1	-27.4	n1a1-1	-24.8	b1a1-1	-18.3	b1w1	-18.3
w1a1-2	-21.5	n1a1-2	-20.1	b1a1-2	-13.9	b1w2-1	-55.7
w1a2	-63.7	n1a1-3	-13.7	b1a2-1	-47.6	b1w2-2	-34.3
w2a1-1	-68.4	n1a2-1	-53.6	b1a2-2	-37.5	b1w2-3	-55.7
w2a1-2	-52.8	n1a2-2	-49.2	b2a1-1	-40.9	b2w1	-41.9
		n2a1-1	-51.8	b2a1-2	-36.1		
		n2a1-2	-50.8				

structures was not investigated. The structures obtained in this way should thus be considered as a more refined educated guess. All estimates of the cluster structure were subsequently optimized at the PBEh-3c level of theory. Their optimized geometries are depicted in Fig. 3.1, and the respective binding energies $\Delta_{\text{bind}}E$ are listed in Table 3.1. Note that all cluster geometries may be found in the supplementary material.

Water / Acetone

Water (**w**) as a pure substance has been excessively studied using the QCE method.^{38,39,52} From the previously constructed cluster sets for pure water four clusters were chosen, namely, the monomer (**w1**), the dimer (**w2**), and the cyclic water trimer in its unsymmetrical (**w3-a**) and its symmetrical, less stable form (**w3-b**). No other pure water dimer or trimer structures (e.g., linear configurations) were found to be stable clusters.

The pure acetone (**a**) clusters include the monomer (**a1**) and an anti-parallel dimer structure (**a2-1**) as well as a less stable planar one (**a2-2**), both of which have been found to be consistent with experimental data from infrared spectroscopy.^{204,205} A cyclic acetone trimer (**a3-1**) and a stacked one (**a3-1**) were found to be nearly equally stable with a difference in the binding energy of 1.12 kJ/mol.

Five mixed clusters were included in the water/acetone system cluster set. These include two water acetone dimer structures where the water molecule either forms a hydrogen bond to the carbonyl oxygen (**w1a1-1**)^{206,207} or forms a stacked conformation with the acetone molecule (**w1a1-2**). The trimers include a stacked acetone dimer which is perturbed by a hydrogen-bonded water molecule (**w1a2**), a cluster where a water molecule is

3. Predicting Miscibility From Small Cluster QCE Calculations

hydrogen bonded to an acetone and another water molecule (**w2a1-1**), and lastly a symmetrical cluster in which the carbonyl oxygen is hydrogen bonded to two water (**w2a1-2**) molecules. The clusters **w1a1-1** and **w1a1-2** have been discussed in Ref. 206 in the experimental context regarding the blue shift of the $n \rightarrow \pi^*$ band in the acetone/water system, where it was found that the acetone molecule is more likely to form only one hydrogen bond, as in **w1a1-1**. A later theoretical investigation²⁰⁸ suggests that in the liquid system there is a higher tendency to form **w2a1-2**.

Acetonitrile / Acetone

Several acetonitrile (**n**) clusters were constructed and found to be in accordance with the literature.^{209–212} These include the monomer (**n1**), an anti-parallel dimer (**n2-1**), a linear head-to-tail coordinated dimer (**n2-2**), and an anti-parallel stacked trimer (**n3-1**), all of which have been experimentally verified to contribute to the structural network of the liquid acetonitrile system.^{211–213} Also included is a cyclic trimer (**n3-2**) that is found to be the global minimum structure.²¹⁰

The mixed acetonitrile/acetone clusters include three dimers, one “anti-parallel” (**n1a1-1**) and two planar (**n1a1-2**, **n1a1-3**), resembling the dipole arrangement of several acetonitrile and acetone dimers. Trimers include two structures that resemble the stacked dimer with a second acetone molecule coordinating at different positions, in an anti-parallel configuration (**n1a2-2**) and an “on-side” one (**n1a2-1**). A stacked trimer (**n2a1-1**) and a cyclic trimer (**n2a1-2**) are included as well.

Benzene / Acetone

Small benzene (**b**) clusters have been extensively studied theoretically^{214–218} and experimentally.^{219–222} The pure benzene cluster set consists of the monomer (**b1**), the well known T-shaped dimer (**b2-1**), the parallel-displaced graphite like dimer (**b2-2**), the C_3 symmetrical trimer (**b3-1**), and a doubly t-shaped trimer (**b3-2**).

The mixed benzene/acetone clusters include a stacked near parallel dimer (**b1a1-1**) and one with a perpendicular conformation to the benzene plane (**b1a1-2**). All trimers (**b1a2-1**, **b1a2-2**, **b2a1-1**, **b2a1-2**) resemble combinations of the presented neat and mixed dimer structures.

Benzene / Water

Mixed benzene/water clusters include the theoretically^{223–225} and experimentally²²⁶ well described benzene-water dimer (**b1w1**), in which water forms a weak hydrogen bond to the π -electron system of the benzene ring, two trimers where a water molecule interacts with the benzene ring and accepts a hydrogen bond from a second water molecule (**b1w2-1**,

b1w2-3), a trimer that is constructed by mirroring the **b1w1** dimer on itself (**b1w2-2**), and a trimer with a V-shaped benzene configuration (**b2w1-1**). The clusters **b1w1**, **b1w2-3**, and **b2w1** have been described in the literature.²²³ In Ref. 227 it is suggested that in diluted mixtures benzene is coordinated as in **b1w2-2**.

3.3 Results and Discussion

3.3.1 Pure Components

In order to calculate properties of mixed systems, it is essential to ensure a sufficient description of the pure components by the QCE model. The Gibbs energy of mixing $\Delta_{\text{mix}}G$ is a measure of the energetic difference between a mixed phase of several components and their reference systems, in the case of a binary system the neat liquids (see Eq. (3.15)). Hence, the Gibbs energy of the reference systems must be well described. Experimental Gibbs energies can only be obtained as differences to an arbitrarily chosen reference point. Peacemaker potentials are absolute quantities and conveniently a reference temperature can be freely chosen. In Fig. 3.2 plots of the temperature dependent thermodynamic functions ΔG , ΔH , and $-T\Delta S$ are shown for all investigated systems. The reference temperature in these graphs was set to 273.15 K. Figure 3.2 shows a very good agreement between QCE results and experimental data for the neat acetone system. The temperature of phase transition from the liquid to the gaseous state is very well reproduced, noticeable by the change in the slope of ΔG at 329.28 K. The thermodynamic functions of the neat benzene and water systems are also well reproduced, although with less accuracy than the acetone system. ΔH and $-\Delta TS$ exhibit a less steep growth with temperature than the respective experimental functions for both benzene and water. This leads consequently to an error cancellation for the Gibbs energy. Compared to the experimental data ΔG shows a steeper progression with temperature, possibly indicating a slight over-stabilization of the neat systems by the QCE model. Since no experimental values could be obtained for the acetonitrile system, no comparison is possible. Nonetheless, the QCE results are shown in Fig. 3.2.

3.3.2 Thermodynamics of Mixing

The critical quantity that determines if a multi-component system of a certain composition will mix or form multiple liquid phases is the Gibbs energy of mixing $\Delta_{\text{mix}}G$. From the QCE model thermodynamic data are available over a wide range of temperatures and system compositions. The Gibbs energy of mixing for a binary system is calculated as

$$\Delta_{\text{mix}}G(x) = G(x) - x \cdot G(1) - (1 - x) \cdot G(2) \quad (3.15)$$

3. Predicting Miscibility From Small Cluster QCE Calculations

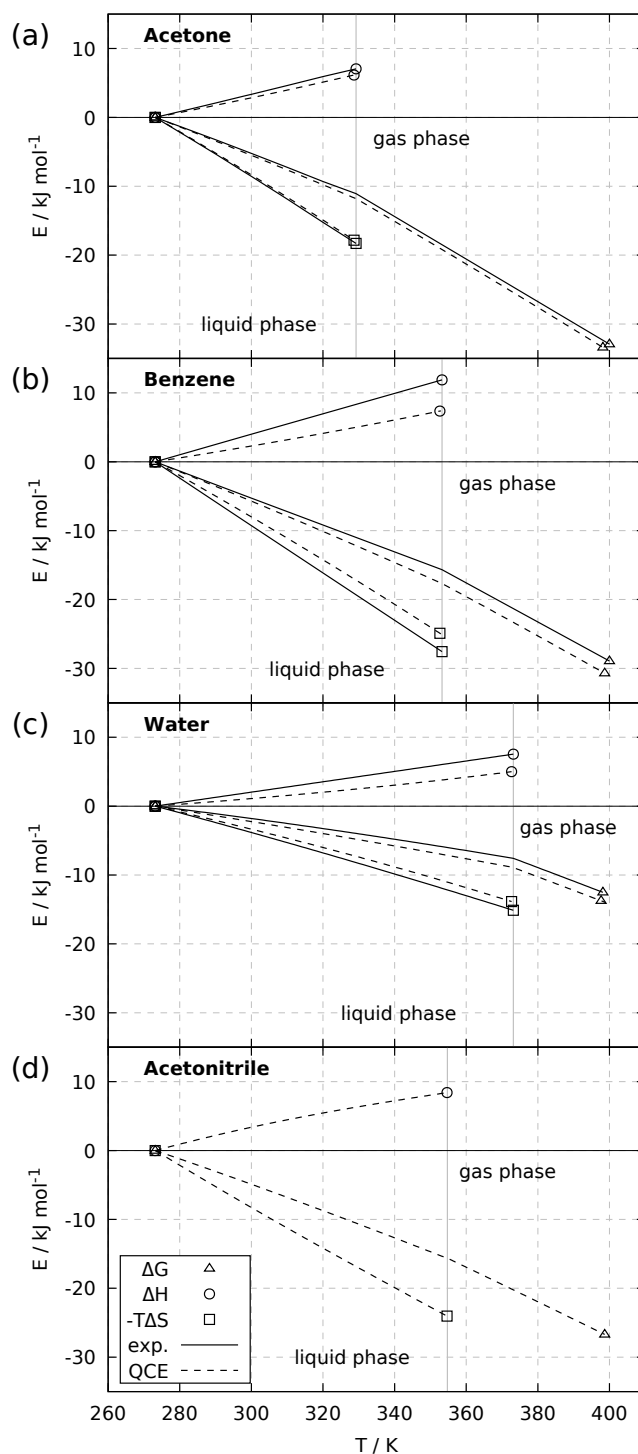


Figure 3.2: Thermodynamic functions ΔG , ΔH and $-\Delta TS$ for the neat (a) acetone, (b) benzene, (c) water, and (d) acetonitrile at standard pressure. The reference energies $\Delta E_{273\text{K}}^{\text{QCE,ref}}$ in kJ/mol for ΔG , ΔH , and $-\Delta TS$, respectively, are (a) 156.82, 211.51, and -54.69 , (b) 208.64, 265.71, and -57.06 , (c) 6.20, 28.48, and -22.28 , (d) 63.55, 111.70, and -48.15 . Experimental data from Refs. 228 and 229 (a), Ref. 197 (b), and Ref. 46 (c).

where $G(1)$ and $G(2)$ are the absolute Gibbs energies of the neat substances. As was demonstrated before,⁴⁵ the QCE model is able to qualitatively reproduce the Gibbs energy of mixing even with only small clusters describing the mixed phase. This result is further investigated in this work in that pure and mixed clusters are all of the size $n \leq 3$. In this regard, the goal of this work is not a quantitatively correct description of the systems but rather a qualitative prediction of their mixing behavior. Figures 3.3a–d show experimental and calculated results for $\Delta_{\text{mix}}G$ obtained from calculations with fully optimized parameters and with approximated linear interpolation parameters as described in Sec. 3.2.3. Furthermore, the optimized parameters a_{mf} and b_{xv} are plotted in Figs. 3.4a–d as functions of the mole fraction x_{a} of acetone for all acetone containing systems and x_{b} of benzene for the water/benzene system.

The acetonitrile/acetone binary system has been found to exhibit a near ideal behavior.²³⁰ The excess Gibbs energy at $x_{\text{a}} = 0.5$ has been measured to be in the range of 1 to 8 J/mol at 45 to 50 °C^{213,231,232} and thus is negligible. It is convenient to treat the Gibbs energy of mixing of this system to be ideal at 298.15 K. Figure 3.3a shows the QCE results for both interpolated and fully sampled calculations. Both approaches predict mixing of both substances over the whole composition range. The location of the minimum in the Gibbs energy of mixing at a mole fraction of $x_{\text{a}} = 0.5$ and the overall form of the curve are correctly reproduced. As will be shown by the other systems, these are not trivial results, and the near symmetrical form is neither inherent to the linear approximation of the empirical parameters nor to the QCE model itself. The results are also quantitatively considerably good with a maximum deviation of 0.25 kJ/mol and 0.44 kJ/mol for the fully sampled and interpolated QCE results, respectively. As would be expected, the fully sampled calculations produce a better description of the system. The approximated results are remarkable considering that no experimental data from the mixed system were used and only clusters up to size $n = 3$ were included. Both empirical parameters show a near linear progression with x_{a} , as shown in Fig. 3.4a. Thus, the linear interpolation is a good approximation for the acetonitrile/acetone system.

The benzene/acetone binary system exhibits a positive deviation from Raoult’s law and so, although both substances are completely miscible, cohesive forces between like molecules remain stronger in the mixture than adhesive forces between molecules of different species. Experimental Gibbs energies of mixing for the system are available from a Redlich–Kister polynomial¹⁹⁰ that is shown in Fig. 3.3b alongside the QCE results at a temperature of 313.15 K. For the fully sampled QCE run, there is a very good agreement between calculated and experimental results with a maximum deviation of 0.08 kJ/mol. The location of the minimum at $x = 0.5$ as well as the general form is well reproduced. These results nicely demonstrate the QCE model’s capability to predict thermodynamic data for temperatures that were not originally included in the sampling of the empirical parameters. The QCE run with interpolated parameters gives less accurate results with a maximum

3. Predicting Miscibility From Small Cluster QCE Calculations

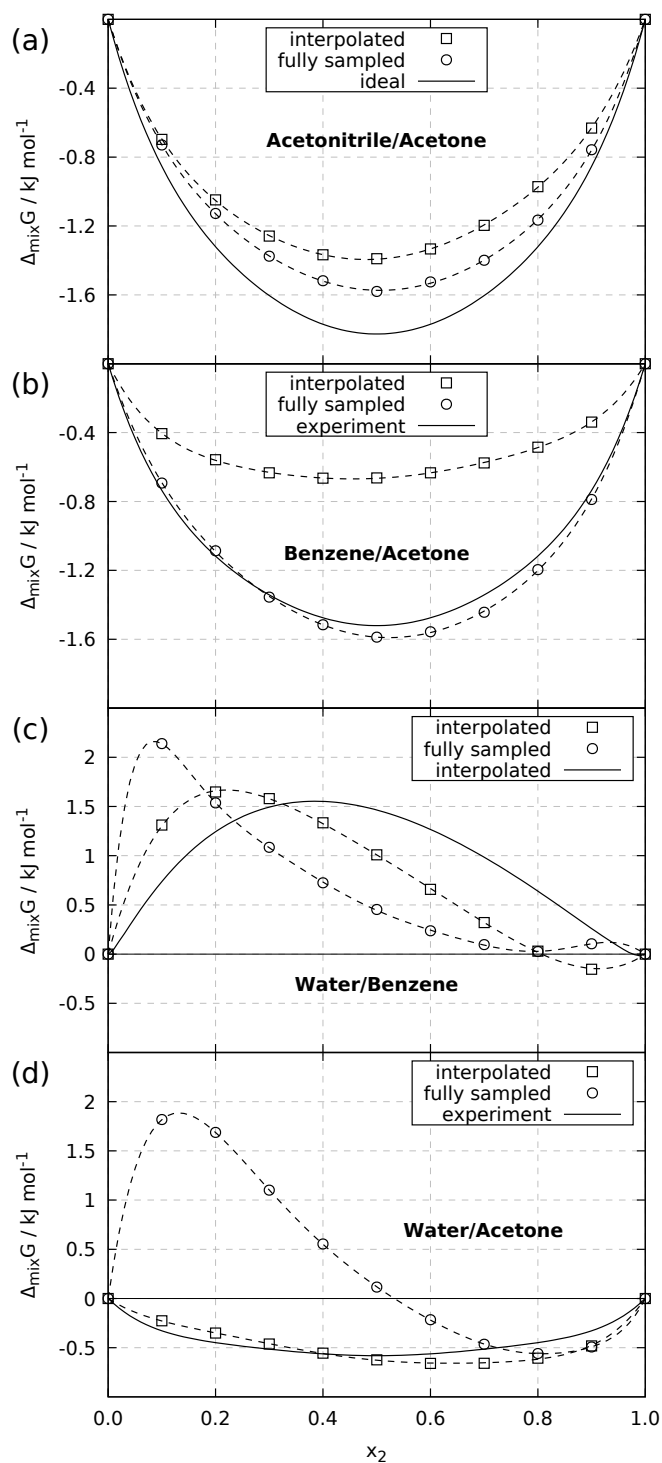


Figure 3.3: Calculated and experimental¹⁹⁰ Gibbs energies of mixing $\Delta_{\text{mix}}G$ for different mole fractions x_2 of acetone or benzene in the binary systems: (a) acetonitrile/acetone, (b) benzene/acetone, (c) water/benzene, and (d) water/acetone at 298.15 K or 313.15 K. Results from the QCE run with interpolated (squares) and fully sampled (circles) empirical parameters. The UNIFAC plot in (c) was calculated with parameters from Ref. 193. Broken lines are meant to guide the eye.

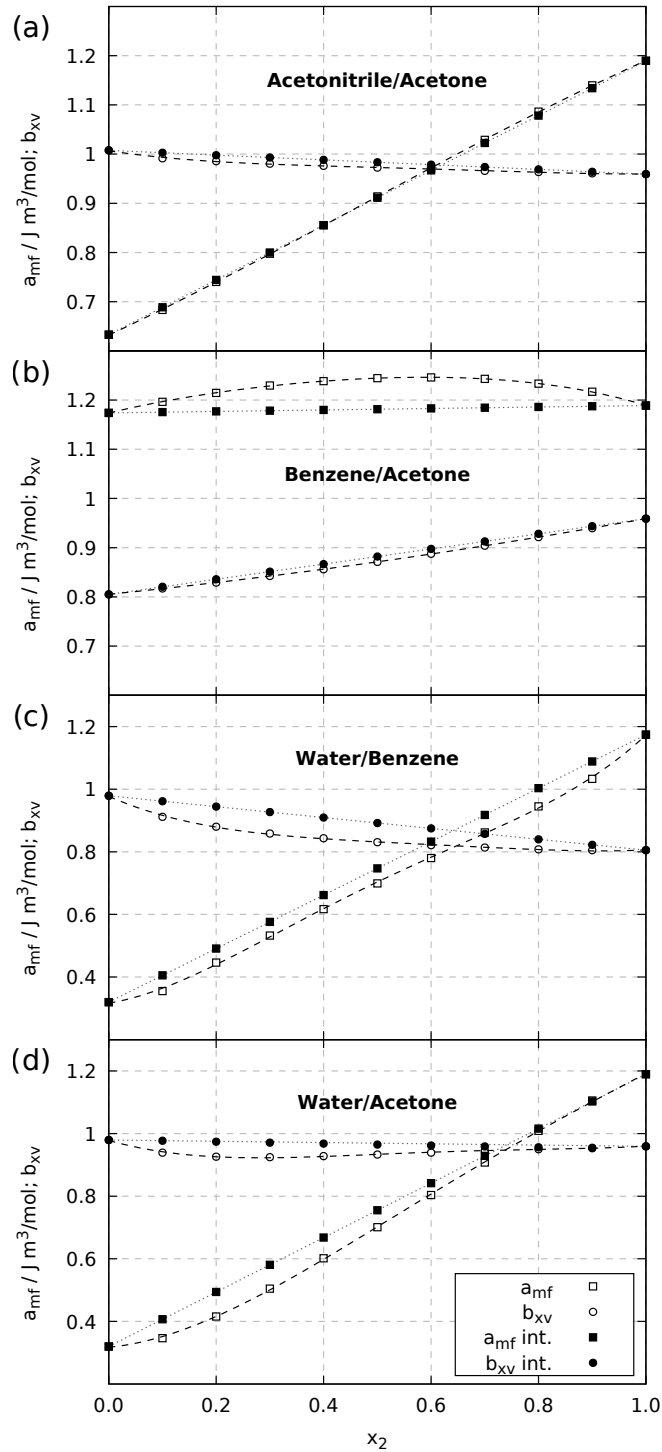


Figure 3.4: Optimized mean-field parameters a_{mf} and exclusion volume scaling parameters b_{xv} as a function of the mole fraction x_2 of acetone or benzene in the binary systems (a) acetonitrile/acetone, (b) benzene/acetone, (c) water/benzene, and (d) water/acetone. Broken lines are meant to guide the eye.

3. Predicting Miscibility From Small Cluster QCE Calculations

deviation of 0.86 kJ/mol and a shifted minimum at $x \approx 0.45$. However, the approach correctly predicts mixing of both substances over the whole composition range and also indicates a positive deviation from ideality. While the empirical parameter b_{xv} increases nearly linearly with the acetone mole fraction and only a small error is introduced by approximating it via linear interpolation, the same cannot be observed for a_{mf} . The empirical mean-field parameter shows a clearly nonlinear progression and has a maximum at $x_a = 0.6$. The error introduced by the linear approximation of a_{mf} is responsible for the less accurate description of $\Delta_{mix}G$ in the interpolated data.

The water/benzene binary system is hardly miscible ($x_{b,max} = 4.02 \times 10^{-4}$ and $x_{w,max} = 3.14 \times 10^{-3}$ at 298.15 K for benzene in water and vice versa, respectively²³³). Thus, the Gibbs energy of mixing is expected, due to the accuracy of the investigation, to be positive over the complete range of composition. No experimental data for the Gibbs energy of mixing are available. However, the UNIFAC model can provide data for comparison. Water and benzene form a heteroazeotrope at $x_b = 0.702$ with a minimum boiling temperature of 342.35 K.¹⁹⁷ As a heteroazeotrope, the system will boil at the azeotropic temperature over a wide range of composition. Thus, this knowledge can be used as the experimental input for parameter sampling within the QCE calculations. It is important to note that the QCE model treats the mixture as a single phase system and cannot describe a phase separation. A metastable single phase liquid solution is searched that fits the experimental data of the real benzene/water system with separate phases. The hypothetical solution is compared to the neat reference systems and $\Delta_{mix}G$ is expected to be positive, whereas $\Delta_{mix}G^{real}$ of the real system after phase splitting is negative and near zero. The results are shown in Fig. 3.3c alongside a UNIFAC plot calculated with parameters from Ref. 193. The fully sampled QCE run correctly predicts immiscibility over the complete range of composition investigated. A minimum exists at $x_b = 0.8$, close to the azeotropic point. It is not known if this feature is connected to the azeotropic composition and hence indicates a particularly stable state at this composition. This would be a significant result and the QCE model could possibly extend the molecular understanding of the formation of azeotropes. No QCE studies have been done on azeotropes before though, and more systems need to be investigated to give significance to this result. Although positive, the minimum lies too low on the energy scale and for higher temperatures a false range of mixing is predicted. The QCE calculation with interpolated parameters produces a similar curve, but both the maximum and minimum are shifted to higher mole fractions of benzene. The approximation leads to a false prediction of miscibility at $x_b = 0.8$ and higher mole fractions, but overall the result shows that even without the experimental data of the binary system immiscibility is correctly predicted over the widest part of the composition range. Both QCE calculations give results that lie within the same order of magnitude as the UNIFAC plot. All three curves are steeper in the water-enriched composition range and are, in comparison, shallow in the benzene-enriched range which hints

at the higher solubility of water in benzene than vice versa. In this system, both empirical parameters, shown in Fig. 3.4c, show deviations from the linear behavior. a_{mf} increases linearly in the range of 0.1 to 0.9 for mole fraction x_a but deviates from this behavior at the neat substances. Consequently, there is a nearly constant offset from the linear interpolation between the neat liquid values. This reflects the constant azeotropic boiling point that was used as the experimental input in the mixed range. The b_{xv} parameter decreases monotonously from pure water to pure benzene with a steeper progression in the water rich range and a very shallow, nearly constant progression in the benzene rich range. This somewhat reflects the behavior of $\Delta_{\text{mix}}G$ itself. The approximation by linear interpolation introduces errors for both parameters, resulting in a wrongly predicted range of mixing, but still an otherwise physically reasonable estimation of the Gibbs energy of mixing is obtained. The reason as to why benzene is immiscible with water is generally understood to be the hydrophobic effect, first described by Kauzmann in 1959.¹⁸⁸ Associated with the hydrophobic hydration of benzene is a negative entropy contribution ΔS due to the strengthening of the hydrogen bond network of the water phase.²²⁷ This decrease of entropy could not be reproduced by the QCE calculations. It is likely that a larger cluster set is needed to sufficiently describe the effects of hydrophobic hydration in the context of the QCE model.

Water and acetone are completely miscible in any composition. The binary system exhibits positive deviations from Raoult’s law. From experiments it is known that interactions between water and acetone molecules are stronger than those between acetone-acetone molecules but not as strong as water–water interactions.²³⁴ The water network stays mostly intact in dilute concentrations of acetone.^{234,235} Therefore, the experimental Gibbs energy of mixing is small in comparison to the other two investigated miscible systems. It is shown in Fig. 3.3d along with the QCE results. Surprisingly the fully sampled QCE run does fail to predict the miscibility of the system and falsely predicts immiscibility over the complete water-enriched composition range where $x_a \lesssim 0.5$. This failure is possibly due to an unbalanced description of interactions in neat and mixed clusters and could not be resolved yet. In Sec. 3.3.1 a possible over-stabilization of the pure water system was addressed. This is not necessarily troubling since this over-stabilization is carried through the mixed phase but must be balanced by an equally well descriptive mixed cluster set. The result suggests that either important motifs in the mixed cluster set are missing or larger clusters with sizes of $n > 3$ are needed in order to achieve a balance between the mixed system and the neat liquids. The latter appears to be the more likely explanation, as a similar problem as in the benzene/water system arises regarding the description of hydrophobicity of the acetone molecule’s methyl groups. Upon the addition of small quantities of acetone to water, the water structure is strengthened due to an increase in order.²³⁴ This causes a decrease in entropy but also an increase in enthalpy that unlike in the benzene/water system outweighs the negative entropy contri-

3. Predicting Miscibility From Small Cluster QCE Calculations

bution. It is likely that to reproduce this effect in QCE calculations, larger clusters will be needed. Interestingly the QCE calculation with interpolated parameters produces a quite good estimation of the Gibbs energy of mixing with a shifted minimum and a maximum deviation of 0.18 kJ/mol. Both a_{mf} and b_{xv} , shown in Fig. 3.4d, increase nearly linearly in the range of $x_a > 0.3$ but deviate from this behavior in the water rich composition range. The linear interpolation introduces only a small error at high concentrations of acetone leading to similar results in $\Delta_{mix}G$ for both approaches, but a rising error is made with higher water concentrations, coinciding with the error in $\Delta_{mix}G$ that is made by the fully sampled QCE run. From this result, it seems likely that the good description of the Gibbs energy of mixing with approximated parameters is due to an error cancellation for this particular system.

3.3.3 Population Analysis

One of the most important benefits of the QCE model is that it provides equilibrium populations of the different clusters included in the calculations. These monomer normalized populations I_φ give a measure of the importance of a specific structure motif. Cluster dependent molecular properties can be weighted by their population and thus provide information about their role in the dynamics of the liquid system and equilibrium quantities can be calculated for a wide temperature range from a statistical perspective. This has been used to calculate the average number of hydrogen bonds per monomer in water as well as the average oxygen-oxygen distance in the system.³⁹ Remarkably from this analysis a maximum in density could be found in the range of 278 to 281 K. The weighting by population approach has also been used to calculate spectroscopic properties of the liquid phases of *N*-methylacetamide.³⁴ In binary systems information about the liquid structure of the mixture can be obtained in dependence of the mole fraction. If the cluster set is sufficient, it should be possible to see from QCE results how strongly the liquid structure of the neat substances is disturbed by the process of mixing. This was nicely demonstrated in good accordance with the experiment in Ref. 43. Figures 3.5a–d show the summed up populations of neat and mixed clusters for all investigated systems. The acetonitrile/acetone system has been shown to exhibit a near ideality behavior experimentally^{213,231,232} and similar results were obtained in this work (see Fig. 3.3a). This indicates that in this system interactions between molecules of different species are of similar strength as those between molecules of the same component. In Ref. 213 it has been found that the acetonitrile self association is favored over the acetonitrile-acetone dimerization. Equilibrium constants corresponding to the formation of some dimers shown in Fig. 3.1 have been found to be $K_{n2-1} = 8.35$, $K_{n2-2} = 2.1$, and $K_{n1a1} = 2.5$. Therefore, it should be expected that the population of mixed clusters does not exceed the population of neat acetonitrile clusters around $x_a = 0.5$ and only at low concentrations of acetoni-

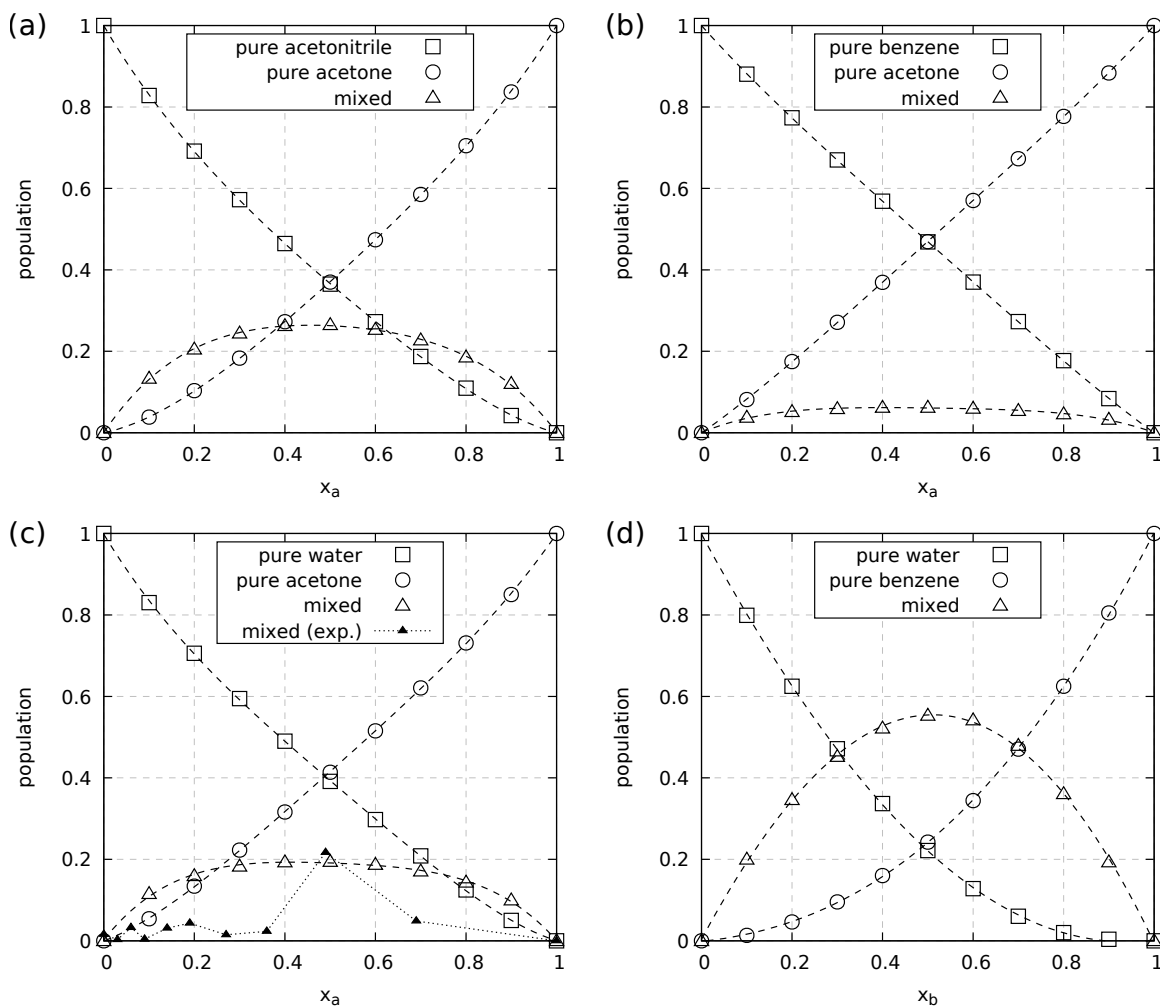


Figure 3.5: Monomer normalized populations of pure and mixed clusters as a function of the mole fraction x for the systems (a) acetonitrile/acetone, (b) benzene/acetone, (c) water/acetone, and (d) water/benzene at 298.15 K. The experimental reference in (c) is taken from Ref. 236. Lines are meant to guide the eye.

trile should the mixed clusters dominate the diluted acetonitrile liquid structure. The respective QCE populations in Fig. 3.5a do qualitatively agree with these findings.

The benzene/acetone system is a weakly interacting mixture.^{237,238} The molar excess enthalpy ΔH^E has a value of 0.144 kJ/mol at a mole fraction of $x_a = 0.5$,¹⁹⁰ indicating an unfavorable interaction between acetone and benzene. No quantitative data could be found to be used as a reference for the QCE populations. In Ref. 238 mixed clusters of acetone and benzene are described to be present but insignificant. A similar result is obtained from the QCE calculations, as shown in Fig. 3.5b. The mixed clusters' population reaches a shallow maximum at $x_a = 0.5$ of 6.2% and does at no point in the composition range exceed the neat cluster populations.

The water/acetone system has been extensively studied in experiments^{234–236,239} and theoretical investigations.^{206–208,235,240} For many years, the clustering within the mixed water/acetone system could not be studied by molecular dynamics simulations in a reliable

3. Predicting Miscibility From Small Cluster QCE Calculations

manner due to demixing.²⁴⁰ It has been suggested from a comparative study of several water and acetone force field combinations that micro-heterogeneity is in fact a real feature of the mixture. As was mentioned in Sec. 3.3.2, thermodynamics imply that the water network retains its structure in the mixture.²³⁴ From a combined nuclear magnetic resonance (NMR) and near-infrared spectroscopy study,²³⁶ where independent component analysis was applied to the water/acetone system, populations for the mixed clusters are available. The experimental data do agree with the thermodynamic findings in which cluster formation between water and acetone is found to be scarce but not negligible. The experimental populations of mixed clusters are below 5% at all investigated compositions except for a maximum population of about 22% at $x_a = 0.5$. When compared to these experimental values, the QCE results, shown in Fig. 3.5c, overestimate the mixed cluster populations by far. In the dilute ranges of $x_a < 0.2$ and $x_a > 0.8$, the mixed clusters are predicted to dominate over the pure acetone and water clusters, respectively. Only at $x_a = 0.5$ do experimental and QCE results agree. This rise in the mixed cluster population at this composition is attributed by the authors to a cluster of 2:2 acetone-water ratio. Two other important clusters are identified by the authors with compositions of 1:3 and 1:2 (possibly matching cluster **w2a1-1**, see Fig. 3.1). Since only the latter was included in the cluster set due to the applied size limit, these results further support the assumption made earlier, that larger clusters are needed, to accurately describe the water/acetone system.

The hydrogen bond in the water-benzene dimer is well established in the literature.^{223–226} The water/benzene binary liquid system has been subject to many experimental and theoretical investigations, but mostly at dilute concentrations due to the immiscibility of the components. As was argued before in Sec. 3.3.2, the QCE method does not describe phase separation but instead a hypothetical single phase liquid state is searched that matches the experimental input. This means that interactions between clusters of the same component are calculated within the same mean-field approximation as interactions between clusters of different components. Therefore the QCE populations of the water/benzene system, shown in Fig. 3.5d, must not be considered as a representation of the real system's molecular structure. That said, due to the hydrophobic effect and the strengthening of the hydrogen bonding network of the liquid water system upon dilution of benzene, only small populations of mixed clusters should be expected. Surprisingly though, the mixed clusters reach the highest population of any of the investigated systems. In the range of 0.3 to 0.7 of benzene mole fraction x_b , the mixed clusters dominate the liquid structure, making up as much as 53.6% of the general population at $x_b = 0.5$. This can be mainly attributed to the **b1w1** cluster that makes up as much as 47% of the population at that composition. While this result seems perplexing, the removal of the **b1w1** cluster and subsequent parameter optimization leads to a lowering of $\Delta_{\text{mix}}G$ and wrong prediction of miscibility in the range of 0.6 to 0.9 of x_b . The removal of **b1w1** reduces the maxi-

mum mixed cluster population to 14.7% at $x_b = 0.4$, the highest populated mixed cluster being **b1w2-3** at all mole fractions. This indicates that a high population of mixed clusters does not necessarily coincide with the prediction of solubility. In fact, the highly populated **b1w1** cluster leads to an increase of $G(x)$ and hence to an increase of $\Delta_{\text{mix}}G$ (see Eq. (3.15)). This might indicate that destabilizing clusters are needed to sufficiently describe an immiscible system.

3.4 Conclusion and Outlook

The QCE method was applied to four different binary mixtures of standard solvents with varying success. The method of cluster set construction (see Sec. 3.2.4) by running a genetic structure optimization at a classical force field level of theory and subsequent optimization employing the low-cost PBEh-3c functional is a computational inexpensive way to build the fundamental cluster set of a given system. In future, this method will be investigated and discussed in greater detail.²⁴¹

A reasonably good description of thermodynamic functions of the pure systems could be obtained with small cluster sets and little experimental input. Especially for the pure acetone system, a good agreement with experimental reference was achieved, while the strongly associating water system and the aromatic benzene system contain a larger error. Binary combinations of the investigated pure systems were studied by the QCE method over the whole composition range. Good results were achieved for the weakly interacting acetonitrile/acetone and benzene/acetone systems, where dispersive forces are the main contribution to intermolecular interactions. Small clusters were sufficient to reproduce the Gibbs energy of mixing $\Delta_{\text{mix}}G$ quantitatively within 0.25 kJ/mol. The approach in this work fails to predict the solubility of the water/acetone system, with results worsening at higher concentrations of water, where hydrogen bonding becomes increasingly important. The water/benzene system is correctly predicted to be immiscible over the whole composition range, indicating repulsive interactions. However, the thermodynamics of the hydrophobic effect are not reproduced. Thus, although going in the right direction and achieving the goal of predicting solubility, the system cannot be considered correctly described. Literature^{227,234} indicates that the dynamics of mixing in both the water/acetone and water/benzene systems are similar to some extent and in fact micro-heterogeneity has been suggested to be a feature of the water/acetone system.²⁴⁰ Therefore, it is likely that both systems suffer from the same error, that is, the insufficient description of inner liquid structures by small clusters. Whether the inclusion of larger clusters fully solves this problem remains subject to a further study.

The approximation of empirical parameters by linear interpolation yields acceptable results for all systems with an exception of the water/benzene system at high benzene concentrations. The approximation works well for acetonitrile/acetone and benzene/acetone,

3. Predicting Miscibility From Small Cluster QCE Calculations

but with less accuracy than the fully sampled QCE calculations. Interestingly both water containing systems are seemingly improved by the approximation, with results for $\Delta_{\text{mix}}G$ closer resembling the respective reference. This further indicates that the same error is present in both systems and that the approximation leads to a type of error cancellation. We conclude that non-associating liquids and mixtures can be adequately described by the QCE method using small clusters only, but strongly associating systems like water and mixtures containing water need larger clusters. This result is in line with a previous QCE study on the water/*N*-methylformamide mixture. Future studies may incorporate Weinhold's suggestion³⁶ of treating binary mixtures without the experimental input (Sec. 3.2.3), which could improve the results obtained by the simple approximation applied in this work. The concept of balancing cluster sets^{43,45} remains an important component of treating binary systems with the QCE method.

Acknowledgments

The authors are grateful to the Deutsche Forschungsgemeinschaft (DFG) for funding under the mixture project No. KI768/8-1.

4 A Cluster Approach for Activity Coefficients: General Theory and Implementation

Johannes Ingenmey,* Jan Blasius,* Gwydyon Marchelli,* Alexander Riegel,* and Barbara Kirchner*

Received: August 31, 2018, Published: December 21, 2018

Reprinted (adapted) with permission from

J. Ingenmey, J. Blasius, G. Marchelli, A. Riegel, and B. Kirchner, *J. Chem. Eng. Data*, 2019, **64**, 255–261

Copyright © 2018 American Chemical Society

DOI: 10.1021/acs.jced.8b00779

Contributions to the manuscript

- Co-developing the theory
- Performing and supervising the calculations
- Analyzing and discussing of the results
- Writing the manuscript

*Mulliken Center for Theoretical Chemistry, Institut für Physikalische und Theoretische Chemie, Rheinische Friedrich-Wilhelms-Universität Bonn, Berlingstraße 4+6, 53115 Bonn, Germany

Abstract In the framework of the binary quantum cluster equilibrium theory, we introduce a cluster approach to access activity coefficients of binary mixtures. This approach allows derivation of activity coefficients based on quantum chemically calculated clusters. The cluster sets in this work comprise clusters ranging in size from one to six molecules of either a single or two species. For each cluster size up to five conformers if detectable are considered such that important liquid motifs are included. Via self-consistent-field calculations the binary quantum cluster equilibrium theory gives the Gibbs energies and thus the excess Gibbs energies of mixing. Derivation with respect to the particle number allows access to activity coefficients. To achieve an analytical expression, we apply the standard approach of fitting a Redlich–Kister polynomial to the excess Gibbs energy and calculate its derivative, which leads to good results for the binary mixture cases of acetonitrile/benzene and methanol/ethanol, as well as satisfying results for acetone/chloroform. Very good results for vaporization enthalpies are obtained for the pure substances.

4.1 Introduction

Activity coefficients indicate the deviation of a mixture or solution from ideality.²⁴² Hence, their values are needed to determine phase equilibria,^{243,244} and they are directly related to phenomena such as vapor pressure lowering and freezing point depression.^{243,244} Their usefulness is also expressed in the increasing number of literature to be found on mixtures of the very popular ionic liquids with molecular liquids and their activity coefficients.^{245–251} Further, the activity coefficient of a salt in electrolyte solutions, which controls its solubility limit, is relevant in current research on alternative energy technologies.^{243,244,252} Consequently, the theoretical determination of activity coefficients is desirable, especially in cases where they are not easily accessible experimentally.

Existing methods for theoretical predictions of activity coefficients can be condensed to some general approaches.²⁵³ Recent advances in these approaches are numerous; however, we can only list a few outstanding examples.

Molecular dynamics or Monte Carlo simulations and derived free energy calculations have been performed to calculate chemical potentials,^{254–256} often based on the famous Widom particle insertion method. For dense liquids, where the insertion probability is low, this usually fails.^{257,258} To circumvent this problem, several techniques have been suggested.^{257–261} Furthermore, there are the Gibbs ensemble simulation techniques and related methods which directly simulate phase equilibria in fluids.^{254,255,262,263} In this context we also want to mention the ingenious adaptive resolution simulation method.^{264,265} Recently, Vrabec and co-workers extended their *ms2* simulation software package, specifically in order to obtain chemical potentials from different methods.^{256,266} Among others, they included the OPAS (osmotic pressure for the activity of the solvent) method in *ms2*

which was developed by Horsch and co-workers²⁴³ and further developed by Kohns and co-workers.²⁴⁴

A quite different approach are group contribution methods²⁶⁷ as well as continuum models. These were summarized, widely investigated, and extended in Ref. 268. While the group contribution methods are very accurate, they rely on very large parameter sets (>1000). In comparison, the parameter sets for continuum models are much smaller (<20). Vrabec, Lin, and co-workers²⁶⁸ found that including dispersion corrections within the continuum models increases the accuracy tremendously, and showed that further developing such models is relevant to current research.²⁶⁸ As further improvement the authors recommend to include directional hydrogen bonding.^{268,269} A very neat approach for estimating activity coefficients of target components in mixtures has been suggested by Hasse and co-workers.²⁷⁰

In this article we choose an alternative approach based on the binary quantum cluster equilibrium (bQCE) theory.^{43,45} By applying models of statistical thermodynamics to quantum chemically calculated clusters, the thermodynamic description of liquids, their mixtures, and gases at nonzero temperature and pressure is possible. Within this approach, a substance is described as an equilibrium distribution of distinct cluster structures, which build up a cluster set. As a crucial part, self-consistent-field calculations lead to equilibrium populations of these clusters and thus an ensemble of different structural states is generated similar to molecular dynamics simulations.^{39,43,45}

The article is organized as follows. In the next Section 4.2 we describe shortly the binary quantum cluster equilibrium method, how to obtain the activity coefficients from it, and the computational details as well as the generation of cluster sets. Following this, we present some applications in case studies in Section 4.3. We end the article with conclusions.

4.2 Methods and Computational Details

4.2.1 The bQCE Method

Detailed derivations of the bQCE theory can be found in earlier works.^{8,38,43,45} In this work, we will only present a short overview of the key equations of bQCE. First, we consider a system of noninteracting clusters, built up from one (neat substances) or two (binary systems) monomers. This cluster gas is assumed to be in thermodynamic equilibrium. The equilibrium reaction between clusters of a binary system reads



4. A Cluster Approach for Activity Coefficients

where $i(\varphi)$ and $j(\varphi)$ denote the number of monomers of each component C_1 and C_2 that form the cluster φ . The system's total partition function Q^{tot} at volume V and temperature T is given by

$$Q^{\text{tot}}(\{N_\varphi\}, V, T) = \prod_{\varphi=1}^N \frac{1}{N_\varphi!} [q_\varphi^{\text{tot}}(V, T)]^{N_\varphi}, \quad (4.2)$$

where q_φ^{tot} is a single cluster partition function corresponding to cluster φ and $\{N_\varphi\}$ is the full set of total cluster populations N_φ . Calculating Q^{tot} gives access to the thermodynamic properties of the system. Each cluster partition function q_φ^{tot} can be evaluated as product of partition functions corresponding to the cluster's different degrees of freedom:

$$q_\varphi^{\text{tot}}(V, T) = q_\varphi^{\text{trans}}(V, T) q_\varphi^{\text{rot}}(T) q_\varphi^{\text{vib}}(T) q_\varphi^{\text{elec}}(T). \quad (4.3)$$

Here, q_φ^{trans} , q_φ^{rot} , and q_φ^{vib} are the translational, rotational, and vibrational partition functions, which can be calculated from standard equations for the particle in a box, rigid rotator and harmonic oscillator.^{38,50} The electronic partition function q_φ^{elec} can be calculated from the adiabatic binding energy $\Delta_{\text{bind}}\epsilon_\varphi^{\text{elec}}$ of the cluster.

To describe the translational partition function more accurately, the phase volume V must account for an exclusion volume V_{ex} which attributes a volume v_φ to the nonpunctiform clusters. Since cluster volumes are sensitive to the choice of atomic radii, a scaling parameter b_{xv} is introduced. The exclusion volume now reads

$$V_{\text{ex}} = b_{\text{xv}} \sum_{\varphi=1}^N N_\varphi v_\varphi, \quad (4.4)$$

where v_φ is the cluster volume. Further, the electronic partition function is extended by a term accounting for interactions between clusters in form of a volume and cluster size dependent mean-field energy. The electronic partition function is then calculated as

$$q_\varphi^{\text{elec}}(V, T) = \exp \left\{ - \frac{\Delta_{\text{bind}}\epsilon_\varphi^{\text{elec}} - [i(\varphi) + j(\varphi)] \frac{a_{\text{mf}}}{V}}{k_{\text{B}}T} \right\}, \quad (4.5)$$

where k_{B} is the Boltzmann constant, and the mean-field parameter a_{mf} is a second parameter, scaling the strength of inter-cluster interactions. In an optimized bQCE calculation, the parameters are chosen such that the deviation of the bQCE results from a given experimental input such as densities and phase transition temperatures becomes minimal.

To calculate Q^{tot} , all independent variables ($\{N_\varphi\}, V, T$) need to be known. Hence, the temperature is set by the user, and the volume is restricted to be in accordance with an externally applied pressure

$$p = k_{\text{B}}T \left(\frac{\partial \ln Q^{\text{tot}}}{\partial V} \right)_{T, \{N_\varphi\}}. \quad (4.6)$$

If several combinations of V and $\{N_\varphi\}$ exist that fulfill this condition, then the solution with the lowest Gibbs energy

$$G = -k_{\text{B}}T \ln Q^{\text{tot}} + V k_{\text{B}}T \left(\frac{\partial \ln Q^{\text{tot}}}{\partial V} \right)_{T, \{N_\varphi\}} \quad (4.7)$$

is chosen. Using this approach, in several examples very good performance has been demonstrated for mixed systems.^{1,2}

4.2.2 Activity Coefficients from bQCE

Since absolute Gibbs energies of the system are available at any temperature the Gibbs energy of mixing $\Delta_{\text{mix}}G$ is easily accessible for any mole fraction x_i :^{1,8,43,44}

$$\Delta_{\text{mix}}G(x_i) = G(x_i) - x_i \cdot G(0) - (1 - x_i) \cdot G(1), \quad (4.8)$$

where $G(0)$ and $G(1)$ are the absolute Gibbs energies of the neat substances and $G(x_i)$ is the mixed system's absolute Gibbs energy at a given mole fraction x_i . The excess Gibbs energy of mixing $\Delta_{\text{mix}}G^e$ can then be calculated as

$$\Delta_{\text{mix}}G^e = \Delta_{\text{mix}}G - \Delta_{\text{mix}}G^{\text{id}}, \quad (4.9)$$

where $\Delta_{\text{mix}}G^{\text{id}}$ is the ideal Gibbs energy of mixing. Activity coefficients f_i are directly related to the excess Gibbs energy of mixing (hereafter labeled as G^e) by

$$f_i = \exp \left(\frac{1}{RT} \frac{\partial G^e}{\partial N_i} \right), \quad (4.10)$$

where R is the ideal gas constant, T is the temperature, and N_i is the particle number of component i . Since no analytical expression for G^e is available, we can calculate its derivative numerically as

$$\frac{\partial G^e}{\partial N_i} \approx \frac{G^e(N_i + dN_i) - G^e(N_i - dN_i)}{2dN_i}. \quad (4.11)$$

by performing additional bQCE calculations with a small change dN_i to the molar amount of component i .

4. A Cluster Approach for Activity Coefficients

However, as will be obvious from our results in the following section, bQCE results often deviate from a perfectly smooth curve and single values may vary positively or negatively from the expected behavior. Since Eq. 4.11 is sensitive to local inconsistencies, instead of calculating it from bQCE directly, we employ a Redlich–Kister (RK) style polynomial fit to smooth out all local inconsistencies,¹⁸⁹ which we call $G_{\text{RK}}^e(x_i)$:

$$G_{\text{RK}}^e(x_i) = x_i(1 - x_i) \sum_n g_n (1 - 2x_i)^n, \quad (4.12)$$

where g_n labels the Redlich–Kister parameters.¹⁸⁹ In this work we used up to five parameters ($0 \leq n < 5$). With $x_i = \frac{N_i}{N_i + N_j}$ we can write G_{RK}^e as a function of N_i and N_j :

$$G_{\text{RK}}^e = N_i \left(1 - \frac{N_i}{N_i + N_j}\right) \sum_n g_n \left(1 - 2 \frac{N_i}{N_i + N_j}\right)^n. \quad (4.13)$$

Equation 4.13 gives an analytical expression for G^e that can be differentiated with respect to the number of particles N_i :

$$\begin{aligned} \frac{\partial G_{\text{RK}}^e}{\partial N_i} &= \frac{N_j^2}{(N_i + N_j)^2} \sum_n g_n \left(1 - 2 \frac{N_i}{N_i + N_j}\right)^n \\ &\quad - \left(N_i - \frac{N_i^2}{N_i + N_j}\right) \frac{2 \cdot N_j}{(N_i + N_j)^2} \cdot \sum_n n \cdot g_n \left(1 - 2 \frac{N_i}{N_i + N_j}\right)^{n-1}. \end{aligned} \quad (4.14)$$

Again, with $x_i = \frac{N_i}{N_i + N_j}$ we can reformulate Eq. (4.14) as

$$\begin{aligned} \frac{\partial G_{\text{RK}}^e}{\partial N_i} &= x_j^2 \sum_n g_n (1 - 2x_i)^n \\ &\quad - 2 \cdot x_i \cdot x_j^2 \sum_n n \cdot g_n (1 - 2x_i)^{n-1}. \end{aligned} \quad (4.15)$$

Analogously, we can evaluate

$$\begin{aligned} \frac{\partial G_{\text{RK}}^e}{\partial N_j} &= x_i^2 \sum_n g_n (2x_j - 1)^n \\ &\quad + 2 \cdot x_j \cdot x_i^2 \sum_n n \cdot g_n (2x_j - 1)^{n-1}. \end{aligned} \quad (4.16)$$

Inserting these expressions into Eq. 4.10 allows the evaluation of the activity coefficients.

4.2.3 Computational Details

Geometry optimizations and frequency analyses were performed on all structures using the semi-empirical extended tight binding method GFN-xTB 5.8.1,¹⁸⁷ which includes the D3 dispersion correction^{87,200} accounting for the London dispersion energy.

bQCE calculations were performed with the Peacemaker 2.7 program package^{8,39} which has successfully been used to describe binary mixtures previously^{1,44,45} and which is freely available as described in Ref. 8. All calculations were performed at a fixed pressure of 101.325 kPa and temperature range of 273 to 400 K. Differently from previous works, cluster volumes were not calculated employing the Gepol93 solvent-excluding surface algorithm²⁰¹ but as van der Waals volumes with radii taken from Bondi’s compilation.²⁰² The parameters a_{mf} and b_{xv} were sampled on a rectangular grid evenly distributed between 0.0 and 2.0. Note that the mean-field parameter a_{mf} has the dimension energy·volume and is specified in $\text{J m}^3/\text{mol}$ and the exclusion volume scaling parameter b_{xv} is dimensionless. In the sampling process, the phase transition temperature T_{b} and the density ρ at a specified temperature is used to determine the pair of parameters that minimizes the deviation from the respective experimental values according to

$$\frac{|T_{\text{b}} - T_{\text{b}}^{\text{exp}}|}{T_{\text{b}}^{\text{exp}}} + \frac{|\rho - \rho^{\text{exp}}|}{\rho^{\text{exp}}}. \quad (4.17)$$

4.2.4 Cluster Sets

Constructing the cluster set is a crucial step in applying the bQCE method.^{39,43} In a previous work we have shown that the bQCE method can predict the correct mixing behavior of binary molecular mixtures with clusters not larger than three molecules.¹ The boiling point of protic ionic liquid ethylammonium nitrate could be predicted by bQCE⁰ within an accuracy of 2 K using only clusters of four or less ion pairs and without fitting to any experimental data.² In this work we restricted the clusters to a size of one up to six molecules. At each size we allowed up to five conformers if they were detectable. The fundamental units of a cluster set are the reference monomers of each component. All larger clusters are built from these monomers. In earlier studies the cluster set generation can be described as somewhat random process, combining a systematic global minimum search with structures found in the literature or by chemical intuition. This approach could possibly introduce bias to the cluster set and thus interfere with the results. In this work, we modified our strategy so that the cluster set generation is completely systematic. As before, the global minimum structure for each cluster composition was searched for by running a genetic structure optimization at a classical force field level of theory. For this purpose the OGOLEM framework,^{168,169} the AMBER 2016 molecular dynamics package,²⁰³ and the generalized Amber force field (GAFF),¹⁷⁰ implemented therein, were used. The pool size, that is, the number of individual structures in each generation of the genetic optimization, as well as the total number of iterations were set accordingly to the cluster size. For each possible cluster composition, between 2000 and 6000 individual structures were evaluated. The pool size of individual structures in each generation was varied with the cluster size, ranging between 100 for dimers and 300 for hexamers.

4. A Cluster Approach for Activity Coefficients

All clusters of the final generation were subsequently optimized at the GFN-xTB level of theory.¹⁸⁷ During this geometry optimization many of the individuals will collapse to the same structure and if ranked by their electronic energy, few distinct structures can be identified (with an energy criterion of $\Delta E \geq 0.001 E_h$). A maximum of five of these clusters are included in the cluster set, thus providing a diverse representation of different binding situations that can be found in the system. Since no clusters were manually constructed no user bias is introduced. Note, the cluster geometries can be obtained from the authors upon request and are listed in the Supporting Information.

4.3 Case Studies

Before we consider the thermodynamic properties of the binary systems, we first examine their neat states. Setting $a_{mf} = 0$ and $b_{xv} = 1$ as reference for the gas phase as previously carried out,² we can easily calculate enthalpies $\Delta_{\text{vap}}H$ of vaporization at standard conditions. Table 4.1 lists the results for the liquids investigated in this work, namely acetonitrile (N), benzene (B), methanol (M), ethanol (E), acetone (A), and chloroform (C). Excellent results for $\Delta_{\text{vap}}H$ are obtained for acetonitrile, and methanol with an error ≤ 1 kJ/mol. Satisfying accuracy within an error margin of ≤ 4 kJ/mol is achieved for the other liquids with the exception of benzene. These are remarkable results considering the low level of theory that the semi-empirical GFN-xTB method operates on and little amount of experimental data used to optimize the two parameters. The failure for benzene may indicate that the cluster set is not sufficient for this system as, for example, only the stacked dimer was found to be stable on the GFN-xTB level. A systematic underbinding in π -stacked systems was observed for the GFN-xTB method,¹⁸⁷ possibly resulting in an understabilized liquid phase in this study. Alternatively, a higher level of theory might be necessary for the quantum chemical calculations.

In earlier works we could demonstrate that the bQCE method is able to reproduce quantitatively the experimental Gibbs energies of mixing $\Delta_{\text{mix}}G$ if fitted to physicochemical

Table 4.1: Calculated and experimental enthalpies $\Delta_{\text{vap}}H$ and $\Delta_{\text{vap}}H^{\text{exp}}$ of vaporization in kJ/mol for several neat liquids at standard conditions. Experimental enthalpies of vaporization are taken from the NIST Chemistry WebBook.²⁷¹

	$\Delta_{\text{vap}}H$	$\Delta_{\text{vap}}H^{\text{exp}}$
acetonitrile	33.09	32.94 ± 0.06
benzene	17.10	33.9 ± 0.1
methanol	38.10	37.6 ± 0.5
ethanol	44.09	42.3 ± 0.4
acetone	32.60	31.27
chloroform	27.68	31.32 ± 0.08

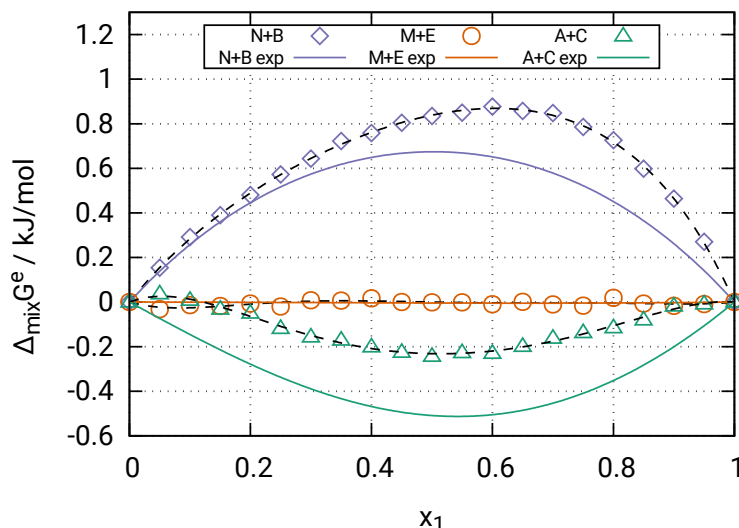


Figure 4.1: Calculated and experimental¹⁹⁰ Gibbs energies of mixing $\Delta_{\text{mix}}G^e$ for different mole fractions x_1 of acetonitrile, methanol, or acetone in the binary systems acetonitrile/benzene (N+B), methanol/ethanol (M+E), and acetone/chloroform (A+C) at 323.15 K, 313.15 K, and 323.15 K respectively. Broken lines are fitted Redlich–Kister polynomials.

properties such as the density and phase transition temperature.^{1,45} The activity coefficients are directly connected to the excess Gibbs energy of mixing $\Delta_{\text{mix}}G^e$ via Eq. (4.10). The acetonitrile/benzene binary system exhibits positive deviations from Raoult’s law and so, although both substances are completely miscible, cohesive forces between like molecules remain stronger in the mixture than adhesive forces between molecules of different species. Experimental excess Gibbs energies of mixing for the system at 323.15 K are available from a Redlich–Kister polynomial¹⁹⁰ and are shown alongside the bQCE result in Fig. 4.1. While the position of the maximum is shifted from the equimolar mixture at $x = 0.5$ to the acetonitrile-rich region, the bQCE method can predict the excess Gibbs energy of mixing quantitatively correct within an error margin of 0.3 kJ/mol. Note that this result is obtained without fitting to any thermodynamic data of either the neat compounds or the mixture but instead the two parameters are fitted to density and boiling point at each mole fraction. Furthermore, instead of employing high-level quantum chemical methods, we used the fast semi-empirical GFN-xTB method; hence, our approach is easily applicable to many different systems. This is possible, since the mean-field parameter a_{mf} can, to some degree, compensate for the level of the underlying electronic structure method.

The methanol/ethanol binary system is a near ideal mixture with a negligible enthalpy of mixing.¹⁹⁰ Hence, the excess Gibbs energy of mixing for this system is near zero and a similar result is obtained from the bQCE treatment, as can be seen in Fig. 4.1 for a temperature of 313.15 K. Even though the bQCE results fluctuate around the experimental result with a maximum deviation of 0.03 kJ/mol, on average the same zero excess Gibbs energy of mixing is reproduced.

4. A Cluster Approach for Activity Coefficients

Table 4.2: Activity coefficients f_i of each component in the binary mixtures acetonitrile/benzene, methanol/ethanol, and acetone/chloroform.

x_1	acetonitrile + benzene				methanol + ethanol				acetone + chloroform			
	f_N	f_B	f_N^{exp}	f_B^{exp}	f_M	f_E	f_M^{exp}	f_E^{exp}	f_A	f_C	f_A^{exp}	f_C^{exp}
0.00	3.53	1.00	3.01	1.00	0.75	1.00	1.00	1.00	1.46	1.00	0.58	1.00
0.10	2.46	1.02	2.31	1.01	1.01	0.99	1.00	1.00	0.85	1.02	0.59	1.00
0.20	2.03	1.05	1.88	1.05	1.05	0.98	1.00	1.00	0.75	1.04	0.62	0.99
0.30	1.81	1.09	1.61	1.11	1.02	0.99	1.00	1.00	0.78	1.03	0.67	0.96
0.40	1.65	1.15	1.42	1.18	0.99	1.01	1.00	1.00	0.84	0.98	0.73	0.92
0.50	1.52	1.23	1.29	1.28	0.99	1.01	1.00	1.00	0.91	0.93	0.80	0.86
0.60	1.39	1.37	1.19	1.42	1.00	1.00	1.00	1.00	0.96	0.86	0.86	0.78
0.70	1.26	1.64	1.11	1.61	1.00	1.00	1.00	1.00	1.00	0.80	0.92	0.69
0.80	1.14	2.21	1.05	1.89	1.00	1.01	1.00	1.00	1.02	0.76	0.96	0.60
0.90	1.05	3.75	1.01	2.33	1.00	1.00	1.00	0.99	1.01	0.80	0.99	0.51
1.00	1.00	9.48	1.00	3.07	1.00	0.90	1.00	0.99	1.00	1.07	1.00	0.43

To complete our set of diverse binary mixtures, we included a system at a temperature of 323.15 K with negative excess Gibbs energy of mixing, namely the acetone/chloroform mixture, which is shown in Fig. 4.1. While the position of the minimum is correctly reproduced and the maximum deviation from the experimental reference is 0.3 kJ/mol, the bQCE method fails to correctly describe the chloroform, in which a positive excess Gibbs energy of mixing is obtained. Nonetheless, for the larger part of the mixing range negative deviation from ideality is correctly predicted.

From these systems we can reinforce our findings from earlier studies, that bQCE is able to correctly describe the thermodynamics of mixing in the liquid phase from quantum chemically optimized clusters.^{1,43,45} With excess Gibbs energies of mixing available over the whole range of mixing, we can now calculate activity coefficients as described in the Section 4.2.2. As can be seen from Fig. 4.1, Redlich–Kister style polynomials can be nicely fitted to the bQCE data. The fitting parameters g_n can be inserted in Eqs. (4.15) and (4.16) and Eq. (4.10) then gives the activity coefficients f_i . This has been done for all investigated systems and the results are given in Table 4.2.

Activity coefficients f_N of acetonitrile in benzene are in good agreement with experimental values. However, for benzene in acetonitrile the activity coefficients f_B are overestimated. In general, agreement for any compound is reasonably good around $x_i = 0.5$, but worsens in the more dilute regions. This is because activity coefficients are sensitive to the slope $\Delta_{\text{mix}}G^e$, which is often not well reproduced, as is obvious from Fig. 4.1. A possible explanation is the limited cluster size of a maximum of six molecules. It is thinkable, however not yet tested, that the inclusion of larger clusters with a more representative composition for the diluted ranges improves the results at limiting mole fractions.

4.4 Conclusion

In this article we introduced a novel way to obtain activity coefficients of binary mixtures based on a cluster approach. This approach relies on the binary quantum cluster equilibrium theory.^{43,45} To perform such a calculation a few clusters consisting of molecules from each substance either in pure or mixed form have to be constructed. Here we build clusters up to a size of six monomers. Subsequent quantum chemical calculations were based on a semi-empirical method¹⁸⁷ and ensured fast access of the input to the cluster partition functions. These undergo a self-consistent-field calculation, and the results are populations of the clusters as well as Gibbs energies. Very satisfying results for the vaporization enthalpies of the pure substances could be calculated. Using Redlich–Kister polynomials and taking their derivatives allowed access of the activity coefficients. We showed for the example of acetonitrile/benzene, methanol/ethanol, and acetone/chloroform that this is a valuable approach. The approach is applicable in principle to all kinds of mixtures and temperature or pressure ranges. Improvements may be possible by the choice of a higher level of quantum chemical calculations as well as by considering analytical derivatives at the level of the partition function. In the past, improvements to QCE results could be observed by considering anharmonicity effects in the neat hydrogen chloride system.⁷⁴ Anharmonic effects are of importance in strongly interacting systems with an extended hydrogen bond network. Hence, mixtures of alcohols like the investigated methanol/ethanol system might be improved by considering anharmonic effects. Another concern regarding the bQCE method is the treatment of long-range interactions between clusters by a simple mean-field approach. It was observed that this approach is problematic in systems where both polar as well as dispersive interactions contribute significantly to the system. This is because apolar molecule parts such as alkyl chains will usually coordinate toward the vacuum and their contributions to the system’s cohesive and repulsive interactions are neglected. The extent of this problem is yet unknown and will be investigated together with possible solutions in a future work. In this article we could demonstrate the bQCE’s ability to produce reasonable activity coefficients for binary mixtures of organic solvents. We developed a new systematic and computationally low-cost procedure to arrive at these results. This new approach can now be applied to a larger range of systems, which will help to identify and possibly eliminate deficits of the current bQCE method.

Acknowledgment

The authors express their gratitude to the ETN Socrates (<http://etn-socrates.eu/>) because this project has received funding from the European Union’s EU Framework Programme for Research and Innovation Horizon 2020 under Grant Agreement No 721385. Furthermore, we thank the BMBF for their support under project 03EK3051A.

Part II

Proton Transfer Equilibria in Ionic and Molecular Liquids

Summary of Part II

The second part of the thesis contains three studies that describe different approaches to model proton transfer equilibria in different types of liquids. These are based on the bQCE method and AIMD simulations and include ionic, molecular, and pseudo-ionic liquids, which fall between the two limit states.

Chapter 5 describes the first application of the bQCE method to protic ionic liquids in combination with the PBEh-3c functional. A range of alkylammonium-based PILs is considered, including the well-studied ethylammonium nitrate (EAN) and the related ethylammonium formate (EAFm). The cluster sets include the neutral acid and base species as reference monomers and ion pair clusters of up to ten ion pairs. By employing the parameter-free bQCE⁰ approach the boiling point of EAN can be predicted with an excellent accuracy of 1 K and good to acceptable accuracy of <50 K for the other PILs. Through increasing the maximum cluster size in the cluster set, the agreement with the experiment systematically improves until the size of four ion pairs and quickly converges afterwards. This is because at elevated temperatures close to the boiling point the larger clusters of five or more ion pairs are lowly populated. When the bQCE method is employed with optimized parameters, the vaporization enthalpy $\Delta_{\text{vap}}H$ can be calculated. It is shown that extrapolating the gas phase enthalpy from temperatures above the boiling point to room temperature leads to unreasonably high estimates of $\Delta_{\text{vap}}H$. The reason is, that at the boiling point the gas phase is dominated by neutral acid and base species, in accordance with experiment.²⁷² Instead, allowing the bQCE method to find an equilibrium distribution of neutral acid and base species and ion pairs, leads to significantly better estimates. In close agreement with experiment, it is shown that at room temperature the vapor phase of EAN is dominated by single ion pairs and only at temperatures beyond 400 K the neutral parent species start to form. Estimates of $\Delta_{\text{vap}}H$ get worse with increasing alkyl chain length, as the clusters can not sufficiently account for dispersion interactions. By introducing clusters to the cluster set that, next to a number of ion pairs, include a neutral acid or base molecule, the concentration of neutral species in the system and thereby the proton transfer degree can be calculated. For EAN a negligible concentration of neutral species of 1.64×10^{-6} mol/l is found. In contrast, a concentration of 1.47×10^{-3} mol/l is found for EAFm, several orders of magnitude higher compared to EAN. These values agree well with the experimentally observed trends and can explain their different properties, such as the higher vapor pressure and lower conductivity of EAFm.

As a natural successor, Chapter 6 focuses on the equimolar mixture of *N*-methylimidazole and acetic acid (C₁Im–HOAc), which is considered a pseudo-PIL for its low proton transfer degree,¹¹⁵ but exhibits remarkable proton conductivity. Experimental estimates of the content of neutral species vary strongly between 7.2% and >99%, depending on the

employed method.^{115,124,273} Six AIMD simulations of this system are carried out with different starting conditions, assuming either a complete proton transfer, an equal mixture of ionic and neutral species, or fully neutral mixture. All simulations quickly converge to an equilibrium distribution of about 60 to 90 % neutral species, with an average of about 80 %, which is in good agreement with an experimental estimate based on calorimetric titration.¹²⁴ Diffusion rates calculated from the AIMD trajectories show no distinct behavior for the proton, proving that its motion is coupled to the imidazolium cation and acetic acid. The high proton conductivity observed for this system cannot be explained by a simple vehicle mechanism for proton diffusion, however. Instead, a deeper look into the simulations reveals frequent proton transfer reactions in extended chains of hydrogen bonded acid and base molecules. Near simultaneous proton hopping in chains of up to four molecules can be observed directly, resembling the Grotthuss diffusion mechanism that is responsible for water’s high proton conductivity.²⁷⁴ Therefore, the high proton conductivity in the C₁Im–HOAc pseudo-PIL can be explained by structural diffusion. Based on this insight, quantum chemical calculations are carried out to find potential candidates for Grotthuss-enabled PILs. Various combinations of differently functionalized anions and cations are evaluated for their likelihood to feature structural proton diffusion. *N*-methylimidazolium trifluoroacetate and *N*-methylimidazolium formate are identified as good candidates, that are easy to synthesize.

Prior to its application to PILs, the bQCE method was demonstrated capable of reproducing the temperature dependence of the ionic product of water with remarkable accuracy.⁴⁰ Chapter 5 shows its ability to predict proton transfer equilibria in complex binary systems. As a combination of both approaches and to complete the range of ionic to molecular systems in this part, Chapter 7 describes the application of the bQCE method in combination with the PBEh-3c functional to predict the proton transfer degree in aqueous solutions of formic and acetic acid. By adding clusters to the cluster set that, next to a number of neutral acid and water molecules, include hydronium cation and a formate or acetate anion, the concentration of dissociated species can be calculated at different mole fractions. The experimental acid strengths of both formic and acetic acid at infinite dilution can be reproduced reasonably well, with calculated pK_a s of 2.62 and 4.26 compared to their experimental values of 3.75 and 4.76, respectively. These are impressive results, considering the simplicity of the approach. Furthermore, the bQCE method allows prediction of the ion concentration over the whole mixing range. It is shown that the common assumption of a constant, concentration-independent pK_a value leads to unreasonably high predictions of the dissociation degree at high concentrations of the acids. Instead, the bQCE calculations reveal that the ion concentration reaches a maximum at a low mole fractions of $x = 0.04$ the acid and rapidly falls afterwards. This behavior closely resembles the conductivity measured in both solutions, which reaches a maximum at mole fractions of 0.14 and 0.06 in formic and acetic acid, respectively.

5 Thermodynamics and Proton Activities of Protic Ionic Liquids with Quantum Cluster Equilibrium Theory

Johannes Ingenmey,^{*} Michael von Domaros,^{*} Eva Perlt,^{*} Sergey P. Verevkin,[†] and Barbara Kirchner^{*}

Received: October 26, 2017, Revised: January 18, 2018, Published: February 9, 2018

Reprinted (adapted) with permission from

J. Ingenmey, M. von Domaros, E. Perlt, S. P. Verevkin, and B. Kirchner, *J. Chem. Phys.*, 2018, **148**, 193822.

Copyright © 2018 American Institute of Physics.

DOI: 10.1063/1.5010791

Contributions to the manuscript

- Developing the general approach to modeling PILs with bQCE
- Construction of cluster sets and performing the DFT calculations
- Running the QCE calculations
- Analyzing and discussing the results
- Providing the figures
- Writing the computational parts of the manuscript

^{*}Mulliken Center for Theoretical Chemistry, Institut für Physikalische und Theoretische Chemie, Rheinische Friedrich-Wilhelms-Universität Bonn, Berlingstraße 4+6, 53115 Bonn, Germany

[†]Abteilung Physikalische Chemie, Universität Rostock, Dr.-Lorenz-Weg 2, 18059 Rostock, Germany

Abstract We applied the binary Quantum Cluster Equilibrium (bQCE) method to a number of alkylammonium-based protic ionic liquids in order to predict boiling points, vaporization enthalpies, and proton activities. The theory combines statistical thermodynamics of van der Waals-type clusters with *ab initio* quantum chemistry and yields the partition functions (and associated thermodynamic potentials) of binary mixtures over a wide range of thermodynamic phase points. Unlike conventional cluster approaches that are limited to the prediction of thermodynamic properties, dissociation reactions can be effortlessly included into the bQCE formalism, giving access to ionicities, as well. The method is open to quantum chemical methods at any level of theory, but combination with low-cost composite density functional theory methods and the proposed systematic approach to generate cluster sets provides a computationally inexpensive and mostly parameter-free way to predict such properties at good-to-excellent accuracy. Boiling points can be predicted within an accuracy of 50 K, reaching excellent accuracy for ethylammonium nitrate. Vaporization enthalpies are predicted within an accuracy of 20 kJ/mol and can be systematically interpreted on a molecular level. We present the first theoretical approach to predict proton activities in protic ionic liquids, with results fitting well into the experimentally observed correlation. Furthermore, enthalpies of vaporization were measured experimentally for some alkylammonium nitrates and an excellent linear correlation with vaporization enthalpies of their respective parent amines is observed.

5.1 Introduction

Research on ionic liquids (ILs) continues with constantly growing interest.¹¹⁰ This is motivated by their numerous potential applications as solvent and proton conductors in fuel cells, as protein crystallization agents, or as solvents in synthetic chemistry both in academical and industrial processes, to name but a few.^{89,275} ILs are salts, most often including an organic cation, that are liquid at moderate temperatures. In the face of a growing awareness for the impact of industrial chemistry on environment and availability of resources, ILs are often tested for application in more sustainable processes.^{89,110,113} Despite their toxicity, ILs were considered to be more environmentally friendly due to their generally low vapor pressure and hence negligible volatility.⁸⁹ Other properties shared by most ILs include their ionic conductivity and vast liquid range. Physicochemical properties of ILs can be tuned by interchanging cations or anions, variation of functional groups, or increasing the length and configuration of alkyl chains. The myriad of potential cations and anions to combine makes the design of new ILs relatively easy,⁸⁹ but their usefulness for specific applications can only be determined by investigating their physicochemical properties. According to Wasserscheid and Welton, finding methods to predict potential ILs' properties is a relevant task of current research, opening a path to

application-driven synthesis.⁸⁹ A possible solution is the computational investigation of fundamental structure–activity relationships.

A subgroup of this enormous class of substances consists of those ILs, which are formed by a proton transfer between a Brønsted acid and a Brønsted base,



These are termed protic ILs (PILs) to differentiate them from aprotic ILs (AILs).¹¹⁰ The unifying property of PILs is the acidic proton, bound to the cation. The availability of this proton is a requirement for their application as proton conductors in fuel cells.¹⁰⁹ On the other hand, for many applications of ILs, one desires a high availability of free charge carriers in the solvent, which is counteracted by the presence of neutral acid and base species in PILs due to an incomplete proton transfer. Some authors refer to these effects as “protic impurities.”⁸⁹ In fact, a high proton activity deteriorates exactly those properties, which make ILs an interesting alternative to molecular solvents, namely, low vapor pressure, vast liquid range, and high ionic conductivity.¹⁰⁹ Experimental investigations of proton activities have been done only for few PILs,^{105,122,124,125} and a consistent thermodynamically justified model to predict proton activities is not available. Construction of such a model is a relevant task, which must be solved in order to facilitate the application-driven design of PILs. Of similar importance is the knowledge and understanding of a PIL’s vaporization process, its thermostability, and related properties such as vapor pressure and vaporization enthalpy. This is especially true for applications at elevated temperatures.

A potential approach to solve both tasks, prediction of proton activity and vaporization properties, is given by the quantum cluster equilibrium (QCE) method. First introduced by Frank Weinhold in 1998,^{36,52} the QCE method combines elements of statistical thermodynamics and quantum chemistry in order to describe liquids in an equilibrium state. Since its first introduction, the QCE method has been applied to an abundance of neat molecular liquids.^{52,56,68,69,71,72,79} We extended the method to include binary systems.^{1,43,45}

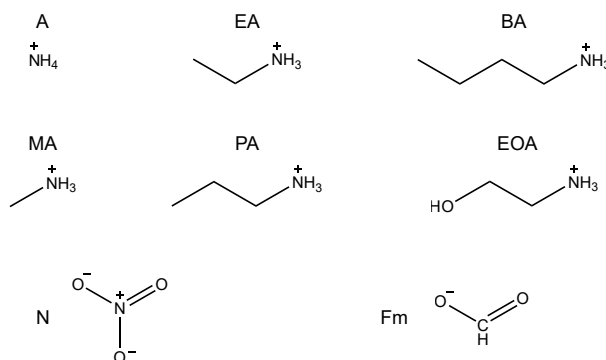


Figure 5.1: Structural formulas of cations and anions investigated in this work.

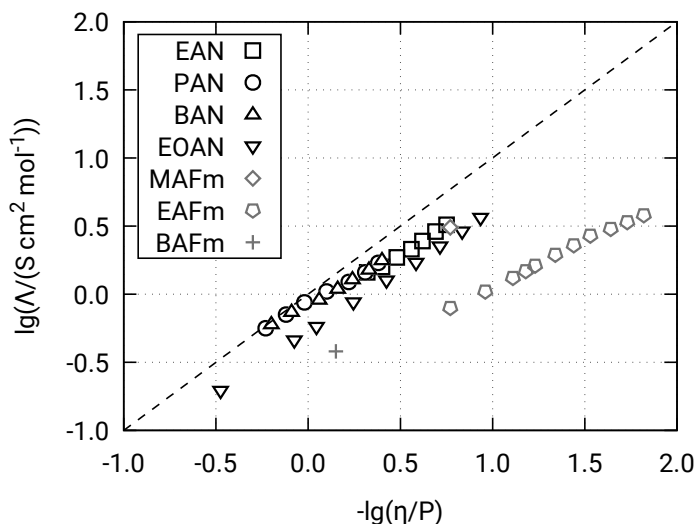


Figure 5.2: Walden plot of the PILs investigated in this work. Data is taken from Ref. 282 for EAN–BAN, Ref. 109 for EOAN and EAFm, and Ref. 110 for MAFm and BAFm.

The QCE method is closely related to mixture models from the late fifties to early sixties.^{276–281} The QCE method applies models of statistical thermodynamics to quantum chemically calculated clusters in order to build up a thermodynamic description of liquid and gaseous phases based on the system’s partition function. For this purpose, a cluster set is constructed, including relevant structures that represent the fundamental interactions within the system. Equilibrium populations of the clusters are obtained, which provide a structural understanding of the system’s properties on a molecular level. Recently, the QCE method was used successfully to predict the ion product of water, demonstrating its capability to predict equilibrium constants of autoprotolysis reactions in liquid systems.⁴⁰

In this work, we present the first treatment of PILs with our binary QCE (bQCE) method. For this purpose, we investigate some of the most simple alkylammonium-based PILs, including the experimentally very well investigated ethylammonium nitrate (EAN). Other investigated PILs are methylammonium nitrate (MAN), *n*-propylammonium nitrate (PAN), *n*-butylammonium nitrate (BAN), and ethanolammonium nitrate (EOAN), as well as two formate based PILS methylammonium formate (MAFm) and ethylammonium formate (EAFm). Furthermore, we present enthalpies of vaporization for some of the investigated PILs measured using the transpiration method (for details, see the supplementary material).²⁸³ The cations and anions composing all PILs investigated in this work are shown in Fig. 5.1, and some of their basic properties are summarized in Table 5.1.

Angell et al. suggested a correlation between several proton activity dependent properties of a PIL and its $\Delta pK_a = pK_a(\text{HB}^+) - pK_a(\text{HA})$ value.¹¹⁶ They found that PILs with $\Delta pK_a > 8$ exhibit near ideal Walden behavior.^{109,116} The Walden plot, which shows the

Table 5.1: Melting point T_m (K), boiling point T_b (kelvin), density ρ (g/cm³), viscosity η (cP), ionic conductivity κ (mS/cm) and difference ΔpK_a , calculated with values from Ref. 197, for several alkylammonium compounds at 298 K. If not specified otherwise, data is taken from Ref. 110.

Anion/cation	Symbol	T_m	T_b	ρ	η	κ	ΔpK_a
Nitrates							
Ammonium	AN	436.65	496.95 ^a				10.63
Methylammonium	MAN	377.85	479.95 ^a				12.04
Ethylammonium ^b	EAN	286.15	513.15	1.210	27.8	24.4	12.03
Propylammonium ^b	PAN	277.15		1.151	75.3	9.8	11.92
Butylammonium ^b	BAN			1.104	55.1	8.6	11.98
Ethanolammonium	EOAN	247.95	528.55	1.265	113	9.4	10.88
Formates							
Ammonium	AFm	393.15	453.15	1.260			5.50
Methylammonium	MAFm	251.45	435.25	1.087	17	43.8	6.91
Ethylammonium	EAFm	200.25	449.25	1.039	32	12.2	6.90
Propylammonium	PAFm	217.75	486.25	0.996	96.7 ^c		6.79
Butylammonium	BAFm	226.35	497.65	0.968	70	3.1	6.85

^a Decomposes.

^b ρ , η and κ taken from Ref. 282.

^d Measured at 293.15 K.

relation between a PIL's molar ionic conductivity and its viscosity, is given for several PILs investigated in this work and is shown in Fig. 5.2. All PILs shown fall below the ideal 0.01 M KCl line, indicating the aggregation of ions to neutral complexes, reformation of neutral acid and base molecules as indicated by Eq. (5.1), or other effects^{131,137,284} lowering their ionicity,^{130,285,286} meaning the effective portion of charge carriers available for ionic conduction.¹¹⁶ Comparing the Walden behavior of each PIL with its ΔpK_a value (listed in Table 5.1), a correlation between a PIL's ΔpK_a and ionicity, and by extension its proton activity, seems reasonable. However, the approximative nature of ΔpK_a is obvious from the fact that ΔpK_a values are measured in aqueous systems. In this work, we present the first theoretical approach to calculate proton activities and further investigate their correlation with ΔpK_a .

5.2 Model and Methods

5.2.1 The bQCE Method

Detailed derivations of QCE theory and its extension to binary systems can be found in earlier studies.^{36,38,43,45} Hence, we will limit this section to a brief overview of the underlying theory. The QCE method starts its description of liquid and gaseous phases with a system of differently populated, noninteracting clusters, built up from one (neat

5. Thermodynamics and Proton Activities of Protic ILs with QCE Theory

substances) or two (binary systems) monomers. This cluster gas is assumed to be in thermodynamic equilibrium. The equilibrium reaction between clusters of a binary system can be written as



where $i(\varphi)$ and $j(\varphi)$ denote the number of monomers of each component C_1 and C_2 that build up the cluster φ . The QCE procedure's central quantity is the system's total partition function Q^{tot} , which for volume V and temperature T is given by

$$Q^{\text{tot}}(\{N_\varphi\}, V, T) = \prod_{\varphi=1}^N \frac{1}{N_\varphi!} [q_\varphi^{\text{tot}}(V, T)]^{N_\varphi}, \quad (5.3)$$

where q_φ^{tot} is a single cluster partition function corresponding to cluster φ and $\{N_\varphi\}$ is the full set of cluster populations N_φ . The cluster partition function can be evaluated as product of partition functions corresponding to the clusters' degrees of freedom

$$q_\varphi^{\text{tot}}(V, T) = q_\varphi^{\text{trans}}(V, T)q_\varphi^{\text{rot}}(T)q_\varphi^{\text{vib}}(T)q_\varphi^{\text{elec}}(V, T). \quad (5.4)$$

Here, q_φ^{trans} , q_φ^{rot} , and q_φ^{vib} are the translational, rotational, and vibrational partition functions, which can be calculated from standard equations for the particle in a box, rigid rotator, and harmonic oscillator. The electronic cluster partition function q_φ^{elec} is calculated from the electronic ground state energy $\epsilon_\varphi^{\text{elec}}$.

Two empirical parameters are introduced. In order to describe the translational partition function more accurately, the phase volume V must account for an exclusion volume V_{ex} , which adds a volume v_φ to the non-punctiform clusters. Since cluster volumes are sensitive to the choice of atomic radii, an empirical scaling parameter b_{xv} is introduced. The exclusion volume is then given by

$$V_{\text{ex}} = b_{\text{xv}} \sum_{\varphi=1}^N N_\varphi v_\varphi. \quad (5.5)$$

The electronic partition function is extended by a term accounting for interactions between clusters. Inter-cluster attractions are described in the form of a volume and cluster size dependent mean-field energy

$$q_\varphi^{\text{elec}}(V, T) = \exp \left\{ - \frac{\epsilon_\varphi^{\text{elec}} - [i(\varphi) + j(\varphi)] \frac{a_{\text{mf}}}{V}}{k_B T} \right\}, \quad (5.6)$$

where k_B is the Boltzmann constant and the mean-field parameter a_{mf} is a second empirical parameter, scaling the strength of inter-cluster interactions. In an empirically optimized QCE calculation, the parameters are chosen such that the deviation of the

QCE results from a given experimental input such as densities and phase transition temperatures becomes minimal. In 1998 Weinhold showed that the QCE method is capable of reproducing two features of liquid water, namely, the phase transition and the enthalpy of vaporization, even without optimizing the empirical correction parameters. This non-empirical approach was labeled QCE⁰. In QCE⁰ we set $a_{mf} = 0$ and $b_{xv} = 1$, effectively treating the system as a gas of clusters with no interactions occurring between them, similar to an ideal gas but differing in that the exclusion volume is still considered.

From the system’s total partition function Q^{tot} , all thermodynamic properties can be calculated. However, to calculate Q^{tot} , all independent variables ($\{N_\phi\}, V, T$) need to be known. The temperature is determined by the user and the volume is restricted to be in accordance with an externally applied pressure

$$p = k_B T \left(\frac{\partial \ln Q^{\text{tot}}}{\partial V} \right)_{T, \{N_\phi\}}. \quad (5.7)$$

The cluster populations $\{N_\phi\}$ are chosen such that the system’s total Gibbs energy G is minimized, as described in more detail in Ref. 43.

5.2.2 Computational Details

Geometry optimizations and frequency analyses were performed on all structures using density functional theory (DFT) with the ORCA program package.¹⁹⁸ All calculations were performed by employing the low-cost PBEh-3c composite method of Grimme et al.,¹⁸⁶ which uses a modified def2-SV(P) basis set termed def2-mSV(P). The method involves a geometrical counterpoise (gCP) correction^{186,199} in order to deal with the intermolecular as well as intramolecular basis set superposition error (BSSE). Furthermore, the London dispersion energy is accounted for by Grimme’s empirical dispersion correction D3.^{87,200} Tight SCF convergence criteria were applied in each geometry optimization. Harmonic frequencies were calculated as analytical derivatives of the energy gradient.

bQCE calculations were performed with the Peacemaker 2.5 program package³⁹ which has successfully been used to describe binary mixtures previously.^{1,43–45} All calculations were performed at a fixed pressure of 101.325 kPa and temperature ranging from 273 to 700 K. Cluster volumes were calculated by employing GEPOL93’s solvent excluding surface algorithm²⁰¹ with van der Waals radii taken from Bondi’s compilation.²⁰² All shown results were obtained treating the PILs as binary mixtures of their respective parent acid and base. This means that the reference monomers of each system are the neutral, isolated acid and base molecules, each representing one of the mixture’s components. Each calculation included equal amounts of both compounds, modeling a perfectly neat PIL. This work includes results from the parameter free bQCE⁰ approach as well as optimized bQCE calculations. Optimizations were performed using boiling points and densities,

which are summarized in Table 5.1. Further details regarding the empirical optimization can be found in the supplementary material.

To test the bQCE results' dependence on the quantum chemical method and basis set, EAN was also investigated at the B3LYP/6-31+G* and B3LYP/def2-TZVP levels of theory, employing the D3 and gCP correction. The recently introduced semi-empirical GFN-xTB¹⁸⁷ method of the Grimme group was also tested. These results can be found in the supplementary material. While for B3LYP/6-31+G* results of similar or worse accuracy were found, all results except the phase transition temperature were improved by employing the B3LYP/def2-TZVP method (see Table C.4 in the supplementary material). However, the improvement is only small and does not justify the greater computational cost. GFN-xTB yields very good estimates of the vaporization enthalpy, improving on the PBEh-3c results, but predicts too high boiling points.

5.2.3 Cluster Sets

Constructing the cluster set is a crucial step in applying the bQCE method.^{39,43} As has been demonstrated for neat systems and mixtures,^{1,43,45} neither the clusters nor the cluster set itself need to be large in order to produce physically meaningful results. The clusters should include important structural motifs characterizing the investigated system. In a previous work, we have shown the bQCE method to be able to predict the correct mixing behavior of binary molecular mixtures with clusters not larger than three monomers.¹ Other cluster approaches to ILs have yielded reasonable accordance to experimental results^{272,287,288} with the maximum cluster size ranging from 6 to 10 ion pairs. As the electronic interaction energy per ion pair seems nearly converged at a cluster size of 8 ion pairs, we chose this number as maximum cluster size in this work. Clusters of the size of 9 and 10 ion pairs were calculated for EAN and EAFm, but no improvement of the bQCE results was observed employing these clusters.

The fundamental units of a cluster set are the reference monomers of each component. In this work, we treat PILs as binary mixtures of their respective parent acid and base. Hence, the reference monomers are the neutral, isolated acid and base molecules. In the case of EAN, these are nitric acid and ethylamine. It is in principle possible to treat PILs as a single compound system, using a single ion pair as the reference monomer. However, experiments by Ludwig et al. have shown that the neutral monomers must be considered for a realistic modeling of the gas phase.²⁷² Thus, every cluster set employed in this work includes the single acid and base molecules as reference monomers. Furthermore, it is important to note that the single ion pair, composed of one alkylammonium cation and one nitrate or formate anion, is not stable in the gas phase quantum chemical optimization. Instead, the proton transfers back to the anion in all cases, consistent with earlier studies of other groups.^{272,287} However, these clusters show a markedly different behavior than the

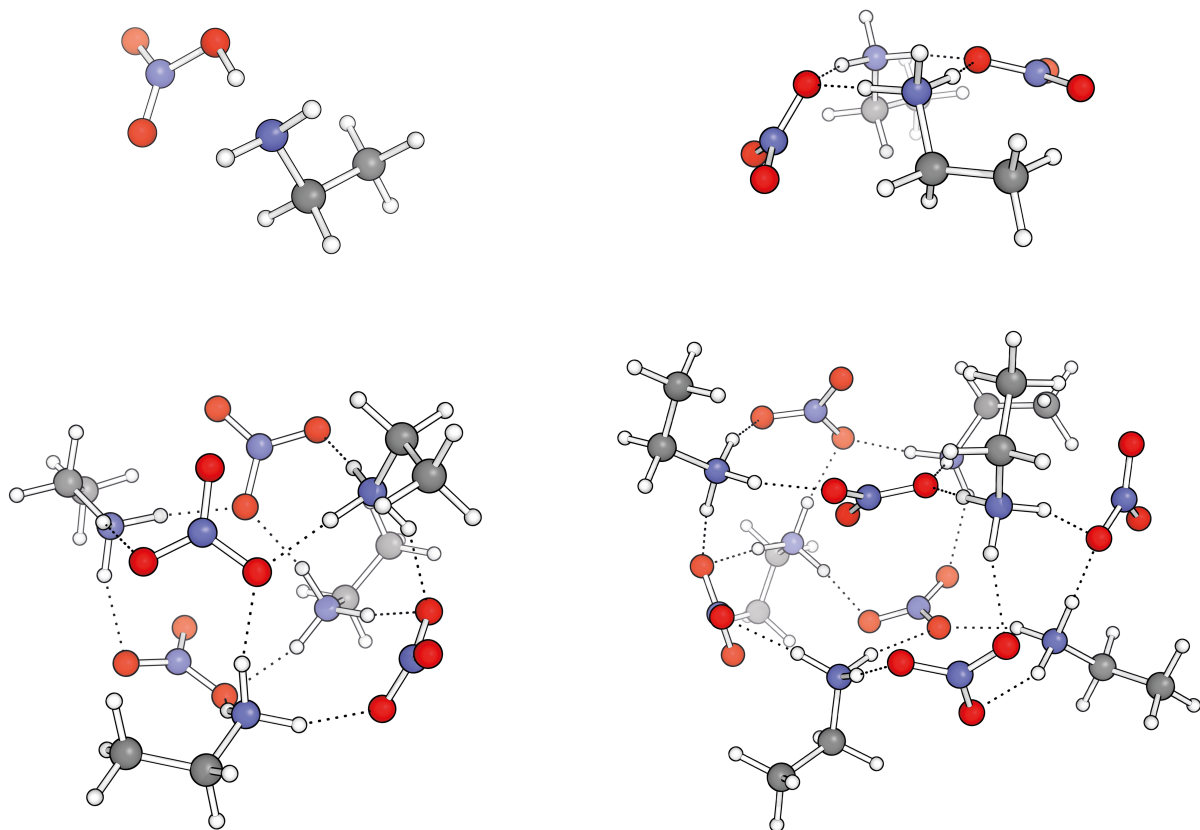


Figure 5.3: EAN clusters with 1, 2, 4, and 6 ion pairs optimized at the PBEh-3c level of theory. As can be seen, the proton transfers back to the anion in the case of a single ionic couple. Thus, we call it a pseudo-ion pair.

isolated molecules similar to what was identified as contact ion pairs in Ludwig’s study. Thus, we term it the single pseudo-ion pair (p-IP).

The large number of internal degrees of freedom of even simple ILs like EAN makes finding relevant and energetically favorable structures a difficult task. A systematic search of the PES’s global minimum by manual cluster construction quickly becomes a nearly impossible task even if only small clusters of size $n \leq 8$ are considered. Therefore, a computationally efficient method to construct reasonable candidates for the global minimum structure is needed. In this study, we performed a global energy minimization for each cluster size, utilizing a genetic structure optimization algorithm at a classical force field level of theory. This was done using the OGOLEM framework^{168,169} in combination with the AMBER 2016 molecular dynamics package,²⁰³ and the generalized AMBER force field (GAFF)¹⁷⁰ implemented therein. A large number of individual structures were evaluated for each cluster size, ranging from 10 000 to 30 000 individuals depending on the cluster size and the number of internal degrees of freedom. As there is no guarantee that the global minimum obtained at the force field level corresponds to the global minimum of the DFT potential energy surface, several clusters have been optimized quantum chemically for each cluster size and only the most stable one was added to the cluster set. A selection of these structures is shown in Fig. 5.3.

bQCE results are directly dependent on the employed clusters and must always be interpreted keeping the cluster set in mind. We will refer to a bQCE calculation employing a cluster set, where the largest cluster includes n ion pairs, as bQCE(n). More specifically, a bQCE(n) cluster set includes global minima found for all cluster sizes up to the number of n ion pairs as well as the neutral reference monomers. A calculation labeled bQCE(0) only includes the neutral monomers and no ionic clusters are considered. In Sec. 5.3.3, the cluster sets are extended by such clusters that next to a number of ion pairs also include a single acid or base molecule. Note that this approach is different from the one employed in a recent QCE study on predicting the ionic product of water.⁴⁰ Therein, net-neutral clusters of water were included, containing one hydronium cation and one hydroxide anion each, stabilized by a number of water molecules. In this work, due to the binary model and reversed nature of the auto-dissociation reaction, we are able to add single neutral molecules to clusters of ion-pairs.

Neat clusters consisting solely of acid or base molecules were calculated for EAN but found to be insignificantly populated and so were not included in the calculations.

In this work, we will not include a detailed structure analysis, as this has already been done for EAN, PAN, and BAN by Bodo et al.²⁸⁷ and our clusters feature the same geometric characteristics. Geometry data of all optimized structures used in this work is available in the supplementary material.

5.3 Results and Discussion

5.3.1 Boiling Points

The boiling point is one of the most basic physicochemical properties and of special importance when PILs are used for applications at elevated temperatures. However, only few attempts have been made to predict boiling points of PILs by ab initio techniques. Ludwig et al. were able to predict EAN's boiling temperature of 513 K within an accuracy of 13 K, applying statistical mechanics to quantum chemically calculated clusters.²⁷² Ludwig's cluster approach, first demonstrated in 2008,²⁸⁸ is related to the QCE⁰ approach but differs in that only cluster partition functions were considered instead of the population dependent total partition function of the system.

bQCE⁰ calculations were carried out for all investigated PILs. Figure 5.4 shows the phase volume of EAN for different numbers of ion pairs n building up the largest cluster in the respective cluster set. For a cluster set including only the neutral parent molecules ($n = 0$), a completely linear volume dependence of the temperature is observed, closely obeying Charles's law ($V/T = \text{const.}$). This is the expected behavior, as no cluster reformation reaction takes place in this system described by a minimal cluster set. However, with the inclusion of the p-IP ($n = 1$), the behavior drastically changes. At low tempera-

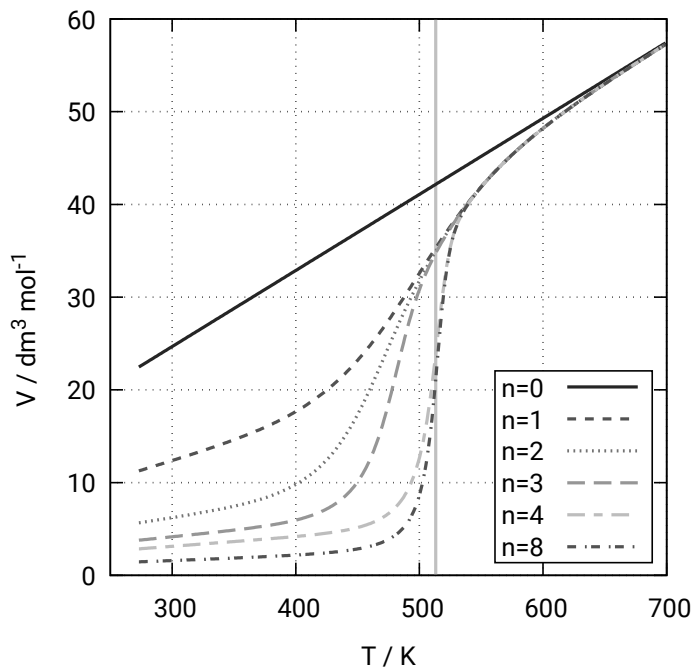


Figure 5.4: bQCE⁰(n) phase volume of EAN for different cluster sizes n , where $n = 0$ indicates that only the neutral species are included. The experimental boiling point of EAN $T_b = 513$ K is denoted by a vertical line.

tures, below 350 K, and high temperatures, exceeding 650 K, the system obeys Charles’s law. Note that the bQCE⁰ method does not realistically describe the low temperature phase volume, as no mean-field interaction leads to a condensed fluid-like system. In the temperature range in-between, we can observe a distinct increase of the phase volume, where the system gradually transfers from a high-density state to a low-density state with increasing temperature. We can interpret this behavior as a quasi phase transition. Figure 5.4 shows that with increasing cluster set size, this transition does not only become sharper but also closely matches the experimentally observed boiling point of EAN.

The isobaric heat capacity C_p , while quantitatively unrealistic, features the characteristic maximum and minimum of a first order phase transition as can be seen from Fig. 5.5. We define the quasi phase transition temperature T_b^* to be the unique temperature of the maximum in C_p , which closely matches the point of inflection in the phase volume. Using this approach for EAN, the bQCE⁰(8) calculation gives a value of $T_b^* = 514$ K which matches the experimental boiling point of 513 K within an accuracy of 1 K. It is noteworthy that even from bQCE⁰(4), employing only clusters up to the tetramer, the experimental boiling point is correctly predicted within an accuracy of 2 K, while smaller cluster sets fail to reproduce the correct phase transition temperature. This is because at temperatures near the boiling point, the tetramer becomes the dominant species in the system, being favored over the octamer.

Theoretical boiling points have been calculated for all investigated PILs and are summarized in Table 5.2. The accuracy observed for EAN drastically drops for the other

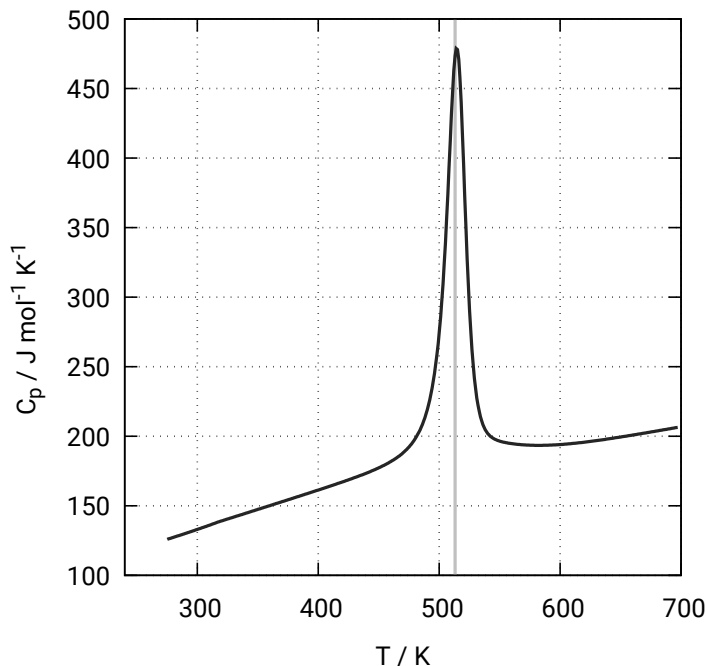


Figure 5.5: bQCE⁰(8) isobaric heat capacity C_p of EAN. The experimental boiling point of EAN $T_b = 513$ K is denoted by a vertical line.

PILs to an error of about 50 K for both MAN and EAFm. For MAN, this error can be explained, as it vaporizes neither into ion pairs nor into neutral acid and base molecules, but rather decomposes into a multitude of different compounds, including water, carbon dioxide, formamide, and nitrogen oxides.²⁸⁹ This decomposition reaction cannot be described by our bQCE⁰(8) approach (nor is it the aim of the bQCE approach to describe decomposition reactions in general), and thus, the theoretical boiling point T_b^* cannot be directly compared to the experimental value. While the formates correctly show far lower boiling points compared to the nitrates, T_b^* underestimates the experimental values of MAFm and EAFm by 28 K and 49 K, respectively. A possible explanation might be that the cluster generation method described in Sec. 5.2.3 does not find stable enough clusters, as perhaps the interaction of the hydrogen in the formate anion is not well de-

Table 5.2: bQCE⁰(8) phase transition temperatures T_b^* and experimental¹¹⁰ boiling points T_b^{exp} in K for several PILs.

	T_b^*	T_b^{exp}
MAN	530	480
EAN	514	513
PAN	522	-
BAN	519	-
EOAN	549	529
MAFm	407	435
EAFm	400	449

scribed by our classical force field approach. EOAN's boiling point is correctly predicted to be higher than EAN's, owing to the additional attractive interactions of the hydroxyl group. However, the boiling point is overestimated by 20 K compared to the experimental value. The opposite argument may be true in this case, in that the ionic clusters are possibly over-stabilized at the PBEh-3c level of theory compared to the single molecules acting as gas phase reference. While nearly the same, PAN shows a lower T_b^* than BAN, which cannot be compared to experimental values, but is consistent with their respective viscosities (see Table 5.1).

Another source of error might stem from the experimental side, in that the liquids could contain impurities.²⁹⁰⁻²⁹² The boiling points of the investigated PILs listed in Table 5.1 were measured by Angell and Belieres, who state the water content is below 1 wt.% for each PIL and less than 0.025 wt.% in the case of EAN.^{109,110}

5.3.2 Thermodynamics of Vaporization

While PILs generally show a higher vapor pressure compared to AILs, which is attributed to the volatilization of the neutral parent molecules,^{110,112} in the case of EAN, a measurable vapor pressure was only observed for temperatures above 373 K.²⁷²

Connected to the vapor pressure is the enthalpy of vaporization $\Delta_{\text{vap}}H$ which is known only for few ILs.^{272,288,293} For AILs, $\Delta_{\text{vap}}H$ lies in the range of 120 to 200 kJ/mol,^{293,294} whereas for PILs, enthalpies of vaporization lie in the range of 90 to 140 kJ/mol.^{272,295-297} When discussing the vaporization enthalpy of PILs, it is important to define the processes involved in the vaporization. It has been established that the vapor phase of PILs can include both ion pairs and the neutral acid and base parent molecules in a ratio depending on the temperature, pressure, and acid and base strength of the parent species.^{272,295-298} Most PILs are observed to evaporate into their respective parent molecules and only PILs with particularly large ΔpK_a values evaporate as neutral ion pairs.^{110,298} From this, three possible vaporization mechanisms can be distinguished: (a) the vaporization of the PIL as contact ion pair, (b) the vaporization as ion pair followed by neutralization into the parent molecules via proton transfer in the gas phase, and (c) neutralization via proton transfer in the liquid phase and subsequent vaporization of the neutral species. If the latter two processes are favored over the vaporization as ion pair, measurements of the vaporization enthalpy will involve the reaction enthalpy of the proton transfer. Therefore, we differentiate between $\Delta_{\text{ip}}H$ which corresponds to the vaporization of a single ion pair, $\Delta_{\text{dis}}H$ which corresponds to the dissociation of an ion pair into neutral acid and base molecules, and $\Delta_{\text{vap}}H$ which is the enthalpic change associated with the vaporization of 1 mol of the liquid PIL into the gaseous state with a temperature and pressure dependent ratio of neutral species in both phases.

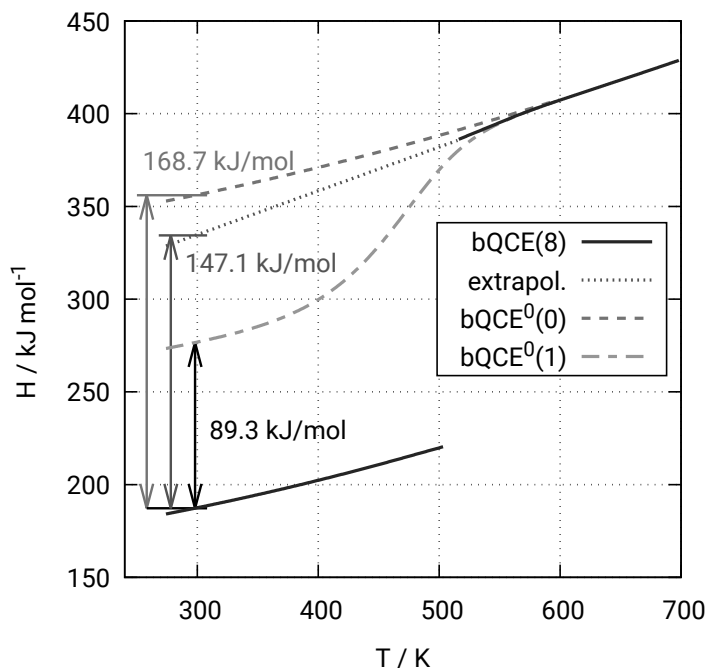


Figure 5.6: EAN’s total enthalpy H of the optimized bQCE(8) and two bQCE⁰ calculations, serving as gas phase reference. $\Delta_{\text{vap}}H$ values at 298 K are shown for different gas phase references.

The QCE method allows calculation of thermodynamic quantities for any temperature and pressure range. While the QCE⁰ method has been shown to be able to predict phase transition temperatures, the approach does not realistically describe some properties like phase volume and heat capacity. Optimizing the empirical correction parameters a_{mf} and b_{xv} corrects this insufficiency and makes also possible reasonable predictions of thermodynamic properties like the enthalpy $\Delta_{\text{vap}}H$ and entropy $\Delta_{\text{vap}}S$ of vaporization.^{39,52}

Figure 5.6 shows the total enthalpy H of EAN obtained from an optimized bQCE(8) calculation. At the boiling temperature, a jump in enthalpy can be seen, typical for first order phase transitions.²⁹⁹ At this temperature, the enthalpy of vaporization can be easily calculated as difference of the total enthalpy at the phase transition. This gives a value of $\Delta_{\text{vap}}H(513\text{ K}) = 162.34\text{ kJ/mol}$ far higher than the experimentally measured 105.3 kJ/mol at 298 K (see Table C.2 in the supplementary material). This is because at that temperature the gas phase consists mostly of the neutral parent molecules and $\Delta_{\text{dis}}H$ significantly contributes to $\Delta_{\text{vap}}H$.

To calculate $\Delta_{\text{vap}}H$ at 298 K, a gas phase reference for that temperature is needed. Here, we follow Ludwig’s suggestion²⁷² and consider two reference gas phases. One that consists exclusively of the neutral acid and base parent molecules and a second that consists of the parent molecules and the p-IP in a temperature dependent ratio. These are given in the form of a bQCE⁰(0) and bQCE⁰(1) calculation, respectively, shown in Fig. 5.6. Consistent with Ludwig’s findings, a purely neutral gas phase reference yields an enthalpy of vaporization $\Delta_{\text{vap}}H = 168.7\text{ kJ/mol}$ at 298 K far higher than the experimental value.

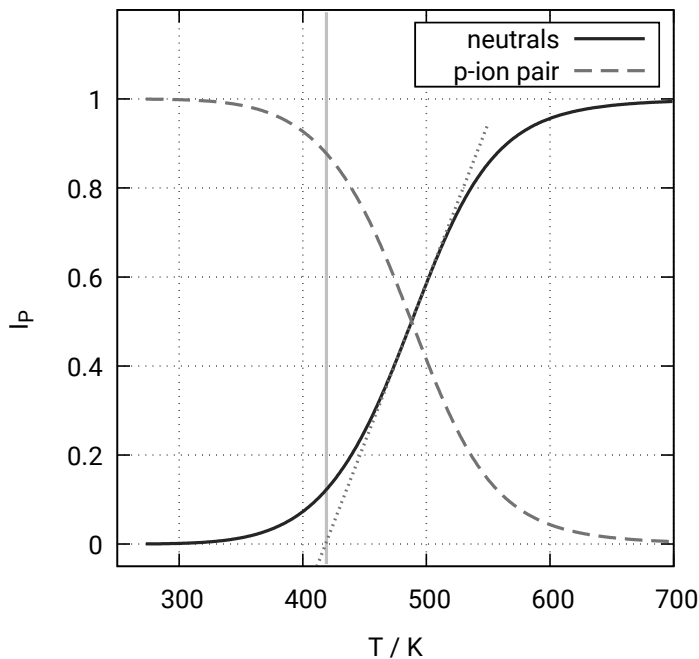


Figure 5.7: Monomer normalized populations I_φ of neutral monomers and the p-IP from bQCE⁰(1). The vertical line marks the temperature of 419 K at which the neutral species are first experimentally observed.²⁷² The dotted line is an extrapolation of the steepest ascent at 488 K.

Using bQCE⁰(1) as reference, we obtain an improved result of 89.3 kJ/mol at 298 K. This underestimates the experimental results at 298 K by 16 kJ/mol but is still sufficient to show that at low temperatures EAN predominantly evaporates into ion pairs. Furthermore, we can calculate $\Delta_{\text{dis}}H$ from this as the difference between the enthalpies of the purely ionic and purely molecular gas phase to be 79.4 kJ/mol, which is in good agreement with the experimental value of 83(2) kJ/mol.¹²³ Note, however, that this experimental value was measured in the liquid phase. In Sec. 5.3.3 of this work, we will employ another method to calculate $\Delta_{\text{dis}}H$ corresponding to the proton transfer within the liquid phase rather than the gas phase.

While at low temperatures the bQCE⁰(1) enthalpy increases nearly linearly, in the temperature range of 400 to 500 K, a drastic increase in the system’s total enthalpy can be observed. At temperatures exceeding the boiling point of EAN, both bQCE(8) and bQCE⁰(1) yield the same results. This behavior can be explained by looking at Fig. 5.7, which shows the equilibrium cluster populations I_φ . It is obvious from this graph that at low temperatures the gas phase consists solely out of p-IPs. With increasing temperature, the neutral molecules’ population rises and at 489 K they dominate the system. Their population further increases until at 700 K the gas phase consists solely of neutral parent molecules. Figure 5.8 shows the Gibbs energies of the neutral parent molecules, the p-IP, and the octamer. The p-IP is enthalpically favored over the neutral molecules and at low temperatures it is more stable in the gas phase. The neutralization of the p-IP

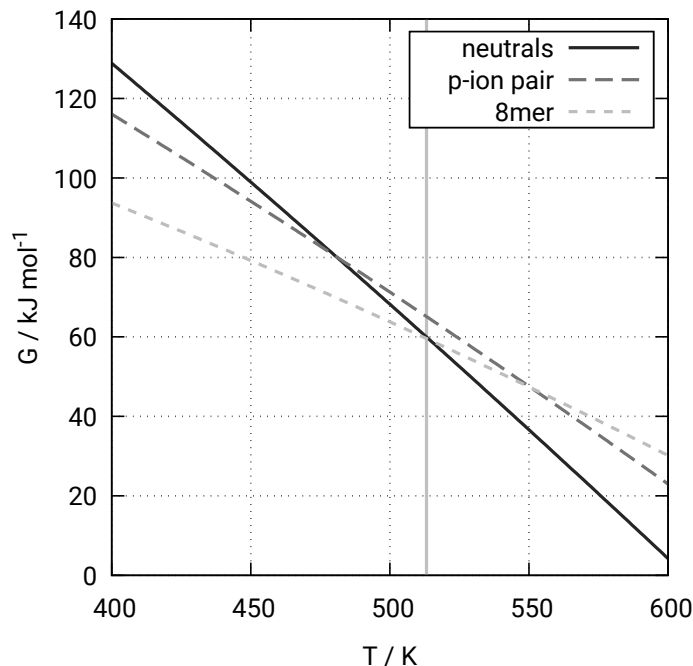


Figure 5.8: Total Gibbs energy G of the neutral monomers, the p-IP, and the octamer. The vertical line denotes the boiling point of EAN $T_b = 513$ K.

is entropically favored and at 489 K the neutral molecules are the more stable gas phase state. These results agree very well with the experimental findings of Ludwig et al., which suggests that the bQCE⁰(1) calculation is fit as gas phase reference.

Applying the same approach to the remaining PILs, the results given in Table 5.3 are obtained. Also shown are the Gibbs energy $\Delta_{\text{vap}}G$ and entropy $\Delta_{\text{vap}}S$ of vaporization. Note that for EOAN the empirical optimization was not successful, thus allowing no reasonable calculation of vaporization quantities. In the sequence EAN–PAN–BAN as well as MAFm–EAFm, $\Delta_{\text{vap}}H$ increases with increasing chain length although the difference between PAN and BAN is marginal. The chain length dependence is consistent with what has been observed for AILs, where $\Delta_{\text{vap}}H$ is influenced both by the electrostatic interac-

Table 5.3: Experimental enthalpy $\Delta_{\text{vap}}H^{\text{exp}}$ of vaporization and bQCE(8) enthalpy $\Delta_{\text{vap}}H$ (kJ/mol), Gibbs energy $\Delta_{\text{vap}}G$ (kJ/mol), and entropy $\Delta_{\text{vap}}S$ (J/(mol K)) of vaporization at 298 K for several PILs as well as their theoretical vapor pressure p (10^5 Pa) calculated by Eq. (5.8).

	$\Delta_{\text{vap}}H^{\text{exp}}$	$\Delta_{\text{vap}}H$	$\Delta_{\text{vap}}G$	$\Delta_{\text{vap}}S$	p
EAN	105.3 ± 1.3	89.31	39.17	168.17	1.37×10^{-7}
PAN	110.6 ± 0.6	93.64	41.98	173.27	4.41×10^{-8}
BAN	117.0 ± 2.0	93.82	41.07	176.92	6.38×10^{-8}
EOAN	151.1 ± 3.0^a	-	-	-	-
MAFm	-	80.66	27.31	178.95	1.64×10^{-5}
EAFm	-	87.76	34.80	177.62	8.00×10^{-7}

^a Calculated from the linear dependence for the experimental alkylammonium nitrates (see Fig. 5.9).

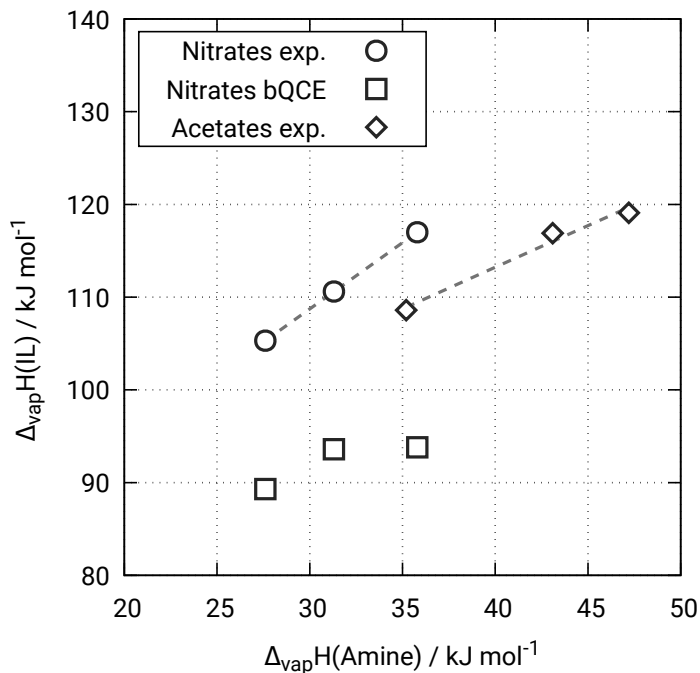


Figure 5.9: Relation between $\Delta_{\text{vap}}H$ of some PILs and their respective parent amines. The shown data points correspond to the nitrates EAN, PAN, and BAN and the acetates [HDMBUA][OAc], [HTMEDA][OAc], and [HDMEtA][OAc] at 298 K. Experimental data for the nitrates was measured by author Verevkin, experimental data for the acetates was measured by Reid et al.³⁰¹ (see Table C.2 in supplementary material).

tions between anions and cations and the dispersive interactions of the alkyl chains.³⁰⁰ Recent experimental investigations have shown that $\Delta_{\text{vap}}H$ is more sensitive to the change of the alkyl chain length than the change of the anion to another one of similar size.^{295,296} Changing the anion from nitrate to formate in EAN and EAFm leads to a change of $\Delta_{\text{vap}}H$ of only 1.5 kJ/mol. By contrast, increasing the alkyl chain length from MAFm to EAFm leads to a rise of $\Delta_{\text{vap}}H$ by 7.1 kJ/mol. Thus, our bQCE results suggest the same general behavior as the experiments.

In 2008, Ludwig proposed calculating vapor pressures of ILs according to

$$\Delta_{\text{vap}}G(T) = -RT \ln \left(\frac{p(T)}{p_0} \right) \quad \text{with } p_0 = 10^5 \text{ Pa}, \quad (5.8)$$

where $p(T)$ is the vapor pressure and p_0 is the standard pressure.²⁸⁸ As $\Delta_{\text{vap}}G$ can be easily obtained by bQCE, theoretical vapor pressures can be calculated and are presented in Table 5.3. As expected for ILs in general, all PILs have vapor pressures far below most standard solvents. The formates have higher vapor pressures, which is especially true for MAFm exceeding that of EAN by two orders of magnitude. While there is no experimental data to evaluate these results, the mass loss of formate PILs (MAFm: 77 %, EAFm: 25 %) observed by Greaves et al. after long-term storage,¹¹² while none was observed for EAN, may serve as qualitative evidence for the plausibility of our results.

Figure 5.9 shows the correlation between $\Delta_{\text{vap}}H$ values of some PILs and their respective parent amines. A nearly perfect linear correlation is observed for the nitrates EAN, PAN, and BAN, for which $\Delta_{\text{vap}}H$ values have been experimentally measured (see Table 5.3). For comparison, a good linear correlation is also observed for the acetates *N,N*-dimethylbutylammonium acetate ([HDMBUA][OAc]), 2-(dimethylamino)-*N,N*-dimethylethylammonium acetate ([HTMEDA][OAc]), and *N,N*-dimethylethanolammonium acetate ([HDMEtA][OAc]), which have been investigated by Minas et al.³⁰¹ While generally too low by about 20 kJ/mol, our bQCE results for $\Delta_{\text{vap}}H$ do not reproduce this linear behavior, as PAN and BAN show nearly identical enthalpies of vaporization. On the other hand, the rise in $\Delta_{\text{vap}}H$ between EAN and PAN is well reproduced. A possible explanation for both the too low $\Delta_{\text{vap}}H$ values and the near identical results for PAN and BAN is a lacking description of the dispersive attractions between the alkyl chains, which add significantly to the cohesive forces of the liquid system.¹¹⁰ As our clusters are optimized in the gas phase, all alkyl chains point outwards to the vacuum (see Fig. 5.3). This missing attraction then leads to an easier volatilization, which is especially true for systems with long alkyl chains.

From the observed linear correlation for the nitrates, we can predict the enthalpy of vaporization of EOAN to be 151.1 kJ/mol, indicating a significant additional contribution of the hydroxyl group to the cohesive forces within the liquid system compared to EAN.

5.3.3 Proton Activity

PILs often show low ionicity which is possibly caused by an incomplete proton transfer resulting in the presence of neutral acid and base molecules in the liquid system.¹¹⁰ The fraction of neutral molecules in the PIL is not available as a potential charge carrier to participate in ionic conduction, which leads to a decrease in ionic conductivity. On the other hand, PILs have been successfully tested as solvents and proton-conductors in fuel cells, which requires a high availability of protons and thermal stability at elevated temperatures.^{302,303} Hence, independent of its specific applications, studying and quantifying a PIL's proton activity seems a worthwhile effort.

Some efforts have been made in the past to quantify the proton activity in a consistent way similar to the pH scale for aqueous solutions. Byrne and Angell et al. proposed the $\delta(\text{N-H})$ proton chemical shift to describe proton activity.¹⁰⁵ However, their approach requires anhydrous conditions and does not allow direct comparison between PILs with different X-H bonds. Another approach, introduced by Kanzaki et al.,¹²² is to describe proton activity by means of the self-dissociation constant K_s or $\text{p}K_s$, which can be deduced from the equilibrium described by Eq. (5.1) in a similar fashion as the ion product of water,

$$K = \frac{[\text{HA}] \cdot [\text{B}]}{[\text{A}^-] \cdot [\text{HB}^+]}$$

$$\begin{aligned}
K_s &= [\text{HA}] \cdot [\text{B}] \quad \text{with} \quad [\text{A}^-][\text{HB}^+] \approx \text{const.} \\
\text{p}K_s &= -\lg([\text{HA}] \cdot [\text{B}])
\end{aligned}
\tag{5.9}$$

K_s corresponds to the reverse proton transfer according to Eq. (5.1). In comparison, $\Delta\text{p}K_a$ corresponds to the same reaction in aqueous systems,

$$\begin{aligned}
\Delta\text{p}K_a &= \text{p}K_s(\text{HB}^+) - \text{p}K_s(\text{HA}) \\
&= -\lg\left(\frac{[\text{H}_3\text{O}^+] \cdot [\text{B}]}{[\text{HB}^+]}\right) + \lg\left(\frac{[\text{H}_3\text{O}^+] \cdot [\text{A}^-]}{[\text{HA}]}\right) \\
&\approx -\lg\left(\frac{[\text{HA}] \cdot [\text{B}]}{[\text{A}^-] \cdot [\text{HB}^+]}\right) \\
&= -\lg([\text{HA}] \cdot [\text{B}]) + \lg([\text{A}^-] \cdot [\text{HB}^+]).
\end{aligned}
\tag{5.10}$$

Obviously, this is only valid in the rare case that $[\text{H}_3\text{O}^+] \approx [\text{H}_3\text{O}^+]$. Nonetheless, by comparing Eqs. (5.9) and (5.10), a connection between $\Delta\text{p}K_a$ and the proton activity seems possible. Several PILs have been investigated by Kanzaki et al. including EAN using ion-selective field effect transistor (ISFET) electrodes, and a good correlation between $\text{p}K_s$ and $\Delta\text{p}K_a$ values could be observed.^{122–125}

Using the bQCE method, $\text{p}K_s$ values can be calculated theoretically. For this purpose, we added clusters to the cluster sets that include a single neutral acid or base molecule surrounded by up to $n = 7$ ion pairs. This was done for EAN and EAFm. For example, in the case of EAN, 14 clusters were added, two for each cluster size n , including a neutral molecule of ethylamine or nitric acid, respectively. From the population of these clusters as obtained in an optimized bQCE calculation and the bQCE phase volume, the concentration of neutral molecules in the liquid system is accessible. Using the current bQCE formalism, K_s can be calculated as

$$K_s = \left[\frac{\sum_{\varphi} n_{\varphi}(\text{HA})N_{\varphi}}{V} \right] \left[\frac{\sum_{\varphi} n_{\varphi}(\text{B})N_{\varphi}}{V} \right],
\tag{5.11}$$

where $n_{\varphi}(X)$ denotes the number of neutral acid or base molecules in the cluster φ , which is 1 or 0 for all clusters investigated in this work. The bQCE method involves the conservation of mass,⁴³ ensuring that the populations of neutral acid and base molecules will be the same in a pure PIL.

The bQCE(8) calculation for EAN predicts the concentration of ethylamine and nitric acid to be $1.64 \times 10^{-6} \text{ mol dm}^{-3}$ at 298 K. This corresponds to a $\text{p}K_s$ value of 11.57, which is very near to EAN's $\Delta\text{p}K_a$ of 12.04 and fits the observed correlation proposed by Angell et al. and other groups. Furthermore, our approach correctly predicts a higher proton activity than $\Delta\text{p}K_a$. The calculated concentration is off by about one order of magnitude compared to the experimentally found concentration of 10^5 mol/l .¹²² Thus, our

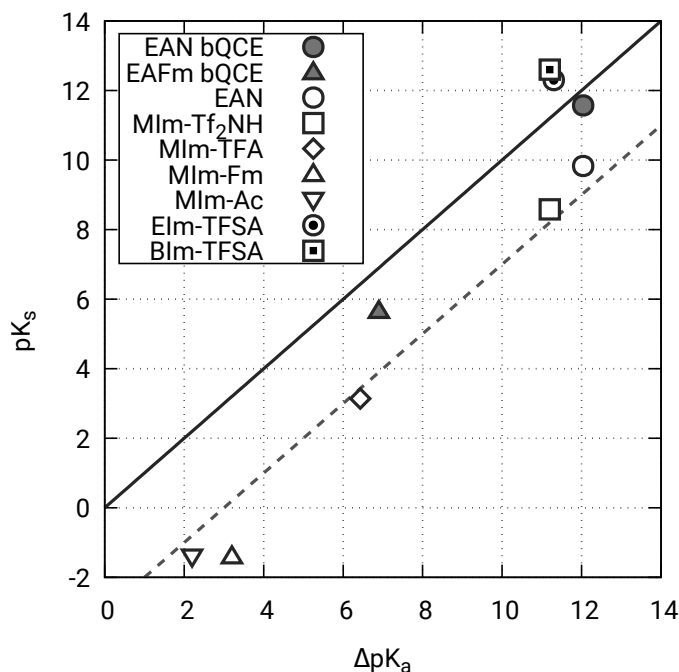


Figure 5.10: Relation between pK_s and ΔpK_a values for some PILs. Filled symbols show the bQCE results of this work, open symbols show experimental results of Kanzaki et al.,^{122,124} and the dotted line shows the linear relation between pK_s and ΔpK_a proposed by them. Half filled symbols show the results of Hashimoto et al.¹²⁰

theoretical pK_s value is off by about 1.74 log units compared to the experimental value of 9.83.

As indicated before, formate-based PILs can be suspected to contain significantly higher concentrations of neutral parent molecules compared to EAN. This is implied by their large deviation from ideal Walden behavior and their low ΔpK_a values. The bQCE(8) calculation for EAFm yields a concentration of ethylamine and formic acid of 1.47×10^{-3} mol/l at 298 K, which is two or three orders of magnitude higher compared to the experimental and theoretical concentration of neutral molecules in EAN, respectively. Thus, the calculated pK_s value of EAFm is 5.66, which is in good correlation with its ΔpK_a value of 6.9, yet predicts a higher proton activity. This result is able to explain several properties of EAFm. Its low ionicity, low boiling temperature, and, compared to other PILs, high volatility may be caused by the high concentration of neutral molecules within the liquid system. The cluster populations further imply that 50% of ethylamine molecules in the liquid phase exist as free monomers not bound to larger cluster structures and thus are more easily vaporized.

To put these results into perspective, Fig. 5.10 shows our theoretical pK_s values next to some experimentally measured proton activities of several PILs plotted against their respective ΔpK_a values. Based on their own results, Kanzaki et al. proposed a simple linear relationship $pK_s = \Delta pK_a - 3$.¹²⁴ Our results lie between this line and the line marking equality, fitting the observed trend that PILs usually have a higher proton activity

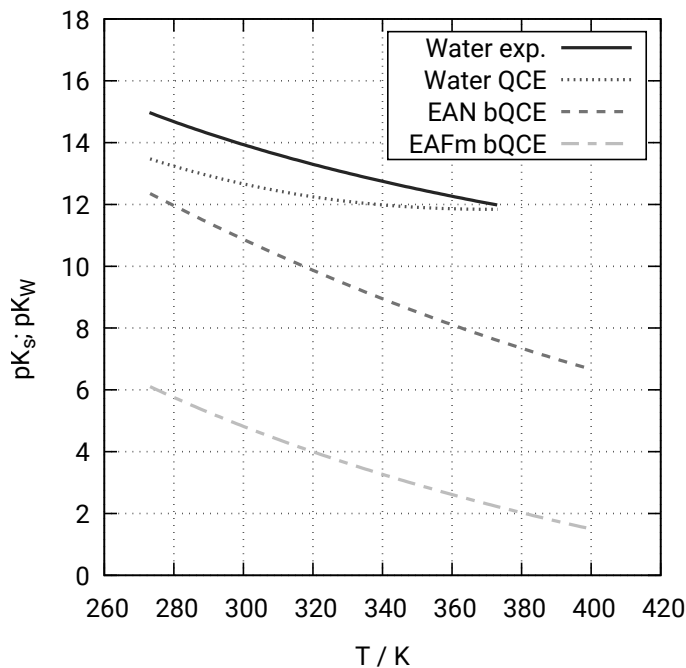


Figure 5.11: Temperature dependence of pK_s obtained from bQCE(8) calculations for EAN and EAFm. For comparison, the experimental temperature dependence of the ionic product of water³⁰⁴ and its theoretical QCE counterpart⁴⁰ are shown.

than predicted by ΔpK_a . However, Hashimoto et al. investigated two ionic liquids with pK_s higher than their respective ΔpK_a values,¹²⁰ proving that the relationship between both constants is more complex and the linear relationship is not strictly valid.

The discussed results were obtained for a temperature of 298 K at atmospheric pressure. However, the bQCE method is able to predict pK_s values over a wide range of temperatures as is shown in Fig. 5.11. For comparison, the experimental temperature dependence of the ionic product of water³⁰⁴ and its theoretical QCE counterpart are shown.⁴⁰ The pK_s values decrease with temperature, indicating a rising concentration of neutral molecules within the liquid. The temperature dependence for both PILs is of a similar form as that of the ionic product of water pK_w with a negative but decreasing slope, indicating that with rising temperature the relative growth of the concentration of neutral molecules decreases. Of the two PILs, EAN shows the stronger temperature dependence.

To investigate the thermodynamic plausibility of these results, van't Hoff plots of both PILs are shown in Fig. 5.12. Note that we used the equilibrium constant $K = [HA][B]/[A^-][HB^+]$ instead of K_s . The plot yields nearly perfectly straight lines for both PILs. From the slope and intercept, we can estimate the enthalpy and entropy of the dissociation reaction in EAN to 94.00 kJ/mol and 0.13 kJ/(mol K), respectively. Both slightly overestimate their respective experimental values of 83(2) kJ/mol and 0.09(1) kJ/(mol K),¹²³ but they present good estimates. We calculate the Gibbs energy of the reaction to 54.02 kJ/mol which is in very good agreement with the experimental value of 54.9(3) kJ/mol, due to an error cancellation. For the dissociation reaction of

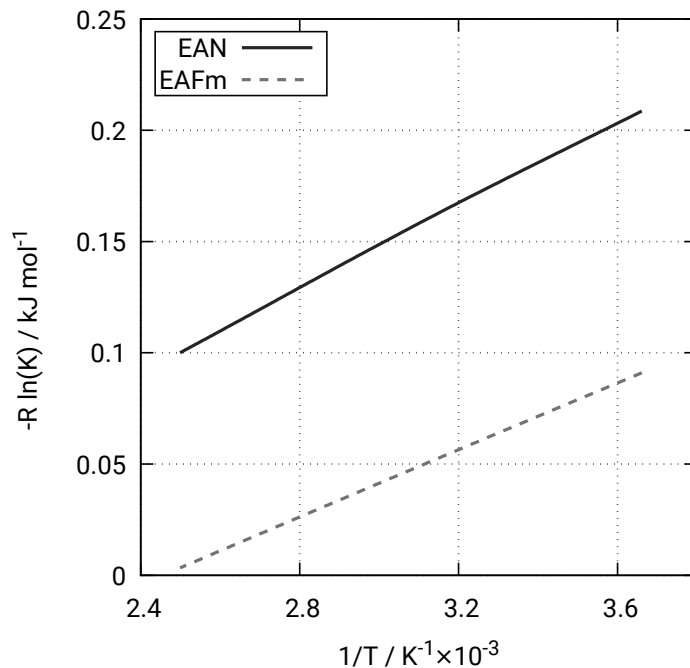


Figure 5.12: van't Hoff plots of EAN and EAFm as obtained from bQCE(8) calculations, with $K = [\text{HA}][\text{B}]/[\text{A}^-][\text{HB}^+]$.

EAFm, the enthalpy, entropy, and Gibbs energy are 75.51 kJ/mol, 0.19 kJ/(mol K), and 20.29 kJ/mol, respectively. The reaction enthalpy is considerably lower for EAFm. Since both PILs have the same cation, we conclude that this difference is due to the lower acidity of formic acid compared to nitric acid.

5.4 Conclusion

From the preceding presentation and discussion of results, it became clear that the thermodynamic characterization of PILs is a conceptually and practically difficult task, not only for theory but for experiment, as well. The vaporization mechanism and the nature of the gas phase have a direct impact on thermodynamic properties and their interpretation may thus be challenging.

Here, we presented a method to predict thermodynamic properties and proton activities from a theory that is computationally efficient and systematic. We were able to calculate boiling points with deviations from experiment ranging from 50 K to only 1 K, by employing parameter-free bQCE theory. While these deviations are partially large, care must be taken, when comparing to experimental references, which may be subject to considerable errors originating from impurities or ambiguities arising due to decomposition.^{290–292}

We could reach a similar accuracy for vaporization enthalpies, after carefully considering the composition of the gas phase and transformations taking place during the vaporization process. Unfortunately, reference data for these properties is rare and limited to fixed

temperatures. The QCE method, however, provides any desired thermodynamic potential over a wide range of phase states. We extended the available experimental data on enthalpies of vaporization of PILs by PAN and BAN and found an excellent correlation with their respective parent amines, making possible reasonable predictions for not yet investigated PILs like EOAN.

The true strength of QCE, however, lies in the possibility to include dissociation reactions into the cluster formation process, as demonstrated in a previous study on the ionic product of water.⁴⁰ We demonstrated that simple counting of cluster populations gives access to proton activities by means of self-dissociation constants K_s and related properties, which fit remarkably well with experimentally verified results.

In principle, QCE is open to any quantum chemical level of theory, but in combination with low-cost composite DFT methods, such as PBEh-3c, it provides a computationally very efficient way to obtain the aforementioned properties. On the DFT level, we cannot report significantly improved results by changing to more expensive functionals or basis sets. The largest room for improvement in future studies is expected by inclusion of further cluster motifs (that are not global minima), which are known to have a major impact on QCE results.^{39,52} In this study, we deviated from our common praxis to search for such motifs and presented a procedure for generating a cluster set in a systematic fashion, instead. By combination of such a systematic cluster set generation scheme with the low-cost methods discussed above, we were able to show that QCE theory has predictive power for ionic liquids that may even be rendered into an affordable black box procedure.

Supplementary Material

See supplementary material for a detailed description of the transpiration method and our experimental results. Furthermore, details about the empirical parameter optimization and a comparison of bQCE results for several underlying electronic structure methods can be found therein. Finally, it includes a complete collection of all employed cluster geometries optimized at the PBEh-3c level of theory and their electronic energies.

Acknowledgments

The authors are grateful to the Deutsche Forschungsgemeinschaft (DFG) for funding under Project No. SPP KI768/15-1. Sergey P. Verevkin is grateful to the DFG for funding under Project No. SPP 1807(1) VE265/9-1.

6 How to Harvest Grotthuss Diffusion in Protic Ionic Liquid Electrolyte Systems

Johannes Ingenmey,* Sascha Gehrke,* and Barbara Kirchner*

Received: March 3, 2018, Published: June 21, 2018

Reprinted (adapted) with permission from

J. Ingenmey, S. Gehrke, and B. Kirchner, *ChemSusChem*, 2018, **11**, 1900–1910.

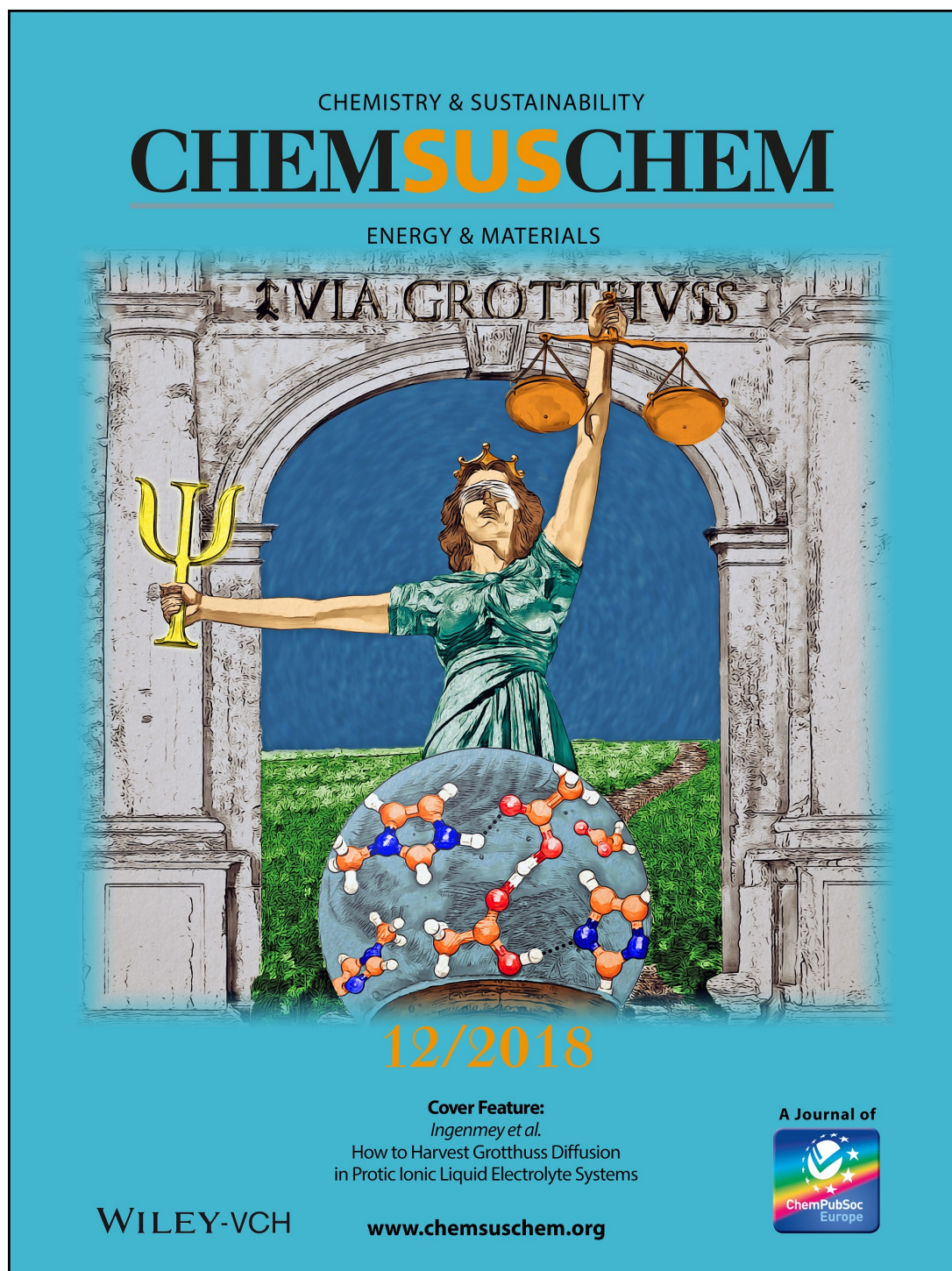
Copyright © 2018 Wiley-VCH.

DOI: 10.1063/1.4980032

Contributions to the manuscript

- Running classical MD simulations to pre-equilibrate the AIMD simulations
- Analyzing the AIMD trajectories
- Providing the AIMD-related figures
- Discussing the results
- Co-writing the manuscript

*Mulliken Center for Theoretical Chemistry, Institut für Physikalische und Theoretische Chemie, Rheinische Friedrich-Wilhelms-Universität Bonn, Berlingstraße 4+6, 53115 Bonn, Germany



The Cover Feature shows the goddess Justitia guarding a path, labeled Via Grotthuss. The Grotthuss mechanism provides a fast path for ionic conduction and is desired in protic ionic liquids, for example, when considering their usage as electrolytes in fuel cells. Ab initio molecular dynamics simulations of a 50:50 mixture of *N*-methylimidazole and acetic acid provide an explanation for the unexpectedly high ionic conductivity of this system, in that Grotthuss-like proton conduction can be directly observed, as depicted in the sphere. Using static quantum chemical calculations, symbolized by Justitia's attributes Ψ and scales, possible candidates of acid–base combinations can be identified that use this easy path of proton conduction. Reprinted with permission from J. Ingenmey, S. Gehrke, and B. Kirchner, *ChemSusChem*, 2018, **11**, 1888.

Abstract Hydrogen is often regarded as fuel of the future, and there is an increasing demand for the development of anhydrous proton-conducting electrolytes to enable fuel-cell operation at elevated temperatures exceeding 120 °C. Much attention has been directed at protic ionic liquids as promising candidates, but in the search for highly conductive systems the possibility of designing Grotthuss diffusion-enabled protic ionic liquids has been widely overlooked. Herein, the mechanics of proton transfer mechanism in the equimolar mixture of *N*-methylimidazole and acetic acid was explored using ab initio molecular dynamics simulations. The ionicity of the system is approximated with good agreement to experiments. This system consists mostly of neutral species but exhibits a high ionic conductivity through Grotthuss-like proton conduction. Chains of acetic acid molecules and other species participating in the proton transfer mechanisms resembling Grotthuss diffusion could be directly observed. Furthermore, based on these findings, a series of static quantum chemical calculations was conducted to investigate the effect of substituting the anion and cation with different functional groups. We predict whether a given combination of cation and anion will be a true ionic liquid or a molecular mixture and propose some systems as candidates for Grotthuss diffusion-enabled protic ionic liquids.

6.1 Introduction

In light of global warming, increasing energy demands, and the impending exhaustion of fossil fuels, the research on sustainable processes and technologies continues with constantly growing interest. In this context, hydrogen is considered a convenient energy-storage medium and extensive investigations are performed to increase efficiency of hydrogen use in clean and zero emission technologies such as fuel cells, in particular polymer electrolyte membrane fuel cells (PEMFC).

Promising candidates for the use as electrolyte are ionic liquids (ILs), which are salts that are liquid at moderate temperatures.⁸⁹ Owing to their unique properties such as low volatility, high ionic conductivity, and vast liquid range, they receive considerable attention in current research. Even though most ILs are in fact toxic, they are considered environmentally friendly, due to their generally low vapor pressure and hence, compared to commonly used molecular solvents, negligible volatility.⁸⁹ Furthermore, introduction or modification of their functional groups as well as varying the carbon-chain lengths opens up the possibility of tuning their physicochemical properties for specific applications. Functionalized ILs were first introduced by Davis and Forrester,³⁰⁵ who later established the concept of task-specific ionic liquids,³⁰⁶ which are ILs with functional groups added for special applicability. A subgroup of this vast class of substances consists of those ILs

that are formed by a proton transfer between a Brønsted acid (AH) and a Brønsted base (B), termed protic ILs (PILs):



In contrast to most aprotic ILs (AIL), PILs have a mobile proton bound to the cation. Although PILs have been less investigated than AILs due to proton activity deteriorating exactly those properties that make ILs an interesting alternative to molecular systems, it is exactly the proton reactivity that is a requirement for their application in fuel cells. In a PEMFC, molecular hydrogen is oxidized at the anode to form protons and release electrons. At the same time, on the cathode molecular oxygen is reduced to form water with available protons. Hence, a proton-conducting electrolyte is needed. The advantage of using PILs in fuel cells is that they work in non-aqueous conditions. Other than currently used PEMFCs that mostly utilize Nafion as polymer electrolyte membrane, PIL-based fuel cells do not require constant hydration and can thus potentially be operated at high temperatures $>120^\circ\text{C}$. Watanabe and co-workers investigated several PILs with regard to their potential application in fuel cells.³⁰² Diethylmethylammonium triflate ($[\text{N}_{\text{H}122}][\text{OTf}]$) was found to be the most promising candidate, featuring a considerable ionic conductivity of 43 mS/cm at 120°C and a vast liquid range with a melting point of -13.1°C and a decomposition temperature of 360°C .

Although the usage of PILs in fuel cells has been investigated in several studies in the past two decades, little effort has been made to quantify proton activities in these systems. The $\Delta\text{p}K_{\text{a}} = \text{p}K_{\text{a}}(\text{HB}^+) - \text{p}K_{\text{a}}(\text{HA})$ value is commonly used as approximative measure of the proton activity.¹¹⁰ Angell and co-workers suggested a correlation between several proton-activity-dependent properties of a PIL and its $\Delta\text{p}K_{\text{a}}$ value.¹¹⁶ They found that PILs with $\Delta\text{p}K_{\text{a}} > 8$ exhibit near-ideal Walden behavior. The Walden plot shows the relation between the molar ionic conductivity of a PIL and its viscosity, using an aqueous 0.1 M KCl solution as ideal reference. Watanabe and co-workers³⁰⁷ reported a correlation between the open-circuit potential (OCP) of a PIL in hydrogen fuel cells and its $\Delta\text{p}K_{\text{a}}$ value. The OCP increased with increasing $\Delta\text{p}K_{\text{a}}$ to a maximum at $\Delta\text{p}K_{\text{a}} \approx 17$ after which the OCP decreases. In PILs with low $\Delta\text{p}K_{\text{a}}$, the proton transfer is potentially incomplete and the presence of neutral acid and base molecules in the system decrease the OCP, for example by oxidation of the neutral species. For high $\Delta\text{p}K_{\text{a}}$ PILs the bonding between proton and base might be too strong, so that the availability of the proton for conduction is decreased. Hence, investigation of proton activities in PILs and the mechanism of proton conduction within these systems is an obvious task when considering the application of PILs in fuel cells.

Using ion-selective field-effect transistor (IS-FET) electrodes, the proton activities of several PILs have been quantified by Umebayashi and co-workers in terms of the

$\text{p}K_s = -\lg([\text{HA}] \cdot [\text{B}])$ value, where $[\text{HA}]$ and $[\text{B}]$ label the concentrations of neutral acid and base molecules in the PIL.^{122–125} K_s corresponds to the reverse proton transfer according to Eq. (6.1). Surprisingly, Umebayashi and co-workers found the equimolar mixture of *N*-methylimidazole (C_1Im) and acetic acid (HOAc), which has a rather low $\Delta\text{p}K_a$ of 2.4,¹⁹⁷ to consist primarily of neutral acid and base molecules with $\text{p}K_s \approx -1.4$.^{115,124} Hence, it cannot be considered a true PIL and was labeled a “pseudo ionic liquid”.¹¹⁵ Despite of this majority of neutral molecules, this system features a considerable ionic conductivity of 4 mS/cm, which cannot be understood by considering only the ratio of neutral-to-ionic species. According to Angell’s classification scheme, which is based on the Walden behavior of a PIL, this liquid would be labeled a good or even superionic liquid (for details, see Ref. 115). Thus, a Grotthuss-like proton conduction mechanism was proposed to take place within the system wherein a facile proton hopping can occur often between the ionic and neutral species without a high energy barrier.^{115,124}

Grotthuss diffusion in PILs is desirable as it is much faster than the alternative vehicle mechanism. The Grotthuss diffusion mechanism was investigated for molecular liquids, especially water, to a large extent.²⁷⁴ Simplified, the Grotthuss mechanism can be described as rearrangement of hydrogen bonds that involves the forming of the Zundel (or Eigen) cation $\text{H}_3\text{O}^+ + \text{H}_2\text{O} \rightleftharpoons \text{H}_5\text{O}_2^+ \rightleftharpoons \text{H}_2\text{O} + \text{H}_3\text{O}^+$.²⁷⁴ Through this mechanism, the proton does not need to travel broad lengths through the liquid system, but rather the charge is transported through the extended three-dimensional hydrogen bond network by bond shifting. Consequently, the proton seemingly has a considerably higher diffusion rate compared to other cations in aqueous systems. An extended three-dimensional hydrogen bond network was proven to exist at the nanostructure of ethylammonium nitrate,³⁰⁸ and similar networks should exist in other PILs as well.³⁰⁹ However, even though the possible importance of the Grotthuss mechanism for future applications of ILs is now accepted,³¹⁰ only a few investigations regarding Grotthuss-like conduction processes in ILs have been made so far. One of the first ab initio molecular dynamics (AIMD) studies of a Grotthuss-like mechanism in ionic liquid-like systems was carried out in 2007 where it was shown that in 1-ethyl-3-methylimidazolium chloroaluminate-based PILs $[\text{C}_2\text{C}_1\text{Im}][\text{AlCl}_4] \cdot 32\text{AlCl}_3$ ($[\text{C}_2\text{C}_1\text{Im}]$ =1-ethyl-3-methylimidazolium) constantly rearranges to large anions by structural diffusion.^{86,311,312} Further studies of other groups show rapid iodide anion conduction in ILs containing the I^-/I_3^- redox couple,^{313–315} as well as Grotthuss-like carbon dioxide transport in molten calcium carbonate.^{27,95} The structural diffusion of AlCl_3 units in material synthesis carried out in $[\text{C}_2\text{C}_1\text{Im}][\text{Cl}] \cdot 1.3\text{AlCl}_3$ was shown to play a key role.³¹⁶ A Grotthuss-type hopping mechanism of Br^- anions was proposed to take place in the 1-hexyl-3-methylimidazolium nonabromide ($[\text{C}_6\text{C}_1\text{Im}][\text{Br}_9]$) system investigated by Riedel and co-workers.³¹⁷ Finally, proton hopping in PILs was observed.^{114,115} These studies showed that Grotthuss-like transport is a more general mechanism than was thought in the past.¹¹⁴ However, evidence is scarce and our un-

Understanding of the dynamics of proton conduction in PILs is limited. Hence, we need theoretical and experimental investigations on these mechanisms to design superprotonic systems. Related to this is also the proton activity of acids in deep eutectic solvents or ionic liquids, which have been recently investigated and quantified in terms of pK_a values, but have not been studied on a molecular level yet.^{119,318}

Herein, we present AIMD studies on the equimolar C₁Im-HOAc mixture to provide evidence of Grotthuss diffusion from first principles calculations. AIMD is especially suited as it calculates the forces from electronic structure methods on the fly and was used by our group in several published studies investigating ILs.^{86,292,311,312,316,319} This allows the observation of spontaneous events provided that their energy barrier is low enough to be overcome by thermal fluctuations. We investigate possible pathways of proton hopping and discuss the relevant structural aspects of this mechanism. We consider the C₁Im-HOAc mixture as model system as it allows observation of proton-hopping events even with small system sizes. Static quantum chemical calculations were carried out to investigate the effect of substituted species, thus providing some possible guidance for designing superprotonic PILs.

6.2 Results and Discussion

To understand different possible proton transfer mechanisms, we modeled the C₁Im-HOAc mixture from AIMD simulations. AIMD simulations are especially suited if spontaneous events such as Grotthuss or structural diffusion occur and the according barrier is low enough to be overcome by thermal fluctuations.^{311,316} Observing such events is impossible using standard classical simulations where the force fields are created prior to the simulation and all events must be known beforehand. In literature, differing values for the density of the C₁Im-HOAc mixture can be found. Hou et al. measured a density of 1.1551 g/cm³,³²⁰ Qian et al. got 1.0753 g/cm³,³²¹ and Umebayashi and co-workers obtained 1.0725 g/cm³.¹¹⁵ Thus, we set up two sets of simulations employing different densities, which we abbreviate set **A** for simulations with a density of 1.1551 g/cm³ and set **B** for simulations with 1.0753 g/cm³. For both densities we started three simulations with different start configurations, one consisting only of the ions (abbreviated **ion**), one consisting only of the neutrals, that is, *N*-methylimidazole and acetic acid (termed **neu**), and one with a molar 50:50 ratio of neutral and ionic species (termed **mix**). Note, that we excluded the first 10 ps of the simulation as the system undergoes an equilibration phase during the first ps, resulting in a total simulation time of 80 ps. As will be shown in the following sections, the proton originally either bonds to the oxygen atom of the acetate or to the nitrogen atom of the imidazole, but is mobile and can exist in an unbonded state, or covalently bonded to either the imidazole resulting in the imidazolium cation or to the acetate anion resulting in the acetic acid molecule, see also Eq. (6.1). Hence, we

label this particular hydrogen atom H^* in the following sections. Further computational details regarding the simulation as well as our post-processing methods can be found in the Supporting Information.

6.2.1 Ionicities From *ab initio* Molecular Dynamics

The ionicity in PILs is an important aspect of these systems and was frequently discussed.^{116,130,285,286} It can be understood as the effective portion of charge carriers available for ionic conduction with respect to the total number of species in the system.¹¹⁶ The ionicity in PILs is often found to be below the ideal level,¹¹⁰ which can be attributed to aggregation of ions to neutral complexes, reformation of neutral acid and base molecules as indicated by Eq. (6.1),³²² or other effects such as polarisation or charge transfer between the unlike ions,^{131,137,284} lowering the availability of mobile charge carriers. Umabayashi and co-workers measured pK_s values using potentiometry for several PILs as a measure of their proton activities.^{122–125} Different to other PILs such as ethylammonium nitrate (EAN), no jump in the potentiometric titration curve could be observed for the C_1 Im-HOAc mixture. They estimated a negative pK_s of -1.4 based on calorimetric titration. According to Umabayashi’s density measurements, this corresponds to a content of neutral species of 66.4%. Slightly different values of 68.6% or 62.7% are calculated employing the density measurements of Qian et al.³²¹ and Hou et al.,³²⁰ respectively. However, in their following study, Umabayashi and co-workers estimated the content of neutral species to be at least 99.0%, with the aid of Raman spectra.¹¹⁵ A very different result was recently published by Chen et al., who determined the content of neutral species to be 7.2% based of nuclear magnetic resonance (NMR) spectroscopy.²⁷³ All different values agree that ionicity in the C_1 Im-HOAc mixture is low and that it can not be classified as a true

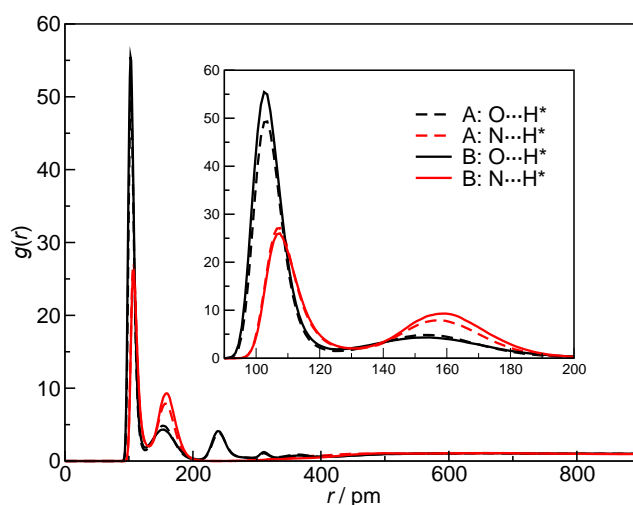


Figure 6.1: RDFs of the $O \cdots H^*$ and $N \cdots H^*$ hydrogen bonds for set **A** and set **B** respectively. Inset: magnification of the first two peaks.

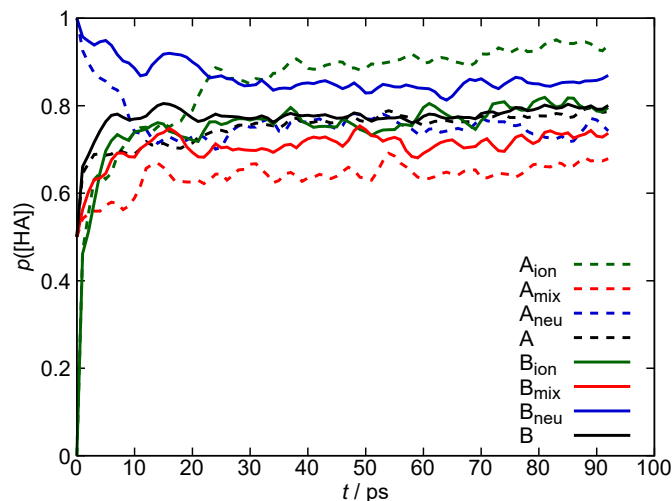


Figure 6.2: Content of neutral acetic acid molecules in the system over simulation time.

PIL. In this section we will add theoretical estimations of the neutral species content and thus, ionicity of the system. Recently, we published—to the best of our knowledge—the first theoretical estimation of proton activities in PILs by ab initio quantum chemical calculations.² Here, we will demonstrate that AIMD simulations are in principle able to reproduce experimental ionicity measurements.

To arrive at this ionicity estimate, we consider first the $O \cdots H^*$ and the $N \cdots H^*$ radial pair distribution function $g(r)$ (RDF) (Fig. 6.1). If at a certain distance r a peak with $g(r) > 1$ is observed, it is highly likely to find atom pairs with this distance. RDFs are normalized by the density. Integrating it and subsequent multiplication by $4\pi r^2 \rho$ (ρ : average density in the simulation) allows the estimation of coordination numbers also termed number integrals. From these coordination numbers we can estimate the ionicity. The RDFs show typical patterns observed for hydrogen-bonded systems. Both set **A** and set **B** show mostly similar results. The first high peak marks the intramolecular H–O/N bond. More details can be obtained from the inset of Fig. 6.1. With the peak maximum situated at 103 pm the O–H bond is on average shorter than the N–H bond with 107 pm, indicating a stronger intramolecular bond. The second peak represents the non-covalent hydrogen bond. For the $O \cdots H^*$ RDF several interactions possibly contribute to this peak, namely the hydrogen bond between anion–cation, anion–acid, acid–cation, and acid–acid. For the $N \cdots H^*$ RDF it is likely that mainly the base–acid hydrogen bond contributes to the second peak but possibly also base–cation interactions. Again, the $O \cdots H^*$ hydrogen bond with an average length of 152 pm is shorter compared to the $N \cdots H^*$ bond with an average length of 158 pm. As the acetate has two hydrogen bond acceptor sites, a third peak is visible in the $O \cdots H^*$ RDF located at 242 pm. This peak can be attributed to the interaction between the carboxyl group and the hydrogen atom of the acid. The RDFs decay at larger distances properly to 1. The individual RDFs for each simulation are shown in the Supporting Information.

By treating the first minimum in the RDFs as maximum bond length for the covalent O–H and N–H bond, respectively, we can determine the approximate coordination number, that is, the relative number of non-dissociated acid or protonated base molecules through the above-described number integral. The O \cdots H* RDFs are integrated up to a distance of 127 pm, which is the average location of the first minimum. Likewise the N \cdots H* RDFs are integrated up to a distance of 133 pm. If we take the O coordination-to-N coordination ratio, we can estimate the ratio of neutral to ionic species. In Fig. 6.2 we show the development of the content of neutral species in the system with simulation time. We analyzed 180 000 steps (90 ps) starting from the equilibrium search and at each time point average over the last 5000 steps (2.5 ps). Clearly, we see that before the 10 ps mark the system is still under large rearrangement. Both ion simulations undergo a rapid reverse proton transfer in the first few ps. On the other hand, in the neu simulations protons quickly transfer from the acid to the base molecules. We can observe that independent from the initial configuration all systems move to a state in which 60 to 90 % of the acid molecules are undissociated. Clearly, the equilibrium concentration of neutral species in the system lies in this range, which is in good agreement with the experimental range of 62 to 68 % based on the pK_s values of the mixtures. Looking at the average of each set, we see a stable content in the 75 to 80 % range.

6.2.2 Insight into the Proton Transfer Mechanisms

To understand the dynamic behavior of the proton transfer, we first consider dynamic properties of the systems. It is apparent from the earlier section that proton transfer does occur in our simulations regardless of the initial configuration of molecules and that the equilibrium state is a mixture of neutral and ionic species. In this section we will explore

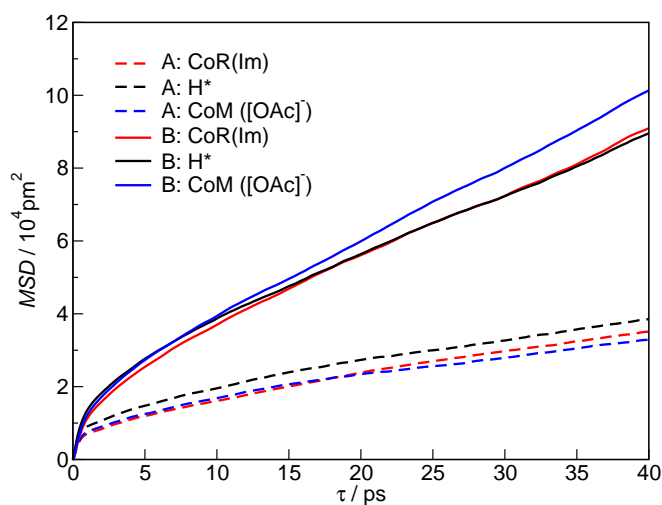


Figure 6.3: MSD for the center of ring (CoR) of the imidazole, the “active” proton (H*), and the center of mass of the acetate. The three simulations **ion**, **mix** and **neu** are averaged for each set **A** and set **B**.

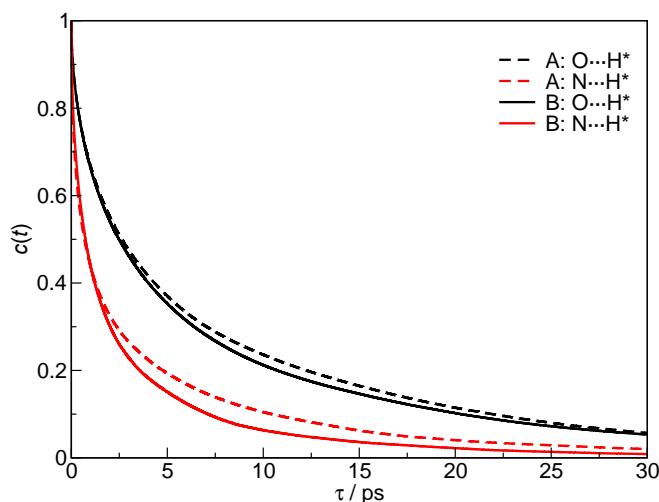


Figure 6.4: Continuous autocorrelation function $c(t)$ for the $\text{N}\cdots\text{H}^*$ and $\text{O}\cdots\text{H}^*$ association. The three simulations **ion**, **mix** and **neu** are averaged for each set **A** and set **B**.

the dynamics and structural aspects of the proton transfer and showcase several instances of this process, including Grotthuss-like chain reactions.

The most simple process for proton conduction is the vehicle mechanism, in which the proton is carried by a molecule or cation acting as “vehicle”. The proton conductivity is then limited by the diffusion rate of the carrier species. The Grotthuss mechanism circumvents this by bond shifting through an extended hydrogen bond network. Other fast movements of small particles are possible through the movement of holes in liquids, but these are reflected in a faster diffusion behavior of the small particle (see Fig. 1 in Ref. 323). From AIMD simulations we can gather information on the diffusion behavior of the different species in the system, that is, in our case, the imidazole, the anion, and the proton. This is done in terms of the mean square displacement (MSD) which is given in Fig. 6.3.

The behavior compares well to previous AIMD simulations of $[\text{C}_2\text{C}_1\text{Im}][\text{SCN}]$.³²⁴ Consistent with the lower density, the species in set **B** diffuse faster (compare dashed versus solid lines in Fig. 6.3). As there is no marked difference between the diffusion of the proton and the molecules or ions, we can exclude a process in which the proton diffuses on its own through tunnels in the liquid structure. However, because the vehicle mechanism cannot explain the experimentally observed conductivity, it can be expected that the proton conduction is really based on a Grotthuss-like or structural diffusion mechanism, which is also visible when visualizing the trajectories.

Another way of investigating the proton mobility is by measuring the time lengths, for which a proton resides at one acceptor site. Next to the MSD, functions illustrating the decay of associates might be helpful to understand the particular mechanism. Figure 6.4 shows the continuous autocorrelation function $c(t)$ of the $\text{N}\cdots\text{H}^*$ and $\text{O}\cdots\text{H}^*$ association, it thus gives an estimate of how the proton–imidazole ($\text{N}\cdots\text{H}^*$) and the proton–acetate

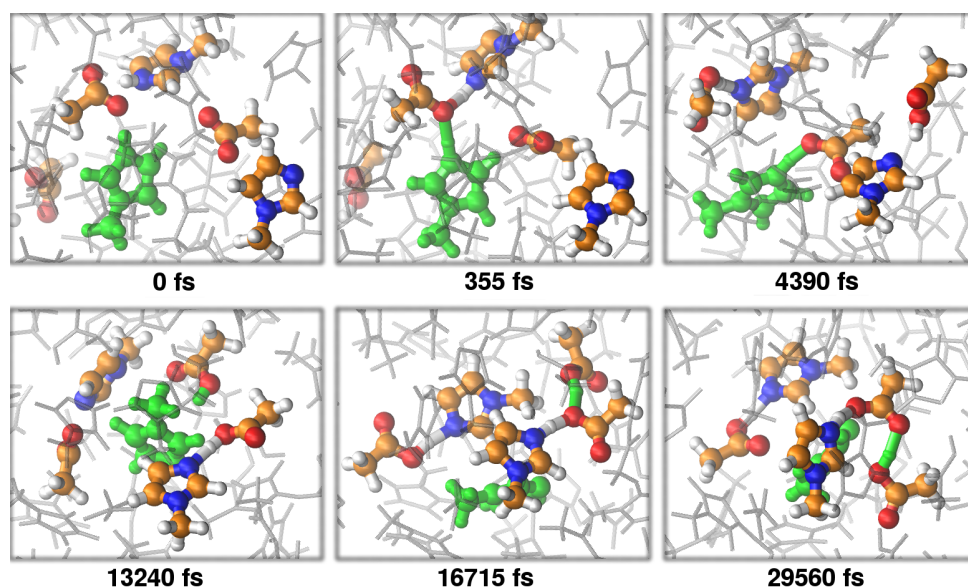


Figure 6.5: Snapshots at different simulation times in femtoseconds given below each panel along the trajectory of simulation \mathbf{B}_{ion} showing several proton transfers. The central imidazolium cation is marked in green and some of the neighboring partners are marked in the following color code: carbon—orange, nitrogen—blue, oxygen—red, and hydrogen—white. The remainder of the molecules or ions are portrayed in gray.

($\text{O} \cdots \text{H}^*$) association decay. The association is considered as being populated if the proton is closer to the atom than the distance given by the first minimum of the corresponding RDF (127 pm and 133 pm for $\text{O} \cdots \text{H}^*$ and $\text{N} \cdots \text{H}^*$, respectively). No distinctive differences can be observed between both sets. It is apparent that, independent of the density of the system, interactions between the proton and nitrogen atom are shorter lived than those between the proton and oxygen atom, which indicates the dominance of neutral species. It is in principle conceivable to deduce ionicities from ion life times. Calculating pseudo-life times, for set **A** we obtain 17.9 ps and 7.2 ps for the $\text{O}-\text{H}^*$ and $\text{N}-\text{H}^*$ bonds, respectively. This yields a content of neutral species of 83.3% if both oxygen atoms of the acetate anion are considered individually or 71.3% if we consider only one possible $\text{O}-\text{H}$ bond per acetate anion, both values agreeing well with the content derived from RDFs. However, as will be discussed in the following sections, there is a wide variety of bonding situations for the active proton. For example, a proton that is rapidly transferred between two acetate anions will decrease the $\text{O}-\text{H}^*$ life times, but does not influence the content of neutral species. Thus, the RDF approach is a more stable method to determine the ionicity of a system.

One of the great advantages of AIMD simulations is that electronic structures and forces are calculated on the fly. Thus, we can directly observe chemical reactions such as proton transfer and visualize the processes at hand. Figures 6.5–6.7 show several mechanisms of the proton transfer exemplary for all trajectories.

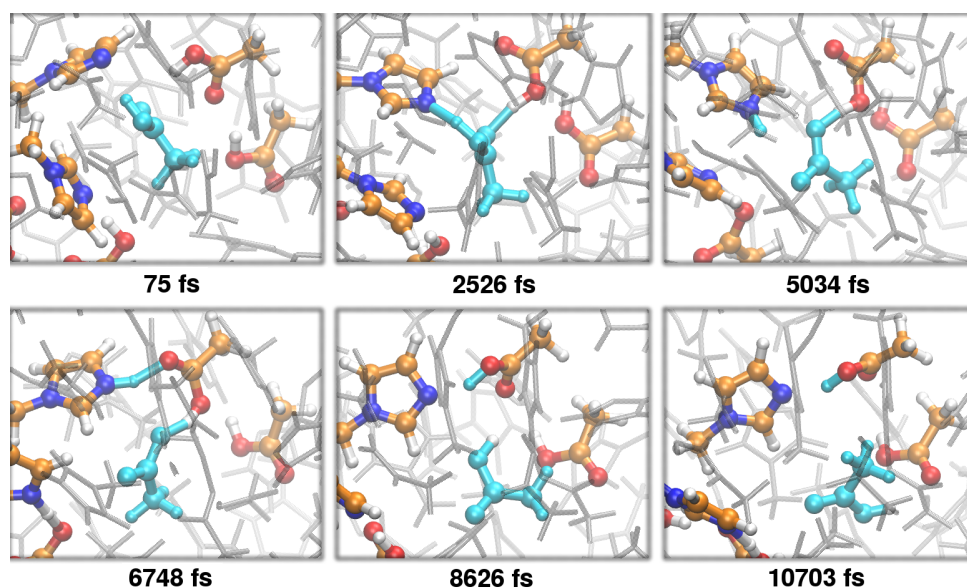


Figure 6.6: Snapshots at different simulation times in femtoseconds given below each panel along the trajectory of simulation \mathbf{A}_{neu} showing several proton transfers. The central acetic acid is marked in cyan and some of the neighboring partners are marked in the following color code: carbon—orange, nitrogen—blue, oxygen—red, and hydrogen—white. The remainder of the molecules or ions are portrayed in gray.

In Fig. 6.5 snapshots taken from the \mathbf{B}_{ion} trajectory are shown. The central green molecule is the imidazolium cation. The proton is shared for some amount of time before it is transferred to the corresponding acceptor atom. This is not exclusively a two-body process but a complicated interplay of many cooperative effects (e.g., at 355 fs or 16 715 fs). At 29 560 fs it is apparent that, although the green proton originally from the central imidazolium cation is transferred from one acetate molecule to another, the donating acetate molecule almost simultaneously accepts another proton.

In Fig. 6.6, which shows snapshots taken from \mathbf{A}_{neu} , we see the proton transfer starting from the acetic acid molecule marked in cyan. The proton is transferred in cooperative processes (2526 fs and 6748 fs), involving several molecules. Even though the RDF (Fig. 6.1) and the life time (Fig. 6.4) indicate that the acetic acid molecule is slightly more preferred by the proton, Fig. 6.6 shows that not only the reverse proton transfers from the imidazolium cation to the acetate anion is possible but also that the acetic acid molecule donates its proton to the imidazole molecule. This is especially visible but not restricted to the equilibration phase, in which too many acetic acid molecules are existing in the system and the 60 to 90 % content of neutral species, as discussed in the section on ionicity, is still to be reached. In the time range 5034 to 8626 fs, we can observe an acetic acid molecule accepting a proton from a cation and simultaneously donating its proton to an acetate anion, which then reorientates and interacts with another acid molecule.

In Fig. 6.7, which shows snapshots of the \mathbf{B}_{mix} simulation, we see an imidazolium cation portrayed in yellow interacting with an acetate anion, but no reverse proton transfer takes

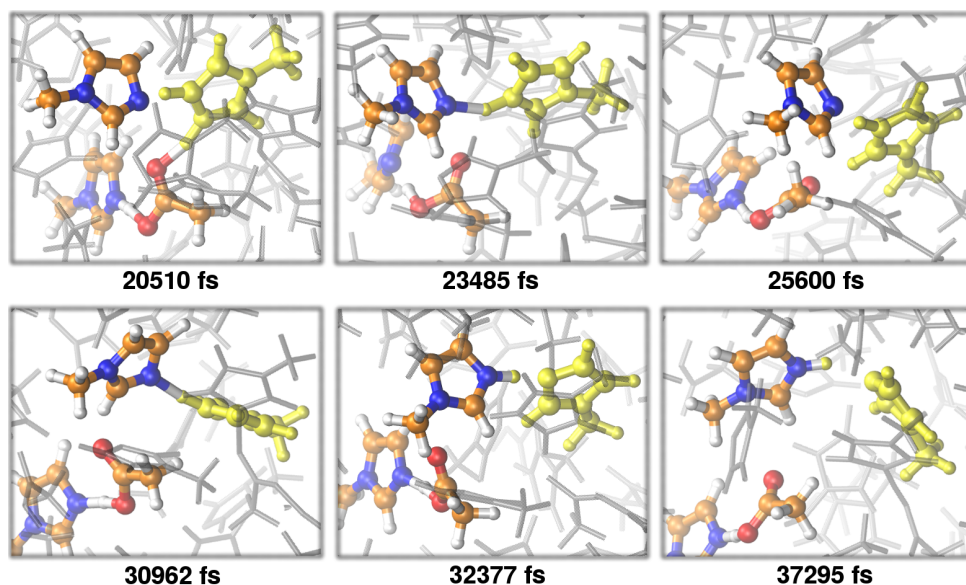


Figure 6.7: Snapshots at different simulation times in femtoseconds given below each panel along the trajectory for simulation \mathbf{B}_{mix} . The central imidazolium cation is marked in yellow and some of the neighboring partners are marked in the following color code: carbon—orange, nitrogen—blue, oxygen—red, and hydrogen—white. The remainder of the molecules or ions are portrayed in gray.

place. Instead the cation forms a hydrogen bond to an imidazole molecule (23 485 fs) and finally donates its proton (32 377 fs) before both molecules move apart.

These pictures in Figures 6.5–6.7, while still showing only a restricted number of possibilities, indicate the plethora of different proton-transfer mechanisms occurring within this liquid. In general, it is possible that the acetate anion accepts two protons. Interestingly, this can either occur by accepting each one at its two oxygen atoms or by accepting two active hydrogen atoms at one oxygen atom. In this way chains can be formed in which several active protons are participating. We observe chain lengths of up to four molecules in which the imidazole cation can be an outer acceptor, indicating the possibility of Grotthuss-like proton hopping.

An overview over all possible H^* transfers from X to Y can be obtained by plotting combined distribution functions (CDFs) of the $\text{X}\cdots\text{H}^*$ RDF versus the $\text{Y}\cdots\text{H}^*$ RDF, see Fig. 6.8. The CDFs visualize the probabilities of interactions at certain distances. For instance, from the left-hand side of Fig. 6.8 we can see that the hydroxy group O–H has an average bond length of 103 pm and is most likely to interact with another oxygen atom over a distance of 152 pm. By comparing the CDFs, we can determine which interactions are most common in the system. Although these do not reflect all possibilities of the cooperative proton transfers, one can still gain insight focusing only on two acceptor atoms and one active proton. Clearly, a transfer between two oxygen atoms as well as between nitrogen and oxygen atoms is very likely, whereas the transfer from nitrogen atom to nitrogen atom rarely takes place. Nevertheless, as discussed before and as can

6. How to Harvest Grotthuss Diffusion in Protic IL Electrolyte Systems

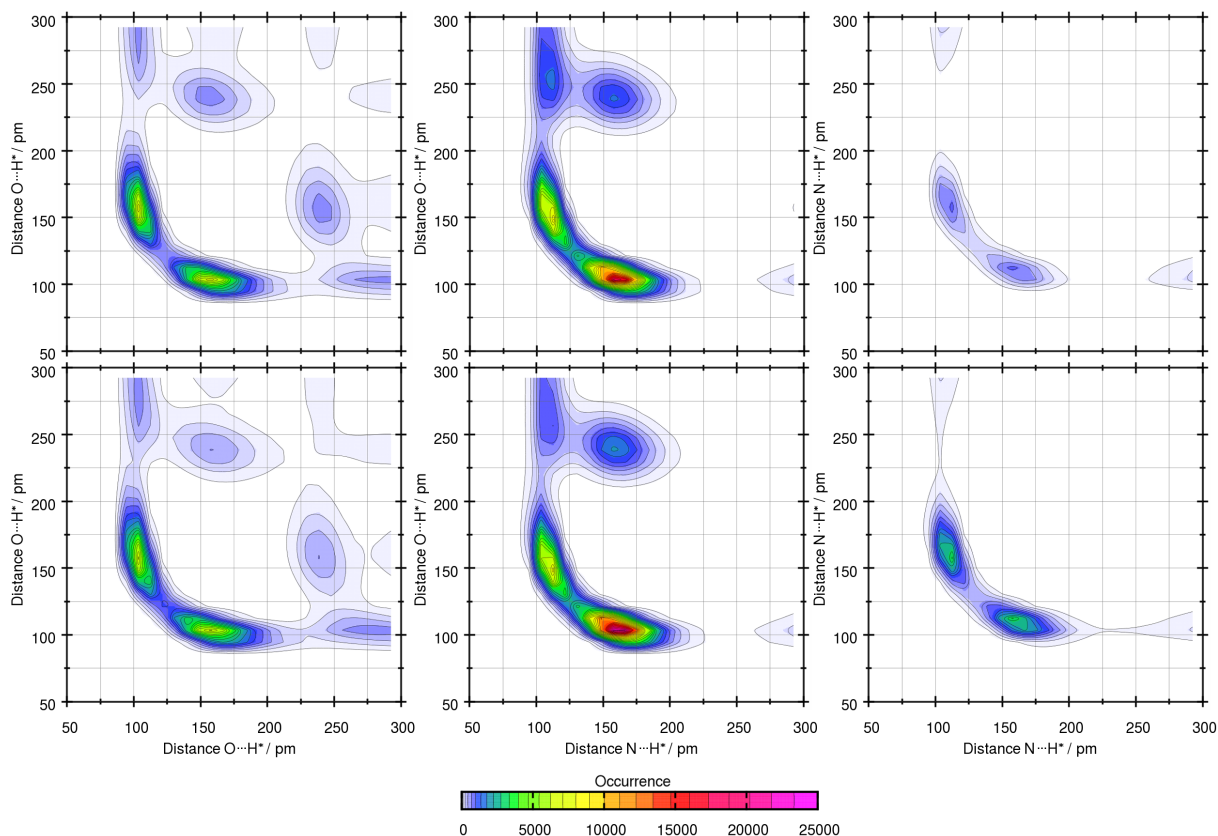


Figure 6.8: Combined RDFs (top: set **A**; bottom: set **B**) of the $\text{O}\cdots\text{H}^*$ vs. $\text{O}\cdots\text{H}^*$ distance (left), $\text{O}\cdots\text{H}^*$ vs. $\text{N}\cdots\text{H}^*$ distance (center), and $\text{N}\cdots\text{H}^*$ vs. $\text{N}\cdots\text{H}^*$ distance (right).

be seen from the right-hand side of Fig. 6.8, it does occur. From all CDFs involving the oxygen atom, clearly a second oxygen atom is present in the molecule. However, the CDFs on the left-hand side do not indicate a transfer path of the proton between both oxygen atoms of the same molecule. Thus, an intramolecular proton transfer seems not to occur. Instead, in Fig. 6.6 we can observe a switch of the proton-accepting oxygen atom in an acetic acid molecule via a proton transfer channel involving two further molecules. Agreeing with our previous results, it is clear that the active proton prefers the oxygen atom (see the middle panel of Fig. 6.8). The CDFs show a marked path for the transfer of a proton between oxygen and nitrogen atoms. This further proves that even after the equilibration phase of 10 ps is finished, which is not part of the CDFs, proton transfers frequently occur. Less distinct, but still very much visible is the transfer path between two oxygen atoms. In the context of Grotthuss-like proton conduction, this is an important result as the imidazole and the imidazolium cation can only accept or donate one proton at a time and could thus not enable Grotthuss diffusion on their own. As seen from the snapshots, the acetic acid molecule can donate and accept protons at the same time and frequently does so in the investigated system. Interestingly, the conductivity of neat acetic acid is only 8×10^{-6} mS/cm.³²⁵ Even though mostly neutral species are present in the $\text{C}_1\text{Im-HOAc}$ mixture, we see a drastic increase in conductivity to 4 mS/cm. Hence,

Table 6.1: Average coordination in set **A** (set **B** in parentheses) of the active proton with any acceptor atom N or O atom and the other way around in percentage. The upper block lists the data when a 130 pm cutoff is considered, the lower block lists numbers for a 210 pm cutoff.

neighbour	0	1	2
130 pm			
H*	17.9 (18.5)	80.6 (79.7)	1.5 (1.8)
N	80.8 (78.2)	19.2 (21.8)	0.0 (0.0)
O	67.8 (69.2)	32.2 (30.8)	0.0 (0.0)
210 pm			
H*	4.5 (4.0)	31.3 (31.8)	64.2 (64.2)
N	50.5 (46.6)	49.5 (53.4)	0.0 (0.0)
O	48.7 (49.0)	47.5 (48.5)	3.8 (2.5)

the imidazole molecule seems to have an enabling effect on the proton transfer between two oxygen atoms.

Table 6.1 gives an overview over the average coordination pattern for protons with acceptor moieties and vice versa for two different cutoff criteria. We chose two cutoffs, one according to the first RDF minimum (130 pm), thus marking the covalent bonds, and a second one (210 pm) allowing all hydrogen bonds to be counted as well. Clearly, with a larger cutoff higher coordination numbers can be observed. Looking at set **A** (set **B** in parentheses), at the 130 pm cutoff, on average 80.6 % (79.7 %) of the active protons are surrounded by one acceptor, 17.9 % (18.5 %) exist with no current acceptor, and 1.5 % (1.8 %) are bound by two acceptors. The nitrogen atom of the imidazole molecule accepts in no case two protons, which holds true even when the distance is increased such that hydrogen bonding is taken into account. A majority of 80.8 % (78.2 %) of imidazole molecules have no proton in close proximity, whereas 19.2 % (21.8 %) bind one proton. These values change to 50.5 % (46.6 %) and 49.5 % (53.4 %), respectively, when hydrogen bonding is considered. As the system is mostly neutral, it is clear that a lesser amount of non-bonding is observed for oxygen atoms than for the imidazole molecule. Interestingly, for 3.8 % (2.5 %) oxygen atoms a twofold acceptance, that is, two active protons at one oxygen atom, is observed.

For both trajectory sets, we further analyzed the bonding situation at the two oxygen atoms O1 and O2 of each one acetate moiety. For 35.5 % (38.4 %) both oxygen atoms share no proton if a cutoff of 130 pm is chosen. However, for 64.4 % (61.6 %) one of the oxygen atoms binds one of the active protons. The situation changes largely if hydrogen bonding is taken into account, that is, if a cutoff distance of 210 pm is selected. With this larger distance criterion we clearly observe a larger variety of bonding situations. 3.7 % (2.9 %) occupy a state in which O1 is coordinated by one and O2 by two protons. 12.8 % (15.2 %) of the cases have one proton at each oxygen atom. In 3.9 % (2.1 %) of the cases one oxygen atom is not bound to a proton and the other one shares two protons. Here

as well, 65.8 % (63.7 %) of the acetate moieties consist as acetic acid, that is, one oxygen atom binds one proton. In only 13.8 % (16.1 %) of the cases neither oxygen atoms share a bond with an active proton. The twofold acceptance of protons by one oxygen atom as well as the simultaneous coordination of both oxygen atoms of a single acetate moiety are bonding situations that facilitate Grotthuss diffusion.

Based on all results discussed in this section, including the direct visualization of proton-transfer processes, we can conclude that the equilibrium state of the investigated mixture involves continuous exchange of protons between ionic and neutral species. Several proton-transfer mechanisms take place in the system, involving cooperative effects. Grotthuss-like proton conduction must involve a species that is able to simultaneously accept and donate protons, which is in this case the acetic acid molecule. We observed chains up to four molecules participating in proton-transfer processes, reminiscent of Grotthuss diffusion, with species other than acetic acid acting as terminating partners. Further, we quantified bonding situations that are likely to participate in Grotthuss-like conduction mechanisms.

6.2.3 Suggesting Candidates with High Grotthuss Diffusion Ability

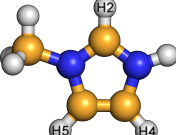
A Grotthuss-like diffusion mechanism is the desired process for proton conduction in fuel-cell electrolytes in favor of the much slower vehicle mechanism. However, for Grotthuss diffusion to occur the energy barrier for the proton transfer must be low. Although PILs with a high ΔpK_a tend to have higher thermal stability and ionicity,³²⁶ conduction by proton hopping is unlikely in these systems. In PILs with $\Delta pK_a > 17$ a decreasing proton conductivity was observed, attributed to a too strong bonding of the proton by the base, leading to a stable cation.³⁰⁷

In PILs, the equilibrium state of Eq. (6.1) is supposed to be located on the ionic side, with only small concentrations of neutral species present in the liquid system. For EAN this concentration was experimentally determined to be 10^{-5} mol/l,¹²² but the subideal Walden behavior of EAN implies that no proton hopping takes place in the system. For aqueous solutions of the C₁Im-HOAc mixture, the ratio of neutral acid and base molecules to their ionic counterparts was estimated to be 1:250 based on the ΔpK_a value of 2.4.¹¹⁵ In the neat equimolar C₁Im-HOAc mixture, however, a majority of neutral acid and base molecules is observed. This shows that the dynamics in PILs and non-aqueous acid–base mixtures can differentiate drastically from those observed in aqueous systems. Furthermore, PILs with similar ΔpK_a values can exhibit quite different proton activities as was observed experimentally by Stoimenovski et al., who could show that for alkylammonium acetate-based PILs with similar ΔpK_a the completeness of the proton transfer depends on whether the alkylammonium cation is primary, secondary, or tertiary.¹²⁶ The proton transfer in triethylammonium acetate is less complete compared to ethylammonium acetate. Hence,

Table 6.2: Gibbs energies ΔG in kJ/mol of the reverse proton transfer according to Reaction (6.1) for several substituted subspecies of the parent anion and cation acetate and *N*-methylimidazolium, respectively, calculated on the PBEh-3c/def2-mSV(P) level of theory. A red colored box indicates a more neutral equilibrium state, while a blue colored box indicates a more ionic equilibrium state.^a

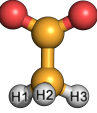
		Anion													
		Me			Parent	NH ₂			F			CN			
		1	2	3		1	2	3	1	2	3	1	2	3	
Cation	CN	1	-100.4	-100.4	-100.8	-97.9	-93.7	-88.7	-87.0	-75.7	-54.8	-33.5	-60.2	-8.8	118.4
		2	-96.7	-96.7	-97.1	-94.1	-90.0	-84.9	-83.3	-72.0	-51.0	-29.7	-56.5	-5.0	122.2
		3	-84.1	-84.1	-84.5	-81.6	-77.4	-72.4	-70.7	-59.4	-38.5	-17.2	-43.9	7.5	134.7
		4	-147.7	-147.7	-148.1	-145.2	-141.0	-136.0	-134.3	-123.0	-102.1	-80.8	-107.5	-56.1	71.1
		5	-179.1	-179.1	-179.5	-176.6	-172.4	-167.4	-165.7	-154.4	-133.5	-112.1	-138.9	-87.4	39.7
		6	-127.2	-127.2	-127.6	-124.7	-120.5	-115.5	-113.8	-102.5	-81.6	-60.2	-87.0	-35.6	91.6
	F	1	-84.1	-84.1	-84.5	-81.6	-77.4	-72.4	-70.7	-59.4	-38.5	-17.2	-43.9	7.5	134.7
		2	-87.9	-87.9	-88.3	-85.4	-81.2	-76.1	-74.5	-63.2	-42.3	-20.9	-47.7	3.8	131.0
		3	-62.8	-62.8	-63.2	-60.2	-56.1	-51.0	-49.4	-38.1	-17.2	4.2	-22.6	28.9	156.1
		4	-122.6	-122.6	-123.0	-120.1	-115.9	-110.9	-109.2	-97.9	-77.0	-55.6	-82.4	-31.0	96.2
		5	-140.6	-140.6	-141.0	-138.1	-133.9	-128.9	-127.2	-115.9	-95.0	-73.6	-100.4	-49.0	78.2
		6	-103.8	-103.8	-104.2	-101.3	-97.1	-92.0	-90.4	-79.1	-58.2	-36.8	-63.6	-12.1	115.1
	Parent	1	-48.1	-48.1	-48.5	-45.6	-41.4	-36.4	-34.7	-23.4	-2.5	18.8	-7.9	43.5	170.7
		2	-40.6	-40.6	-41.0	-38.1	-33.9	-28.9	-27.2	-15.9	5.0	26.4	-0.4	51.0	178.2
		3	-43.5	-43.5	-43.9	-41.0	-36.8	-31.8	-30.1	-18.8	2.1	23.4	-3.3	48.1	175.3
		4	-43.5	-43.5	-43.9	-41.0	-36.8	-31.8	-30.1	-18.8	2.1	23.4	-3.3	48.1	175.3
		5	-34.3	-34.3	-34.7	-31.8	-27.6	-22.6	-20.9	-9.6	11.3	32.6	5.9	57.3	184.5
		6	-30.5	-30.5	-31.0	-28.0	-23.8	-18.8	-17.2	-5.9	15.1	36.4	9.6	61.1	188.3
	Me	1	-37.7	-37.7	-38.1	-35.1	-31.0	-25.9	-24.3	-13.0	7.9	29.3	2.5	54.0	181.2
		2	-33.1	-33.1	-33.5	-30.5	-26.4	-21.3	-19.7	-8.4	12.6	33.9	7.1	58.6	185.8
		3	-45.2	-45.2	-45.6	-42.7	-38.5	-33.5	-31.8	-20.5	0.4	21.8	-5.0	46.4	173.6
		4	-39.7	-39.7	-40.2	-37.2	-33.1	-28.0	-26.4	-15.1	5.9	27.2	0.4	51.9	179.1
		5	-36.8	-36.8	-37.2	-34.3	-30.1	-25.1	-23.4	-12.1	8.8	30.1	3.3	54.8	182.0
		6	-27.6	-27.6	-28.0	-25.1	-20.9	-15.9	-14.2	-2.9	18.0	39.3	12.6	64.0	191.2
NH ₂	1	-37.7	-37.7	-38.1	-35.1	-31.0	-25.9	-24.3	-13.0	7.9	29.3	2.5	54.0	181.2	
	2	-33.1	-33.1	-33.5	-30.5	-26.4	-21.3	-19.7	-8.4	12.6	33.9	7.1	58.6	185.8	
	3	-45.2	-45.2	-45.6	-42.7	-38.5	-33.5	-31.8	-20.5	0.4	21.8	-5.0	46.4	173.6	
	4	-39.7	-39.7	-40.2	-37.2	-33.1	-28.0	-26.4	-15.1	5.9	27.2	0.4	51.9	179.1	
	5	-36.8	-36.8	-37.2	-34.3	-30.1	-25.1	-23.4	-12.1	8.8	30.1	3.3	54.8	182.0	
	6	-27.6	-27.6	-28.0	-25.1	-20.9	-15.9	-14.2	-2.9	18.0	39.3	12.6	64.0	191.2	

[a] Substitution assignments:



Substitution Cation:

- 1 H2
- 2 H4
- 3 H5
- 4 H2, H4
- 5 H2, H4, H5
- 6 H4, H5



Substitution Anion:

- 1 H1
- 2 H1, H2
- 3 H1, H2, H3

proton activities cannot be estimated from ΔpK_a values alone and the functionalization of the cation and anion plays a crucial role when discussing proton-transfer dynamics in PILs.

The design of electrolyte systems with the desired thermal stability and a fast proton conduction mechanism requires reference data. Some previous studies have provided quantum chemical data on proton transfer in several PILs.^{128,327} In this section we present the results of static quantum chemical calculations, investigating the proton transfer between the parent *N*-methylimidazolium cation and acetate anion as well as several functionalized subspecies of these molecules. Table 6.2 shows the Gibbs energies of reaction ($\Delta_r G$) for the reverse proton transfer according to Eq. (6.1) as calculated on the PBEh-3c level of theory for single ion pairs. For more details on the computations see the Supporting Information.

6. How to Harvest Grotthuss Diffusion in Protic IL Electrolyte Systems

Indicated by the color Scheme, clear trends for $\Delta_r G$ can be observed depending on the functional groups and their location on cation and anion. For *N*-methylimidazolium acetate we calculated $\Delta_r G = -45.6$ kJ/mol indicating that the neutral parent molecules are favored over their ionic counterparts. We will later treat this number as estimate for the energy range of $\Delta_r G$ in which to find potential candidates for Grotthuss diffusion. Adding methyl groups to the anion and thus increasing the electron density in the acid group through the positive inductive effect ($+I$ effect) of the methyl group shifts the equilibrium further to the neutral side. However, the number of additional methyl groups has only little effect on $\Delta_r G$.

Substituting the acetate anion with amino groups, fluorine atoms, or nitrile groups, all of which exhibit a $-I$ effect on the system, leads to a positive shift in $\Delta_r G$ with the trifluoroacetate being the first entry on the list for which the ionic species are favored over the neutral acid and base molecules, owing to the electron-withdrawing $-I$ effect of the fluorine atoms. An even higher shift is observed for the addition of nitrile groups with dicyanoacetate and tricyanoacetate anions being heavily stabilized in the ionic state, owing to the strong $-I$ effect of the nitrile group. Note that we included nitrile substitution as it is regarded with great interest in electrochemistry and several electrolytes exist that employ this functional group, including applications in fuel cells.³²⁸⁻³³⁰

The cation offers several potential substitution sites, which we have considered in different combinations. Adding methyl groups leads to a positive shift in $\Delta_r G$. Despite their $-I$ effect, amino groups lead to a positive shift as well owing to the mesomeric stabilization of the positive charge in the cation ($+M$ effect). In comparison, the $+M$ effect of fluorine atoms is much weaker and their electron-withdrawing character leads to a destabilization of the cation and thus a negative shift in $\Delta_r G$. Again, the strongest shift is observed for the addition of nitrile groups, which heavily destabilize the ionic system leading to a large negative shift in $\Delta_r G$.

According to Table 6.2, we can make predictions on whether a given combination of cation and anion will actually form a PIL or if a molecular mixture of the neutral acid and base is more likely. Treating the $C_1\text{Im-HOAc}$ mixture as reference, it is unlikely that any combination with $\Delta_r G < -45$ kJ/mol will form a true PIL. On the other hand, systems with $\Delta_r G > 0$ are likely to consist mostly of ionic species in the liquid phase. For example, *N*-methylimidazolium trifluoroacetate ($[\text{HC}_1\text{Im}][\text{TFA}]$) stands out as conveniently simple candidate with $\Delta_r G = 18.8$ kJ/mol and in fact was found to be a PIL with a melting point of 51 °C and conductivity of 1 mS/cm.³²² Umebayashi and co-workers estimated its pK_s to be 3.14, corresponding to a concentration of neutral species of 0.03 mol/l. Combinations with higher $\Delta_r G$ will likely have higher ionicities compared to $[\text{HC}_1\text{Im}][\text{TFA}]$ and can be expected to be true PILs.

We also considered the *N*-methylimidazolium formate ($[\text{HC}_1\text{Im}][\text{OCH}_3]$) for which we calculated a $\Delta_r G = -34.2$ kJ/mol. Thus, based on our results it is likely to be a pseudo-PIL

like the C₁Im-HOAc mixture and this is in fact what Umebayashi and co-workers observed experimentally, who estimated its pK_s to be -1.4 .¹²⁴ Furthermore, compared to the C₁Im-HOAc mixture it has an improved thermal stability and a higher ionic conductivity of 20 mS/cm.³²² As Umebayashi’s measurements imply that the equimolar mixture of *N*-methylimidazole and formic acid is mostly neutral, it is highly likely that this system too involves a Grotthuss-like conduction mechanism.

Using the results of Table 6.2, we can make first recommendations for possible candidates in which a Grotthuss-like proton conduction mechanism can occur. Using the investigated C₁Im-HOAc mixture as reference, $\Delta_r G$ should lie between -45 kJ/mol and 45 kJ/mol allowing for rapid proton hopping. An overly stabilized ionic system will decrease proton mobility as is observed in high $\Delta_p K_a$ PILs. On the other hand, systems where the neutral parent molecules are much more stable than their ionic counterparts will form molecular mixtures rather than true PILs, as is observed with the C₁Im-HOAc mixture. Note that in systems with $\Delta_r G > 0$ the predominantly ionic environment might have implications on the proton transfer mechanism that shift the upper bound of 45 kJ/mol. Furthermore, it should be kept in mind that the existence of neutral species in the system usually increases the volatility. Further calculations are discussed below, which investigate the energetic reaction profiles of these systems and discuss activation barriers. However, even without explicit investigation of the activation barriers, we can mostly exclude cations and anions with more than one nitrile group from future investigations based on Table 6.2. Also fluorination of the cation can be considered impractical in the context of identifying superprotonic systems. One exception might be 1-methyl-5-fluorimidazolium trifluoroacetate, which has a $\Delta_r G$ value close to zero and potentially allows rapid proton hopping. Fluorinated systems have been investigated by Riedel and co-workers.^{331,332}

Besides the feasibility of a proton transfer in terms of the thermodynamics, the kinetic activation barriers are of interest. Unfortunately, finding the transition state is a challenging task for the optimization algorithm due to the strong imbalance in stability of the ionic complex (see Fig. 6.9A) compared to its neutral counterpart (see Fig. 6.9C). To bypass this problem, we scanned the energy profile of the C₁Im-HOAc complex by optimizing the structure of the complex constraining the distance between the oxygen and the nitrogen atoms to the distance obtained by the optimization of the complex while varying the distance between the oxygen and the hydrogen atoms stepwise. The resulting plot (Fig. 6.9 left graph) shows a small maximum **B** with a demand of 7.4 kJ/mol in electronic energy and falls afterwards into a significantly larger minimum for structure **C**. Interestingly, the electronic energy demand of the transition state is nearly absolutely neutralized by the zero point energy correction and consequently the maximum vanishes on the Gibbs free energy surface. As barriers below 20 kJ/mol are low enough to be overcome in AIMD, we can observe proton transfer in our simulations.

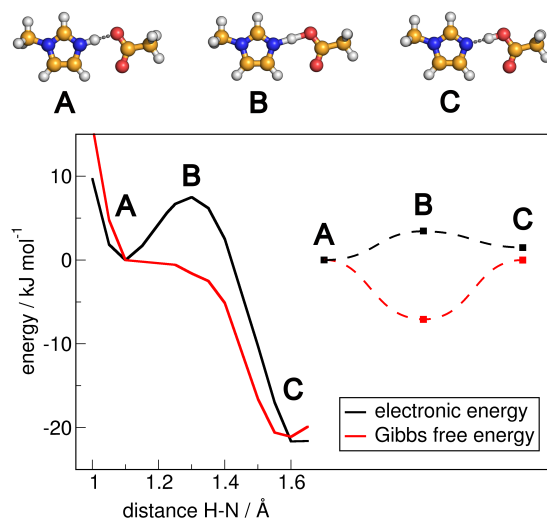


Figure 6.9: Energy profiles of the proton transfer between cation and anion. The left profile visualizes the scan of the path of the hydrogen atom between the cation and the anion in the C₁Im-HOAc-system. The right profile shows the energies of the ionic complex **A**, the transition state **B**, and the neutral complex **C** of the C₁Im-cation with the doubly fluorinated anion. It is revealed that the kinetic hindrance is very small in comparison with the thermodynamic sink in the parent system.

It should be noted here, that the applied method to calculate the zero point energy is based on a harmonic approximation and because of the strong anharmonicity of the potential well the correction may be strongly overestimated. This problem becomes even more obvious in the case of more balanced combinations of cations and anions, for example, the doubly fluorinated anion (see Fig. 6.9 right graph). The strong overestimation of the zero point energy transforms the electronic transition state **B** into a minimum on the Gibbs free energy surface. The estimated zero point energy is even higher than the electronic energy barrier given by the corresponding transition state. However, an anharmonic analysis is out of the scope of this work.

Nevertheless, due to the fact that in the transition state a vibrational mode is converted into a translational mode – and consequently, the total zero point energy of the complex is reduced – the barrier on the electronic energy surface can be seen as an upper limit of the Gibbs free energy barrier. Therefore, it can be stated that the kinetic hindrance of the proton transfer between the cation and anion is very small in comparison with the hindrance induced by the thermodynamic sink of imbalanced cation–anion systems.

The transfer between acid and anion as well as the transfer between cation and imidazole molecule is very similar to the situation of a balanced cation–anion transfer because the hydrogen-donating molecule is exactly the same as the accepting one. In all these cases the barrier in electronic energy is mostly consumed by the zero point energy correction and very small compared to the thermodynamic sink of most systems. Therefore, the influence of the kinetic hindrance on the Grotthuss-like diffusion can be seen as negligible.

6.3 Conclusions

In this work we presented a detailed analysis of the proton transfer in a model system representing low- ΔpK_a protic ionic liquids (PILs) with high proton activities. It is possible to determine the content of neutral species in the liquid system with good agreement with experiments, which is to the best of our knowledge the first time that the ionicity of a potential PIL could be determined by ab initio molecular dynamics (AIMD) simulations. Of course, more sophisticated sampling approaches will increase the accuracy by far.³³³ The system involves a continuous exchange of protons between ionic and neutral species. The equilibrium concentration of neutral species is set in the 70 to 80% range. Hence, we can confirm that the equimolar *N*-methylimidazole and acetic acid (C₁Im-HOAc) mixture consists mostly of neutral species.

It was proposed that the system involves Grotthuss-like proton conduction that gives rise to the surprisingly high ionic conductivity. We could demonstrate this to be true. Protons show similar diffusion rates to anions and cations; thus, a diffusion mechanism in which the proton travels through tunnels within the liquid structure can be excluded. However, the proton transfer in this system takes place through several different mechanisms involving both ionic and neutral species. The proton transfer between nitrogen and oxygen atoms occurs frequently in the system, but proton transfer between oxygen atoms plays a major role. Although rare, even the transfer of a proton from an imidazolium cation to an imidazole molecule could be directly observed. Grotthuss-like proton conduction must involve a species that can simultaneously accept and donate protons, which is in this case the acetic acid. We could directly observe the formation of proton transfer chains with up to four participating molecules, resembling a Grotthuss-like conduction mechanism on the scale of our simulation size and time. Species other than acetic acid act as terminating partners. It is thus concluded that proton hopping happens mainly between chains of acetic acid molecules terminated but also enabled by other species.

Furthermore, static quantum chemical results on the energetics of proton transfer between several differently functionalized anions and cations were also presented. Using these results, predictions can be made on whether a given combination of anion and cation will form a true PIL or a molecular mixture. Based on the investigated system as reference an energy range of -45 to 45 kJ/mol for the Gibbs energy of reaction ($\Delta_r G$) of the proton transfer is proposed for potentially Grotthuss conduction-enabled systems. We investigated the kinetics of the proton transfer between the *N*-methylimidazolium cation and the acetate anion and found that the activation barrier is negligible and can be easily overcome in the liquid system. This is the reason for such a remarkable proton activity in the simulations.

Low ΔpK_a systems can exhibit high ionic conductivities through Grotthuss-like proton conduction mechanisms that are not accessible to high ΔpK_a PILs. These systems are

usually avoided because compared to high ΔpK_a PILs they show inferior thermal stability and higher volatility. Nonetheless, there is potential of identifying highly conductive media by target-oriented design of PILs with low energetic hindrance to proton transfer. In this work we gathered and offer helpful information to reach this goal. The exploitation of Grotthuss diffusion in PILs has great potential and should be further pursued in the future.

Acknowledgments

B. Kirchner and coworkers would like to thank for the support from the Deutsche Forschungsgemeinschaft under the SPP 1708 project KI 768/15-1. The authors acknowledge the priority program 1708 under the project KI 768/15-1. S. Gehrke was supported by the International Max Planck Research School for Reactive Structure Analysis for Chemical Reactions.

7 Predicting Mole-Fraction-Dependent Dissociation for Weak Acids

Jan Blasius,^{*} Johannes Ingenmey,^{*} Eva Perlt,[†] Michael von Domaros,[†] Oldamur Hollóczki,^{*} and Barbara Kirchner^{*}

Received: October 16, 2018, Published: February 25, 2019

Reprinted (adapted) with permission from

J. Blasius, J. Ingenmey, E. Perlt, M. von Domaros, O. Hollóczki, and B. Kirchner, *Angew. Chem. Int. Ed.*, 2019, **58**, 3212–3216; *Angew. Chem.*, 2019, **131**, 3245–3249.

Copyright © 2019 Wiley-VCH

DOI: 10.1002/anie.201811839

Contributions to the manuscript

- Supervising the construction of the cluster sets
- Supervising and analyzing the bQCE calculations
- Discussion of the results
- Providing the figures
- Co-writing the manuscript

^{*}Mulliken Center for Theoretical Chemistry, Institut für Physikalische und Theoretische Chemie, Rheinische Friedrich-Wilhelms-Universität Bonn, Berlingstraße 4+6, 53115 Bonn, Germany

[†]Department of Chemistry, 1102 Natural Sciences II, University of California, Irvine, CA 92697, USA

Abstract We demonstrate for formic and acetic acid dissolved in water as examples that the binary quantum cluster equilibrium (bQCE) approach can predict acid strengths over the whole range of acid concentrations. The acid strength increases in a complex rather than a simple way with increasing mole fraction of the acid from 0 to 0.7, reflecting the complex interplay between the dissociated ions or conjugate bases available as compared to the acid and water molecules. Furthermore, our calculated ion concentrations meet the experimental maximum of the conductivity with excellent agreement for acetic acid and satisfactorily for the formic acid/water mixture. As only a limited number of simple quantum chemical calculations are required for the prediction, bQCE is clearly a valuable approach to access these quantities also in non-aqueous solutions. It is a highly valuable asset for predicting ionization processes in highly concentrated solutions, which are relevant for biological and chemical systems, as well as technological processes.

7.1 Communication

Acid–base theory is one of the most fundamental concepts in chemistry.³³⁴ Its relevance spans from catalysis (e.g., acid catalysis) and inorganic chemistry (e.g., leaching processes) through food chemistry (e.g., fermentation technologies) to biochemistry (e.g., amino acids, proton pump membrane proteins). A key application of this theory is its use to predict the pH value of any given solution, which is directly related to the degree of dissociation of the acid. Towards accomplishing this goal, there have been many successful attempts of predicting the pK_a values of weak acids computationally. The hitherto established approach is based on estimating the deprotonation energy of the isolated acid, which is then refined by considering the solvation energies of the acid, the proton, and the conjugate base.^{335–344} The calculations are completed by transforming the obtained solvation-corrected deprotonation enthalpies and entropies into pK_a values. Solvation free energies of the conjugate bases of some acids were calculated by Pliego and Riveros with the aid of the cluster-continuum model, which combines explicit solvation of the solute in molecular clusters with implicit solvation by a continuum model. Charged particles and acids were calculated, leading to pK_a values with an average accuracy of $<2 pK_a$ units.^{345,346} However, despite the high accuracy achieved when predicting pK_a data for dilute weak acids, this method has limited applicability for systems with higher concentrations, which include the majority of chemically, technologically, and biologically most interesting systems. These shortcomings are due to the fact that the pK_a value is meant to describe ideal, infinitely dilute systems,³³⁴ in which the solvation of the species can be considered to be independent of the concentration. In reality, however, strong deviations from ideality can be observed already at concentrations >0.01 M, which poses a significant challenge to the computational methods aiming at the aforementioned goals. The only approach developed thus far that should, in principle, be capable of predicting acidities

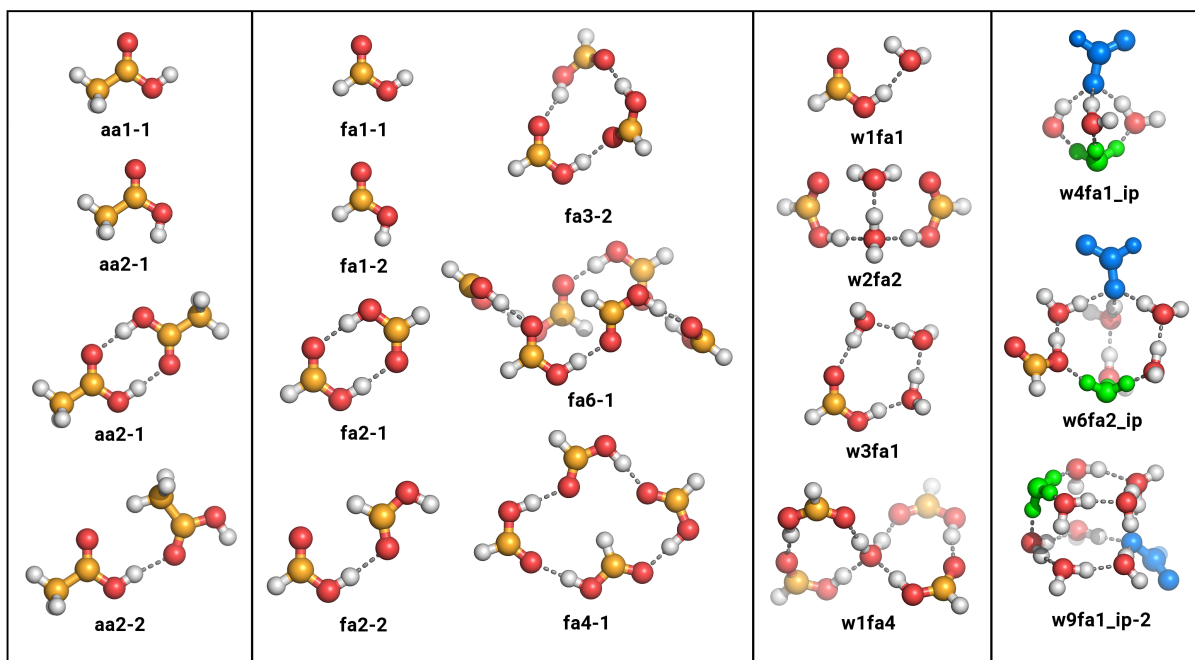


Figure 7.1: Examples of different clusters used in this work. Please note that these clusters are not necessarily the ones that are populated, they were selected for display for clarity reasons. The first column shows two monomers (*cis* and *trans*) and dimers for the neat acetic acid (aa) clusters. The next column contains formic acid (fa) instead of aa clusters up to the hexamer. It is clearly visible that the clusters feature different hydrogen-bonding motifs and that, where possible, both acids adopt similar ones. The third column shows how some mixed fa/water clusters are built up. In the last column, the dissociated clusters are exemplified. The anions are shown in blue while the hydronium cations are shown in green. In total, 15 neat water (with 4 dissociated) clusters, 13 each neat acetic and formic acid clusters, 32 each mixed fa/water and aa/water clusters, and 13 each dissociated fa/water and aa/water clusters were included in the bQCE calculations. The geometries of all employed clusters are given in the Supporting Information.

of non-ideal systems in a concentration-dependent fashion was reported by Vasudevan and Tummanapelli, who used *ab initio* molecular dynamics simulations to describe proton transfer processes of amino acids and carboxylic acids in solution.^{347,348} Although an excellent accuracy of 0.1 p*K*_a units was achieved for the chosen systems, the computational demand of these calculations, and the need to repeat them for every composition of interest, renders the applicability of this method limited to a few selected cases at a time.

Herein, we demonstrate for formic acid (fa) and acetic acid (aa) as examples that by treating the aqueous acid solution as a water/acid mixture within the binary quantum cluster equilibrium (bQCE) theory,^{39,43} the ionization process and its thermodynamic properties can be described fairly accurately over the whole concentration range at reasonable computational cost.

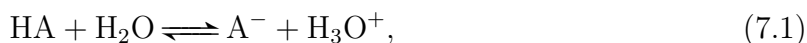
This cluster approach derives the mole-fraction-dependent system partition function from a few quantum chemically calculated clusters (see Fig. 7.1 for some examples). The

7. Predicting Mole-Fraction-Dependent Dissociation for Weak Acids

clusters can be constructed containing only acid or water molecules (neat clusters)⁴⁷ or both (mixed clusters).⁴⁴ For each cluster size, a few conformers are considered such that important liquid motifs are included. The clusters that contain the conjugate base and a solvated hydronium-like cation are constructed to cover ion pair distances from 340 to 620 pm. Thus they cover contact ion pair as well as solvent-separated ion pair motifs. It has been shown in many MD and ab initio molecular dynamics (AIMD) simulations (e.g., Ref. 349) that the free energy surface of the ion pair separation has a minimum and a barrier ($> 5 k_B T$) upon going from the contact ion pair to the solvent-separated ion pair. The energetic penalty between the solvent-separated ion pair and the fully separated ion pair is negligible or less than $0.5 k_B T$. Through self-consistent solution of a set of polynomial equations, the bQCE theory evaluates the population weights of the different clusters and finally the system partition function as a product of weighted single cluster partition functions. A full description of the method can be found in earlier works^{39,43} and in the Supporting Information. All calculations were carried out with our own Peacemaker software package.^{8,43}

Pure formic acid has been investigated by the same theory, but for neat substances, before,⁷⁷ and the thermodynamics in the liquid and the vapor phase of this compound could be described accurately. We could reproduce these results in the present work (see the Supporting Information for details).

In aqueous solution, the dissociation of an acid HA is expressed by



with A^- and H_3O^+ being the conjugate base and the hydronium ion, respectively. The equilibrium constant K_{eq} is defined by the law of mass action (values in square brackets denote equilibrium concentrations):

$$K_{\text{eq}} = \frac{[\text{H}_3\text{O}^+][\text{A}^-]}{[\text{H}_2\text{O}][\text{HA}]}. \quad (7.2)$$

Any of these four concentrations can be directly obtained from the bQCE populations of each cluster. Usually, by assuming $[\text{H}_2\text{O}]$ to be constant, K_{eq} can be simplified to K_{a} :

$$K_{\text{a}} = K_{\text{eq}} \times [\text{H}_2\text{O}] = \frac{[\text{H}_3\text{O}^+][\text{A}^-]}{[\text{HA}]}. \quad (7.3)$$

The negative decadic logarithm of K_{a} gives the $\text{p}K_{\text{a}}$ value:

$$\text{p}K_{\text{a}} = -\lg(K_{\text{a}}). \quad (7.4)$$

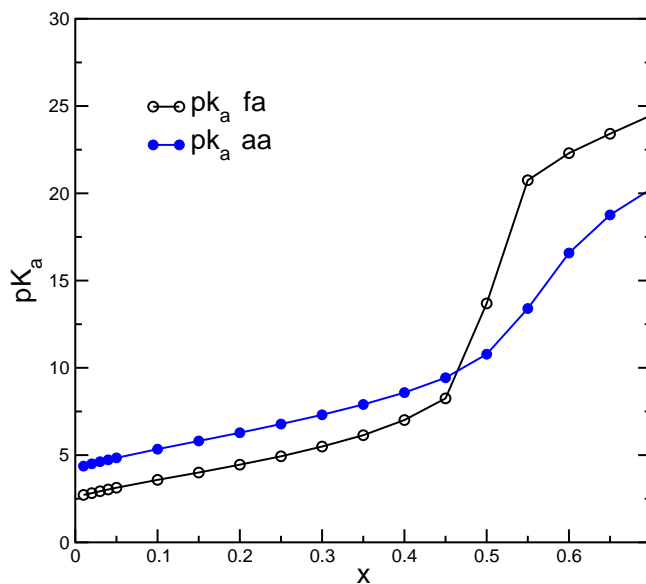


Figure 7.2: Calculated pK_a values for different compositions of aqueous solutions of formic acid (black) and acetic acid (gray). With increasing acid concentration, higher pK_a values indicate a decreasing degree of ionization. The sudden increase at $x = 0.5$ indicates an excess of acid molecules due to the lack of free water molecules.

Considering its dominance in the literature, K_a and not K_{eq} must be chosen for comparisons with experimental data. In Fig. 7.2, the pK_a^{bQCE} values for mole fractions between 0.01 and 0.7 are plotted (for the numerical data, see the Supporting Information).

With a concentration of about 0.55 mol/l, the most dilute systems considered here ($x = 0.01$) are still relatively concentrated. Thus an extrapolation to infinite dilution based on the five lowest mole fractions was performed to obtain neat pK_a values for both acids. The strengths of both acids were somewhat overestimated by this approach, with pK_a^{bQCE} being 2.62 and 4.26 for formic and acetic acid, respectively, compared with the experimentally obtained pK_a values of 3.75 and 4.76.³⁵⁰ The calculated pK_a^{bQCE} values increase with increasing acid concentration, indicating a decreasing degree of ionization (i.e., fewer acid molecules dissociate) at large acid mole fractions. The values show a steady increase up to a mole fraction of approximately 0.4, where a sudden increase in the pK_a^{bQCE} values can be observed as from this concentration onwards, the acid molecules are in excess, leaving them without a free water molecule for protonation. At mole fractions larger than 0.5, the slope of the curve becomes lower again.

Knowing the equilibrium concentrations of the ions, it is possible to calculate the dissociation ratio:

$$\alpha = \frac{[A^-]}{[HA]}. \quad (7.5)$$

This ratio does not contain the water concentration in either of the terms, and therefore provides a simple way to observe how the bQCE approach treats non-ideal effects over the whole concentration range. We calculated α by two different approaches. The more

7. Predicting Mole-Fraction-Dependent Dissociation for Weak Acids

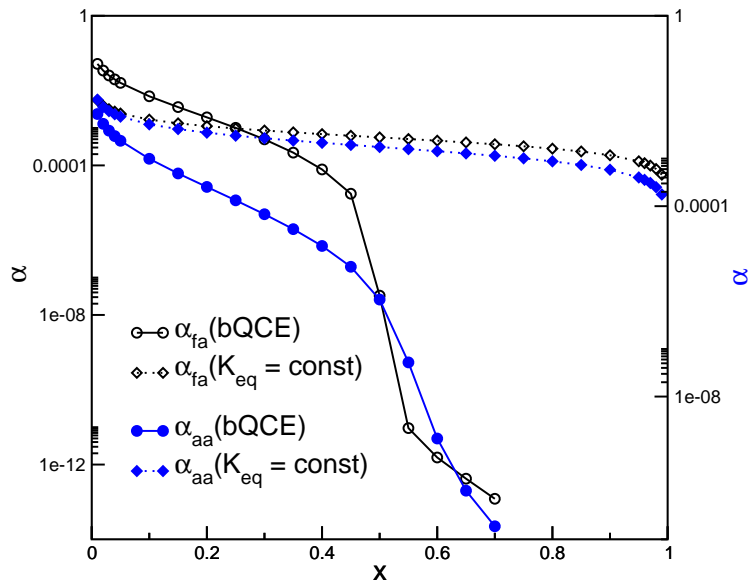


Figure 7.3: Logarithmic dissociation constants α of the acids calculated with the bQCE method (bQCE) and by assuming pK_a to be constant ($K_{eq} = \text{const}$).

obvious one is the direct evaluation of Eq. (7.5) with concentrations obtained by directly summing up bQCE populations ($\alpha(\text{bQCE})$). The other approach is based on simply assuming that the equilibrium constant pK_{eq} is composition-independent, $pK_{eq} = \text{const}$ ($\alpha(K_{eq} = \text{const})$). This allows the calculation of α based on calculated or experimental pK_a values according to Eqs. (7.2) and (7.5), in principle over the whole concentration range. Results obtained with both approaches are shown in Fig. 7.3. The differences between the two pairs of curves are apparent already at first glance. Whereas at low concentrations only a slight difference is observable between the $\alpha(K_{eq} = \text{const})$ and $\alpha(\text{bQCE})$ data, the inherently required drop in the dissociation ratio at higher acid concentrations is clearly not described by the $\alpha(K_{eq} = \text{const})$ curves. At a mole fraction of 0.7, the differences between the values obtained from the two different approaches amount to 10 to 12 orders of magnitude. Although $\alpha(K_{eq} = \text{const})$ is based on experiment and $\alpha(\text{bQCE})$ on our calculations, discrepancies of this extent point much beyond a simple experiment/theory mismatch, as the shape of the curve in Fig. 7.3 would not be affected at all by using a different pK_a value, but only shift to slightly higher or lower values (cf. $\alpha(K_{eq} = \text{const})$ for aa and fa).

As direct experimental data on the dissociation ratio is unavailable for higher concentrations, it is not possible to assess directly whether $\alpha(\text{bQCE})$ or $\alpha(K_{eq} = \text{const})$ is more reliable. The species that are produced by the dissociation (i.e., ionization) process are, however, ionic, and hence they contribute greatly to the conductivity of the system. Accordingly, comparing the concentration of the ions in the solution to the experimental conductivity across the concentration range can serve as a qualitative validation for the two approaches.

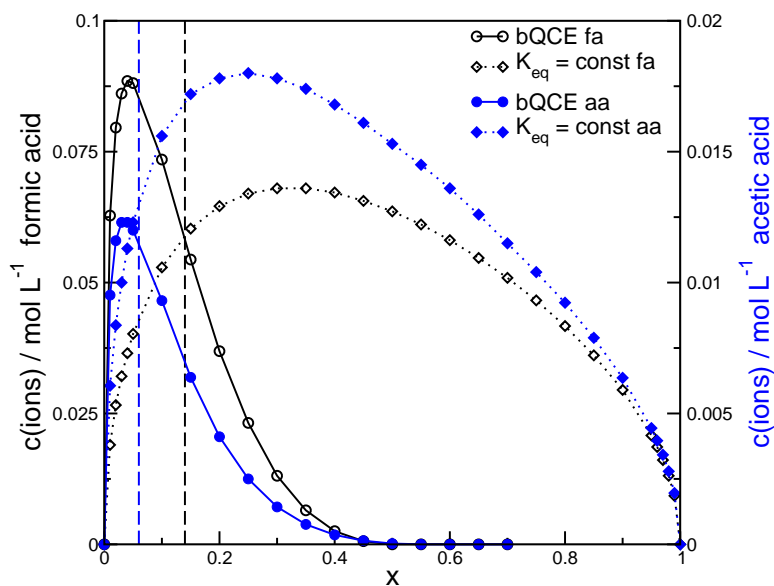


Figure 7.4: Total ion concentration of aqueous formic (black) and acetic (gray) acid solutions calculated from bQCE (solid lines) or by assuming $K_{\text{eq}} = \text{const}$ (dotted lines). The vertical dashed lines indicate the experimentally obtained conductivity maxima.

Similarly to α , the total ion concentration (defined as $c(\text{ions}) = [\text{A}^-] + [\text{H}_3\text{O}^+]$) for different mole fractions can be calculated through the two approaches above. It can be calculated directly from the populations obtained in the bQCE calculations as a simple sum of the total ion concentrations, or it can be expressed as a function of K_{a} :

$$c(\text{ions}) = 2\sqrt{K_{\text{a}} \times [\text{HA}]}. \quad (7.6)$$

In Fig. 7.4, the data obtained for both acids with both approaches are shown. Experimentally, the conductivities reach maxima at $x_{\text{fa}} = 0.14$ and $x_{\text{aa}} = 0.06$,¹⁹⁷ (Fig. 7.5) as the number of ions in the system initially increases when more acid is added to the system, and then drops at higher concentrations as dissociation is suppressed. The present bQCE calculations predict the ion concentration to be highest at $x_{\text{fa}} = 0.04$, whilst the $K_{\text{eq}} = \text{const}$ curve shows a maximum at $x_{\text{fa}} = 0.3$, which is notably farther away from the experimental value (Fig. 7.4). For acetic acid, an ion concentration maximum at $x_{\text{aa}} = 0.04$ was obtained from the bQCE calculations, which is in excellent agreement with the experimental result, while the $K_{\text{eq}} = \text{const}$ curve has its maximum at $x_{\text{aa}} = 0.25$. It is even more convincing to compare the decay of the curves after the maxima. While the ion concentration curves produced by assuming $K_{\text{eq}} = \text{const}$ are concave and decrease slowly until they reach the neat acid scenario, the bQCE derived ion concentration curves show a sudden drop in ion concentrations, and after an inflection point their decay is convex. The experimental conductivity–concentration plots (Fig. 7.5) confirm the validity of the latter behavior, which makes it clear that using bQCE to predict acid dissociation over the whole concentration range provides at least qualitatively reasonable

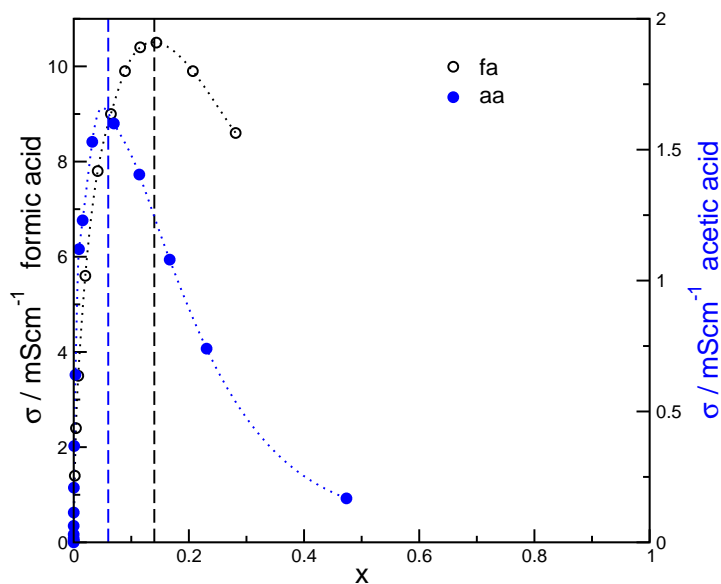


Figure 7.5: Experimental conductivities of aqueous formic (black) and acetic (gray) acid solutions. The vertical lines indicate the conductivity maxima.¹⁹⁷

results. Our results are also in good agreement with a study of the water/acetic acid mixture, which used the dependence of the K_{eq} value on the dielectric constant of the system to calculate the ion concentration over the mixing range.³⁵¹

As in previous predictions through quantum chemical calculations only acidities for infinitely dilute systems were accessible, applying those theoretical techniques to concentrated solutions has to rely on assuming that the K_{eq} value is independent of the concentration. The severe limitations of this simplification were demonstrated above, and the superiority of bQCE for more concentrated systems is also obvious.

In summary, we have applied a cluster approach (bQCE) to obtain mole-fraction-dependent acid strengths. This novel acidity prediction approach is based on a limited number of simple and easily accessible quantum chemical calculations, which can be performed for any acid and any medium, allowing the investigation of such systems at any density and in different phases. Although currently restricted to binary systems, this simplicity makes bQCE a valuable asset for predicting the acidity of and the underlying proton transfer processes in concentrated solutions, opening possibilities for understanding and designing chemical processes of practical relevance.

Acknowledgments

E.P. and M.v.D. are funded by the Deutsche Forschungsgemeinschaft (DFG, German Research Foundation; project numbers 391320977 and 409294855).

Part III

Ionicity and Ion Association in Ionic Liquids

Summary of Part III

The final part of the thesis contains two studies dealing with the concept and implications of ion pairing and ion association in ILs. First, the evidence for and against significant ion pair formation in neat ILs and the various estimates for the degree of ion pairing obtained by different methods are discussed and extended by a new analysis of ion pair dynamics in a common IL based on AIMD and static quantum chemistry. Thereafter, the ion association and coordination sphere of a solute salt in a multi-component IL-based electrolyte is studied.

Ion pair formation has often been invoked as explanation for low conductivities and ionicities observed in many ILs.¹³⁰ By the formation of neutral aggregates like ion pairs, it is assumed, the effective number of charge carrying species participating in conduction is reduced. However, estimates for the degree of ion pair formation vary strongly from 99.997 %^{132,140} to 20 to 50 %¹³⁰ to <1 %, ^{141,144} depending on the employed method. Chapter 8 provides an overview of the available experimental and theoretical evidence. The discussion is based on the definition of ion pairing as given by Robinson and Stokes which explicitly includes the life time.³⁵² The Walden plot is often interpreted to indicate low ionicity in ILs that fall below the ideal reference line of an KCl electrolyte. This has been criticized, however, as there is no inherent reason why an ideal ionic liquid should behave similar to an aqueous KCl electrolyte^{353,354} and the observed behavior can be explained by accounting for ion size differences.^{133,353,354} Gebbie et al. propose a picture of ILs as dilute electrolytes of mostly neutral ion pairs and 0.003 % of free unassociated ions based on direct surface force measurements.^{132,140} This was criticized as their approach was biased towards dilute electrolytes and surface measurements do not necessarily paint an accurate picture of bulk properties.^{355–357} A Fourier-transform infrared spectroscopic investigation found evidence for 8 to 30 % of ion pairs,^{358,359} but must be interpreted with its time scale in the subpicosecond range in mind. In contrast, dielectric and NMR spectroscopy capture processes on much larger time scales and find no evidence of long-lived ion pairs,^{142,360} implying an upper bound of their life times in the low picosecond range.¹⁰¹ Computational investigations by molecular dynamics simulations find little to no evidence for long-lived ion pair formations.^{131,137,143–145,361}

To add to these results, the ion pair dynamics in the common IL 1-butyl-3-methylimidazolium triflate are investigated by means of AIMD simulations and static quantum chemical calculations. Radial distribution functions show evidence for a solvation shell of six anions surrounding the cation, but no evidence for distinct ion pairs can be seen. A combined distribution function of ion pair displacement and life time shows that ion pairs exist only for short time frames below 2 ps. Their joint diffusion does not exceed distances of 200 pm, which is shorter than the average interionic distance. An analysis of ion diffusion by their velocity autocorrelation function shows collision times that are

too short to support long-lived ion pairs. To complete the study, an analysis of the electrostatic potential of the ions is carried out at the B3LYP/def2-TZVP level of theory. Comparing the ions in their isolated state to the associated ion pair, reveals significant charge transfer between anion and cation. A charge analysis based on the CHELPG method³⁶² shows that the net charges of both ions have decreased from ± 1 to ± 0.83 , in reasonable agreement with its reported ionicity of 0.57.¹³⁰ Such charge transfer effects have been demonstrated to occur in the liquid phase^{137–139} and reduce ion pair formation.¹³⁷ Based on these new results and the discussed evidence reported in literature so far, it is concluded that a view of ILs as dilute electrolytes of mostly neutral ion pairs is currently not supported. The observed ionicities of ILs may be sufficiently explained by ion size effects on diffusion and charge transfer effects, without the need to introduce long-lived ion pairs into the IL picture.

Chapter 9 describes a combined experimental and theoretical investigation of the effects of two additives on the reversibility of magnesium deposition and dissolution in an IL-based electrolyte. The experimental setup involves a glassy carbon electrode in 1-butyl-1-methylpyrrolidinium bis(trifluoromethylsulfonyl)imide (BMP-TFSI), on which Mg deposition and dissolution is measured by means of cyclic voltammetry at varying concentrations of MgTFSI₂, Mg(BH₄)₂, and 18-crown-6 ether (18c6). The reversibility of charge and recharge cycles in Mg batteries is often found to be low, as the electrodes will be insulated by decomposition products of the electrolyte.¹⁵⁹ This is also the case in MgTFSI₂-containing BMP-TFSI without additives, in which Mg deposition and dissolution is effectively inhibited by decomposition of the TFSI⁻ anion. In electrolytes of this kind, TFSI⁻ is known to form ion pairs or aggregates with one or multiple metal ions.^{160,162,163} The addition of Mg(BH₄)₂ and 18-crown-6 as additives, either separately or in combination, are found to drastically improve reversibility from 35 % to around 75 %. It is assumed that the BH₄⁻ anion acts mainly as a water scavenger, reducing detrimental effects caused by trace amounts of water impurities in the employed chemicals, but may also coordinate to the Mg²⁺ cation and prevent its coordination to TFSI⁻. The chelating 18-crown-6 additive is assumed to coordinate to the Mg²⁺ cation and thereby displace the TFSI⁻ anion from its coordination sphere.

This is investigated by means of quantum chemical calculations on clusters of MgTFSI₂, cut from classical MD simulations, in the presence of up to two BMP-TFSI ion pair and up to one 18-crown-6 molecule. The coordination energy of the 18-crown-6 ether in the MgTFSI₂ + 18c6 cluster is found to be -369 kJ/mol, vastly exceeding the coordination energy of -132 kJ/mol by a BMP-TFSI ion pair in the MgTFSI₂ + BMP-TFSI cluster. The addition of a second BMP-TFSI ion pair (MgTFSI₂ + 2 BMP-TFSI) does not result in an increase in coordination energy, as the Mg is already fully coordinated in the presence of three TFSI⁻ anions. An analysis of the coordination geometry shows that 18-crown-6 coordinates the Mg²⁺ cation five-fold in a planar arrangement, which prevents

the two-fold coordination by a TFSI⁻ anion. The partial reduction of Mg²⁺ to Mg⁺ drastically decreases the coordination energy, so that subsequent thermal detachment from its coordination sphere to allow Mg deposition seems possible. An analysis of the electron affinities of 18-crown-6 and TFSI⁻ in different clusters reveals, that the interaction with the Mg²⁺ cation significantly decreases the reductive stability of the TFSI⁻ anion, moving it into the potential range of Mg deposition. The 18-crown-6 ether is found stable against reductive decomposition and improves the stability of TFSI⁻ by displacing it from the coordination sphere of the cation, thereby improving the reversibility.

8 Ion Pairing in Ionic Liquids

Johannes Ingenmey,* Oldamur Hollóczy,* and Barbara Kirchner*

Received: October 07, 2020, Published: December 8, 2020

Reprinted (adapted) with permission from

J. Ingenmey, O. Hollóczy, and B. Kirchner, in *Encyclopedia of Ionic Liquids*, ed. S. Zhang, Springer, Singapore, 2021.

Copyright © 2021 Springer Nature

DOI: 10.1007/978-981-10-6739-6_63-1

Contributions to the manuscript

- Performing and analyzing static DFT calculations
- Analyzing the AIMD trajectory
- Providing the figures
- Writing the manuscript

*Mulliken Center for Theoretical Chemistry, Institut für Physikalische und Theoretische Chemie, Rheinische Friedrich-Wilhelms-Universität Bonn, Berlingstraße 4+6, 53115 Bonn, Germany

8.1 What is Ion Pairing?

The nature and degree of ion pairing in ionic liquids (ILs) led to controversial debate in literature.^{131,137,361} Simply put, several factions of contrasting views – on one end describing ILs as systems of mostly free, dissociated ions and on the other end holding the view that ILs are mainly composed of associated, neutral ion pairs – seek to find a solution for what seems to be contradictory evidence. No definitive answer could be reached to this day, with new evidence still emerging on both sides. Despite the fact that this debate has been going on for over a decade, a clear and generally accepted definition of what constitutes an ion pair in a system that is composed solely of ionic particles is still missing. Usually a helpful definition includes the distinction between penetrated or contact ion pairs (two associated ions penetrating each other or in direct contact), solvent-shared ion pairs (the ions are associated but separated by solvent molecules), and solvent-separated ion pairs (the ions are fully separated through their distinct solvation shells). However, their distinction seems problematic when the liquid is composed entirely of ions.^{363,364} Nevertheless, such concepts play a role when solute ions are considered in ionic liquids or their mixtures with other ionic or molecular liquids or when deep eutectic solvents (DES) are studied.^{137,365–372} Traditional theories of dilute electrolyte solutions are only partially applicable and arguments derived from these theories must be taken with care. It is the very lack of a general theory for IL systems that is the root of the ion pairing question.

In the most basic formulation, the concept of ion association describes the phenomenon and effects of two charged particles of opposite signs interacting with each other at close distances. In such a situation the Coulombic attraction shared between both ions may exceed their thermal energy, effectively forming a new bonded entity with a lifetime of larger scale than that of diffusion processes of free ions in the same system.³⁶¹ An ion pair will act as one kinetic entity in the solution, separating its movements and interactions from those of its particular components. In other words, this translates to the condition that “an ion-pair must be long-lived enough to be a recognizable kinetic entity in the solution,” as stated by Robinson and Stokes.³⁵²

The general process of ion association may be formulated as reaction



of cation A^{n+} and anion B^{m-} of charges n and $m-$, respectively. If the joint particles are of the same charge with opposite sign ($n = m$), the resulting ion pair will have no net charge, effectively reducing the number of charge carriers accessible to ionic conduction, leading to a decrease in conductivity. If the charges are not equal ($n \neq m$), the resulting ion pair will have a charge but still decrease conductivity. This is due to the reduced net

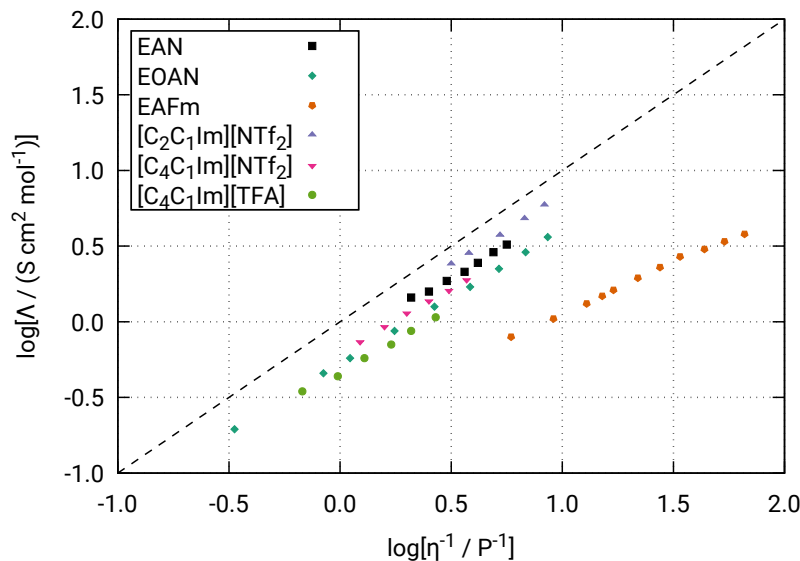


Figure 8.1: Walden plot of several ILs produced from data taken from Ref. 109 (alkylammonium-based ILs) and Ref. 130 (alkylimidazolium-based ILs).

charge of the ion pair compared to the freely moving ions, as well as the increased mass resulting in a higher kinetic barrier to diffusion and thus a slower charge transport.

With the increasing interest in ionic liquids it was soon noticed that one of their defining properties, namely their ionic conductivity,³⁷³ often showed values below expectation.^{133,135} It may seem straightforward that ILs should have high ionic conductivities on the level of molten salts, given that they are composed entirely of ions^{363,364} and are usually liquid at room temperature. While ILs indeed show high conductivities compared to other non-aqueous solvents at ambient conditions, they are much less conductive than aqueous electrolytes.¹³⁵ Their typically high viscosities, which lead to decreased ion mobility and thus lower conductivity, might appear to be an obvious explanation. However, even when the viscosity is accounted for, some ILs were found to exhibit ionic conductivities below expectation.^{116,374,375} This can be easily exemplified via the Walden plot, which is based on the linear relationship between an electrolyte's molar conductivity Λ_m and its viscosity η ,

$$\Lambda_m \propto \frac{1}{\eta}, \quad (8.2)$$

known as the Walden rule.¹³⁴ The implication of this relation is that $\lg(\Lambda_m)$, if plotted against $-\lg(\eta)$, should follow a line of unity slope with increasing temperature. Such a plot is shown in Fig. 8.1, with the diluted aqueous KCl solution as ideal reference. Many ILs fall below the line, which also has led to speculations about the presence of ion pairs.^{116,133,374,375} As discussed above, the presence of such neutral entities would lower the effective number of charged particles available for participation in conduction and thus lower the system's conductivity. Furthermore, the nature and extent of such association

processes may be a relevant factor in the design of new ILs. Hence, understanding the mechanisms at play is of great value.

A very helpful concept in understanding the observed properties of ILs is that of the ionicity scale,¹³⁰ which is based on the comparison of molar conductivity obtained via electrochemical impedance measurements (Λ_{imp}) and the conductivity as calculated from the self-diffusion coefficients of cations (D^+) and anions (D^-), which can be determined by Pulsed-gradient spin-echo NMR. This alternative measure of conductivity, Λ_{NMR} , is calculated as

$$\Lambda_{\text{NMR}} = \frac{N_{\text{A}}e^2}{k_{\text{B}}T}(D^+ + D^-), \quad (8.3)$$

where N_{A} is the Avogadro constant, e is the charge of the electron, k_{B} is the Boltzmann constant, and T is the temperature. Λ_{NMR} is derived from the assumption that all diffusing species in the system detected during the NMR measurements contribute to conductivity, while Λ_{imp} depends on the transport of charged species. It is usually found that $\Lambda_{\text{imp}} < \Lambda_{\text{NMR}}$, which is attributed to the association and coupled motion of cations and anions, forming neutral aggregates like ion pairs. The ratio of these two quantities,

$$I = \Lambda_{\text{imp}}/\Lambda_{\text{NMR}} \quad (8.4)$$

has become known as ionicity I , the effective portion of charge carrying species in the system contributing to conductivity. For a wide range of ILs ionicities below one were found, typically falling in the range of 0.5 to 0.8,¹³⁰ implying that a significant portion of ions are not dissociated.

8.2 Understanding Ion Pairing in Ionic Liquids

The Walden plot has often been interpreted to indicate ion pairing in ILs that fall below the ideal KCl line.¹³³ However, the applicability of the KCl line as ideal reference has been questioned, both in that it is fitted to a single experimental point under the presumption of a unity slope which does not reflect the actual Walden behavior of the aqueous KCl system³⁵³ and in that there is no inherent reason why the proportionality constant of Eq. (8.2) should be the same for an ideal IL as for a diluted electrolyte system like KCl in water.^{353,354} It has been shown¹³³ that adjusting the Walden plot so that the difference in ion size is considered in terms of Stokes radii significantly improves the distinction between “good” and “bad” ILs.^{133,353} Abbott et al.³⁵⁴ criticized the interpretation of deviations from ideal Walden behavior as indication of ion pairing, as the Walden rule was formulated for dilute electrolyte systems and the observed correlation between conductivity and viscosity in ILs may be due to empirical coincidence. They argued that most deviations can be corrected by considering the ion size, disproving ion pairing as explanation.³⁵⁴

8.2.1 Ionic Liquids at Interfaces

In 2013, Gebbie et al. reported direct surface force measurements in $[\text{C}_4\text{C}_1\text{Im}][\text{NTf}_2]$ between charged mica and gold surfaces.¹³² They found a surprisingly large decay length of the attractive force of 11(2) nm, which they treated as effective Debye length κ^{-1} , and fitted their results to a modified Derjaguin–Landau–Verwey–Overbeek model. The Debye length is a measure of a solvent’s screening effect on electric charges and is expected to be small in a system of highly concentrated, dissociated ions, but large in a system of strongly associated and effectively neutral ion pairs. The results were interpreted to mean that ionic liquids behave as dilute electrolyte solutions, in which most ions are associated to ion pairs in an “effectively neutral, coordinated cation-anion network” with only a small fraction of dissociated, freely moving ions.¹³² They challenged the ionicity scale concept with the argument that high concentrations of dissociated ions in the 50 to 80 % range correspond to unreasonably small Debye lengths in the order of 0.1 Å, which is below the radius of a single cation, whereas their measured Debye length of 11(2) nm corresponds to a dissociated ion concentration of 0.003 %. As further evidence, Gebbie et al. calculated the system’s dissociation constant K_d as

$$K_d = \exp \left[\frac{\Delta E_d}{\varepsilon k_B T} \right], \quad (8.5)$$

where ΔE_d is the dissociation energy of a single ion pair obtained from static quantum chemistry, ε the dielectric constant, k_B the Boltzmann constant, and T the temperature. This theoretical approach predicted a dissociation degree in good agreement with that derived from experiment. In contrast, Krossing and coworkers reported an IL $[\text{C}_4\text{C}_1\text{Im}][\text{Al}(\text{hfp})_4]^-$ with an ionicity of 1.03, indicating the total absence of ion pairing in this system.³⁷⁶

The paradigm-changing view of ionic liquids as strongly diluted electrolytes as proposed by Gebbie et al. led to some discussion in literature.^{140,355–357} The applicability of the model used to fit and interpret the experimental data was questioned,³⁵⁶ as it inherently assumes that the system behaves as dilute electrolyte solution. The estimation of the dissociation constant from the quantum chemically derived dissociation energy of a single ion pair in the gas phase considering only a single conformation was criticized as it neglects thermal corrections and solvation effects like charge screening, which cannot be compensated by simple division with the dielectric constant.³⁵⁵ Furthermore, the deduction of bulk properties from surface measurements is nontrivial, as any interface will induce a certain ordering into the liquid.^{284,357} From MD simulations of 1-ethyl-3-methylimidazolium ethyl sulfate ($[\text{C}_2\text{C}_1\text{Im}][\text{C}_2\text{SO}_4]$) and $[\text{C}_2\text{C}_1\text{Im}][\text{NTf}_2]$, it was shown that the degree of ion pairing gradually increases from the bulk phase to the surface.²⁸⁴ Both at liquid-solid and liquid-gas interfaces the solvation of the ions is incomplete and the dynamics may differ

from the bulk phase. It was shown that the chemical behavior of imidazolium-based ILs is highly influenced by the presence of metal surfaces.³⁷⁷ It is thus reasonable to assume that structural shifts at interfaces in ILs hinder the extrapolation from surface properties to the bulk phase.

It has been shown by experiment^{378,379} and theory^{2,284} that ionic liquids evaporate as ion pairs. The vaporization enthalpy $\Delta_{\text{vap}}H$ should thus be connected to the degree of ion pairing in the IL, in that ion pairs in the liquid are already close to their gas phase state and require less energy to transfer to the gas phase. Thus, if ILs had different degrees of ion pairing a correlation between conductivity Λ and vaporization enthalpy $\Delta_{\text{vap}}H$ could be expected. In 2015, we investigated this possible connection for a range of ILs, but found no simple correlation between Λ and $\Delta_{\text{vap}}H$.¹³¹ Contrary to expectation, an opposite trend where $\Delta_{\text{vap}}H$ increases and Λ decreases with increasing side chain length was observed. This was rationalized through other factors such as the increase in molecular weight with longer side chains, leading to an increase in $\Delta_{\text{vap}}H$ while also hindering diffusion and thus lowering the conductivity. Furthermore, simulations show that ions will associate at the liquid-vapor interface and form ion pairs before evaporating to the gas phase.²⁸⁴

8.2.2 Spectroscopy

The picture of ILs as highly diluted electrolyte system seems to be in conflict with a large amount of experimental and theoretical studies that provide no evidence for ion pairing or point to a dissociation degree several orders of magnitude larger than that predicted by Gebbie et al. based on their surface force measurements. For example, a combined Fourier-transform infrared spectroscopy (FTIR) and density functional theory (DFT) study on $[\text{C}_4\text{C}_1\text{Im}][\text{NTf}_2]$ found signals assignable to ion pairs and deduced a concentration of 20 to 30 %, ³⁵⁸ which lies in the same order of magnitude as the $\Lambda_{\text{imp}}/\Lambda_{\text{NMR}}$ -based ionicity.¹³⁰ Weingärtner pointed out¹⁰¹ that the time scale of such measurements is relevant, when interpreting the effect of these ion pairs on liquid properties. FTIR measurements capture processes on the subpicosecond time scale, whereas dielectric spectroscopy³⁶⁰ and NMR spectroscopy^{136,285} work on pico- to nanosecond and micro- to millisecond time scales, respectively, and provide no evidence of long-lived ion pairs in $[\text{C}_4\text{C}_1\text{Im}][\text{NTf}_2]$. In contrast, an investigation of ethylammonium nitrate (EAN) with dielectric spectroscopy measurements by Weingärtner et al. found a concentration of 8 % ion pairs with life times in the order of 10^2 ps,³⁵⁹ whereas later measurements on EAN¹⁴¹ and other aprotic ILs^{142,360} show no evidence of ion pair formation. Two-dimensional infrared spectroscopy (2D-IR) measurements of several 1-ethyl-3-methylimidazolium-based ILs indicate an essentially random ordering of ions with no evidence of long-lived ion pairing.³⁸⁰ These results imply an upper bound to ion pair life times in the low picoseconds range.¹⁰¹

8.2.3 Molecular Dynamics

These findings are in line with theoretical results obtained from molecular dynamics simulations.^{131,137,143–145,361} Liquids and, as such, ILs are dynamic systems and although static quantum chemical calculations can provide helpful insights,³⁸¹ an accurate picture of dynamic processes like ion pairing and diffusion can only be formed from simulations of these liquids long enough to statistically observe the processes under investigation. Zhang and Maginn¹⁴³ performed MD simulations of several ILs and investigated the correlation of transport properties with life times of ion pairs and ion cages, as defined in Ref. 144. Excellent linear correlations between life times and diffusion coefficients as well as conductivities were observed, with ion pair life times ranging mostly from 200 to 1200 ps (with few cases going as high as 1881.6 ps) at a temperature of 350 K and ion cage life times about one order of magnitude smaller than that. Systems that featured long ion pair life times exhibited lower diffusivities and conductivities. It was noted in Ref. 131 that the observed correlations can be rationalized without ion pairing, in that the diffusion coefficients rather than life times are governing all observed quantities. Larger diffusion coefficients imply faster movement and thus higher conductivities, whereas ions diffusing as pairs will lower the conductivity but do not necessarily lower the diffusivity to the same extent,^{131,133} which is also the base assumption of the ionicity scale.¹³⁰ Thus, if ion pairing was indeed present in some of the ILs or affecting some more strongly than others, outliers to the observed linear correlations would be expected.¹³¹ Similarly, in 2009 Zhao et al. studied ion pair life times in $[\text{C}_4\text{C}_1\text{Im}][\text{PF}_6]$ and found that each ion is neighbored by several counterions which form an ionic atmosphere.³⁶¹ However, with the exception of some outliers, ion pairs were found to exist only for few picoseconds before reorientation and no joint diffusion of ions over significant distances could be observed (see also Fig. 8.2). The differences in observed and expected conductivity were attributed to long-time correlated motion of the ions such as electrostatic drag.³⁶¹

A first understanding of the structure in an IL is given by the radial distribution function (RDF), as shown in the upper left panel of Fig. 8.2 for $[\text{C}_4\text{C}_1\text{Im}][\text{OTf}]$. In this plot, $g(r)$ represents the likelihood of finding an anion at distance r to a cation, where the distance is measured between the center of the imidazolium ring and the center of mass on the anion. The first maximum, which describes the most likely interaction distance of anion and cation, lies at 520 pm. The first minimum is found at 780 pm and can be interpreted as the radius of the first counterion solvation shell. From the integral at this distance it is clear that the first solvation shell consists of five to six counterions. There is more than one distinct neighbor and thus ion pairing is not indicated in the MD simulations. This was also confirmed by several experiments.³⁸² As the ion diffuses, the counterions that form this solvation shell may change. The upper right panel of Fig. 8.2 shows a combined distribution function plot in which the displacement of the ion pair is plotted

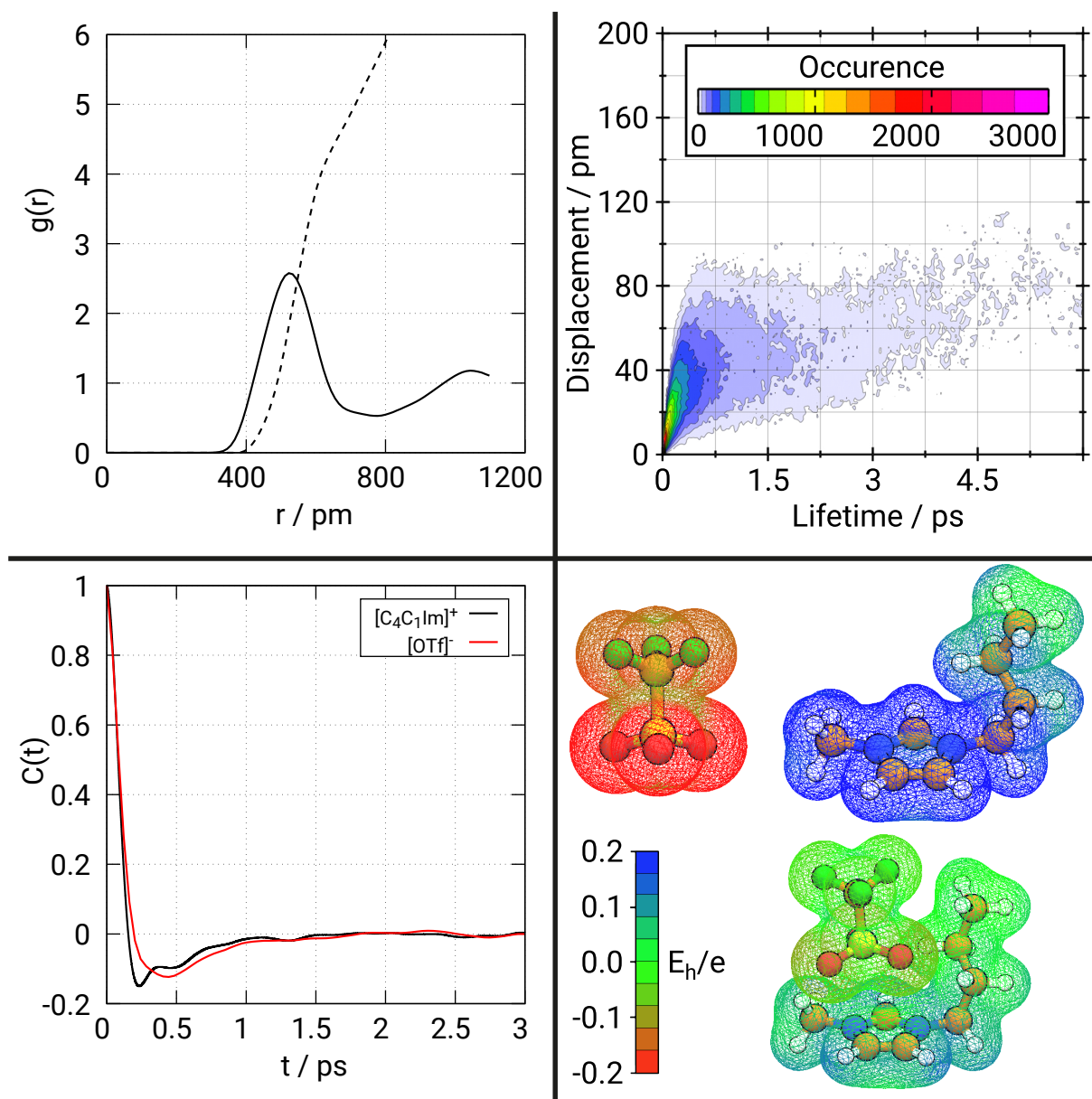


Figure 8.2: Analysis of $[\text{C}_4\text{C}_1\text{Im}][\text{OTf}]$ by different functions calculated from ab initio molecular dynamics (AIMD) and static density functional theory (DFT) calculations. For computational details, please see Appendix A and B of Ref. 131. *Upper left:* radial distribution function $g(r)$ (solid) of the cation-anion distance and its integral (dashed). *Upper right:* Combined distribution function of ion pair displacements vs their respective life times. *Bottom left:* Velocity autocorrelation functions of cation and anion. *Bottom right:* Electrostatic potential of the separated ions (top) and the ion pair (bottom) calculated on the B3LYP/def2-TZVP level of theory.

against the life time, measured from ab initio molecular dynamics (AIMD) simulations of $[\text{C}_4\text{C}_1\text{Im}][\text{OTf}]$ (for computational details, we refer to Appendix B of Ref. 131). Based on the RDF plot, we defined a distance of 780 pm as maximum interaction length of the ion pair. A given cation is treated as associated to the closest anion within this radius. If another anion comes closer, the original ion pair is considered broken and a new ion pair is formed. The graph shows that the displacement of ion pairs in the system does not exceed 200 pm, which is less than the shortest cation-anion interaction distance as shown

in the RDF plot. With the exception of some ion pairs that exceed a life time of 6 ps, most ion pairs exist only shortly with life times below 2 ps before reorientation. In 2015 we reported similar results from AIMD simulations of several ILs.¹³¹ Again, life times were found to be mostly limited to a few picoseconds and joint diffusion did not exceed distances of 300 pm. Interestingly, under the investigated ILs the shortest life times were found for the protic IL ethylammonium nitrate which also has the highest conductivity¹³¹ and a near ideal Walden behavior (see Fig. 8.1). This was interpreted as indication that protic ILs, which often show higher conductivities than aprotic ILs,³⁸³ have even less pronounced ion association,¹³¹ despite their extended hydrogen bond networks.^{308,384} Another way to study ion pairing in ILs by MD simulations is given by the velocity autocorrelation function (VACF).³⁸⁵ If a particle at time $t=0$ has a certain velocity, then the VACF $C(t)$ presents the likelihood that the particle has the same velocity at time t . As the velocity of a particle changes, $C(t)$ will decay and turn negative if the particle collides with another resulting in a reversed velocity. This behavior is known as cage or back scattering effect and is observed in dense liquids such as molten salts.³⁸⁶ An example of such a VACF plot, calculated from an AIMD simulation of $[\text{C}_4\text{C}_1\text{Im}][\text{OTf}]$, is shown in the bottom left panel of Fig. 8.2. The collision times, which can be approximated as the time at which $C(t) = 1/e$, are closely together at 0.10 ps and 0.11 ps for the cation and anion, respectively. The first negative minima lie at 0.23 ps and 0.42 ps for cation and anion, respectively, indicating differences in their respective motions. These results are in well agreement with earlier works by us¹³¹ and Del Pópolo and Voth,³⁸⁷ in both of which collision times in the range of 0.05 to 0.20 ps were found for a variety of ILs. These collision times seem too short to support the notion of long-lived ion pairs.

8.2.4 Charge Transfer

The main reason why ion pairing is inferred is that the observed conductivity falls short of the expected conductivity, which is interpreted as lack of freely available charge carriers. However, the measured conductivity depends not only on the number of charged particles but also on the charge itself. These are often treated as ± 1 , but it is known from experiment¹³⁸ and theory^{131,137,139} that charge transfer effects between anion and cation lead to decreased charges significantly below unity. Charge transfer (or more specifically, partial charge transfer) occurs when electrons are partly transferred from one molecule to another via a weak covalent bond,³⁸⁸ like a hydrogen bond. To illustrate this effect, the electrostatic potential of the separated ions and the associated ion pair of $[\text{C}_4\text{C}_1\text{Im}][\text{OTf}]$ is displayed in the bottom right panel of Fig. 8.2. The negative charge of the isolated triflate anion is distributed over the whole structure but strongest around the oxygen atoms. The positive charge of the isolated cation is distributed over the whole imidazolium ring, but decreases in the alkyl chain with each additional carbon atom. The ion pair sees a

significant decrease in the net charge of both ions and a stronger localization of the charge to the imidazolium ring and oxygen atoms. Following the ion association, the alkyl chain and CF_3 group are effectively neutral. Employing the CHELPG method,³⁶² we carried out a charge analysis and find that the net charge of both ions decreases from ± 1 to ± 0.83 following their association, which is in good agreement with earlier results.¹³⁷ In a combined classical MD and static DFT study we were able to demonstrate the importance of charge transfer in the ionicity scale.¹³⁷ By calculating the effective ion charges from quantum chemical optimizations of ion pairs of several ILs with ionicities in the range of 0.5 to 0.8 we found significant charge transfer for all systems, with ion charges ranging from 0.7 to 0.9. Reevaluating the ionicities with respect to the calculated charges leads to values remarkably closer to the ideal value of 1, offering an alternative explanation for the observed discrepancies between Λ_{imp} and Λ_{NMR} . Through subsequent MD simulations it was demonstrated that charge transfer suppresses the association of oppositely charged ions and thus ion pairing.¹³⁷ In a recent work by Philippi et al.³⁸⁹ the idea that the ionicity scale can be interpreted as measure of charge transfer rather than ion pairing was further developed. The authors developed a quantum chemistry based method that can predict charge transfer from static DFT calculations of the isolated ions. A wide variety of cations and anions were investigated and similar to our work,¹³⁷ a good agreement between theoretical charge transfer and the experimental ionicity was found.

8.2.5 Protic Ionic Liquids

In the special case of protic ILs (PILs)¹¹⁰ the description of ionicity gets even more complex, as in addition to ion pairing also proton transfer processes play a role. In general, a PIL is formed by a proton transfer between a Brønsted acid and a Brønsted base:



Compared to aprotic ILs, PILs often have higher conductivities³⁸³ and are easier and cheaper to synthesize. A property shared between all PILs is the acidic proton bound to the cation. The availability of this proton is a deciding factor for their application as proton conductors in fuel cells.³⁹⁰ However, a high proton activity may lead to a chemical charge transfer via the reverse proton transfer, resulting in the presence of neutral acid and base molecules which have a similar effect on the IL as ion pairs, in that they reduce the effective amount of charge carriers. The connection between proton activity and ion pairing lies in the formation of hydrogen bonds between anions and cations. Extensive hydrogen bond networks have been found and investigated in several PILs.^{308,384} It may seem straightforward that strong hydrogen bonds between anion and cation promote ion pairing and thus reduce ionicity. This behavior was found for several ethylammonium-based PILs, with increasing hydrogen bond strength correlating with decreasing conduc-

tivity.³⁸⁴ However, hydrogen bonds in EAN were found to be significantly stronger than in ethylammonium formate (EAFm),³⁸⁴ but nonetheless EAN shows higher conductivity and ionicity. It was also found that hydrogen bond networks can in fact reduce viscosity and increase ion mobilities and thereby increase conductivity.^{308,391,392} It is thus of interest to study the proton activity in PILs and its effect on ionicity and other properties.^{2,3}

Some efforts were made to quantify the proton activity,^{105,122} including the introduction of $pK_s = -\lg([HA] \cdot [B])$ by Kanzaki et al.,¹²² where K_s is the self-dissociation constant, corresponding to the reverse proton transfer (see Eq. (8.6)). This constant was measured for several PILs using ion-selective field effect transistor electrodes.^{122,124} These included EAN for which a pK_s value of 9.83 was found, corresponding to a bulk concentration of neutral acid and base molecules of 1.2×10^{-5} mol/l.¹²²

These results could later be reproduced from theory by us using the binary quantum cluster equilibrium (bQCE) theory,^{5,38,43,50} a cluster-based method that combines quantum chemistry and statistical thermodynamics.² The bQCE approach is based on the idea that liquids can be described as an equilibrium distribution of quantum chemically accessible clusters built up from monomer species generating an ensemble via population of clusters. We could confirm from theory that EAN and other alkylammonium-based PILs evaporate as associated and effectively neutral ion or molecule pairs at room temperature, but as unassociated acid and base molecules at their boiling point. We note that proton transfer also plays a role in imidazolium-based PILs if the anion can act as proton acceptor, leading to the formation of neutral carbene and acid molecules.³⁹³ This special case of charge transfer was also studied by static quantum chemistry.³⁹³

Furthermore, by introducing clusters that next to a number of ion pairs also include a single acid or base molecule, we could calculate concentrations of neutral species from cluster populations. With $pK_s^{\text{QCE}} = 11.57$ for EAN, the experimental result could be reproduced within an accuracy of 2 log units. Additionally, the self-dissociation constant of EAFm was predicted to be $pK_s^{\text{QCE}} = 5.66$, corresponding to a significant concentration of neutral species of 1.5×10^{-3} mol/l, again proving the connection between high proton activity and below-ideal Walden behavior. These results further establish that additional effects other than ion pairing have to be considered to explain the observed properties.

8.2.6 Grothuss Diffusion

Earlier in this chapter, we have discussed criticisms of both the Walden plot and the ionicity scale. Despite these criticisms, the empirical correlation of Walden behavior, ionicity, and properties such as vapor pressure seems obvious. An exception to this qualitative rule was found by Kanzaki et al.^{115,124} in the equimolar mixture of methylimidazole and acetic acid, which, despite consisting mostly of neutral acid and base molecules and accordingly being labeled a “pseudo ionic liquid”, was found to be highly proton conductive. Despite

its low ionicity due to incomplete proton transfer, the Walden plot indicated “superionic” behavior in the system, which could only be rationalized by assuming a structural conduction mechanism, namely Grotthuss diffusion.¹¹⁵ Grotthuss diffusion describes the transport of charges via structural rearrangement of covalent bonds rather than through diffusion of a charge carrier. The Grotthuss mechanism is much faster than the alternative vehicle mechanism and thus leads to higher conductivities. The proposal of Kanzaki et al. was later confirmed by AIMD simulations, in which a Grotthuss-like hopping of the proton between all neutral and ionic species in the system could be directly observed.³ The mechanism involved chains of acetic acid molecules, which are terminated by a methylimidazolium cation acting as proton donor and a methylimidazole molecule acting as acceptor. After accepting the proton the newly formed cation can start a new chain. These findings support the picture of a dynamic hydrogen bond network in the system, as found in many PILs,^{308,384} but seem to oppose extensive ion pairing, which would hinder the forming of proton conducting chains. Grotthuss diffusion was observed in a range of ILs,^{314,316,394,395} including the structural diffusion of AlCl_3 in $[\text{C}_2\text{C}_1\text{Im}][\text{Cl}]\cdot 1.3\text{AlCl}_3$,³¹⁶ the transport of iodide in $[\text{C}_2\text{C}_1\text{Im}][\text{I}_3]$,³¹⁴ and anion conduction in 1,3-dialkylimidazolium chloride-based ILs.^{394,395} McDaniel and Yethiraj report from AIMD simulations that Grotthuss like conduction of iodide occurs in $[\text{C}_2\text{C}_1\text{Im}][\text{I}_3]$ via the formation of a dianion I_4^{2-} .³¹⁴ This seems electrostatically prohibited, but the authors find that the dianion is stabilized through the ionic environment, which is in conflict with the view of ionic liquids as dilute electrolytes with little charge screening. A dynamic association and dissociation of chloride and phosphorous chloride PCl_3 into PCl_4^- was observed in mixtures of the latter with 1-alkyl-3-methylimidazolium chlorides.^{394,395} In general, although these findings offer no quantitative insight to ionicity or ion pairing, the dynamic nature of Grotthuss diffusion mechanisms in ILs seems to be at odds with the notion of extensive, long-lived ion pairs.

8.2.7 Ionic Liquids in Mixtures

For now, our discussion was limited to pure IL systems. Ion pairing has also been studied in mixtures of ILs and molecular solvents.^{396,397} The formation of ion pairs in mixtures of triethylammonium iodide with solvents of different polarities was studied via FTIR measurements.³⁹⁶ As is known for other electrolytes, apolar solvents favor the formation of contact ion pairs while polar solvents shift the equilibrium toward solvent-separated ion pairs. Similar results could be obtained from DFT calculations on triethylammonium-based PILs solvated in different solvent media.³⁹⁷ The authors investigated the number of solvent molecules required to break a contact ion pair. This number was dependent both on the anion and the solvent polarity. Welton and coworkers investigated the kinetics of an $\text{S}_{\text{N}}2$ reaction and found it followed a different mechanism as compared to molecular liquids, which does not involve the intermediate formation of a contact ion pair.³⁶⁸ Later, they

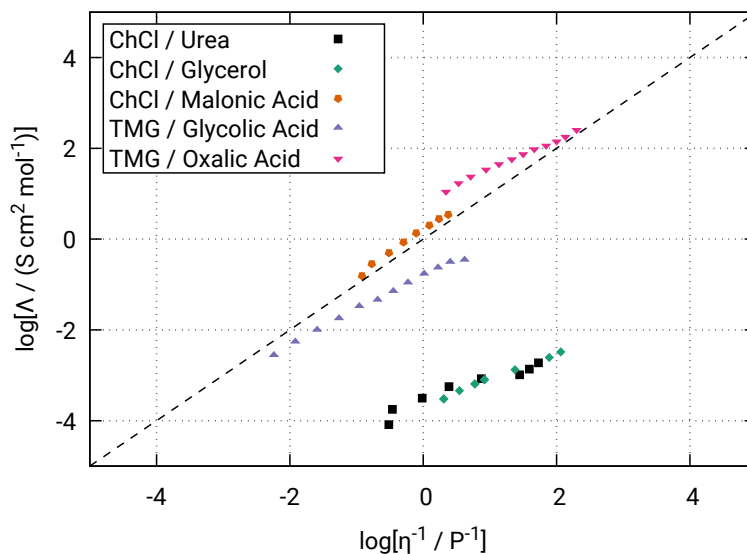


Figure 8.3: Walden plot of several DESs produced from data taken from Ref. 398 (ChCl mixed with urea/glycerol), Ref. 399 (ChCl mixed with malonic acid), and Ref. 400 (trimethylglycine mixed with glycolic/oxalic acid).

found that Kosower’s salt in different ILs shows no preferential ion pairing, contrasting its behavior in molecular liquids.³⁶⁷ Although not strictly referring to ion pairing in neat ILs, these results were interpreted to challenge the idea of ion pairing in ILs.^{31,137}

Another multi-component liquid comprises the deep eutectic solvent (DES) class.^{370–372} In the words of Martins et al. a DES is a eutectic mixture with a eutectic point temperature that is lower than that of an ideal mixture.⁴⁰¹ They are often formed by mixing a salt with a molecular compound, which is usually a hydrogen bond donor, to obtain a low-melting mixture near the eutectic composition. With properties similar to those of ILs, such as their high ionic conductivity and non-flammability, they are often compared with or treated as less toxic alternative to ionic liquids.^{402,403} In comparison to ILs, little research was directed at the ion pairing in DESs, the focus being more on the inter-component interactions and hydrogen bonding rather than inter-ionic interactions. But even in liquids that are not solely composed of ions the association between counterionic or ionic and non-ionic species may be so strong that they form aggregates, reducing the ion mobility and thus lowering the conductivity. Similar to ILs, the Walden plot was used to characterize DESs.^{398–400,402,403} Similar to Fig. 8.1, the Fig. 8.3 shows the Walden plot for a selection of DES systems. The popular mixture of choline chloride (ChCl) with urea⁴⁰³ is found well below the KCl reference line, indicative of low ionicity due to ionic association. This is not a general behavior for DESs though, as some other examples in Fig. 8.3 show. We note that the some of the criticisms directed at the Walden plot as measure of ionicity of ILs still apply in the case of DESs. Cardellini et al. found that DESs formed by mixing zwitterionic sulfobetaines with (1*S*)-(+)-10-camphorsulfonic acid may be classified as “good ionic liquids” according to the Walden plot.⁴⁰⁴ They

note that in contrast to protic ionic liquids which usually are found in the “bad ionic liquid” range unless they have a particularly high ΔpK_a , their novel DES systems show good ionic behavior despite the components’ similar pK_a s. Testing the conductivities for a series of salt/glycerol mixtures at different compositions, Abbott et al. found that the ChCl/glycerol mixture shows a minimum at a salt concentration of 0.25 M, which they attributed to ion pair formation.⁴⁰⁵ Increasing the salt concentration further, the conductivity rises again due to triple ion formation until it reaches a maximum at 4 M, after which the reduced ion mobility causes it to decrease again.⁴⁰⁵ Radial distribution functions of the ionic $\text{Li}^+ - \text{ClO}_4^-$ distance measured as part of a molecular dynamics study on the liquid structure of LiClO_4 /alkylamide DESs done by Kaur et al. show evidence of strong ion pairing between Li^+ and ClO_4^- .⁴⁰⁶ However, no life times of these ion pairs are available.

Figure 8.3 shows that a wide variety of behaviors may be found in different DESs and that examples of DESs with “good” ionic behavior are readily available. DESs are versatile systems with differing ionic concentrations, including both mostly ionic and mostly molecular mixtures, and the same methods of characterizing ionicity and ion pairing in ILs may not be applicable.

8.3 Conclusion

The concept of ion pairing in ILs is still a controversial one and the structural behavior of ILs at microscopic scales still under debate. The experimental evidence is not conclusive. While many experimental studies support the notion of ion pairing, just as many seem to disagree with the idea of long-lived ion pairs. Even among those experiments that do point toward ion pairing, the results from different experimental methods are not consistent with each other, with predictions of the ion pair concentration in the same IL sometimes differing by several orders of magnitude. Furthermore, the interpretation of these experimental results is often based on assumptions. These include, for example, the assumption of unity charges, which was shown to be inaccurate.^{131,137} Considering the reduced ion charges due to charge transfer can resolve the ionicities of some ILs. Theoretical results from MD simulations do not support ion pairing. Instead, in agreement with some spectroscopic experiments,^{141,142,360} the life times of ion pairs lie in the low picosecond range and their joint movement does not exceed a meaningful distance.¹³¹ Nonetheless, we do think that ion pairing is an important concept in that it can help with the targeted design of ILs, although at the current time this is based more on empirical knowledge rather than a theoretical understanding of the microscopic processes at hand. Further insights are required to build a conclusive model of ion pairing in ILs.

Acknowledgments

The authors would like to thank the DFG (SPP 1708 KI 768/15-1 and KI 768/19-1) under the projects and the BMBF under the LuCaMag project 03EK3051A.

9 Influence of Complexing Additives on the Reversible Deposition/Disso- lution of Magnesium in an Ionic Liquid

Isabella Weber,^{*†‡} Johannes Ingenmey,[§] J. Schnaidt,^{*†‡} Barbara Kirchner,[§] and R. Jürgen Behm^{*†}

Received: November 22, 2020, Published: January 26, 2021

Reprinted (adapted) with permission from

I. Weber, J. Ingenmey, J. Schnaidt, B. Kirchner, and R. J. Behm, *ChemElectroChem*, 2021, **8**, 390–402.

Copyright © 2021 Wiley-VCH

DOI: 10.1002/celec.202001488

Contributions to the manuscript

- Extracting the clusters from MD simulations
- Performing the quantum chemical calculations
- Analyzing and discussing the results
- Providing the figures for the computational part
- Writing the computational part of the manuscript

^{*}Institute of Surface Chemistry and Catalysis, Ulm University, Albert-Einstein-Allee 47, 89081 Ulm, Germany

[†]Helmholtz Institute Ulm (HIU) Electrochemical Energy Storage, Helmholtzstraße 11, 89081 Ulm, Germany

[‡]Karlsruhe Institute of Technology (KIT), P.O. Box 3640, 76021 Karlsruhe, Germany

[§]Mulliken Center for Theoretical Chemistry, Institut für Physikalische und Theoretische Chemie, Rheinische Friedrich-Wilhelms-Universität Bonn, Beringstraße 4+6, 53115 Bonn, Germany

Abstract Aiming at a fundamental understanding of the synergistic effects of different additives on the electrochemical Mg deposition/dissolution in an ionic liquid, we have systematically investigated these processes in a combined electrochemical and theoretical study, using 1-butyl-1-methylpyrrolidinium bis(trifluoromethylsulfonyl)imide (BMP-TFSI) as the solvent and a cyclic ether (18-crown-6) and magnesium borohydride as additives. Both crown ether and BH_4^- improve Mg deposition, its reversibility, and cycling stability. The combined presence of both additives and their concentration relative to that of Mg^{2+} are decisive for more facile and reversible Mg deposition/dissolution. These results and those of quantum chemical calculations indicate that 18-crown-6 can partly displace TFSI⁻ from its direct coordination to Mg^{2+} . Furthermore, the interaction between Mg^{2+} and directly coordinated TFSI⁻ is weakened by coordination with 18-crown-6, preventing its Mg^+ -induced decomposition. Finally, Mg deposition is improved by the weaker overall coordination upon Mg^{2+} reduction to Mg^+ .

9.1 Introduction

Despite of the advantages of rechargeable Mg batteries in comparison to conventional lithium-ion batteries (LIBs), such as their generally higher energy density, the possibility of using elemental Mg anodes, the global availability and non-toxicity of Mg, and their recyclability and low costs,^{159,407–413} their technical verification and commercial introduction is still far away. This is mainly due to problems in the reversible deposition and dissolution of Mg, which are – at least in part – related to complications arising from reductive electrolyte decomposition at the anode|electrolyte interface. In contrast to LIBs, where Li^+ transport is possible through the so-called solid electrolyte interphase (SEI) formed at the anode during charge/discharge, these layers often inhibit the Mg deposition/dissolution process.^{408,409,414} Only recently, studies reported on a functional SEI formed upon Mg deposition, e.g., from $\text{Mg}(\text{BH}_4)_2/\text{LiBH}_4$ -containing monoglyme,⁴¹⁵ in Mg/S systems,⁴¹⁶ or on Sn-modified anodes.⁴¹⁷ In general, most investigations so far have focused on salt/solvent combinations that allow reversible Mg deposition/ dissolution without the formation of a protective surface layer. Among those, a limited number of electrolytes consisting of commercially available magnesium salts such as $\text{Mg}(\text{BH}_4)_2$ ^{160–163,418–421} or $\text{Mg}((\text{CF}_3\text{SO}_2)_2\text{N})_2$ (Mg bis(trifluoromethylsulfonyl)imide, MgTFSI_2)^{421–428} have been found to support largely reversible Mg plating and stripping without negative impact on the cell components (such as corrosion, which poses a problem in Cl-containing electrolytes).⁴¹⁰ However, even for these electrolytes, the oxidative instability of the borohydride,⁴¹¹ as well as the Mg^{2+} -^{160,429} and moisture-induced^{162,426,430,431} decomposition of TFSI⁻, severely limit their application. Hence, the development of suitable electrolytes allowing for reversible Mg plating/stripping is still of utmost importance for the introduction of rechargeable Mg-based batteries.^{409,432–437}

Ionic liquids (ILs) are a promising alternative to electrolytes based on organic solvents due to their generally low flammability, high electrochemical stability, and low vapor pressure.^{162,438,439} Specifically, TFSI⁻-based ILs have attracted interest due to their relatively high conductivity, their commercial availability, and the simplicity of the system when adding MgTFSI₂ as Mg salt. This approach, however, has turned out to be little successful so far, as the reductive decomposition of TFSI⁻, which is promoted by the interaction with the Mg²⁺ species,^{164,165,440,441} leads to the formation of passivating films (in particular on Mg metal electrodes⁴³³). The successful use of IL-based electrolytes thus requires either ionic liquids that are stable in the entire potential range also upon interaction with Mg²⁺, or the development of additives that could lower any detrimental interaction between Mg²⁺ and the IL – while still allowing reversible Mg deposition/dissolution.

This is the topic of the present paper, where we report results of a combined experimental and theoretical study on the effect of two different additives, the crown ether 18-crown-6 and borohydride (BH₄⁻), on the deposition/dissolution of Mg from the IL 1-butyl-1-methylpyrrolidinium bis(trifluoromethylsulfonyl)imide (BMP-TFSI) using MgTFSI₂ and, where present, Mg(BH₄)₂ as Mg²⁺ source. Glassy carbon (GC) and, for comparison with realistic battery systems, Mg, were used as working electrodes. In this work, we are especially interested in a basic mechanistic understanding of the interplay between Mg²⁺, the anion TFSI⁻ and the additives Mg(BH₄)₂ and 18-crown-6, and particularly in synergistic effects. A semi-quantitative understanding shall be derived by systematically varying the composition of the electrolyte, both in experiment and in simulations. Here, it is important that stabilization of the electrolyte does not inhibit Mg deposition. Furthermore, the role of the electrode shall be elucidated by comparing results obtained for the rather inert GC model electrodes and the more reactive, realistic Mg electrodes.

While there is a considerable number of studies investigating the Mg–TFSI interaction in organic solvents such as DME, THF or polyethers/glymes,^{160,161,166,167,429,431,442–445} the number of studies performed in electrolytes using a TFSI⁻-containing IL as main component is much less, and such kind of insights as aimed at in the present study have not been reported so far.^{162–164,440,441} Finally, the idea of adding a complexing additive was followed also in a study by Watkins et al., who prepared chelating ILs by adding a polyether chain to the cation.¹⁶³ Compared to that approach, ours seems to be experimentally simpler and more feasible. On the other hand, combining chelating solvents such as glymes with an IL-based Mg source such as MgTFSI₂ (see above) may lose the advantages of a mainly IL-based electrolyte.

The crown ether is a typical complexing agent⁴⁴⁶ and has previously been employed to, e.g., enhance Mg plating/stripping in an ionic liquid.^{164,165} Mg(BH₄)₂ has been repeatedly used as water scavenger in IL-containing electrolytes.^{161–163,166,167,431,447} It was reported to prevent the formation of a passivating surface layer in TFSI⁻-based electrolytes⁴⁴⁸ and also serves as Mg source.⁴⁴⁹ Furthermore, BH₄⁻ has been proposed to act

as Mg^{2+} -complexing agent^{162,420} and/or interact with the anode surface; either by adsorption (similar to chloride-containing electrolytes⁴⁴⁹) or by dissolving passivation layers either during formation or pre-existing ones (native passivation layers) due to its highly reductive character.

In the following, we will first present cyclic voltammetry data on the Mg deposition/dissolution behavior on glassy carbon from a BMP-TFSI-based electrolyte containing either $\text{Mg}(\text{BH}_4)_2$ or a combination of $\text{Mg}(\text{BH}_4)_2$ and crown ether. Next, we show results of similar experiments using electrolytes containing also MgTFSI_2 , where, for a better understanding of possible synergistic effects, the concentrations of the different components were varied systematically. For comparison, we also show data obtained for Mg deposition/dissolution from similar electrolytes on a Mg electrode. Subsequently, we present results of a DFT-based quantum chemical analysis of the stability of clusters derived from classical molecular dynamics (MD) simulations, which contain Mg^{2+} in different coordination states and up to two BMP-TFSI ion pairs with or without 18-crown-6 as additional ligand. Finally, we discuss the implications of both the experimental and theoretical data and summarize the main conclusions derived from these data.

9.2 Results and Discussion

9.2.1 Electrochemical Characterization

In previous experiments, we had already shown that deposition and dissolution of Mg on a GC electrode is essentially inhibited in MgTFSI_2 -containing BMP-TFSI electrolyte.⁴⁴¹ This was reproduced also in the present experiments, though some improvement is achieved for $\text{Mg}(\text{BH}_4)_2$ -containing BMP-TFSI electrolytes. The first and later cycles of the cyclic voltammograms (CVs) recorded at 10 mV/s on the GC substrate, without any additional additives, largely resemble previous findings.¹⁶³ They are displayed and discussed in detail with Figs. F.1a and F.1b. In brief, the negative current increases towards the lower potential limit. A small anodic peak appears at around 1 V in the anodic scan. Within the first few cycles, both peaks decrease significantly. The overall reversibility of the cathodic and anodic processes, as indicated by the overall charge ratio in these potential regimes (Coulombic efficiency), is about 18% in the first cycle (inset in Fig. F.1a) and increases to around 35% in subsequent cycles (see Fig. F.4). Overall, however, the reversibility is very low and Mg deposition/dissolution is (at most) a minor process.

In the following, we will briefly summarize the different effects and influences of borohydride on the Mg deposition/dissolution process that have been reported in the past. First, the addition of reductive, contamination-scavenging additives such as dibutyl Mg (in our case: $\text{Mg}(\text{BH}_4)_2$), which can react with traces of water, oxygen and other protic species, was found to improve the Mg plating/stripping efficiency by forming Mg oxides

and hydroxides in the bulk, which, in return, reduces/avoids surface passivation.^{431,448} Second, reversible Mg plating/stripping was found to require a minimum amount of such additives, which approximately corresponded to a slight excess relative to the estimated water content of the electrolyte.⁴³¹ Third, reversible Mg plating/stripping was possible also from MgTFSI₂-containing solutions when using complexing solvents such as glymes upon addition of Mg(BH₄)₂⁴³¹ or once the electrolyte was carefully dried.⁴²⁶ Finally, high deposition reversibilities were obtained even without additional drying when using Mg(BH₄)₂ as Mg source rather than MgTFSI₂.⁴¹⁹

Overall, these studies support the idea that borohydride acts as efficient water scavenger.^{419,431} As stated above, our results of a very low reversibility for Mg plating/stripping fully agree with previous findings for cycling a Pt electrode in a similar electrolyte.^{160,163} They seem to disagree, however, with the previous findings summarized above, considering that, in our experiments, the amount of Mg(BH₄)₂ added to the electrolytes should always be sufficient to fully remove the water impurities of BMP-TFSI, MgTFSI₂ and crown ether, based both on our estimations and on the suppliers' specifications (see Experimental part) and assuming that each BH⁻ can react with one water molecule. The discrepancy is most likely caused by the different solvents, with only small amounts of TFSI⁻ in the above cases, together with complexing solvents, while in our case the TFSI⁻ is part of the solvent and thus present in large excess and no other complexing species are present.

Electrolyte decomposition in Mg(BH₄)₂-containing BMP-TFSI was explained by the decomposition of TFSI⁻, which is coordinated with the metal ions in such IL mixtures. This kind of complex formation, where TFSI⁻ anions can coordinate to a single metal cation (contact ion pairs, CIPs) or to multiple metal cations in aggregate networks (where the Mg²⁺ cation is in direct contact with the TFSI⁻ anion), has been identified previously by both infrared¹⁶² and Raman spectroscopy.^{160,163,450,451} Theoretical studies have shown that partial reduction of the Mg center, which is expected to happen at the interface at potentials in the Mg deposition regime, leads to a weakening of the C–S bond in the TFSI⁻ anion, which in turn results in TFSI⁻ decomposition rather than in Mg deposition.^{160,429} In contrast, BH⁻ was found to be stable under these conditions. In electrolytes containing both borohydride and TFSI⁻, TFSI⁻ decomposition has been observed in experimental studies.^{160,163,166,442,448,452}

Next, we investigated the influence of 18-crown-6 upon cycling in Mg(BH₄)₂-containing BMP-TFSI. CVs recorded in BMP-TFSI + 0.1 M Mg(BH₄)₂ + 0.1 M 18-crown-6 electrolyte are depicted in Fig. 9.1. The additive leads to increased currents, both in the cathodic and in the anodic scan, as compared to the borohydride-containing IL in the absence of the crown ether (Fig. F.1). The cathodic current densities are at least four times higher and the increase of the anodic currents is even more drastic. These changes may originate from reversible processes, such as Mg plating and stripping, although the

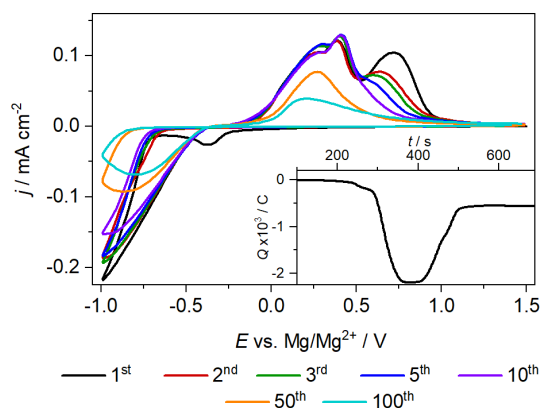


Figure 9.1: First and additional relevant potentiodynamic cycles recorded on a GC electrode in BMP-TFSI + 0.1 M $\text{Mg}(\text{BH}_4)_2$ + 0.1 M 18-crown-6 cycled at 10 mV/s. The inset shows the accumulated charge (i.e., the charge balance of Mg plating/stripping) during the first scan.

present data do not provide definite proof for the latter assignment. A weak peak is observed at -0.4 V in the first cathodic scan, which does not appear anymore in the subsequent cycles. Interestingly, in a crown ether-free, borohydride-containing IL, a similar signal appeared at -0.3 V in the first cathodic cycle (Fig. F.1a). We tentatively assign these peaks to the reductive removal of a surface contamination on the GC substrate, considering that this peak was only observed on the GC electrode, independent of the electrolyte composition. At potentials below -0.7 V, the characteristic current increase for Mg deposition appears. Here, Mg plating takes place with a nucleation overpotential that is by 0.1 V lower than the one observed for 0.1 M $\text{Mg}(\text{BH}_4)_2$ -containing IL without any crown ether additive (see discussion with Fig. F.1). In the subsequent anodic scan, we find the corresponding signal for Mg dissolution at 0.3 V, down-shifted by 0.4 V from the Mg dissolution peak observed in crown ether-free IL. This is followed by two additional peaks at 0.4 V and 0.7 V, which seem to indicate that, next to Mg stripping, oxidation of species formed in cathodic side processes can take place under these conditions.

It is worth noting that the position of the peak at 0.7 V observed in the crown ether-containing system coincides with the position of the anodic peak recorded in the first cycles of the crown ether-free system (Fig. F.1). Therefore, it is also possible that the anodic signal at 0.7 V is due to Mg dissolution from a similar Mg species – as obtained for deposition from $\text{Mg}(\text{BH}_4)_2$ -containing electrolyte – while the peaks at 0.3 V/0.4 V are due to dissolution of Mg deposits created in crown ether-containing electrolyte.

In the following cathodic scan, the process taking place at -0.4 V is inhibited, like the analogous process in the ether-free system. The decreasing currents in the Mg deposition region and, subsequently, in the Mg dissolution region (anodic scan), also indicate an increasing inhibition of the related processes and/or the depletion of oxidizable components with increasing cycling. This current loss is most pronounced for the high-potential peak

at 0.7 V. During the next ten cycles, it decreases and disappears completely, while the anodic signals at 0.3 V and 0.4 V do not change significantly. The peak at 0.4 V starts to decrease only after ten cycles and has disappeared after about 35 cycles (not shown). The signal at 0.3 V also decreases, but much slower, becoming the main anodic peak. It is still visible even after 100 cycles. The reversibility is about 70 % in the first cycle (for comparison, the reversibility of the processes taking place in solely borohydride-containing IL was ~ 18 % in the first cycle) and increases to 78 % within the first ten cycles, as compared to 35% reached in ether-free electrolyte after the same number of cycles. Upon further cycling, however, the reversibility in the $\text{Mg}(\text{BH}_4)_2$ - and 18-crown-6-containing IL decreases, as well, dropping to 25 % after 20 cycles. This remains about constant for the rest of the cycling time (100 cycles in total), indicating that the continuing passivation process not only reduces the current densities both in the cathodic and anodic scan but also affects them in the same way, keeping the charge ratio between them constant (see Fig. F.5).

The results in Fig. 9.1 can be compared with previous data and conclusions, which had already identified positive effects on the reversibility of the Mg plating/stripping process when modifying the IL cation^{160,161,163} or varying the solvents and/or adding complexing additives.^{161,165,420,453,454} Our results are in agreement with reports on an improved Mg deposition/dissolution reversibility in the presence of ethers such as glymes, etc.^{431,444,454,455} As one example, Mandai et al. reported an improved Mg deposition/dissolution activity for tetraglyme-coordinated MgTFSI_2 in BMP-TFSI in the presence of dialkylsulfones as compared to electrolytes with less efficiently coordinating additives, such as DMSO.⁴⁴⁴ Increased current densities for Mg deposition in MgTFSI_2 -containing electrolytes were reported also by Sagane et al. upon addition of 18-crown-6 ether, both in THF⁴⁵⁴ and in *N*-methyl-*N*-propylpiperidinium (MPPp)-TFSI.¹⁶⁵ Similarly, Ma et al. have shown reversible and stable (for more than 280 cycles) Mg plating and stripping from 0.3 M MgTFSI_2 -containing BMP-TFSI/tetraglyme mixtures (1:2) after treatment with 0.019 M $\text{Mg}(\text{BH}_4)_2$.¹⁶¹

Employing ex situ scanning electron microscopy (SEM) characterization, Sagane et al. also observed the formation of Mg dendrites in the Mg deposits formed from 0.5 M crown ether- and 0.5 M MgTFSI_2 -containing THF, which could hardly be dissolved subsequently.⁴⁵⁴ Going to much higher concentrations of both ether additive and TFSI^- salt in an IL electrolyte (MgTFSI_2 , 18-crown-6 and MPPp-TFSI, with molar ratios of 1:1:5 and 1:5:5), the Mg deposits were significantly smoother than the dendritic morphologies obtained in THF-based electrolyte, but still exhibited a ‘mossy’ structure, which the authors attributed to the high viscosity of the ionic liquid as well as to accelerated TFSI^- decomposition.¹⁶⁵ We assume that this is also the reason for the poor reversibility of about 3 % obtained in that study. This deposition/dissolution behavior is very different from the uniform Mg deposits obtained in Grignard-based electrolytes, which also allowed reversible dissolution.⁴⁵⁶

Watkins et al. had proposed that the addition of a chelating agent (in their case, oligoether glymes or 18-crown-6) separates the direct coordination of Mg^{2+} by TFSI^- and results in the formation of $[(\text{Mg}(\text{glyme})_x)^{2+}(\text{TFSI}^-)]^+$ complexes, which they referred to as solvent-separated ion pairs (SSIPs).⁴⁵¹ This was concluded from the disappearance of the Raman band typical for Mg^{2+} -coordinated TFSI^- and the appearance of a new band that was associated with Mg^{2+} -coordinated glyme. Such a separation of TFSI^- from the Mg^{2+} cations could explain the more facile Mg deposition in the measurements in Figure 9.1, but similar results could also be obtained from a weakening of the Mg^{2+} - TFSI^- coordination. Finally, DFT calculations comparing the different abilities to coordinate cations in chloride-containing Mg complexes in monoglyme-, diglyme-, triglyme- and tetraglyme-based electrolytes indicated that the longer and more flexible glymes were increasingly able to adjust their conformation and thus enhance the interaction between Mg and solvent. This was proposed to allow for the formation of larger Mg^{2+} -, Cl^- -, and solvent-containing aggregates, which, in turn, improves the reversibility of Mg deposition/dissolution, though at higher overpotentials.⁴⁵⁷

Focusing on BH^- -containing electrolytes, both experimental studies^{420,447} and calculations^{458,459} for several electrolytes have concluded that the dissociation of the Mg^{2+} - BH^- coordination is a key aspect for Mg deposition, which, in ether-type solvents, is influenced by the number of coordinating oxygen atoms or possibly also by coordinating TFSI^- ions. The Mg^{2+} coordination in BH^- - and TFSI^- -containing diglyme was investigated by Hu et al. in a combined experimental and theoretical study.⁴⁶⁰ Using the electrolyte components without further purification or drying, they found an improved electrochemical performance in the mixed electrolyte as compared to a TFSI^- -free electrolyte. They explained this by a formation of mixed ion pair clusters containing Mg^{2+} as central ion, which is coordinated by BH^- and TFSI^- anions as well as by O-atoms of the glyme molecules. The latter are expected to reduce the strong interaction between Mg^{2+} and BH^- anions, which was claimed to allow for reversible Mg plating and stripping.⁴⁶⁰ Using a special TFSI^- -based IL with an oligoether group in the cation and $\text{Mg}(\text{BH}_4)_2$ as Mg source, Watkins et al. found that Mg deposition/dissolution reversibility are significantly improved compared to that from BMP- TFSI^- .¹⁶³ They attributed this to the complexation of the Mg^{2+} cation by the polyether groups, which prevents the direct TFSI^- coordination and weakens the Mg^{2+} - BH^- coordination. Comparable results were reported by Gao et al.,¹⁶⁰ who, furthermore, observed that the above effects increase with increasing ether functionalization of the cation.

Based on aforementioned results, the crown ether may either displace the TFSI^- anions from the Mg^{2+} coordination sphere and thus prevent the decomposition of the TFSI^- ; or it may weaken the interaction with Mg^{2+} and thus stabilize the TFSI^- against decomposition. In both cases, one would expect an improved reversibility of the Mg deposition/dissolution process and, in particular, a better stability/slower inhibition of these

processes in the presence of the crown ether. Still open, however, is the role of the borohydride in this process. It may either solely act as water scavenger, removing trace impurities of water in the different chemicals (see Experimental section) from the electrolyte, or it may also coordinate to Mg^{2+} . BH^- coordination to Mg^{2+} has indeed been reported to be stronger than that of TFSI^- ,^{160,460} which will be important also for the present case. Finally, also the ratio between the different components seems to be important; as indicated by the results of Hu et al., who observed significant differences in the Mg deposition/dissolution current when varying the ratio of the TFSI^- and BH^- concentration in Mg^{2+} -containing diglyme.⁴⁶⁰

In order to investigate the role of the TFSI^- and BH^- anions and of the crown ether and, in particular, their relative concentrations, in more detail, we prepared electrolytes with different concentrations of these species. In all cases, the Mg^{2+} concentration was kept at 0.1 mol/l. We would expect that, if borohydride acts only as water scavenger and is necessary for that, a certain minimum concentration of borohydride is required for reversible Mg deposition/dissolution. In that case, crown ether would be furthermore required to coordinate to Mg^{2+} and displace TFSI^- . Alternatively, both borohydride and crown ether contribute to the displacement of TFSI^- from the Mg^{2+} coordination sphere. In this case, the total amount of borohydride plus crown ether relative to the amount of Mg^{2+} would be decisive for reversible and reasonably stable Mg deposition/dissolution.

In Fig. 9.2a, we present a set of CVs recorded with a GC substrate in $\text{Mg}(\text{BH}_4)_2$ -, MgTFSI_2 -, and 18-crown-6-containing BMP-TFSI, with a 1:1 molar ratio of crown ether to Mg^{2+} and a 1:1 mixture of $\text{Mg}(\text{BH}_4)_2$ and MgTFSI_2 (0.05 M $\text{Mg}(\text{BH}_4)_2$ + 0.05 M MgTFSI_2 + 0.1 M 18-crown-6). The characteristic features in these CVs are essentially identical to those obtained and discussed before for GC in a solution of 0.1 M $\text{Mg}(\text{BH}_4)_2$ and 0.1 M 18-crown-6 in IL (Fig. 9.1). The reversibility is about 80 % in the first ten cycles, which is comparable to the results obtained for the MgTFSI_2 -free electrolyte (Fig. 9.1). However, with increasing cycling times, the reversibility decreases to about 12 % after 20 cycles (see Fig. F.6) and the electrode is completely inert after 50 cycles (Fig. 9.2a). For comparison, the GC electrode cycled in BMP-TFSI + 0.1 M $\text{Mg}(\text{BH}_4)_2$ + 0.1 M 18-crown-6 (discussed with Fig. 9.1) still displayed more than half of the initial current densities after 50 scans. Considering that the relative increase in TFSI^- concentration is marginal and the concentrations of Mg^{2+} and 18-crown-6 are identical to those in Fig. 9.1, these changes in reversibility must be related to the lower amount of BH^- in the measurement to Fig. 9.2a. Upon further increasing the amount of MgTFSI_2 at the expense of $\text{Mg}(\text{BH}_4)_2$ (Fig. 9.2, 0.09 M MgTFSI_2 + 0.01 M $\text{Mg}(\text{BH}_4)_2$ + 0.1 M 18-crown-6), we observe a pronounced decay of the current density and a down-shift of the Mg deposition potential (blue curve). Obviously, the increasing lack of BH^- is detrimental for the Mg^{2+} deposition process. The current trace in the anodic scan is affected even more and shows only a very weak and broad Mg dissolution feature. Hence, both Mg plating and Mg stripping are reduced

9. Influence of Complexing Additives on Mg Deposition/Dissolution in an IL

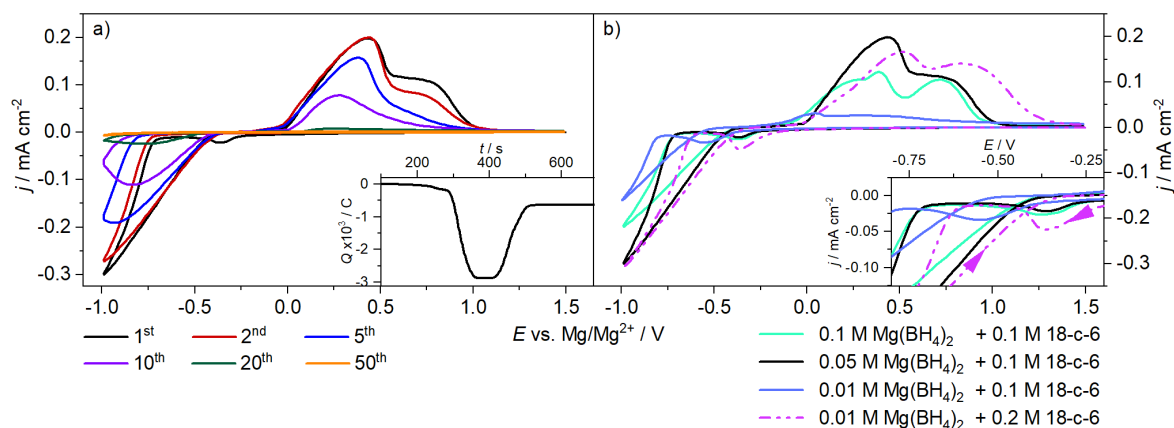


Figure 9.2: Sets of CVs recorded on GC in BMP-TFSI + 0.05 M $\text{Mg}(\text{BH}_4)_2$ + 0.05 M MgTFSI_2 + 0.1 M 18-crown-6 (a) and in BMP-TFSI with different concentrations of $\text{Mg}(\text{BH}_4)_2$, MgTFSI_2 and 18-crown-6 (b, first cycle). The concentration of MgTFSI_2 is 0.1 M – concentration of $\text{Mg}(\text{BH}_4)_2$. The inset in (a) shows the accumulated charge during the first scan, in (b) an enlarged section of the lower potential region between -0.2 V and -0.8 V . All scan rates are 10 mV/s .

when replacing BH^- by TFSI^- , or the other way around, when reducing the amount of BH^- , while keeping the concentration of crown ether constant.

Interestingly, when doubling the amount of crown ether added to this $\text{Mg}(\text{BH}_4)_2/\text{MgTFSI}_2$ mixture (Fig. 9.2b, violet dashed curve, $0.09\text{ M MgTFSI}_2 + 0.01\text{ M Mg}(\text{BH}_4)_2 + 0.2\text{ M}$ 18-crown-6, for more cycles see Fig. F.7), the high current densities are restored again and the reversibility is significantly improved. The latter increases from 75% in the first cycle to 82% in the second cycle, then decreases again continuously to 75% in the 10th cycle. This trend in the reversibility, with an initial increase and a later decrease, is very similar to that obtained for the sample cycled in IL containing $0.05\text{ M Mg}(\text{BH}_4)_2 + 0.05\text{ M MgTFSI}_2 + 0.1\text{ M}$ 18-crown-6 (Fig. 9.2a). We assume that the similar trends reflect that, in both cases, an increasing excess of BH^- plus crown ether relative to the Mg concentration is beneficial for the Mg deposition/dissolution reaction. Also, the onset potential for Mg deposition (-0.6 V) is slightly more anodic than that obtained in pure borohydride and crown ether-containing IL with no MgTFSI_2 (-0.7 V , equivalent to an up-shift of the onset potential for Mg deposition by 0.1 V), supporting the above conclusion of more facile Mg deposition in this electrolyte. In combination, these results indicate that the sole coordination of TFSI^- with Mg^{2+} is detrimental for the Mg deposition/dissolution processes. However, when either the crown ether or BH^- – or both in combination – are present in the electrolyte in sufficient amounts, TFSI^- can either at least partly be displaced from the inner Mg^{2+} coordination sphere, or the $\text{Mg}^{2+}\text{-TFSI}^-$ interaction can be weakened to an extent that Mg^+ -induced TFSI^- decomposition is inhibited during reaction. Both could enable improved plating and stripping. On the other hand, Hu et al. had demonstrated that an increase of the MgTFSI_2 content, from zero content to four-

fold excess at constant $\text{Mg}(\text{BH}_4)_2$ concentration (0.01 M), leads to a continuous increase in reversible Mg deposition/dissolution from diglyme.⁴⁶⁰ Based on quantum chemical calculations, they proposed that TFSI^- displaces one of the BH^- ligands in the inner coordination shell, which was seen as origin for the improved Mg deposition/dissolution. The apparent discrepancy to our findings – an improved Mg deposition/dissolution upon addition of TFSI^- to $\text{Mg}(\text{BH}_4)_2$ -containing electrolyte in their case vs. an improved Mg deposition performance upon addition of $\text{Mg}(\text{BH}_4)_2$ to TFSI^- -based electrolyte in our experiments – is most likely due to the very different situations in both cases. While in our experiments TFSI^- is present also as solvent and thus in strong excess, they use TFSI^- in rather low concentrations, comparable to that of BH^- , together with an excess of the Mg-coordinating glyme as solvent.

These results point to an equilibrium of Mg^{2+} coordination with the various ligands, where coordination of TFSI^- to Mg^{2+} and, thus, also Mg^+ -induced decomposition of TFSI^- , are still possible as long as BH^- and/or crown ether (or a combination of them) are not present in over-stoichiometric amounts (for crown ether: 1:1). This conclusion also fits well to the results reported by Shao et al., who observed a significant enhancement of the Coulombic efficiency with increasing BH^- concentration, as well as when changing from a monodentate solvent molecule (THF) to bidentate (DME) and finally tridentate (diglyme) molecules.⁴²⁰ They explained this behavior by synergistic effects, without, however, explaining in more detail how this would affect Mg deposition. As mentioned before, we found that, also in the presence of crown ether, a certain amount of BH^- is required, as indicated by the experiment with 0.09 M MgTFSI_2 + 0.01 M $\text{Mg}(\text{BH}_4)_2$ + 0.1 M crown ether, where Mg deposition was strongly hindered. Finally, additional measurements with other concentrations of crown ether (Fig. F.3) further confirmed that a certain minimum amount of BH^- is required for Mg deposition from MgTFSI_2 . Even a tenfold excess of crown ether did not support Mg deposition from MgTFSI_2 if no BH^- was added. This is most easily explained in a picture where some BH^- is necessary for removal of trace impurities of water, and, additionally may coordinate with Mg^{2+} .

Here it should be mentioned that Sagane et al. observed that the addition of stoichiometric (1:1) amounts of 18-crown-6 to MgTFSI_2 in MPPp-TFSI is required and sufficient for a complete displacement of TFSI^- from the coordination sphere of the Mg^{2+} , resulting in the formation of “free” TFSI^- anions. The CV of that mixture shows Mg plating and stripping, but with a very low reversibility.¹⁶⁵ Furthermore, there may be an influence of the IL cation on the complexation process, as these authors used 1-methyl-1-propylpiperidinium (MPPp^+) as cation rather than the 1-butyl-1-methylpyrrolidinium (BMP^+) employed in the present work.

Finally, we want to briefly test for possible effects induced by the nature of the electrode by changing to a Mg electrode. Figure 9.3 displays a CV recorded in 0.1 M $\text{Mg}(\text{BH}_4)_2$ -containing BMP-TFSI with 0.1 M 18-crown-6 on a magnesium substrate. Different from

9. Influence of Complexing Additives on Mg Deposition/Dissolution in an IL

the current traces recorded on the glassy carbon substrates in 0.1 M $\text{Mg}(\text{BH}_4)_2$ and 0.1 M 18-crown-6-containing IL, the first cathodic scan (after a potential step from the OCV to the upper potential limit) already exhibits oxidative currents in the potential range 1.5 to 0 V, which we assume are due to Mg dissolution from the roughened electrode (see Experimental section). This is different from results reported by Ma et al., who only observed dissolution of freshly deposited Mg, but not of the Mg substrate, in 0.5 M MgTFSI_2 /tetraglyme electrolyte containing 6 mM $\text{Mg}(\text{BH}_4)_2$, at least when cycling below 1.0 V. They concluded that, most likely, the underlying Mg surface is passivated completely despite the roughening pretreatment.⁴³¹ Mg deposition starts already at a potential below 0.5 V, i.e., at a lower overpotential compared to that obtained on a glassy carbon electrode in the same electrolyte (Fig. 9.1, around 0.7 V). This indicates a lower nucleation overpotential for the roughened Mg electrode compared to the GC substrate, most likely due to the presence of efficient sites for heterogeneous nucleation on the surface. The corresponding Mg dissolution peak appears at 0.2 V, also down-shifted by 0.1 V compared to the Mg dissolution peak observed on GC. Initially, the current density is almost three times higher than the corresponding current traces on glassy carbon. With increasing cycle number it decreases rapidly, having lost about half the initial current density by the fifth cycle. This loss is far more pronounced than on glassy carbon. We tentatively explain this by the generally higher reactivity of the Mg surface, which reacts more efficiently both with trace impurities in the electrolyte and/or with the solvent during cycling. This reaction may hinder further Mg deposition and thus result in the distinct peak between -0.6 V and -0.7 V in the Mg deposition range, rather than the expected exponential current increase when approaching the lower potential limit. The peak in the anodic scan at about 0.2 V is most likely related to dissolution of the freshly plated Mg, whereas oxidation of the underlying Mg substrate proceeds only in the anodic currents above 0.5 V. Interestingly, while the onset and peak maximum for Mg dissolution remain the same, the onset for Mg deposition shifts to more negative potentials with continued cycling. Overall, compared to Mg plating/ stripping on GC, both these and also the passivation processes are faster on Mg.

It is also worth mentioning that, aside of its role as water scavenger, borohydride may also dissolve the (native) passivation layer present on the Mg surface due to its strongly reducing nature.⁴¹⁹ However, we observed both Mg deposition/dissolution and electrolyte decomposition currents only on in situ roughened Mg electrodes. Hence, the sole presence of borohydride is not enough to dissolve the native passivation layer and allow for reversible Mg plating and stripping.

To learn more about the question in how far these effects are specific for Mg deposition, we studied the plating/stripping behavior on GC in analogous electrolyte systems, employing Ca^{2+} instead of Mg^{2+} . No Ca^{2+} deposition was observed from $\text{Ca}(\text{BH}_4)_2$ -containing BMP-TFSI, neither in the absence nor presence of 18-crown-6 (Figs. F.2 and F.3). We

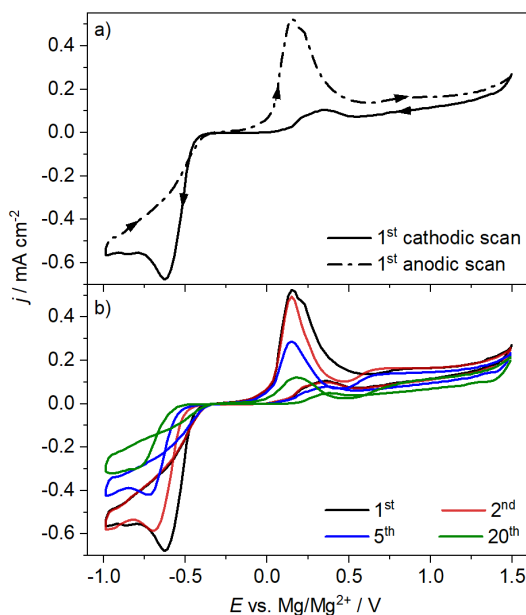


Figure 9.3: First (a) and additional relevant (b) cycles of the potentiodynamic scan of a Mg electrode in 0.1 M $\text{Mg}(\text{BH}_4)_2$ + 0.1 M 18-crown-6-containing BMP-TFSI at 10 mV/s.

speculate that this difference is related to the different mismatch⁴⁴⁶ between the cavity size of the crown ether (2.9 Å for 18-crown-6) and the ion diameters of the two ions (Ca^{2+} 2.0 Å, Mg^{2+} 1.44 Å). The better fit would result in a stronger binding of Ca^{2+} than of Mg^{2+} . In that case, Mg^{2+} deposition could still be possible when it is coordinated to 18-crown-6, while Ca^{2+} is too tightly bound for deposition. This hypothesis is also in agreement with the fact that we found neither Ca nor Mg deposition from BMP-TFSI containing 15-crown-5 (cavity size 2.0 Å), as, as we assume, both cations are too strongly bound for metal deposition.

Finally, we would like to note that the proposed mechanism of a displacement of the anion of the IL solvent/Mg source by the additives requires that the additives coordinate more strongly to the Mg^{2+} cation than the weakly coordinating TFSI⁻ anions and also weaken the Mg^{2+} -TFSI⁻ interaction, but still are sufficiently weakly coordinated to allow facile Mg deposition. The partial displacement of the Mg^{2+} -coordinated TFSI⁻ species and the weakening of the Mg^{2+} -TFSI⁻ interaction of the remaining TFSI⁻ ligands inhibits the decomposition of the TFSI⁻, which is induced by interaction with the Mg⁺ upon partial reduction of the Mg^{2+} ion.⁴²⁹ Hence, we propose that in such cases the optimum additive is one that is i) stable against decomposition itself and that has ii) an optimum interaction with the metal cation; i.e., sufficiently strong that it can partly displace the unstable component (here TFSI⁻) and/or weaken its interaction with the central Mg^{2+} ion, but sufficiently weak that it does not inhibit metal deposition by formation of a stable coordination shell. This also requires that the coordination of the unstable component

be sufficiently weak that it can still be displaced by the additive under the conditions described in ii). These questions were investigated theoretically, as detailed in the next section.

9.2.2 Simulation

To test the above interpretation, we conducted MD simulations and quantum chemical calculations at the density functional level of theory (DFT), comparing the stability of the coordination sphere of the Mg^{2+} cation in the presence and absence of 18-crown-6 (for details, see Experimental section and Supporting Information). Note that in our classical MD simulations, which are used as starting point, the interactions between Mg^{2+} and the solvent molecules are limited to solely electrostatic forces and will not include contributions from covalent interactions between Mg^{2+} and oxygen. However, such interactions are fully captured in the subsequent DFT calculations. In these calculations, the reference level for the energy of the respective clusters was defined by the energy

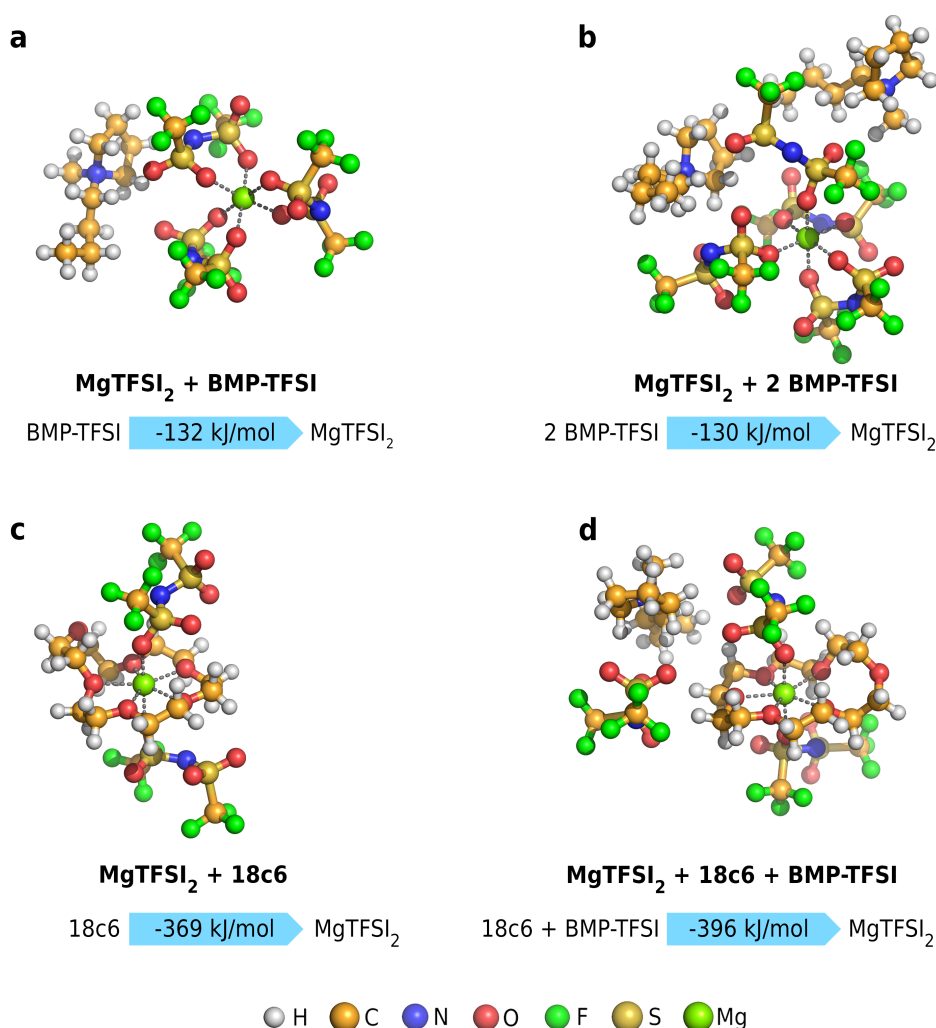


Figure 9.4: Representation of the most stable clusters at different compositions, cut from MD simulations, and the respective coordination energies E_c .

of an isolated MgTFSI_2 cluster plus that of the separate additional ligands (BMP-TFSI ion pairs, 18-crown-6), where the energies were calculated using the frozen geometry of the most stable complete cluster. Accordingly, the coordination energies E_c refer to the energy gained upon coordinating one or more additional ligands to the MgTFSI_2 cluster, while the binding energy E_b of a specific ligand in that cluster refers to the energy required for removing that ligand in a frozen configuration. For selected configurations obtained during the MD simulations, we cut clusters containing the MgTFSI_2 as well as up to two BMP-TFSI ion pairs in the absence and presence of 18-crown-6, which were further optimized geometrically (see Experimental section). For the determination of the coordination and binding energies presented in Figures 9.4 and 9.6 and in Table 9.1, we used the cluster configurations with the most stable final geometry. Note that the structure of the MgTFSI_2 complex included therein may not be the most stable configuration of the isolated MgTFSI_2 cluster.

In Fig. 9.4, we show a selection of clusters cut from the MD simulations consisting of MgTFSI_2 in the presence of up to two BMP-TFSI ion pairs and up to one 18-crown-6 molecule. The Mg^{2+} cation is displayed in different coordination states and geometries, along with the respective (additional) coordination energies. The clusters are portrayed in the most stable configurations observed for the respective coordination. Note that these are not necessarily the configurations with the highest coordination energies. Visualizations of some other clusters considered in this work are provided in the Supporting Information (Fig. F.8). A main characteristic for all clusters is the bond between the Mg^{2+} cation and the oxygen atoms of the TFSI^- anions or of the 18-crown-6 molecule. The different configurations in Fig. 9.4 involve coordination geometries of the Mg^{2+} cation with different numbers of directly coordinating oxygen atoms, as illustrated in Fig. 9.5. The Mg^{2+} cation prefers a seven-fold coordination by oxygen atoms in the presence of 18-crown-6, while a five- or six-fold oxygen coordination, arranged in a pyramidal or octahedral configuration, respectively, is preferred in its absence.

As expected, the increasing coordination of the Mg^{2+} ion in the MgTFSI_2 cluster increases the stability of the cluster. Coordination with an additional BMP-TFSI ion pair leads to a stabilization by -132 kJ/mol (Fig. 9.4a). Note that this denotes the overall energy gain of the system, which may also contain contributions from a change in bonding within

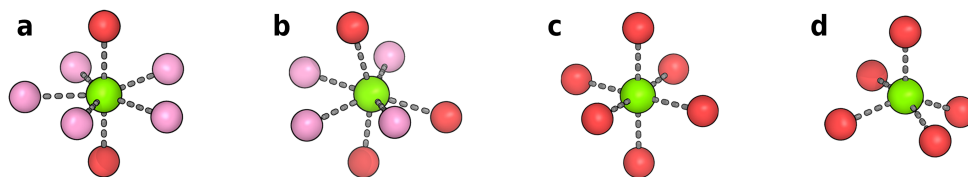


Figure 9.5: Different coordination states of Mg^{2+} , colored in green, in the presence (a, b) and absence (c, d) of 18-crown-6. Oxygen atoms belonging to the 18-crown-6 ring are colored in pink; those belonging to TFSI^- in red.

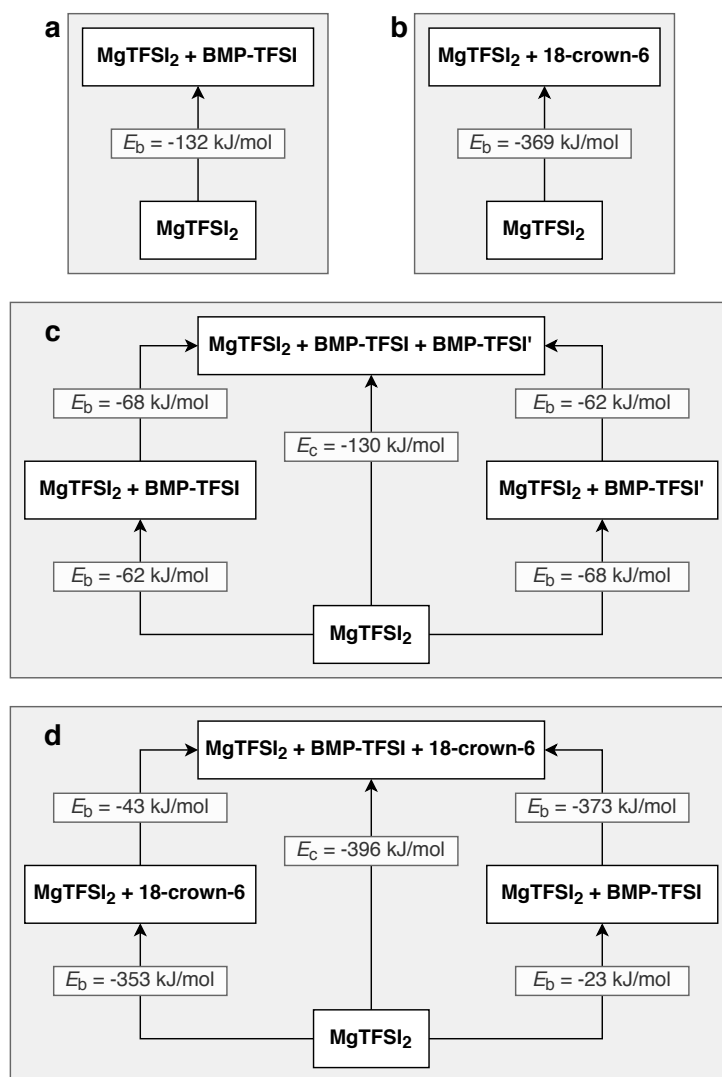


Figure 9.6: Scheme of the coordination energies E_c and binding energies E_b for different cluster compositions.

the original MgTFSI_2 cluster and within the ion pair. Hence, it is not necessarily the strength of the bond between Mg^{2+} and the ion pair, but it would properly describe the energy needed to detach the ion pair. Adding a second BMP-TFSI ion pair to the $\text{MgTFSI}_2 + \text{BMP-TFSI}$ cluster does not lead to a further stabilization of the cluster; the coordination energy of -130 kJ/mol for two BMP-TFSI ion pairs is almost equal to that of a single ion pair (Fig. 9.4b). Qualitatively, this can be understood from the fact that, for coordination with a single BMP-TFSI ion pair, the TFSI^- anion can coordinate via two oxygen atoms, while for coordination by two BMP-TFSI ion pairs each of them coordinates only by a single oxygen atom of the TFSI^- species to the Mg^{2+} cation (see Fig. 9.4). Hence, coordination by the second ion pair weakens the bond to the first ion pair, and this effect is quite significant. Therefore, one would expect an equilibrium between both states at room temperature, which also means that thermal detachment of the second ion pair is easily achieved at room temperature. This weakening of the bond

to the first BMP-TFSI ion pair is illustrated also in the energy scheme in Fig. 9.6. It represents the binding energies for different ligands in the frozen geometry of the final cluster, which were calculated by comparing the cluster energies before and after removal of the respective ligand in that geometry. In this case, the binding energies of the two different BMP-TFSI ion pairs are almost identical (Fig. 9.6c), and they are much smaller than that of the BMP-TFSI ion pair in Fig. 9.4a. Also, it does not seem to matter which of the two ion pairs is added first. Hence, synergistic effects between the two ion pairs are absent.

In a similar way, we explored the additional coordination of an 18-crown-6 molecule to either the MgTFSI_2 (Fig. 9.4c) or the $\text{MgTFSI}_2 + \text{BMP-TFSI}$ (Fig. 9.4d) cluster. In the first case, this results in a stabilization by -369 kJ/mol . Hence, the coordination of the MgTFSI_2 cluster by the crown ether is significantly stronger than that by a BMP-TFSI ion pair. Also, the addition of a single 18-crown-6 molecule to a $\text{MgTFSI}_2 + \text{BMP-TFSI}$ cluster results in a drastic increase in cluster stability by -264 kJ/mol . Qualitatively, this is evident already from the structure of the most stable cluster in Fig. 9.4d. This shows a significant weakening of the coordination to the two original TFSI^- anions, which are coordinated now only via one oxygen atom, and to the third TFSI^- anion (that of the BMP-TFSI ion pair), which is no longer part of the inner coordination sphere. Here, we identify the TFSI^- anion of the ion pair by its stronger interaction to the BMP^+ cation compared to the other two TFSI^- species. On a more quantitative scale, this is illustrated in the energy scheme in Fig. 9.6d. Addition of a crown ether molecule to the MgTFSI_2 cluster, in the frozen geometry of the stable configuration of the $\text{MgTFSI}_2 + \text{BMP-TFSI} + 18\text{-crown-6}$, results in a binding energy stabilization by -353 kJ/mol ; further addition of a BMP-TFSI ion pair stabilizes this by another -43 kJ/mol (total coordination energy -396 kJ/mol), which is even less than the binding energy per BMP-TFSI ion pair in the $\text{MgTFSI}_2 + \text{BMP-TFSI}$ cluster. Also in this case, it almost does not matter whether the crown ether or the ion pair is added first and synergies are very small. Overall, the strong coordination by the crown ether molecule leads to a significant weakening of the bond between Mg^{2+} and the two TFSI^- anions, and essentially a displacement of the BMP-TFSI ion pair. Also considering these effects in the overall energy balance, one expects that the bond between crown ether and Mg^{2+} cation is even significantly stronger than -353 kJ/mol .

In addition to the above calculations, we also explored whether coordination of two 18-crown-6 molecules to the MgTFSI_2 cluster would be strong enough to additionally displace the original TFSI^- anions from their direct coordination to the Mg^{2+} cation. For this purpose, we built and optimized a cluster in which the Mg^{2+} cation is surrounded by two 18-crown-6 molecules and the two TFSI^- anions are displaced to the second coordination layer (Fig. F.9). Here, we find that the total binding energy in that cluster is stronger by -70 kJ/mol , as compared to the coordination states in the absence of 18-crown-6.

9. Influence of Complexing Additives on Mg Deposition/Dissolution in an IL

However, it is less stable by -27 kJ/mol as compared to the coordination by just one 18-crown-6 and two directly coordinating TFSI⁻ anions.

Overall, these calculations indicate that i) the coordination with the 18-crown-6 molecule is much stronger than that with TFSI⁻ anions, that ii) the interaction with the 18-crown-6 molecule leads to a significant destabilization of the remaining coordination to the two TFSI⁻ anions, as indicated by the change from two-fold to one-fold coordination, and, finally, that iii) a complete screening of the Mg²⁺ cation by two 18-crown-6 molecules is energetically unfavorable. In the absence of 18-crown-6, the coordination of MgTFSI₂ with one or two BMP-TFSI ion pairs always results in either a six-fold or five-fold coordination of the Mg²⁺ cation, i.e., in an octahedral or trigonal bipyramidal structure, respectively. In contrast, in the presence of 18-crown-6, the Mg²⁺ cation is coordinated by four to five oxygen atoms of the ether and two to three anions coordinated by a single oxygen atom each.

Next, we considered that Mg deposition requires the cation to be able to (stepwise) strip its coordination shell when attaching to the electrode surface. As evident from the numbers in Figures 9.4 and 9.5, the binding energies with the TFSI⁻ anions in the BMP-TFSI ion pairs calculated are of an order of magnitude that allows their thermal detachment at room temperature. This is true both for coordination of one or two ions pairs – actually, removing the second BMP-TFSI ion pair does not cost any energy – and especially in the presence of a crown ether molecule acting as a second ligand. On the other hand, it would be very hard for the Mg²⁺ cation to escape coordination with 18-crown-6. Previous studies have suggested that the partial reduction of Mg²⁺ to Mg⁺ via an outer sphere electron transfer reaction will weaken the interaction with TFSI⁻.^{160,429} Similar effects may also be expected for the coordination to an 18-crown-6 molecule. Figure 9.7 compares the coordination energies of different 18-crown-6 and/or BMP-TFSI-containing clusters before and after partial reduction of the cation from Mg²⁺ to Mg⁺. Indeed, the coordination energies decrease significantly (strictly speaking, the absolute values of the coordination energies decrease). Most importantly, the coordination energy of the 18-crown-6-containing cluster decreases by -130 kJ/mol, falling to -212 kJ/mol. This moves it significantly closer to the range where Mg deposition seems feasible. On the other hand, while the addition of a second BMP-TFSI ion pair to the coordination sphere of Mg²⁺ does not result in a further stabilization of the cluster (see above), this is different for the reduced Mg⁺ ion. Here, the addition of a second BMP-TFSI ion pair to the coordination sphere of [MgTFSI₂]⁻ reduces the cluster stability, which, in turn, would improve Mg deposition on the electrode due to its reduced coordination. Overall, the data in Fig. 9.7 demonstrate that partial reduction of the Mg²⁺ to Mg⁺, e.g., via an outer sphere charge-transfer step, destabilizes the coordination not only to solvent ion pairs, but also to 18-crown-6 molecules to an extent that detachment of these species becomes feasible at room temperature, which is a precondition for Mg deposition.

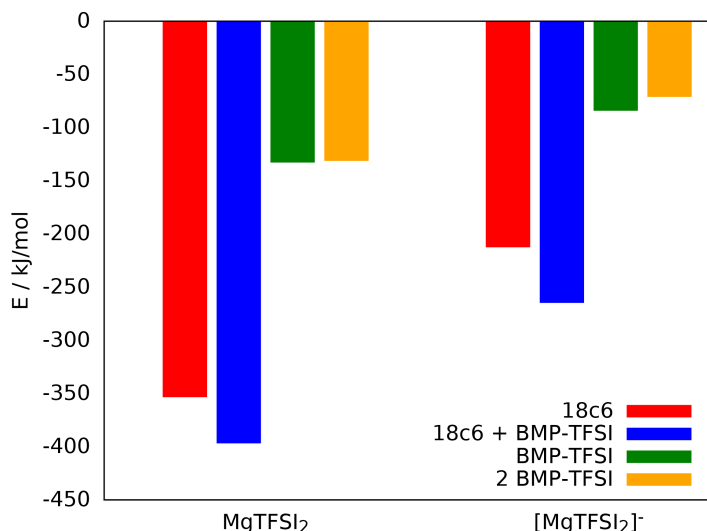


Figure 9.7: Coordination energies of different 18-crown-6 and BMP-TFSI-containing clusters ($\text{MgTFSI}_2 + \text{X}$, X see Figure) with $[\text{Mg}^{2+}\text{-TFSI}_2]$ or $[\text{Mg}^+\text{-TFSI}_2]^-$ as central unit. Coordination energies are referenced to the energies of the respective MgTFSI_2 clusters.

Finally, we investigated the reductive stability of the TFSI^- anions in different clusters. Recently, several groups have proposed to derive trends in the electrochemical stability window calculating reduction and oxidation potentials, rather than using the strongly simplified previous scheme which relates the stability window to the HOMO and LUMO of the solvent molecules.^{461–464} The main difference in this approach is the proper accounting of solvation effects and of contributions from reduction-/oxidation-induced reactions.⁴⁶⁴ Here, we employed a method which is closely related to the general ideas of the thermodynamic cycle method, but proceeds in a different way: namely, by calculating the electron affinities E_A of the solvated clusters based on the adiabatic energy difference between a cluster and its reduced form. As described in the Experimental section, both clusters were geometry-relaxed to the nearest local minimum. Table 9.1 lists the values of E_A for a number of different clusters. For comparison, we also included the isolated TFSI^- anion, the 18-crown-6 molecule, and the MgTFSI_2 cluster. Based on the electron affinities, trends in the equilibrium potential for reduction of the respective molecules/cluster E_{red} can be estimated (see Experimental section), which are listed in Table 9.1 as well.

First of all, we find that the uncoordinated TFSI^- anion shows a significantly higher electron affinity compared to its coordinated state in the MgTFSI_2 cluster. Considering the magnitude of the difference in electron affinities, this trend is significant, even though for these latter two species solvation effects are included only implicitly. A similar trend can be observed for 18-crown-6, which becomes more susceptible to reduction when coordinated to Mg^{2+} . However, both in its free and its coordinated state, 18-crown-6 ether shows significantly lower electron affinities than TFSI^- .

Furthermore, we found that, during geometric relaxation, all TFSI^- -containing clusters exhibit the dissociation of a $-\text{CF}_3$ group upon reduction. Therefore, the electron affinity

Table 9.1: Electron affinity E_A and equilibrium potential E_{red} for molecule/cluster reduction vs. Mg/Mg^{2+} for different molecule/cluster types.

Cluster/molecule	E_A / eV	E_{red} / V
TFSI ⁻	2.16	-1.19
18c6	-0.49	-3.84
Mg^{2+} + 18c6	1.68	-1.67
MgTFSI_2	3.75	0.40
MgTFSI_2 + BMP-TFSI	3.49	0.14
MgTFSI_2 + 2 BMP-TFSI	3.10	-0.25
MgTFSI_2 + 18c6	2.97	-0.38
MgTFSI_2 + 18c6 + BMP-TFSI	2.91	-0.44

of the TFSI⁻-containing clusters is a measure also for the stability against reductive decomposition of the TFSI⁻ group. In contrast, no bond breaking was observed in the 18-crown-6 ether, neither in the free molecule nor when coordinated to Mg^{2+} or MgTFSI_2 . Spin density plots (Fig. F.15) reveal that, in TFSI⁻-containing clusters, the unpaired electron is entirely located on the dissociated $-\text{CF}_3$ group after reduction, whereas in the case of the isolated TFSI⁻ the unpaired electron is shared between both fragments. In the absence of TFSI⁻ and presence of 18-crown-6, the additional, unpaired electron will be entirely located at the Mg^{2+} cation, reducing it to Mg^+ . Hence, the coordination to Mg^{2+} strongly enhances the known tendency of TFSI⁻ to decompose upon reduction via dissociation of a $-\text{CF}_3$ group.^{160,429,465} Similar findings were recently described by Tuerxun et al. for MgTFSI_2 in different organic solvents (THF, diglyme), based on the comparison of the calculated HOMO/LUMO energy levels of the free TFSI⁻ and of the MgTFSI_2 cluster, respectively.⁴²¹ In this case, implicit solvation effects were included, while explicit solvent effects by coordination of solvent molecules were not considered. Furthermore, we found that the addition of one BMP-TFSI ion pair slightly reduces the electron affinity E_A . On the other hand, the reductive stability of the coordinated TFSI⁻ anion is significantly increased by the addition of an 18-crown-6 ligand. Hence, even though there are still two TFSI⁻ anions weakly coordinated to the Mg^{2+} cation also in the presence of the 18-crown-6 molecule, these are less susceptible to reductive decomposition than the strongly coordinated TFSI⁻ species present in the absence of the crown ether. The same trend is indicated by the spin density distribution plots. A high electron affinity correlates with a pronounced localization of the unpaired electron, whereas the clusters with lower electron affinity show a more diffuse spin distribution. In isolated 18-crown-6, the electron is delocalized over the whole ring upon reduction, while the additional electron is localized on the cation upon attachment to Mg^{2+} , reducing it to Mg^+ and increasing the electron affinity. The reduction of isolated TFSI⁻ leads to the dissociation of a $-\text{CF}_3$ group, but the spin density plot shows that the unpaired electron is still shared between both fragments in the stable configuration. Again, the interaction with Mg^{2+} leads to a pronounced

localization of the electron, which is then entirely located on the dissociated $-\text{CF}_3$ group. This leaves the other fragment with a twofold negative charge, which is stabilized by the cation. In the presence of 18-crown-6, the spin density distribution becomes more diffuse again, which goes along with a lower electron affinity.

Overall, on a qualitative scale these calculations can well explain the experimental observation that i) the addition of 18-crown-6 results in a pronounced suppression of the reductive decomposition of TFSI^- species, even though these are present at large excess, and that ii) Mg^{2+} deposition is still possible despite the rather strong coordination of the 18-crown-6 molecule to the Mg^{2+} cation. In the first case, this is due to the fact that coordination to 18-crown-6 prohibits the two-fold coordination to the TFSI^- anions and, thus, decreases their binding energy to the Mg^{2+} cation. On the other hand, for the partly reduced Mg^+ , the interaction of the 18-crown-6 additive with the Mg^+ cation is sufficiently weak that direct interaction with the electrode as a first step for Mg deposition seems to be feasible at room temperature.

9.3 Conclusions

Based on the results of a systematic electrochemical and theoretical study on the influence of additives, in our case 18-crown-6 and $\text{Mg}(\text{BH}_4)_2$, on the reversible deposition/dissolution of Mg on a glassy carbon model electrode in the ionic liquid BMP-TFSI, we could show that these can significantly improve the extent and reversibility of Mg plating/stripping. While Mg^{2+} deposition is inhibited in purely MgTFSI_2 -containing BMP-TFSI, it is improved upon addition of the crown ether and/or of $\text{Mg}(\text{BH}_4)_2$. Varying the amount of the additives while keeping the Mg^{2+} concentration constant reveals i) that either of them can improve the deposition characteristics. However, ii) a certain excess of these species together relative to the Mg^{2+} concentration is required for more facile and reversible Mg deposition, and iii) regardless of the presence of the crown ether, a minimum amount of BH_4^- is required as well, most likely to act as water scavenger. These trends can be convincingly explained by the results of our quantum chemical calculations. Including implicit and explicit solvent effects, they reveal that i) the interaction between Mg^{2+} and the surrounding TFSI^- anions is significantly weakened upon coordination of an 18-crown-6 molecule to MgTFSI_2 or to $\text{MgTFSI}_2 + \text{BMP-TFSI}$, which severely reduces the tendency for Mg^+ -induced TFSI^- decomposition during Mg^{2+} reduction, that ii) increasing coordination stabilizes the resulting cluster, but with a non-linear effect, that iii) partial reduction of Mg^{2+} to Mg^+ , possibly via an outer sphere reduction process, weakens the $[\text{Mg}^+ - \text{TFSI}_2]^-$ interaction, which allows for coordination of the Mg cation to the electrode at room temperature, and that iv) the changes in Mg-TFSI interaction are reflected also by changes in the electron affinity and in the equilibrium potential for reduction of the respective clusters. When using a Mg substrate, as common in realistic

battery systems, instead of the model GC electrode, the passivation process is far more efficient, but otherwise the data appear to be in agreement with our interpretation.

In combination, experiment and calculations result in a detailed mechanistic picture of the role of additives on Mg deposition/dissolution in an ionic liquid electrolyte, including also synergistic effects. The observation of similar trends for reversible Mg plating/stripping on GC model electrodes and realistic Mg electrodes, only with higher currents, indicates that the above picture is not electrode-specific, but of more general validity.

9.4 Experimental Section

9.4.1 Electrochemical Methods

For the preparation of the electrolytes, the appropriate amounts of $\text{Mg}(\text{BH}_4)_2$ (Sigma Aldrich, 95.0 %), MgTFSI_2 (Solvionic, 99.5 %, ≤ 250 ppm H_2O) and 18-crown-6 (Alfa Aesar, ≥ 99.0 %, ≤ 0.29 % H_2O) were dissolved in 1-butyl-1-methylpyrrolidinium bis(trifluoromethylsulfonyl)imide (BMP-TFSI, Solvionic, 99.9 %, ≤ 20 ppm H_2O) by stirring. We prepared the following solutions: BMP-TFSI with a) 0.1 M $\text{Mg}(\text{BH}_4)_2$, b) 0.1 M $\text{Mg}(\text{BH}_4)_2$ + 0.1 M 18-crown-6, c) 0.05 M $\text{Mg}(\text{BH}_4)_2$ + 0.05 M MgTFSI_2 + 0.1 M 18-crown-6, d) 0.01 M $\text{Mg}(\text{BH}_4)_2$ + 0.09 M MgTFSI_2 + 0.1 M 18-crown-6, and e) 0.01 M $\text{Mg}(\text{BH}_4)_2$ + 0.09 M MgTFSI_2 + 0.2 M 18-crown-6. Karl Fischer titration of solutions of 0.1 M MgTFSI_2 +BMP-TFSI and 0.1 M MgTFSI_2 + 0.1 M 18-crown-6 in BMP-TFSI yielded water contents of 23 ppm and 25 ppm, respectively. The water content of $\text{Mg}(\text{BH}_4)_2$ -containing solutions cannot be determined this way due to its reaction with iodide; here we assumed similar water contents in the solvent and that all water originally present in the $\text{Mg}(\text{BH}_4)_2$ -containing electrolyte was reactively removed. Electrochemical measurements were conducted in a beaker cell-type three-electrode setup using glassy carbon (GC, HTW Germany, Sigradur G, 4 mm thickness, $d=8$ mm) or Mg disks (Goodfellow, 1.5 mm thickness, $d=8$ mm, 99.9 %) as working electrode (WE), a gold wire as counter electrode (CE) and a Mg rod (Goodfellow, $d=3.2$ mm, 99.9 %) as quasi-reference electrode (RE). The electrochemical cell consists of a Kelf cell body with three interconnected compartments and a total volume of 0.7 ml. CE and RE are placed in the outermost and middle compartment, respectively. With this configuration, the distance between counter and working electrode is maximized to minimize effects of oxidative reaction products formed at the CE on the processes taking place at the WE. The WE compartment, finally, has an opening at the bottom, with the edges of the opening pressing on the WE. A Viton O-ring (FKM 75, inner diameter 5 mm, cross section 1 mm) between WE and cell body prevents electrolyte leakage. Prior to the assembly, the GC substrates were polished and rinsed with Caroic acid, acetone, and ultrapure water. The cell body and O-rings were rinsed with acetone and then sonicated and boiled in ultrapure water. All cell compo-

nents were finally dried in Ar atmosphere at 100 °C for 16 h. The Mg electrodes (both reference and working electrodes) were polished in an Ar-filled glove box (MBraun Lab-Star, O₂<0.5 ppm; H₂O<1 ppm) before use. The cell was assembled inside the glove box, then quickly filled with electrolyte. In addition, the Mg electrode was roughened immediately after electrolyte filling, using a sharp glass tip. The potential was controlled by a Solartron Analytical Modulab (Pstat 1 MS/s) potentiostat. Cycling involved at least 25 and at maximum 100 cycles between 1.5 V and -1.0 V vs. Mg/Mg²⁺ at 10 mV/s. The electrochemical measurements were always started with a potential step from the OCV to the upper potential limit, with a rest time of 60 s at that point before the CV was initiated with the cathodic scan.

9.4.2 Computational Methods

Classical molecular dynamics (MD) simulations of MgTFSI₂ in BMP-TFSI in the presence and absence of 18-crown-6 were performed using the LAMMPS program package (version 17th of Nov, 2016),⁴⁶⁶ employing the OPLS-AA force field¹⁷¹ for Mg²⁺ and 18-crown-6 and the CL&P force field for the ionic liquid (BMP-TFSI).⁴⁶⁷ In these simulations, the solvent was represented by 256 BMP-TFSI ion pairs. For selected compositions, clusters were cut from these simulations using the post-processing tool TRAVIS.^{468,469} The cluster structures were geometrically optimized to the local energy minimum using density functional theory (DFT) with the ORCA program package,¹⁹⁸ the BP86 functional^{178,179} and def2-SVP⁴⁷⁰ basis set with Grimme’s D3 dispersion correction.⁸⁷ Geometrical counterpoise (gCP) correction was applied to deal with the intermolecular as well as intramolecular basis set superposition error (BSSE).¹⁹⁹ Tight SCF convergence criteria were applied in each geometry optimization. Solvent effects were considered via the MD simulation; furthermore, they were considered explicitly in the DFT calculations by BMP-TFSI ion pairs in the cluster and implicitly by the conductor-like polarizable continuum model (CPCM);⁴⁷¹ setting the dielectric constant to 14.7⁴⁷² and the refractive index to 1.423.⁴⁷³ Note that, while electrostatic interactions are the dominant attractive force between Mg²⁺ and oxygen, covalent interactions may also contribute to this, leading to delocalization of electron density to the cation’s empty 3s and 3p orbitals. Such effects are not included in our classical MD simulations, which serve as starting point, but are fully considered in the subsequent DFT optimizations. Cluster coordination energies and ligand binding energies were obtained by performing single-point calculations of isolated parts of the optimized clusters at the same level of theory, maintaining their frozen structure (see also Sec. 9.2.2). Electron affinities E_A and the equilibrium potential for reduction E_{red} of the respective clusters were obtained by explicitly calculating the adiabatic energy difference between a cluster R and its reduced form R⁻ (all geometry-optimized) via Eq. (9.1):

$$E_A(\text{R}) = E(\text{R}) - E(\text{R}^-) \quad (9.1)$$

and Eq. (9.2):

$$E_{\text{red}}(R) = \frac{E_{\text{A}}(R)}{nF} - E_{\text{ref}} \quad (9.2)$$

where $E(R)$ and $E(R^-)$ are the electronic energies of the solvated clusters, n is the number of exchanged electrons, F is the Faraday constant and E_{ref} is the reference potential calculated for Mg/Mg²⁺. This yields values very close to those obtained by via the thermodynamic cycle method.^{461–464}

Acknowledgments

We would like to thank Dr. Markus Eckardt and Sascha Gehrke for their help with the electrochemical pre-tests and MD simulations, respectively. We gratefully acknowledge financial support by the German Federal Ministry of Education and Research (BMBF) in the project 03EK3051 C (‘LuCaMag: Wege zu sekundären Mg/Ca-Luftbatterien’) and by the Deutsche Forschungsgemeinschaft under project BE 1201/22-1 (‘Zn-Air Batteries’) and ID 422053626 (POLiS Cluster of Excellence). This work contributes to the research performed at CELEST (Center for Electrochemical Energy Storage Ulm-Karlsruhe). Open access funding enabled and organized by Projekt DEAL.

Conclusion and Outlook

In this thesis computational studies were carried out on molecular as well as ionic liquids and their mixtures, respectively. By modeling the bulk liquid phase of these substances, valuable insights into the microscopic origin of their macroscopic properties could be obtained. To this aim, a variety of theoretical methods were used including classical and ab initio molecular dynamics as well as static quantum chemical calculations. A special focus was placed on the computational efficiency of the employed methods, ensuring their feasibility when applied to more complex systems. By combining methods of classical statistical thermodynamics with quantum chemical calculations to model the liquid phase, the binary quantum cluster equilibrium method in particular presents a highly efficient alternative approach to gain access to liquid phase thermodynamics. Building on a wide library of established substance classes that have been studied with the bQCE method, this thesis presents its first applications to non-polar solvents, ionic liquids, and aqueous acid solutions.

The underlying theoretic model of the bQCE method was fundamentally extended to general multi-component systems. The new theory is fully implemented in the Peacemaker 2 code and is currently under research. Possible applications include the modeling of ternary organic solvent mixtures, but also more complex systems are within the scope of the new theory such as mixtures of ionic liquids with water, organic solvents, or with each other. The bQCE method is straightforward in its theory and application and easily modifiable, e.g., to account for anharmonic vibrations⁷⁴ or rotational contributions of low-lying frequencies⁴⁷⁴ by implementing more complex variations of the partition functions.

The first part of the thesis focused on the mixing thermodynamics of binary mixtures of traditional solvents. In two studies the bQCE method was applied to a diverse range of binary mixtures of traditional solvents, including protic and aprotic polar solvents as well as non-polar solvents. These works were motivated by two overall goals. The first goal was to extend the range of liquids studied with the bQCE method by non-polar and mildly polar liquids and test its applicability to such systems. The second goal was to minimize the computational effort by using highly efficient low-cost quantum chemical methods and optimizing the cluster generation method. The first study included the well-mixing acetonitrile–acetone, benzene–acetone, and water–acetone systems and the hardly miscible water–benzene system. In contrast to earlier QCE studies, which aimed to use high-level methods, in this study a low-cost electronic structure method based on density functional theory was used. As an additional effort to minimize computational cost, the cluster size was limited to a maximum of three molecules. Despite these considerable restrictions the thermodynamics of mixing could be reproduced reasonably well for the non-aqueous systems. The aqueous mixtures were found to be problematic, due to their inherently more complex interactions such as the hydrophobic effect,¹⁸⁸ which small clusters fail to model. Nonetheless, the employed structure method was shown to form a reliable and efficient combination with the bQCE method, that was successfully

applied in later studies^{2,5,8,40,74} including ambitious applications such as the prediction of the ionic product of water.⁴⁰

In the follow-up study, the computational effort could be reduced even further by employing a semi-empirical structure method.¹⁸⁷ This allowed an increase in cluster size while still improving on the computational demand in total. It could be demonstrated that even with a low-level semi-empirical method the thermodynamics of mixing and vaporization can be reproduced by the bQCE method with reasonable to excellent accuracy. Vaporization enthalpies of polar solvents can be predicted within 2 kJ/mol accuracy. An exception was found in benzene, the first aromatic to be studied by QCE and bQCE. The calculated vaporization enthalpy of 17.1 kJ/mol significantly underestimates the experimental reference value of 33.9 kJ/mol. In a recent study, the calculated value could be improved to 38.6 kJ/mol by employing an updated structure method⁴⁷⁵ and accounting for rotational contributions of low-lying vibrational frequencies.^{474,476} By fitting the calculated mixing functions to Redlich–Kister-type polynomials,¹⁸⁹ an algebraic expression for $\Delta_{\text{mix}}G^\circ$ was obtained. Derivation of this expression allowed the calculation of activity coefficients. The obtained results are generally in good agreement with the experimental activity coefficients but the error increases in the more dilute regions, possibly due to a lack of clusters representing such dilute concentrations. Nonetheless, the approach developed in this study presents a valuable and novel addition to current activity coefficient models. The theory is formulated in a general way that should in principle be applicable to any multi-component system. Future studies may be conducted on a wider selection of systems and research cluster size effects on the accuracy of the method.

The second part of the thesis was centered around proton transfer equilibria and their effects on macroscopic properties. The three studies in this part each focused on fundamentally different systems, namely ionic, molecular, and, bridging the gap between both, pseudo-ionic liquids. In the first chapter of this part, the bQCE method was used to investigate the proton transfer in the well-studied ethylammonium nitrate and a range of additional alkylammonium nitrates and formates. Ethylammonium nitrate shows near to ideal Walden behavior, whereas ethylammonium formate is considered a “bad” ionic liquid with low ionicity.¹⁰⁹ By introducing clusters to the bQCE description of these systems that, next to a number of ion pairs, contain a neutral acid or base molecule, the degree of proton transfer could be calculated. The concentration of neutral species in the liquid phase of ethylammonium nitrate is negligible, whereas it is several orders of magnitude higher in ethylammonium formate. This may well explain the observed properties such as the higher volatility, lower boiling point, and lower conductivity of ethylammonium formate compared to ethylammonium nitrate. The calculated proton activities are consistent with the experimentally observed trends.^{122,124} Furthermore, the bQCE method allowed the prediction of the proton transfer degree over the whole liquid temperature range. As such data is unavailable from literature, the plausibility of these predictions was

tested by calculating the enthalpy and entropy of the proton transfer reaction from van't Hoff plots, in well agreement with experiment. These are remarkable results, considering this is the first computational approach to quantify the proton transfer degree in protic ionic liquids. Future studies may test this approach on a wider selection of systems with different cations and anions. Recently, Mariani et al.¹¹¹ pointed out the importance of quantifying proton activities and introduced the concept of reduced ionicity to overcome the ambiguity between ionicity and proton transfer degree. The bQCE method was shown to be a valuable tool in this endeavor. With the extension of the bQCE theory to general multi-component systems documented in Chapter 2, aqueous or organic solvent mixtures with ionic liquids are within the scope of this method.

Furthermore, the phase transition dynamics of the investigated systems were studied and are demonstrated to be more complex than in common molecular solvents. At ambient temperatures the vapor phase consists of strongly associated ion pairs. As the temperature rises, an increasing number of neutral acid and base species contribute to the vapor phase until, close to the boiling point, they form the dominant species. The bQCE method was shown to be able to model this equilibrium in close agreement with the experimental observations.²⁷² By employing the parameter-free bQCE⁰ approach the boiling point of ethylammonium nitrate could be predicted with an excellent accuracy of 1 K and good to acceptable accuracy of <50 K for the other PILs. As no parameter optimization is performed, no experimental input is required and the results obtained from this approach can be considered true *ab initio* results. When the parameters were optimized to the experimental isobar, vaporization enthalpies could be predicted with reasonable accuracy. It was shown that reasonable estimates can only be achieved by modeling the correct temperature dependent distribution of ion pairs and neutral molecules in the vapor phase. A weakness of this approach is found to be the underestimation of dispersion interactions between alkyl chains. The increasing deviation from experiment in the order ethyl-, propyl-, butylammonium nitrate shows that dispersion interactions contribute significantly to the binding energy in these systems, but cannot be accurately captured by the employed clusters. Future studies could therefore investigate possible adjustments or corrections to the bQCE approach, as are currently under research for non-polar solvents.⁴⁷⁴ Such efforts could be directed, for example, at the cluster generation method. The cluster approach of Seeger et al.⁴⁷⁷ finds good correlations with experimental data even at longer alkyl chain lengths and may serve as inspiration.

By the aid of *ab initio* molecular dynamics simulations, the equimolar mixture of *N*-methylimidazole and acetic acid was found to be mostly composed of neutral acid and base molecules, in agreement with various experimental studies.^{115,124,273} The measured estimates of the degree of proton transfer vary strongly in the range of two orders of magnitude depending on the employed method.^{115,124,273} Here, by simulating the system directly at molecular level with quantum chemical accuracy, the content of neutral species

in the mixture could be estimated to be 75 to 80 %, which is in good agreement with the measurement by Kanzaki et al. based on calorimetric titration.¹²⁴ An analysis of the diffusion rates of the various species present in C₁Im–HOAc shows that the diffusion of the proton is coupled to that of the molecules and ions, eliminating the option of a detached diffusion through tunnels in the liquid structure. However, the high proton conductivity exhibited by the C₁Im–HOAc system cannot be explained by a simple vehicle mechanism. The ab initio molecular dynamics simulations show a continuous and readily happening transfer of protons between neighboring species. Hydrogen bonded chain structures of neutral and ionic species can be directly observed to participate in a bond shifting mechanism, whereby the participating acid molecules near simultaneously accept and donate a proton. This mechanism is reminiscent of the Grotthuss diffusion mechanism in water,²⁷⁴ and can well explain the observed proton conductivity.

The most important insight from this study is perhaps the direct evidence of Grotthuss-like proton transfer itself, as it is not observed in pure acetic acid³²⁵ and the imidazole appears to have an enabling effect. From this, two conditions for the design of Grotthuss-enabled protic ionic liquids necessarily follow. Since such a mechanism requires that the participating species have, at the same time, a proton acceptor and a proton donor site, a certain concentration of neutral acid species must be present. At the same time, the energy barrier of the proton transfer must be sufficiently low. By means of static quantum chemical calculations, various combinations of differently functionalized imidazolium and acetate ions were tested for their likelihood to exhibit Grotthuss-like proton diffusion. *N*-methylimidazolium trifluoroacetate could be identified as good candidate and was recently investigated by Watanabe et al.⁴⁷⁸ who studied its proton transfer mechanism. Future studies can further explore the potential of pseudo-ionic liquids and expand the scope of such investigations to non-stoichiometric systems, as the conductivity maximum of such system may not lie at the equimolar composition.

Prior to its application to protic ionic liquids, the bQCE method was shown able to reproduce the temperature dependence of the ionic product of water with quantitative accuracy.⁴⁰ By extending the cluster set with ionic water clusters that contain a hydronium cation H₃O⁺ and a hydroxide anion OH⁻ the equilibrium concentration of these species in liquid water could be calculated from the cluster populations. In order to further test this approach and its applicability to other systems, the bQCE method was used to model the proton transfer equilibrium in the aqueous solutions of two weak acids. The experimental acid strengths in form of the p*K*_a values of formic and acetic acid could be reproduced with impressive accuracy, considering the simplicity of the approach and the low computational cost of the methods involved. Furthermore, it could be shown that the commonly made approximation of a constant, concentration-independent p*K*_a leads to unreasonable predictions of the dissociation degree in concentrated solutions. The bQCE

9. Influence of Complexing Additives on Mg Deposition/Dissolution in an IL

approach revealed a maximum in the ion concentration at low mole fractions, coinciding remarkably well with the experimental conductivity maximum measured for either acid. The final part of the thesis focused on ion pairing and ion association in ionic liquids. Before considering a more application-oriented scenario in a multi-component electrolyte, the fundamental aspects of ion pairing in neat ionic liquids were studied. The degree of ion pairing in neat ionic liquids is still under debate,¹³¹ with some suggesting that rather than as liquids composed entirely of ions, they should be understood as strongly diluted electrolytes composed of mostly neutral ion pairs.^{132,140} Here, the formation and life times of ion pairs in the common ionic liquid 1-butyl-3-methylimidazolium triflate ($[\text{C}_4\text{C}_1\text{Im}][\text{OTf}]$) as a model system were investigated by means of ab initio molecular dynamics simulations and static quantum chemical calculations. An analysis of the radial distribution function of the cation-anion distance in this system shows that every cation is surrounded by a solvation shell formed by an average of six anions, rather than forming a contact ion pair at close distance with one distinct anion. Such ion pairs could be shown to exist only for short time frames below 2 ps and their joint diffusion does not exceed lengths of 200 pm. Charge transfer effects were found to cause a significant decrease in the net charge of the constituent ions in well agreement with their experimentally observed ionicities. In conjunction with a rigorous review of the experimental and theoretical evidence found in literature, it was concluded that a picture of ionic liquids as systems of mostly neutral ion pairs is currently not supported. Instead, ion size effects on diffusion, charge transfer effects, and, in the case of protic ionic liquids, the degree of proton transfer might be sufficient to explain the observed ionicities.

In a combined experimental and theoretical study, the effects of the BH_4^- anion and the 18-crown-6 ether on the reversibility of Mg deposition and dissolution in 1-butyl-1-methylpyrrolidinium bis(trifluoromethylsulfonyl)imide ($[\text{C}_4\text{C}_1\text{Pyr}][\text{TFSI}]$) were investigated. The cyclic voltammograms recorded in this system at different concentrations of the various compounds show that the addition of $\text{Mg}(\text{BH}_4)_2$ and 18-crown-6 drastically increases reversibility. By quantum chemical calculations, it was shown that the ion association of Mg^{2+} and TFSI^- drastically decreases the stability of the anion against reductive decomposition and moves its reduction potential into the Mg deposition range, which leads the decomposition of the TFSI^- anion happening at the electrode instead of Mg deposition. By coordinating the cation in a planar configuration, 18-crown-6 partly displaces the TFSI^- anion from the coordination sphere of the cation and prevents its two-fold coordination to the cation. This decreases the susceptibility of the anion to reductive decomposition. Future studies may investigate the role of the BH_4^- anion. A special focus should be on identifying synergistic effects between the BH_4^- anion and the 18-crown-6 ether. In this thesis, important contributions towards the development of a secondary magnesium battery could be made.

In summary, the studies presented in this thesis aim to model liquid phases and liquid phase phenomena of both traditional molecular solvents and more complex systems such as ionic liquids. They provide useful insights into the investigated systems at a microscopic level. The bQCE method in particular was demonstrated to be a valuable tool in establishing a molecular understanding of various physico-chemical properties. In future, this will hopefully inspire its further development to realize its potential in assisting the rational design of novel solvents and electrolytes.

Appendix

A Supporting Information to Chapter 3

Assessment of the PBEh-3c composite method

The PBEh-3c composite method¹⁸⁶ was chosen for its overall good accuracy at low computational cost, making it ideal for the purpose of this article, which is to provide a fast and qualitatively satisfying method to predict miscibilities of binary systems. PBEh-3c derives its accuracy from a systematic exploitation of error cancellation in DFT calculations, combined with empirical, but well-established schemes for dispersion^{87,200} and BSSE correction.^{186,199} The method has been exhaustively tested¹⁸⁶ by its authors: It was shown to yield good results for thermochemical properties in the GMTKN30 database⁴⁷⁹ and excellent performance for non-covalent interaction energies in small and large complexes. Furthermore, it is largely free of BSSE and accounts for most interactions in a physically sound manner. The computational savings compared to the related PBE0-D3/def2-TZVP method are quite large (factor 10-30).¹⁸⁶

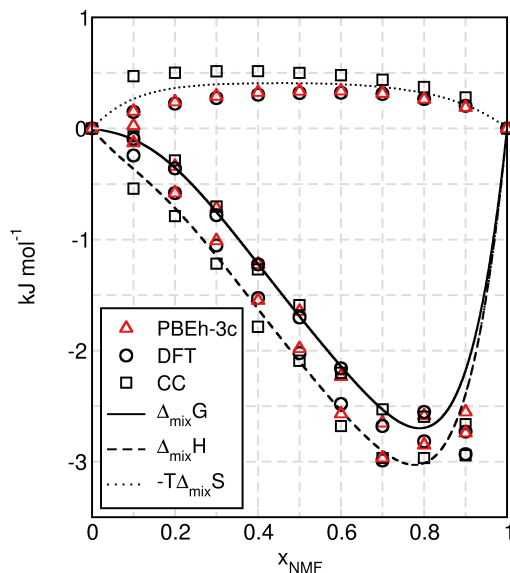


Figure A.1: Gibbs enthalpy $\Delta_{\text{mix}}G(x)$, enthalpy $\Delta_{\text{mix}}H$, and entropy $-T\Delta_{\text{mix}}S$ of mixing as a function of the NMF mole fraction x_{NMF} . Lines are meant to guide the eye. Data shown in black have been previously reported and discussed in Ref. 45. New PBEh-3c data are shown in red.

Table A.1: Adiabatic binding energies $\Delta_{\text{bind}}E$ in kJ/mol of the clusters used in Ref. 45 at different levels of theory.

	PBEh-3c	DFT	CC
Water clusters			
w1	0.0	0.0	0.0
w2	-25.2	-22.5	-20.5
w5	-190.4	-167.3	-149.1
w6	-234.2	-205.3	-184.5
w8	-375.0	-339.3	-301.5
w9	-383.9	-337.1	-301.1
NMF clusters			
c1	0.0	0.0	0.0
t1	-2.6	-3.9	-5.5
c1t1	-42.0	-45.4	-46.3
c2	-62.6	-68.6	-66.6
t2	-36.0	-39.2	-42.2
c3	-80.9	-89.3	-89.1
c3b	-100.8	-110.3	-108.5
t3	-94.1	-104.8	-104.9
t4	-163.3	-174.9	-177.7
t5	-214.0	-226.7	-232.7
t6	-264.8	-277.8	-284.8
Mixed clusters			
w1c1	-42.8	-45.2	-42.3
w1t1	-32.8	-38.2	-37.6
w1c2	-104.1	-103.7	-99.9
w1t2	-63.4	-68.0	-69.1
w2c1	-100.1	-95.2	-87.2
w2t1	-60.3	-65.9	-64.5

The range of systems investigated in this study is not much different from those that PBEh-3c was tested against. In particular water clusters and dimers of benzene are present in the GMTKN30 test sets. Since there is no reason to assume that PBEh-3c performs any better or worse than previously reported for our choice of systems, we refrained from performing reference calculations at higher levels of theory. Furthermore, we could previously show that only improving energies (but not geometries and frequencies) hardly alters QCE results, as systematic energy differences can be compensated by the mean-field approach.⁴⁵

However, we would like to assess the method by comparing it in the context of our previous work on *N*-methylformamide (NMF) and water mixtures. For this reason, we repeated all calculations reported in Ref. 45 with the PBEh-3c functional. The adiabatic binding energies reported in Table A.1 agree well with previously published data. Relatively strong overbinding can be observed for water clusters, whereas slight underbinding is observed

for the NMF clusters. The most crucial thermodynamic property is the Gibbs enthalpy of mixing, shown in Fig. A.1 and calculated according to $\Delta_{\text{mix}}G(x) = G(x) - xG(1) - (1-x)G(0)$, where $G(x)$ denotes the Gibbs enthalpy at mole fraction x . The data are compared to previous calculations at the B3LYP(D2)/def2-TZVPP level of theory, as well as to CCSD(T)(F12*)/cc-pVDZ-F12 single point calculations on top of these DFT geometries. The terms DFT and CC are used to label those calculations. For further computational details, see Ref. 45. As can be seen from Fig. A.1, there are no appreciable quantitative differences between the old and new DFT data. Considering these results and the arguments given above, we are thus confident that the PBEh-3c functional is accurate enough for our purposes.

Cluster structures

The Cartesian coordinates of all quantum chemically optimized cluster structures used in Chapter 3 and their electronic energies at the PBEh-3c/def2-mSVP level of theory are available free of charge from the online version of the Supporting Information at:
https://aip.scitation.org/doi/suppl/10.1063/1.4980032/suppl_file/si.pdf

B Supporting Information to Chapter 4

QCE and Redlich-Kister parameters

The empirical parameters a_{mf} and b_{xv} were sampled on a rectangular grid evenly distributed between 0.0 and 2.0. The mean-field parameter a_{mf} has the dimension energy·volume and is specified in $\text{J m}^3/\text{mol}$, the exclusion volume scaling parameter b_{xv} is dimensionless. In the sampling process, employing the boiling point T_{b} and the density ρ at a specified temperature as experimental reference, the pair of parameters is determined, that minimizes the deviation from the respective experimental values according to

$$\text{error} = w_{\text{d}} \frac{|\rho - \rho^{\text{exp}}|}{\rho^{\text{exp}}} + w_{\text{pt}} \frac{|T_{\text{b}} - T_{\text{b}}^{\text{exp}}|}{T_{\text{b}}^{\text{exp}}}, \quad (\text{B.1})$$

where w_{d} and w_{pt} are weighting parameters both set to 1 in this work. The experimental reference data as well as all optimized parameters are given in Table B.2.

Table B.1 lists the experimental Redlich–Kister coefficients taken from Ref. 190 as well as theoretical parameters obtained from fitting to bQCE data. The fitting was done with Gnuplot 5.0 with five fitting parameters g_n .

Table B.1: Experimental and theoretical Redlich–Kister coefficients g_n of the excess Gibbs energy of mixing $\Delta_{\text{mix}}G^{\text{e}} = x_i(1 - x_i) \sum_n g_n(1 - 2x_i)^n$ in kJ/mol for the binary systems acetonitrile/benzene (N+B), methanol/ethanol (M+E), and acetone/chloroform (A+C) at 323.15 K, 313.15 K, and 323.15 K respectively.

	N + B		M + E		A + C	
	exp.	QCE	exp.	QCE	exp.	QCE
g_0	2.697	3.353	-0.017	-0.001	-2.036	-0.926
g_1	0.028	-1.114	0.015	0.103	0.383	0.102
g_2	0.292	1.041	0.000	0.095	0.180	0.843
g_3	0.000	-0.212	0.000	-0.353	0.000	0.319
g_4	0.000	0.322	0.000	-0.605	0.000	0.695

Table B.2: Densities ρ (g/cm³) at 298.15 K, boiling points T_b (K), and empirically optimized QCE parameters a_{mf} (J m³/mol) and b_{xv} of the binary mixtures for different mole fractions x_1 of the first component. Densities and boiling points of the neat components were taken from the *CRC Handbook of Chemistry and Physics*.¹⁹⁷ Densities of the mixed systems were calculated from excess volume data from Ref. 190. Boiling points of the mixed systems were calculated using the free online service VLE-Calc,⁴⁸⁰ which uses experimental data from the Korean Thermophysical Properties Data Bank⁴⁸¹ and Dortmund Data Bank.⁴⁸²

x_1	acetonitrile + benzene				methanol + ethanol				acetone + chloroform			
	ρ	T_b	a_{mf}	b_{xv}	ρ	T_b	a_{mf}	b_{xv}	ρ	T_b	a_{mf}	b_{xv}
0.00	0.874	353.16	0.878	0.776	0.785	351.44	0.602	0.922	1.479	334.17	1.452	1.288
0.05	0.872	351.28	0.900	0.786	0.785	350.72	0.624	0.928	1.448	334.75	1.458	1.266
0.10	0.869	349.86	0.916	0.796	0.785	349.91	0.636	0.932	1.416	335.39	1.470	1.248
0.15	0.867	348.84	0.932	0.808	0.785	349.12	0.646	0.936	1.384	335.95	1.480	1.230
0.20	0.864	348.10	0.942	0.818	0.785	348.34	0.654	0.942	1.351	336.43	1.486	1.212
0.25	0.861	347.56	0.950	0.830	0.785	347.58	0.660	0.946	1.318	336.79	1.496	1.196
0.30	0.857	347.18	0.954	0.840	0.785	346.84	0.662	0.950	1.285	337.02	1.502	1.180
0.35	0.854	346.93	0.956	0.852	0.785	346.11	0.664	0.954	1.251	337.11	1.502	1.162
0.40	0.850	346.78	0.958	0.864	0.786	345.39	0.664	0.958	1.217	337.07	1.504	1.146
0.45	0.846	346.71	0.958	0.878	0.786	344.69	0.664	0.962	1.183	336.88	1.504	1.130
0.50	0.842	346.73	0.954	0.890	0.786	344.01	0.662	0.966	1.148	336.56	1.502	1.114
0.55	0.837	346.82	0.950	0.904	0.786	343.34	0.660	0.972	1.114	336.12	1.496	1.099
0.60	0.833	347.00	0.942	0.918	0.786	342.68	0.656	0.976	1.079	335.56	1.490	1.083
0.65	0.828	347.27	0.934	0.932	0.786	342.03	0.650	0.980	1.043	334.90	1.480	1.067
0.70	0.823	347.65	0.924	0.948	0.786	341.39	0.644	0.984	1.008	334.17	1.468	1.051
0.75	0.817	348.18	0.914	0.964	0.786	340.76	0.638	0.990	0.971	333.37	1.458	1.037
0.80	0.812	348.88	0.902	0.982	0.786	340.14	0.628	0.994	0.935	332.54	1.444	1.021
0.85	0.806	349.82	0.892	1.002	0.786	339.54	0.620	0.998	0.898	331.67	1.430	1.007
0.90	0.799	351.08	0.878	1.022	0.786	338.94	0.612	1.004	0.861	330.80	1.412	0.993
0.95	0.793	352.44	0.864	1.044	0.786	338.35	0.602	1.008	0.823	329.93	1.398	0.981
1.00	0.786	355.04	0.848	1.068	0.786	337.69	0.590	1.008	0.785	329.23	1.380	0.969

Cluster populations

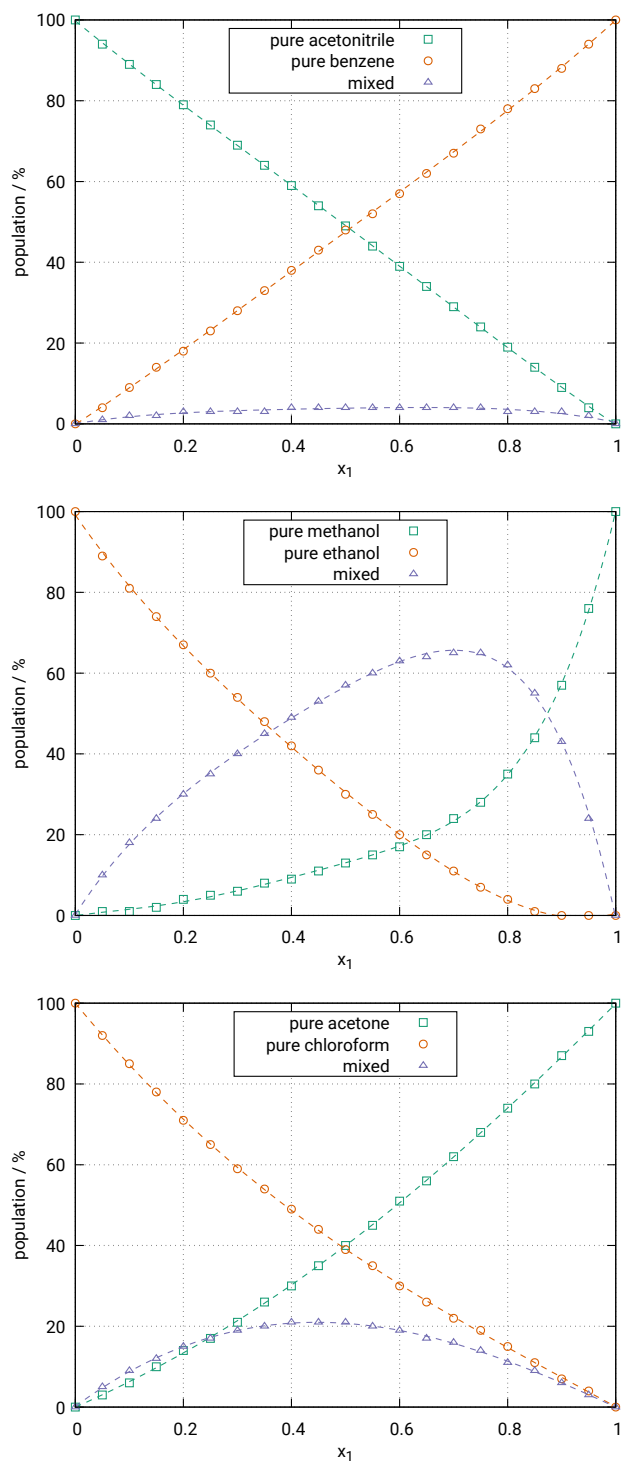


Figure B.1: Monomer normalized populations of pure and mixed clusters in the binary mixtures acetonitrile/benzene (top), methanol/ethanol (center), and acetone/chloroform (bottom) at different mole fractions at 298.15 K.

Cluster Structures

The Cartesian coordinates of all quantum chemically optimized cluster structures used in Chapter 4 and their electronic energies at the GFN-xTB level of theory are available free of charge from the online version of the Supporting Information at:

https://pubs.acs.org/doi/suppl/10.1021/acs.jced.8b00779/suppl_file/je8b00779_si_001.pdf

C Supporting Information to Chapter 5

Transpiration method

The vapor pressures and enthalpies of vaporization $\Delta_{\text{vap}}H$ of a range of alkylammonium nitrates were determined using the method of transference in a saturated stream of inert gas and applying the Clausius-Clapeyron equation. The method is especially applicable at low pressures. It has been described in detail before in Refs.^{283,483} and has proven to give results in good agreement with other established techniques. A sample of approximately 0.5 g was mixed with glass beads and placed in a thermostatted U-tube of length 10 cm and diameter 0.5 cm. A preheated helium stream was passed through the U-tube at constant temperature (± 0.1 K). The flow rate of the helium stream was measured using a soap film bubble flow meter (± 0.2 – 0.3 %) and optimized in order to reach the saturation equilibrium of the transporting gas at each temperature under study. We tested our apparatus at different flow rates of the carrier gas in order to check the lower boundary of the flow, below which, the contribution of the vapor that is condensed in the trap by diffusion becomes comparable to the transpired one. In our apparatus the contribution due to diffusion was negligible at flow rates down to $0.5 \text{ dm}^3/\text{h}$. The upper limit for our apparatus was a flow rate of $12 \text{ dm}^3/\text{h}$. Thus, we carried out the experiments using flow rates ranging from 7 to $10 \text{ dm}^3/\text{h}$ which ensured that the carrier gas was in saturated equilibrium with the coexisting liquid phase in the saturation tube. The material transported was condensed in a cold trap. The amount of condensed product in the trap was determined by weighing (± 0.0001 g).

Table C.1: Experimental vaporization enthalpies $\Delta_{\text{vap}}H$ in kJ/mol and isobaric molar heat capacities C_p in J/(mol K) for alkylammonium nitrates measured by the transpiration method.

PIL	T-range	$\Delta_{\text{vap}}H(T_{\text{av}})^a$	$C_p^l(-\Delta_1^g C_p)^b$	$\Delta_{\text{vap}}H(298.15 \text{ K})$
EAN	379–409 K	99.0	205.6 (64.5)	105.3 ± 1.3
PAN	383–401 K	103.8	239.4 (72.8)	110.6 ± 0.6
BAN	382–408 K	109.2	271.3 (81.1)	117.0 ± 2.0

^a average temperature of the transpiration experiments

^b values of isobaric molar heat capacities C_p^l and differences $\Delta_1^g C_p$ have been derived according to the procedure developed by Chickos and Acree⁴⁸³

Table C.2: Compilation of data on vaporization enthalpies $\Delta_{\text{vap}}H$ at 298.15 K for amines and different alkylammonium nitrates and acetates used for correlations (in kJ/mol).

Amine	$\Delta_{\text{vap}}H(298.15\text{K})$	PIL	$\Delta_{\text{vap}}H(298.15\text{K})$
Ethyl amine	27.6 ± 0.2^{485}	EAN	105.3 ± 1.3^a
Propylamine	31.3 ± 0.2^{485}	PAN	110.6 ± 0.6^a
Butylamine	35.8 ± 0.2^{485}	BAN	117.0 ± 2.0^a
Ethanolamine	59.6 ± 0.3^{486}	EOAN	151.1 ± 3.0^b
<i>N,N</i> -dimethylbutylamine	35.2 ± 0.6^{301}	[HDMBuA][OAc] ^c	108.6 ± 1.8^{301}
<i>N,N,N,N</i> -tetramethyl-ethane-1,2-diamine	43.1 ± 0.5^{301}	[HTMEDA][OAc] ^d	116.9 ± 0.4^{301}
<i>N,N</i> -dimethylethanolamine	47.2 ± 0.3^{301}	[HDMEtA][OAc] ^e	119.1 ± 0.7^{301}

^a from Table C.1^b calculated from the linear dependence for the experimental alkylammonium nitrates (see Fig. 5.9)^c [HDMBuA][OAc] = *N,N*-dimethylbutylammonium acetate^d [HTMEDA][OAc] = 2-(dimethylamino)-*N,N*-dimethylethylammonium acetate^e [HDMEtA][OAc] = *N,N*-dimethylethanolammonium acetate

The saturated vapor pressure p_i^{sat} at each temperature T_i was calculated from the amount of product collected within a definite period of time. Assuming the validity of Dalton's law of partial pressures applied to the helium stream saturated with the substance i of interest, values of p_i^{sat} were calculated according to the ideal gas law. The following equation:

$$R \cdot \ln p_i^{\text{sat}} = a + \frac{b}{T} + \Delta_1^g C_p \cdot \ln \left(\frac{T}{T_0} \right), \quad (\text{C.1})$$

where R is the gas constant, was fitted to the experimental data for pressure p and temperature T using a and b as adjustable parameters. The temperature T_0 appearing in the Eq. C.1 is an arbitrarily chosen reference temperature (which in this case is 298.15 K). Values of $\Delta_1^g C_p$ represent the difference of molar heat capacities of the gaseous and liquid phase. The expression for the enthalpy of vaporization at temperature T has been derived according to the Clausius-Clapeyron equation:

$$\Delta_{\text{vap}}H_m(T) = -b + \Delta_1^g C_p \cdot T. \quad (\text{C.2})$$

Values of the difference of molar heat capacities of the gaseous and liquid phase have been calculated according to a procedure developed by Chickos and Acree⁴⁸³ using the isobaric molar heat capacity of the liquid phase derived by group-additivity from the experimental values $C_p^l = 205.6 \text{ J}/(\text{mol K})$ (at 298.15 K) for EAN.⁴⁸⁴

Parameter optimization

The empirical parameters a_{mf} ($\text{J m}^3/\text{mol}$) and b_{xv} (dimensionless) were sampled on a rectangular grid evenly distributed between values of 0.0 and 2.0. The pair of parameters is chosen that minimizes the deviation from the an experimental reference W according to

$$\text{error} = w_{\rho} \frac{|\rho - \rho^{\text{exp}}|}{\rho^{\text{exp}}} + w_T \frac{|T_{\text{b}} - T_{\text{b}}^{\text{exp}}|}{T_{\text{b}}^{\text{exp}}}, \quad (\text{C.3})$$

where w_{ρ} , w_V , and w_T are weighting parameters for the individual errors of density, isobar, and boiling point, respectively, and N is the number of volumes V_i contained in the isobar. The alkylammonium nitrates were fitted against their experimental isobars reported in Ref. 487. The alkylammonium formates were fitted against their experimental density and boiling point as listed in Table 5.1. All optimized bQCE(8) parameters are given in Table C.3.

Table C.3: Empirically optimized bQCE(8) parameters.

PIL	a_{mf}	b_{xv}	error
EAN	0.1256	0.7568	0.0006
PAN	0.1357	0.7392	0.0004
BAN	0.1471	0.7288	0.0006
MAFm	0.6200	0.8450	0.0009
EAFm	0.9868	0.8342	0.0027

Quantum chemical method

Geometry optimizations and frequency analyses were performed on all structures using density functional theory (DFT) with the ORCA program package.¹⁹⁸ All calculations presented in the article were performed employing the low-cost PBEh-3c composite method by Grimme et al.¹⁸⁶ which uses a modified def2-SV(P) basis set termed def2-mSV(P). The method involves a geometrical counterpoise (gCP) correction¹⁹⁹ in order to deal with the intermolecular as well as intramolecular basis set superposition error (BSSE). Furthermore, the London dispersion energy is accounted for by Grimme’s empirical dispersion correction D3.^{87,200} Tight SCF convergence criteria were applied in each geometry optimization. Harmonic frequencies were calculated as analytical derivatives of the energy gradient.

To test the bQCE results’ dependence on the quantum chemical method and basis set, EAN was also investigated at the B3LYP/6-31+G* and B3LYP/def2-TZVP level of theory, employing the D3 and gCP correction. These results are summarized in Table C.4. While for B3LYP/6-31+G* results of similar or worse accuracy were found, all results

Table C.4: Comparison of bQCE⁰(8) and bQCE(8) results for the boiling point T_b^* in K and the vaporization enthalpy $\Delta_{\text{vap}}H$ in kJ/mol obtained with different underlying quantum chemical methods.

method	T_b^*	$\Delta_{\text{vap}}H$	p <i>K</i> _s
PBEh-3c/def2-mSVP	514	89.31	11.57
B3LYP/6-31+G*	497	89.63	-
B3LYP/def2-TZVP	501	97.80	11.33
Exp.	513	105.3	9.83

Table C.5: Computationally calculated boiling points T_b^* in K and vaporization enthalpies $\Delta_{\text{vap}}H$ in kJ/mol for different PILs and computational methods compared to their respective experimental values.

PIL	PBEh-3c		GFN-xTB		exp.	
	T_b^*	$\Delta_{\text{vap}}H$	T_b^*	$\Delta_{\text{vap}}H$	T_b	$\Delta_{\text{vap}}H$
EAN	514	89.31	626	105.82	513	105.3 ± 1.3
PAN	522	93.64	619	103.99	-	110.6 ± 0.6
BAN	519	93.82	615	110.26	-	117.0 ± 2.0
EOAN	549	-	687	-	529	151.1 ± 3.0

except the phase transition temperature were improved by employing the B3LYP/def2-TZVP method. However, the improvement is only small and does not justify the greater computational cost.

Further calculations were carried out, in which the computationally much cheaper semi-empirical GFN-xTB¹⁸⁷ method was employed. bQCE⁰(8) boiling points were calculated for alkylammonium nitrates EAN–BAN and EOAN and are listed in Table C.5. The GFN-xTB boiling points are considerably larger compared to both DFT and experimental results. In the case of EAN an error of 113 K is observed. However, an improvement of the bQCE results can be observed for the vaporization enthalpies listed in Table C.5. In the case of EAN an excellent agreement between theoretical and experimental results is achieved with an error of only 0.52 kJ/mol. The error increases for PAN and BAN but can still be considered an improvement to the PBEh-3c results. A possible explanation for these results is that the interaction energies of larger ion pair clusters are overestimated compared to the neutral parent acid and base molecules, leading to too high boiling points, but less stable if compared to the single p-IP, resulting in higher vaporization enthalpies. Proton activities could not be obtained on GFN-xTB level, since the bQCE calculations did not converge with the additional clusters included in the cluster set.

Cluster Structures

The Cartesian coordinates of all quantum chemically optimized cluster structures used in Chapter 5 and their electronic energies at the PBEh-3c/def2-mSVP level of theory are available free of charge from the online version of the Supporting Information at:
https://aip.scitation.org/doi/suppl/10.1063/1.5010791/suppl_file/esi.pdf

D Supporting Information to Chapter 6

Computational details

Systems investigated

The experimental density of 1-methylimidazolium acetate has been measured independently by several groups.^{115,320,321} For 298.15 K Hou et al.³²⁰ measured 1.1551 g/cm³, Qian et al.³²¹ measured 1.0753 g/cm³, and Doi et al.¹¹⁵ measured 1.0725 g/cm³, respectively. Hence, we set up two different sets which we abbreviate set **A** and set **B** in the following. For each simulation of set **A** and **B** we employ the densities measured by Hou and Qian respectively extrapolated to 340 K. Each set contains three simulations of 64 particles with a box size of 1880.199946 pm (**A**) or 1937.840666 pm (**B**). The three simulations in each set are labeled **ion**, **mix**, and **neu** for their different starting conditions. The particular initial compositions of each simulation are listed in Table D.1.

Table D.1: Composition of the six simulated trajectories.

System	[HC ₁ Im] ⁺	[OAc] ⁻	HOAc	C ₁ Im
ion	32	32	—	—
mix	16	16	16	16
neu	—	—	32	32

Classical Molecular Dynamics Simulations Details

All components of the systems presented in Table D.1 were built using the software package MOLDEN (version 5.4).⁴⁸⁸ The initial start geometries of the simulation boxes were generated with the aid of the program PACKMOL (version 16.228).^{489,490} Each system was simulated under periodic boundary conditions in order to avoid border/edge effects using the molecular dynamics simulator LAMMPS (version from the 14th May 2016)⁴⁶⁶ and employing parameters from the classical GAFF force field.¹⁷⁰ The simulations were performed at a temperature of 340 K, using a time step of 0.5 fs. The classical simulations served only to find an appropriate start configuration for the AIMD simulations. They involved only two steps, namely the energy minimization of the whole system by adjusting

the atom coordinates iteratively and subsequently, the equilibration of the system over 10 000 000 steps in the NVT ensemble. Here, a tolerance for the energy and the forces of 0 and 1.0E-8, respectively, was used with maximum 1000 iterations of the minimizer and maximum 10 000 000 energy/force evaluations.

Here, a tolerance for the energy and the forces of 0 and 1.0E-8, respectively, was used with maximum 1000 iterations of the minimizer and maximum 10 000 000 energy/force evaluations.

AIMD Simulations

AIMD simulations have been performed using the CP2K³³³ code and the built in QUICKSTEP⁴⁹¹ module at a density functional theory level (DFT). The molecularly optimized double- ζ basis set (MOLOPT-DZVP-SR-GTH)⁴⁹² was chosen for all atoms with the revPBE functional and the corresponding PBE Goedecker–Teter–Hutter pseudopotentials for core electrons.^{493–495} For sake of reproducibility all input-files can be obtained upon request.

The first run was an 100 step optimization run with standard conditions of the CG optimizer. In this run as well as in the next run a 200 Ry density CUTOFF criterion with the finest grid level was employed, together with multigrids number 5 (NGRID 5 and REL_CUTOFF 30) using the smoothing for the electron density (NN10_SMOOTH) and its derivative (NN10).⁴⁹¹ A correction for dispersion interactions has been added by using the DFT-D3 type of a pair potential van der Waals density functional.^{87,200} 1.0×10^{-5} has been chosen as accuracy threshold for the SCF convergence evaluation criteria. The DIIS minimizer was used to reach a faster orbital transformation via direct inversion in the iterative subspace.³³³ The maximum number of SCF iterations to be performed for one iteration was set to 100 while a maximum of 10 iterations was performed for outer SCF loops. A further equilibration over 5 ps (10 000 steps) was performed employing the keyword REGION MASSIVE, which means that for every single atom is thermostated individually for faster equilibration with a time constant of the thermostat chain of 50 fs. The temperature was set to 450 K in order to increase the sampling. Periodic boundary conditions were applied in order to avoid boundary effects.

For the final production run the density CUTOFF criterion was set to 400 Ry and the SCF convergence was set to 1.0E-6. With the aid of the Nosé-Hoover chain thermostats with a time constant of the thermostat chain of 50 the canonical (NVT) ensemble was used at a target temperature of 340 K. The total simulation time is set to 180 000, i.e., 90 ps from which the first 10 ps were discarded.

Analysis

The open source program TRAVIS (Trajectory Analyzer and Visualizer) was used to process the output trajectories of all the simulations.⁴⁶⁸ This tool can generate different kinds of functions allowing the analysis of the interaction among the components of the systems. Intra- and inter-molecular interactions can be taken into account. In this work radial distribution functions (RDFs), number integrals (NIs), and combined distribution functions (CDFs, as combination of RDFs and angular distribution functions) will have a main role to describe the interactions in play. Travis allows the user to choose a specific site of a structure (atom, center of the mass or center of a ring (COR)) to generate the distribution functions, enabling the user to discern between different interactions of the same pair of molecules. All the data obtained have been processed with either XMGRACE or gnuplot for the generation of the plots.

The dynamic nature of the proton transfer in this system can lead to problems with molecule recognition in post-processing. For convenience, we treat the system as mixture of the acetate anion, the neutral *N*-methylimidazole base and a mobile proton. However, this does not mean that the simulations are biased toward Grotthuss diffusion. The simulations are carried out as described before, i.e., with different starting conditions. The transfer of the protons is due to the fact that the electronic structure is calculated in each step according to the specific electronic structure method as described in the computational details.

Static DFT Calculations

The analysis of the thermodynamic and kinetic hindrance of the proton motion was supported by static quantum chemistry calculations. To do so, initial structures for all cations and anions were generated by systematically modifying the parent molecules following the substitution pattern shown in the main article. Afterwards, the structures for the corresponding imides and acids were generated by protonation and deprotonation of the ions.

All calculations were performed by the ORCA software package in the version 4.0.1¹⁹⁸ applying the PBEh-3c functional^{87,186,199,200} with an additional conductor-like continuum polarization model (CPCM)⁴⁷¹ to handle the effects induced by the solvent. The grid level was set to 5.

The convergence criteria for the SCF as well as for the optimization were set to the tight settings of ORCA. The dielectricity constant was chosen to be 50, which is a sophisticated guess based on the reported dielectricities of protic ionic liquids.⁴⁷²

First the separated structures were optimized. Afterwards, the full Hessian of the molecule was calculated with the aim to characterize the obtained structures as minima and furthermore, to obtain the vibrational frequencies – and therefore the Gibbs free energies.

By the systematic combination of all cations with all anions and the comparison of their Gibbs free energies with those of the corresponding imide–acid pairs the thermodynamic relations were estimated.

With the aim to evaluate kinetic effects on the proton motion, each ion was combined with its corresponding neutral entity to a hydrogen bonded complex. Based on these complexes the transition states of the proton transfer were located by applying the same method as described beforehand. The obtained structures were characterized as saddle points by calculating the full Hessian of the system and relaxing the transition state into the next minimum along the imaginary frequency.

It should be mentioned here, that the electronic energy barrier is in all cases very small and mostly even smaller than the calculated zero point energy.

In other words, the transition state is a minimum on the Gibbs free energy surface. Due to the fact that the calculation of the vibrational frequencies are based on a harmonic approximation the calculated Gibbs free energy values are not reliable for these structures. Nevertheless, due to the small barrier in electronic energy, the Gibbs free energy barriers can be assumed to be negligibly small compared to the hindrance induced by thermodynamic or diffusional effects.

The same procedure is performed with a choice of cation-anion complexes which are characterized by very similar Gibbs free energies of the cation-anion pairs compared to the corresponding imide-acid pairs.

Unfortunately, we were not able to find a stable geometry for the energetically less favored complex and consequently for the transition state of the systems with a larger thermodynamic imbalance – like the parent system. To circumvent this problem, we scanned the path of the proton by optimizing several assemblies constraining the distance of the nitrogen, oxygen, and hydrogen atom exemplary for the parent system. The resulting electronic energy profile is characterized by a very small barrier, which vanished on the Gibbs free energy surface analogously to the observations beforehand.

Results

Radial Distribution Functions

Figure D.1 shows all single RDFs calculated for each simulation of set **A** and **B**.

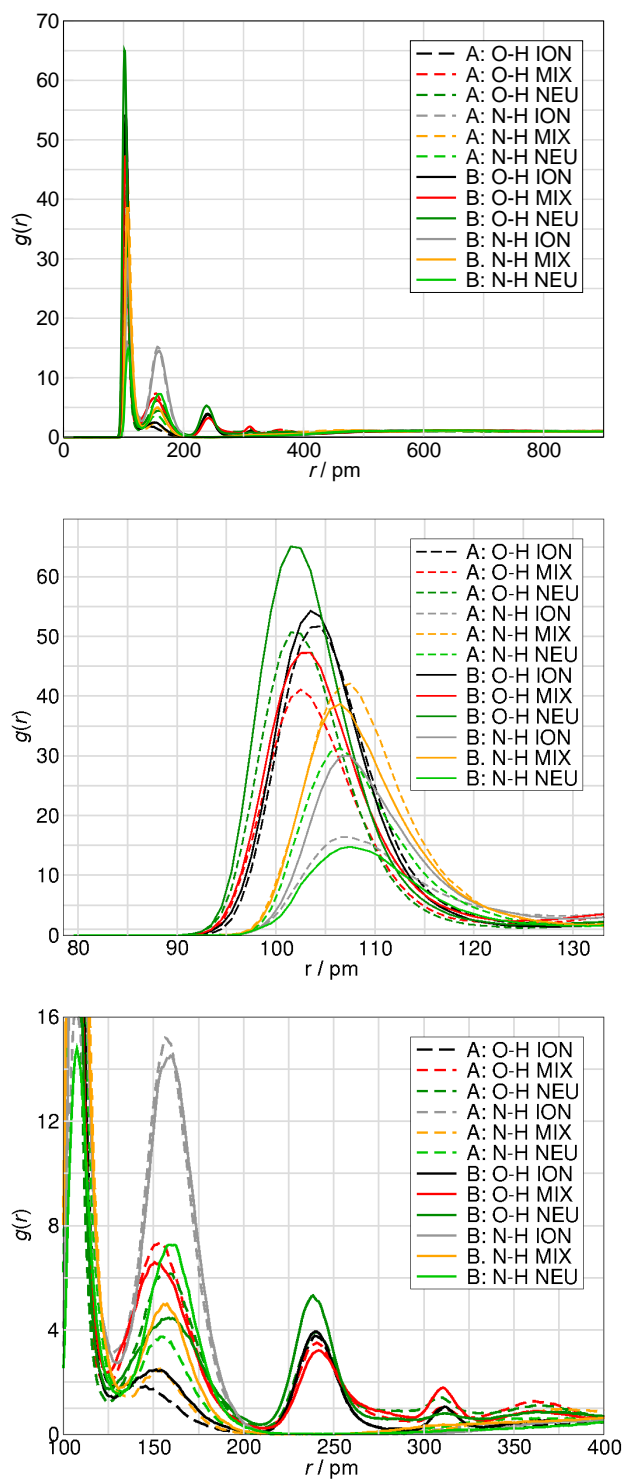


Figure D.1: Radial distribution functions of the $\text{O}\cdots\text{H}^*$ and $\text{N}\cdots\text{H}^*$ hydrogen bonds for all simulations included in set **A** (dashed lines) and **B** (solid lines)

Life Times

Figure D.2 shows all single continuous autocorrelation functions calculated for each simulation of set **A** and **B**.

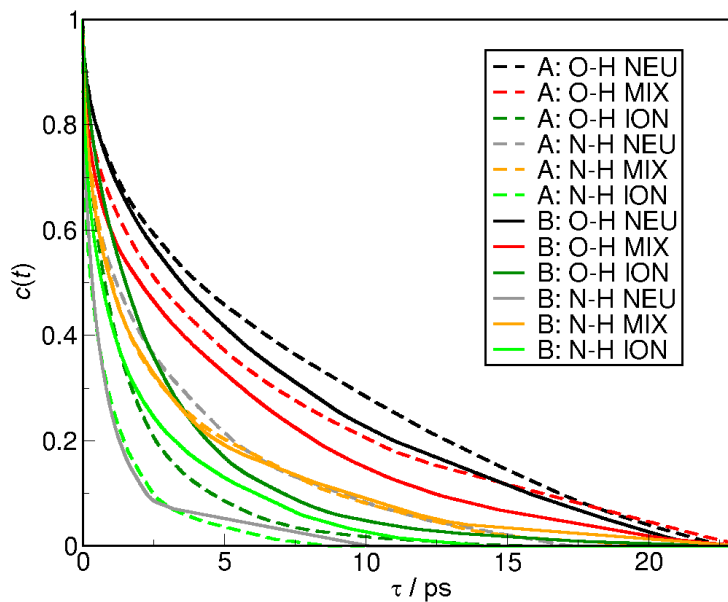


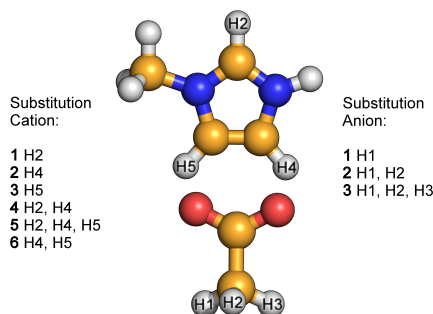
Figure D.2: Continuous autocorrelation function for the $\text{N} \cdots \text{H}^*$ and $\text{O} \cdots \text{H}^*$ association for all simulations included in set **A** (dashed lines) and **B** (solid lines).

Gibbs Energies of Reaction

Figure D.2 shows the Gibbs energy of reaction $\Delta_r G$ for the reverse proton transfer as calculated on the PBEh-3c level of theory for single ion pairs. For computational details, see Sec. D.

Table D.2: Gibbs energies ΔG in kJ/mol of the reverse proton transfer for several substituted subspecies of the parent anion and cation acetate and *N*-methylimidazolium respectively calculated on the PBEh-3c/def2-mSVP level of theory. A red colored box indicates a more neutral equilibrium state, while a blue colored box indicates a more ionic equilibrium state.

		Anion																
		Me			Parent	NH2			F			Cl			CN			
		1	2	3		1	2	3	1	2	3	1	2	3	1	2	3	
Cation	CN	1	-100.4	-100.4	-100.8	-97.9	-93.7	-88.7	-87.0	-75.7	-54.8	-33.5	-70.7	-50.6	-30.5	-60.2	-8.8	118.4
		2	-96.7	-96.7	-97.1	-94.1	-90.0	-84.9	-83.3	-72.0	-51.0	-29.7	-66.9	-46.9	-26.8	-56.5	-5.0	122.2
		3	-84.1	-84.1	-84.5	-81.6	-77.4	-72.4	-70.7	-59.4	-38.5	-17.2	-54.4	-34.3	-14.2	-43.9	7.5	134.7
		4	-147.7	-147.7	-148.1	-145.2	-141.0	-136.0	-134.3	-123.0	-102.1	-80.8	-118.0	-97.9	-77.8	-107.5	-56.1	71.1
		5	-179.1	-179.1	-179.5	-176.6	-172.4	-167.4	-165.7	-154.4	-133.5	-112.1	-149.4	-129.3	-109.2	-138.9	-87.4	39.7
		6	-127.2	-127.2	-127.6	-124.7	-120.5	-115.5	-113.8	-102.5	-81.6	-60.2	-97.5	-77.4	-57.3	-87.0	-35.6	91.6
F	1	-84.1	-84.1	-84.5	-81.6	-77.4	-72.4	-70.7	-59.4	-38.5	-17.2	-54.4	-34.3	-14.2	-43.9	7.5	134.7	
	2	-87.9	-87.9	-88.3	-85.4	-81.2	-76.1	-74.5	-63.2	-42.3	-20.9	-58.2	-38.1	-18.0	-47.7	3.8	131.0	
	3	-62.8	-62.8	-63.2	-60.2	-56.1	-51.0	-49.4	-38.1	-17.2	4.2	-33.1	-13.0	7.1	-22.6	28.9	156.1	
	4	-122.6	-122.6	-123.0	-120.1	-115.9	-110.9	-109.2	-97.9	-77.0	-55.6	-92.9	-72.8	-52.7	-82.4	-31.0	96.2	
	5	-140.6	-140.6	-141.0	-138.1	-133.9	-128.9	-127.2	-115.9	-95.0	-73.6	-110.9	-90.8	-70.7	-100.4	-49.0	78.2	
	6	-103.8	-103.8	-104.2	-101.3	-97.1	-92.0	-90.4	-79.1	-58.2	-36.8	-74.1	-54.0	-33.9	-63.6	-12.1	115.1	
Cl	1	-78.2	-78.2	-78.7	-75.7	-71.5	-66.5	-64.9	-53.6	-32.6	-11.3	-48.5	-28.5	-8.4	-38.1	13.4	140.6	
	2	-81.6	-81.6	-82.0	-79.1	-74.9	-69.9	-68.2	-56.9	-36.0	-14.6	-51.9	-31.8	-11.7	-41.4	10.0	137.2	
	3	-66.1	-66.1	-66.5	-63.6	-59.4	-54.4	-52.7	-41.4	-20.5	0.8	-36.4	-16.3	3.8	-25.9	25.5	152.7	
	4	-111.3	-111.3	-111.7	-108.8	-104.6	-99.6	-97.9	-86.6	-65.7	-44.4	-81.6	-61.5	-41.4	-71.1	-19.7	107.5	
	5	-127.2	-127.2	-127.6	-124.7	-120.5	-115.5	-113.8	-102.5	-81.6	-60.2	-97.5	-77.4	-57.3	-87.0	-35.6	91.6	
	6	-97.1	-97.1	-97.5	-94.6	-90.4	-85.4	-83.7	-72.4	-51.5	-30.1	-67.4	-47.3	-27.2	-56.9	-5.4	121.8	
Parent		-48.1	-48.1	-48.5	-45.6	-41.4	-36.4	-34.7	-23.4	-2.5	18.8	-18.4	1.7	21.8	-7.9	43.5	170.7	
Me	1	-40.6	-40.6	-41.0	-38.1	-33.9	-28.9	-27.2	-15.9	5.0	26.4	-10.9	9.2	29.3	-0.4	51.0	178.2	
	2	-43.5	-43.5	-43.9	-41.0	-36.8	-31.8	-30.1	-18.8	2.1	23.4	-13.8	6.3	26.4	-3.3	48.1	175.3	
	3	-43.5	-43.5	-43.9	-41.0	-36.8	-31.8	-30.1	-18.8	2.1	23.4	-13.8	6.3	26.4	-3.3	48.1	175.3	
	4	-34.3	-34.3	-34.7	-31.8	-27.6	-22.6	-20.9	-9.6	11.3	32.6	-4.6	15.5	35.6	5.9	57.3	184.5	
	5	-30.5	-30.5	-31.0	-28.0	-23.8	-18.8	-17.2	-5.9	15.1	36.4	-0.8	19.2	39.3	9.6	61.1	188.3	
	6	-37.7	-37.7	-38.1	-35.1	-31.0	-25.9	-24.3	-13.0	7.9	29.3	-7.9	12.1	32.2	2.5	54.0	181.2	
NH2	1	-33.1	-33.1	-33.5	-30.5	-26.4	-21.3	-19.7	-8.4	12.6	33.9	-3.3	16.7	36.8	7.1	58.6	185.8	
	2	-45.2	-45.2	-45.6	-42.7	-38.5	-33.5	-31.8	-20.5	0.4	21.8	-15.5	4.6	24.7	-5.0	46.4	173.6	
	3	-39.7	-39.7	-40.2	-37.2	-33.1	-28.0	-26.4	-15.1	5.9	27.2	-10.0	10.0	30.1	0.4	51.9	179.1	
	4	-36.8	-36.8	-37.2	-34.3	-30.1	-25.1	-23.4	-12.1	8.8	30.1	-7.1	13.0	33.1	3.3	54.8	182.0	
	5	-27.6	-27.6	-28.0	-25.1	-20.9	-15.9	-14.2	-2.9	18.0	39.3	2.1	22.2	42.3	12.6	64.0	191.2	
	6	-37.7	-37.7	-38.1	-35.1	-31.0	-25.9	-24.3	-13.0	7.9	29.3	-7.9	12.1	32.2	2.5	54.0	181.2	



E Supporting Information to Chapter 7

Computational Details

Geometry optimizations and frequency analyses were performed using density functional theory (DFT) with the ORCA program package.¹⁹⁸ All DFT calculations were performed employing the highly efficient low-cost PBEh-3c composite method by Grimme et al.,¹⁸⁶ which uses a modified def2-SV(P) basis set termed def2-mSV(P). The method includes a geometrical counterpoise (gCP) correction¹⁹⁹ in order to correct the intermolecular as well as intramolecular basis set superposition error (BSSE). To account for the long-range London dispersion effects, the method involves Grimme’s empirical dispersion correction D3.^{87,200} Tight SCF convergence criteria were applied in each geometry optimization. Harmonic frequencies were calculated as analytical derivatives of the energy gradient. The QCE and bQCE calculations were performed using the PEACEMAKER 2.5 program package,³⁹ which has successfully been used in previous studies to investigate pure liquids and binary mixtures.^{1,43–45} For all calculations pressure was fixed at 101.325 kPa and temperature ranged from 250 to 500 K. Cluster volumes were calculated using van der Waals radii taken from Bondi’s compilation.²⁰² The reference monomers of each system are the neutral, isolated acid molecules and the water molecule. Optimizations were performed using molar volumes for different compositions of the solutions over the whole sampled temperature range. The data were taken from experimental studies of Manzurola and Apelblat⁴⁹⁶ and Korpela.⁴⁹⁷ The QCE parameters a_{mf} and b_{xv} were sampled on a rectangular grid with values evenly distributed between 0.0 and 2.0. The pair of parameters was chosen so that the deviation from the experiment is minimized according to:

$$\frac{|\rho - \rho^{\text{exp}}|}{\rho^{\text{exp}}} + \frac{|T_b - T_b^{\text{exp}}|}{T_b^{\text{exp}}}. \quad (\text{E.1})$$

Cluster sets

Construction of the cluster set is the most important, but also the most critical step in the QCE method.^{39,43} A good cluster set should include all the important structure motifs that characterize the system, such as chains, rings, polycyclic structures and so on. With few exceptions, we constructed clusters up to a size of ten monomers for this

Table E.1: Calculated vaporization enthalpies $\Delta_{\text{vap}}H = H^g - H^l$ and experimental¹⁹⁷ vaporization enthalpies $\Delta_{\text{vap}}H^{\text{exp}}$ in kJ/mol as well as calculated vaporization entropies^{61,504} $\Delta_{\text{vap}}S = S^g - S^l$ and estimated experimental vaporization entropies $\Delta_{\text{vap}}S^{\text{exp}} = \Delta_{\text{vap}}H^{\text{exp}}/T_{\text{b}}$ in J/(mol K) at the boiling point of the neat acids ($T_{\text{b,fa}} = 373.95 \text{ K}^{197}$ and $T_{\text{b,aa}} = 391.25 \text{ K}^{197}$).

	$\Delta_{\text{vap}}H$	$\Delta_{\text{vap}}H^{\text{exp}}$	$\Delta_{\text{vap}}S$	$\Delta_{\text{vap}}S^{\text{exp}}$
formic acid	22.92	22.69	61.29	60.64
acetic acid	21.66	23.70	55.36	60.61

work. For the neat components water, formic acid and acetic acid, starting structures for the geometry optimization were taken from the literature.^{38–40,52,498–503} Additionally, we obtained structures by running a global energy minimization for each cluster size, using a genetic structure optimization at a classical force field level of theory. Therefore the OGOLEM framework^{168,169} and the AMBER 2016 molecular dynamics package²⁰³ with the implemented Generalized Amber Force Field (GAFF)¹⁷⁰ were used. This was especially done for the mixed clusters, but also for the neat acids to supplement the structures taken from the literature. Since the global minimum at a force field level does not necessarily correspond to the global minimum of the DFT potential energy surface, we optimized several structures for each cluster size. We added the most stable, but also energetically less favorable structures to the cluster set, since local minima are required for the Boltzmann distribution at high temperatures. The reference molecules are the *trans*-monomers **fa1-1** and **aa1-1**.

Thermodynamics and populations of the neat acids

Restricting the cluster set to neat acid clusters, we examine the thermodynamics of the vaporization process as well as the cluster populations for the neat states of the acids. Table E.1 shows excellent agreement between experimental and calculated enthalpies as well as entropies of vaporization for **fa** and good agreement for **aa**. The calculated temperature dependence of the enthalpy and entropy are shown in Fig. E.1. The small deviations between calculated and experimental vaporization entropies of **aa** probably originate from the incompleteness of the cluster set, which – through the lower number of possible states – are expected to have a significant influence on the entropy. Additionally, approximations like the harmonic oscillator or the neglect of rovibrational coupling can be error sources in the QCE method. According to Trouton’s rule, the entropy of vaporization is about 85 to 90 J/(mol K) for organic liquids.⁵⁰⁴ Although this rule fits to many experimental entropies of vaporization, our calculated as well as the experimental results for both acids are remarkably smaller. This observation indicates the existence of an ordered structure in the gas phase.

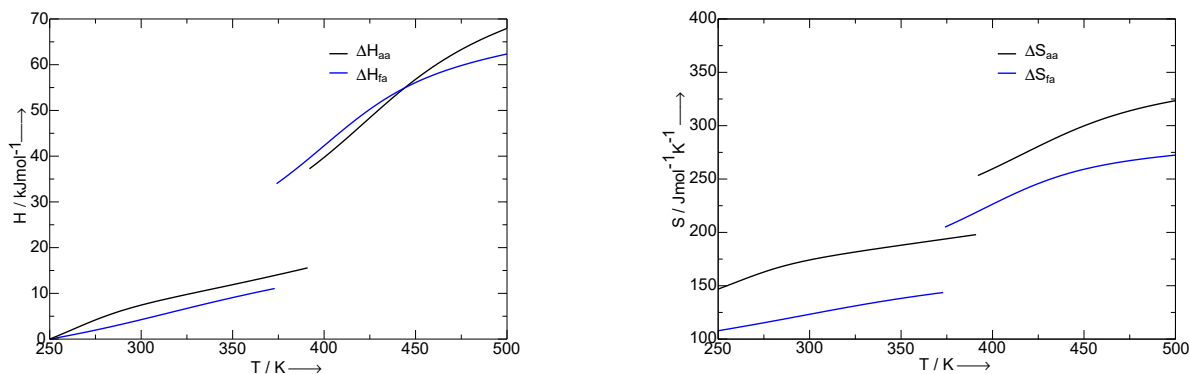


Figure E.1: Calculated temperature dependence of the enthalpy (left) and entropy (right) of formic and acetic acid.

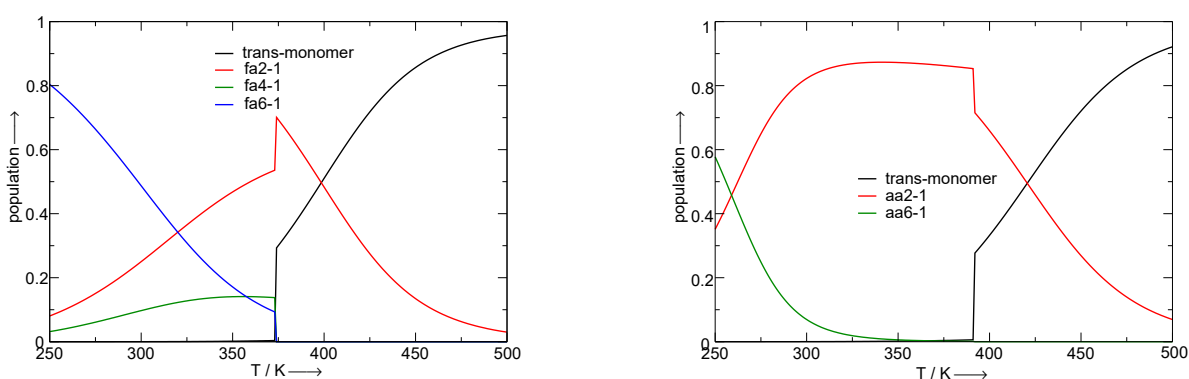


Figure E.2: Cluster populations of the most important clusters in formic (left) and acetic (right) acid.

Indeed, our calculations – in agreement with earlier measurements of vapor densities,⁵⁰⁵ spectroscopic observations^{506,507} and an earlier QCE study⁷⁷ – confirmed that carboxylic acids form C_{2h} symmetric cyclic dimers in the gas phase thus lowering the total entropy. Figure E.2 shows populations of the neat clusters which were found to be the most important ones in our QCE calculations.

Mole-fraction-dependent concentrations and cluster populations of the acetic acid/water system

Summed, monomer-normalized cluster populations for all water clusters, undissociated acetic acid clusters, undissociated acetic acid/water clusters, dissociated water clusters and dissociated acetic acid/water clusters as a function of mole fraction are shown in Fig. E.3. The population of the mixed acetic acid/water clusters increases with increasing mole fraction, whereas the neat acetic acid clusters are only populated significantly for mole fractions larger than 0.5. The population of the dissociated water clusters is about four orders of magnitude smaller than the population of the dissociated mixed clusters.

E. Supporting Information to Chapter 7

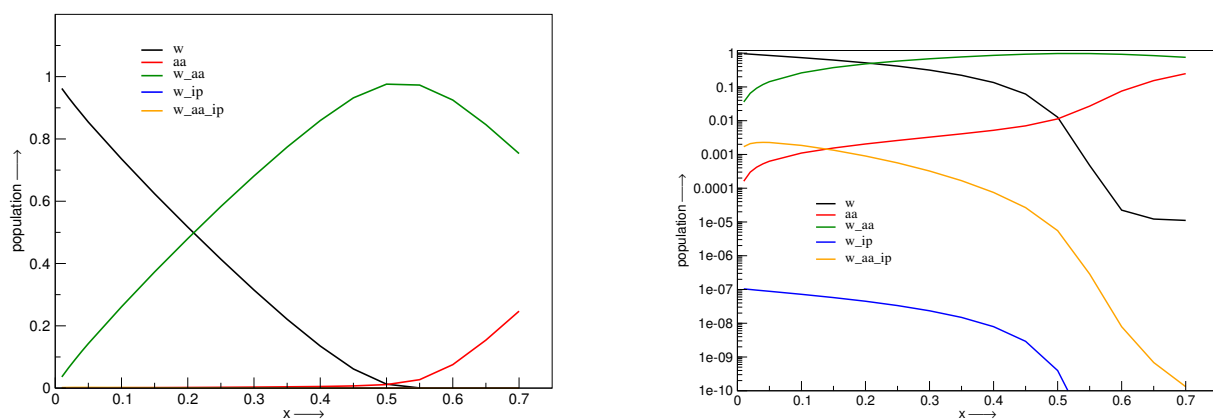


Figure E.3: Summed, monomer-normalized cluster populations of the undissociated water (w), acetic acid (aa), and mixed (w_{aa}) clusters, as well as the dissociated water (w_{ip}) and mixed clusters ($w_{aa_{ip}}$) as a function of the mole fraction with linear (left) and logarithmic (right) scale.

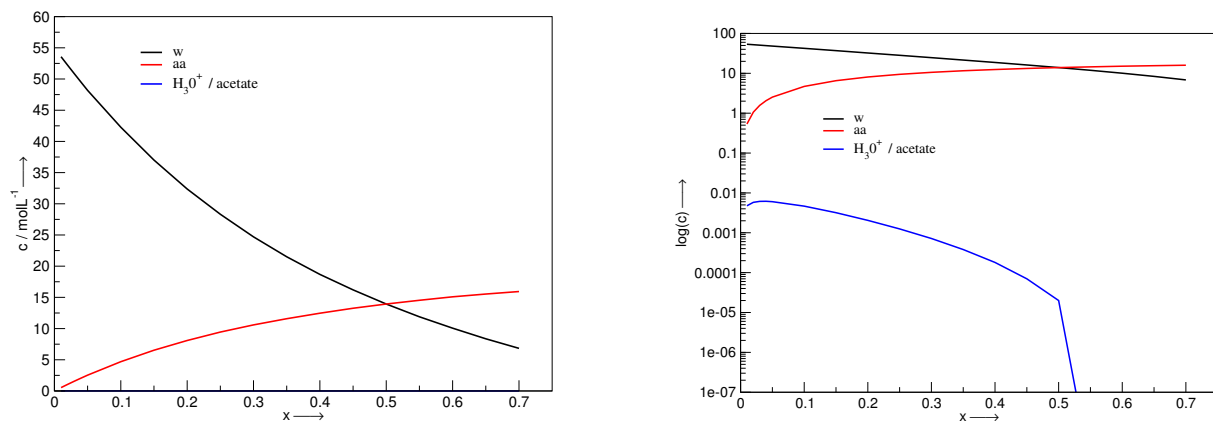


Figure E.4: Concentrations of water, acetic acid, and H_3O^+ /acetate as obtained from fully optimized QCE calculations with linear (left) and logarithmic (right) scale.

As a general trend, a decreasing population of the dissociated clusters with increasing mole fraction is observed. However, the mixed dissociated clusters show a maximum in their population at a mole fraction of 0.04.

In Fig. E.4, the calculated mole-fraction-dependent concentrations of water, acetic acid, H_3O^+ and acetate ions are shown. As expected, the water concentration decreases and the acid concentration increases continuously with increasing mole fraction. The ion concentration shows a maximum at a mole fraction of 0.04 and decreases with increasing mole fraction. At a mole fraction of 0.5 the ion concentration drastically drops due to the lack of proton accepting water molecules.

Calculating the H_3O^+ concentration using a constant pKa value

The equilibrium constant K_{eq} of the reaction



is given by

$$K_{\text{eq}} = \frac{[\text{H}_3\text{O}^+][\text{A}^-]}{[\text{H}_2\text{O}][\text{HA}]} \quad (\text{E.3})$$

with the factors being the equilibrium concentrations of all species. The concentration of the acid $[\text{HA}]$ is given by

$$[\text{HA}] = [\text{HA}]_0 - [\text{H}_3\text{O}^+] \quad (\text{E.4})$$

where the subscript 0 indicates that the concentration does not correspond to the equilibrium concentration but to the initial concentration of the acid. Combining Eqs. (E.3) and (E.4), and assuming $[\text{H}_3\text{O}^+] = [\text{A}^-]$ yields

$$K_{\text{eq}} = \frac{[\text{H}_3\text{O}^+]^2}{[\text{H}_2\text{O}][\text{HA}]_0 - [\text{H}_2\text{O}][\text{H}_3\text{O}^+]}. \quad (\text{E.5})$$

Rearranging Eq. (E.5) yields

$$[\text{H}_3\text{O}^+]^2 = K_{\text{eq}}[\text{H}_2\text{O}][\text{HA}]_0 - K_{\text{eq}}[\text{H}_2\text{O}][\text{H}_3\text{O}^+] \quad (\text{E.6})$$

and finally the quadratic equation

$$[\text{H}_3\text{O}^+]^2 + K_{\text{eq}}[\text{H}_2\text{O}][\text{H}_3\text{O}^+] - K_{\text{eq}}[\text{H}_2\text{O}][\text{HA}]_0 = 0. \quad (\text{E.7})$$

Solving Eq. (E.7) yields

$$[\text{H}_3\text{O}^+] = \frac{-K_{\text{eq}}[\text{H}_2\text{O}]}{2} + \sqrt{\left(\frac{K_{\text{eq}}[\text{H}_2\text{O}]}{2}\right)^2 + K_{\text{eq}}[\text{H}_2\text{O}][\text{HA}]_0}. \quad (\text{E.8})$$

Knowing the experimental value for $\text{p}K_{\text{a}}$, K_{eq} can be calculated by

$$K_{\text{eq}} = \frac{10^{-\text{p}K_{\text{a}}}}{[\text{H}_2\text{O}]} \quad (\text{E.9})$$

How to obtain concentrations from cluster populations

In the current implementation PEACEMAKER calculates concentrations for all clusters by summing up equilibrium populations. For example for $[\text{H}_3\text{O}^+]$,⁴⁰

$$[\text{H}_3\text{O}^+] = \left[\frac{1}{V} \sum_{i=1}^K n_i(\text{H}_3\text{O}^+) N_i \right], \quad (\text{E.10})$$

where the sum runs over all K clusters, V denotes the phase volume, N_i the equilibrium population of cluster i and $n_i(\text{H}_3\text{O}^+)$ equals the number of hydronium ions present in cluster i . This reduces the calculation of equilibrium constants to summing up equilibrium concentrations and yields the following equation for the calculation of K_a :

$$K_a = \frac{\left[\frac{1}{V} \sum_{i=1}^K n_i(\text{H}_3\text{O}^+) N_i \right] \left[\frac{1}{V} \sum_{i=1}^K n_i(\text{A}^-) N_i \right]}{\left[\frac{1}{V} \sum_{i=1}^K n_i(\text{HA}) N_i \right]}. \quad (\text{E.11})$$

Cluster structures and thermodynamic functions

Additional information including the Cartesian coordinates, electronic energies, and thermodynamic functions of all quantum chemically optimized clusters used in Chapter 7 and detailed tabulations of the calculated $\text{p}K_a$ and ion concentrations are available free of charge from the online version of the Supporting Information at:

https://onlinelibrary.wiley.com/action/downloadSupplement?doi=10.1002%2Fanie.201811839&file=anie201811839-sup-0001-misc_information.pdf

F Supporting Information to Chapter 9

Cyclic Voltammograms: Mg/Ca Deposition and Dissolution

Figures F.1a and F.1b present the first and later cycles of the CVs recorded in 0.1 M $\text{Mg}(\text{BH}_4)_2$ -containing BMP-TFSI at 10 mV/s on a glassy carbon (GC) substrate, without any additional additives. The first cycle (Fig. F.1a) shows that the reductive processes start at about 0.3 V in the cathodic scan. These, we attribute to side processes; such as electrolyte reduction or the decomposition of traces of water and other contaminants. This current signal is overlaid by a small peak at -0.3 V, whose origin is unclear so far. However, it also appears in the CV recorded in the presence of crown ether (see discussion with Fig. 9.1). At -0.8 V, the reduction current increases steeply until reaching the lower potential limit. While this may, at least in part, be attributed to Mg deposition,^{162,163,419,431,454,508} it more likely results from electrolyte decomposition. In the subsequent anodic scan, we find the typical hysteresis up to -0.7 V, with more pronounced negative currents than in the cathodic scan in this potential regime. Continuing to more positive potentials in the anodic scan, the small plateau around -0.5 V is, likely due to ongoing reduction processes, similar to those described above for the cathodic cycle. Next, a small oxidative current peak appears at 0.7 V, which may be due to either Mg dissolution or to the oxidation of side products formed upon reduction at more cathodic potentials (see above). The overall reversibility of the cathodic and anodic processes, as indicated by the overall charge ratio in these potential regimes (Coulombic efficiency), is only about 18% in the first cycle (inset in Fig. F.1a). This low reversibility further indicates that the reductive currents observed in the cathodic scan are not due to Mg deposition, at least not as a major contribution.

In the second cycle (Fig. F.1b), the initial reductive processes between 0.3 V and -0.8 V are not observed anymore, i.e., the source of the reductive (side) reactions occurring in the first cathodic cycle has either been depleted or the surface has been passivated for these processes. This is in agreement with the loss of both reductive and oxidative currents in the Mg deposition region. Due to the stronger relative loss of the cathodic currents, the Coulombic efficiency increases to 23% in the second cycle and continues to rise up to

the fifth cycle, where it stabilizes at around 35 % (see Fig. F.4). At the same time, the cathodic and anodic current contributions decrease continuously.

As evident from the rapidly decreasing plating currents observed in the CVs in Fig. F.1b, the electrode surface is increasingly passivated as a result of TFSI-decomposition, also in the presence of $\text{Mg}(\text{BH}_4)_2$. This, and also the high contribution from irreversible processes in the Mg deposition region, agrees well with previous findings for Pt electrodes in 1 M $\text{Mg}(\text{BH}_4)_2$ -containing BMP-TFSI by Watkins et al.¹⁶³ and Gao et al.,¹⁶⁰ who also observed largely irreversible Mg deposition and dissolution in this electrolyte. Furthermore, Vardar et al. reported the absence of Mg plating/stripping both from $\text{Mg}(\text{BH}_4)_2$ - and MgTFSI_2 -containing 1-methyl-1-propylpyrrolidinium-TFSI (MPP-TFSI) and suggested that TFSI^- plays a dominant role in the surface passivation, either via anion adsorption or via anion decomposition/side reactions with contaminants.¹⁶⁶ Finally, Shterenberg et al. had proposed that the formation of an initial Mg layer via Mg deposition in the first cycle on the anode in TFSI^- -containing, DME-based electrolyte is immediately followed by subsequent surface passivation, most likely due to instantaneous adsorption and decomposition of TFSI^- .⁴⁴⁸ Their results are in agreement with those reported by Tutusaus et al. in a comparable electrolyte.⁴⁵² The latter authors, however, suggested that Mg passivation occurs via the adsorption of products of the side reaction between Mg and TFSI^- .

Compared to the Mg deposition characteristics reported by Ma et al.,⁴³¹ who observed only very small losses even up to 500 cycles, the cycling stability in our experiments was much less, as indicated by a low reversibility and a rapid fading of the deposition currents. We assume that this difference is mainly caused by the different electrolyte compositions and chemistries, in particular the different Mg^{2+} coordination in tetraglyme and BMP-TFSI-based electrolytes, respectively, rather than by the water contents.

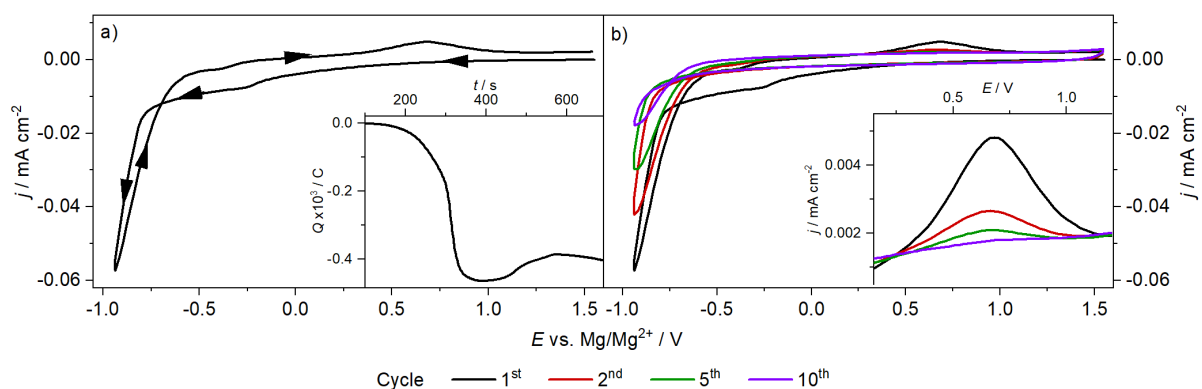


Figure F.1: First (a) and selected additional (b) potentiodynamic cycles recorded on a GC electrode in BMP-TFSI + 0.1 M $\text{Mg}(\text{BH}_4)_2$. The inset in a) shows the accumulated charge (i.e., the charge balance of Mg plating/stripping) during the first scan, the one in b) is a close-up on the anodic peak.

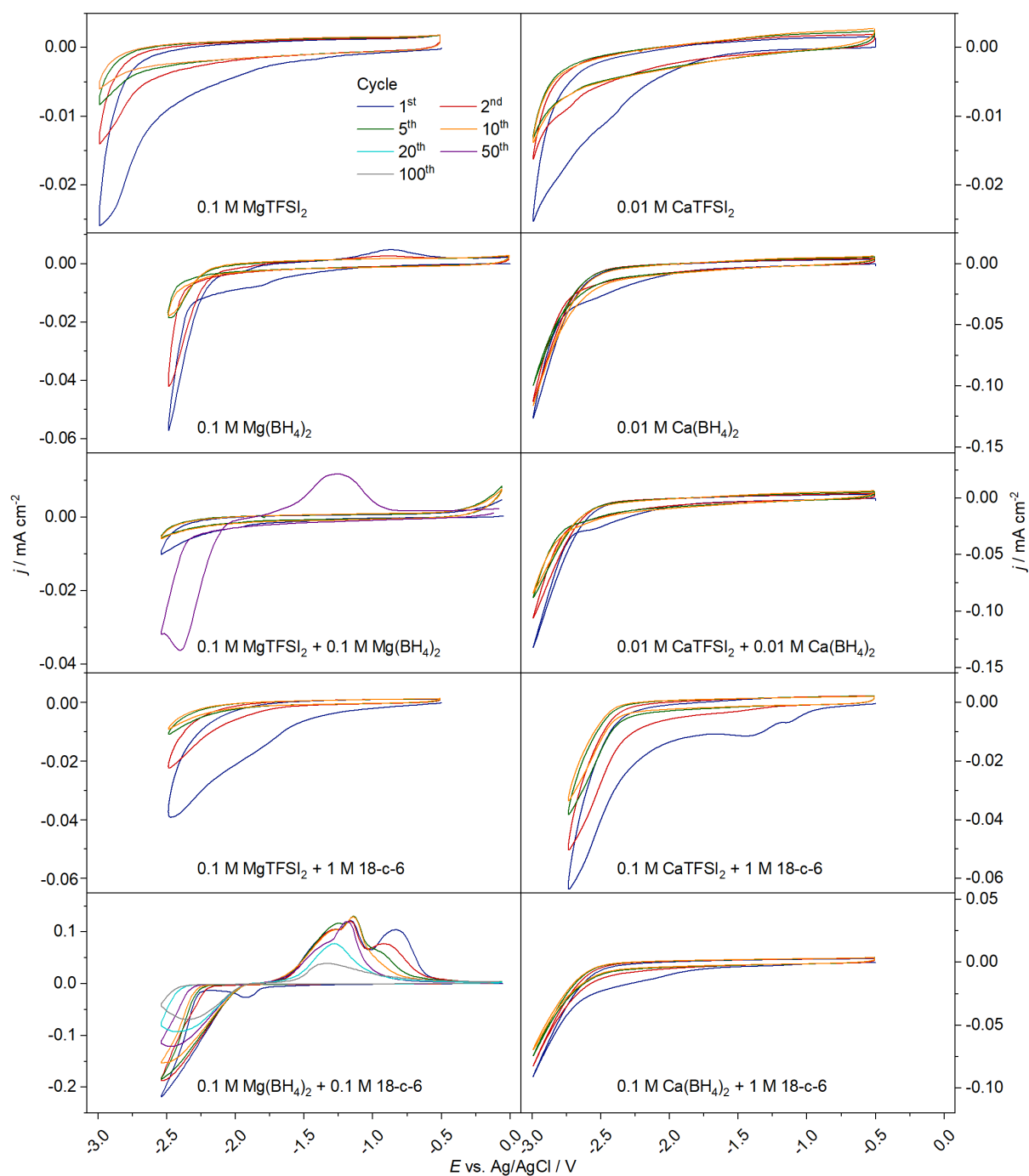


Figure F.2: Selected cycles of the CVs recorded on GC in $\text{Mg}^{2+}/\text{Ca}^{2+}$ -containing BMP-TFSI at 10 mV/s in a beaker-type half-cell setup. Reference electrodes were a Mg rod (polished in the glove box) and an Ag/AgCl wire for the $\text{Mg}^{2+}/\text{Ca}^{2+}$ -containing electrolytes, respectively. All potentials were converted to Ag/AgCl (-1.55 V vs. Mg/Mg $^{2+}$). As counter electrode, an Au wire was used. The salts employed for each electrolyte are indicated in each panel of the figure.

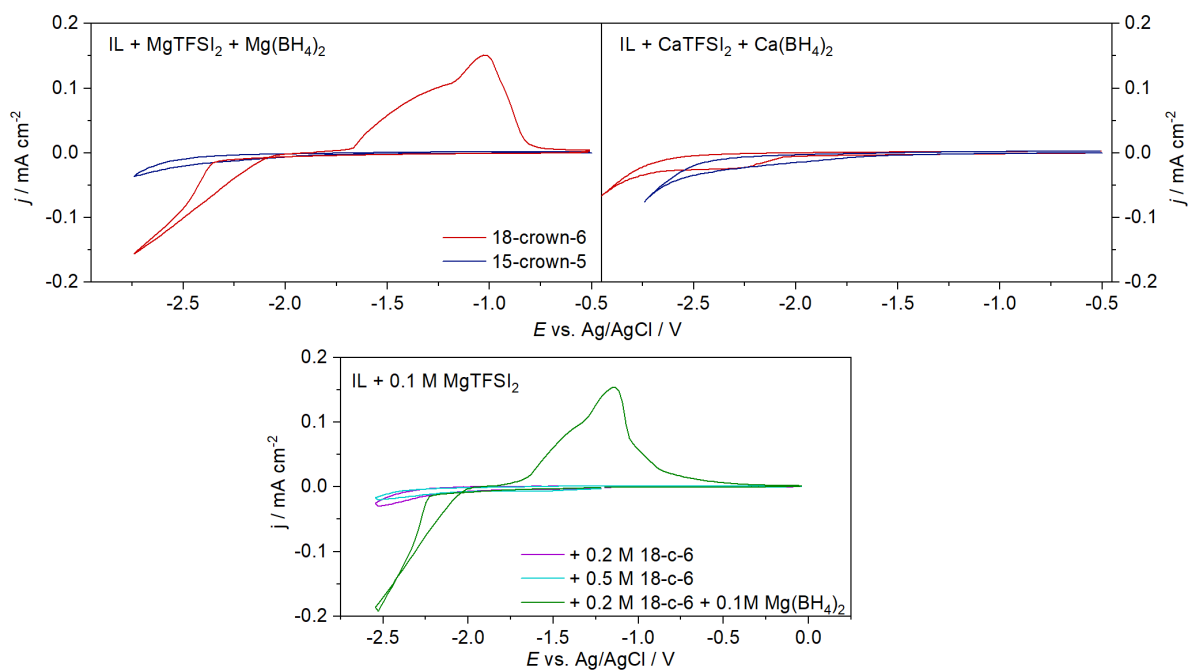
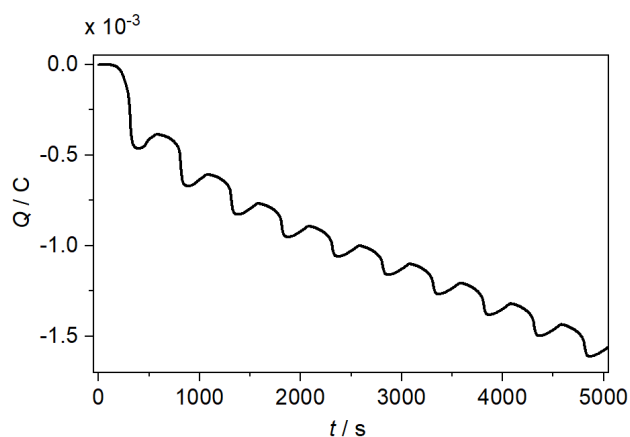


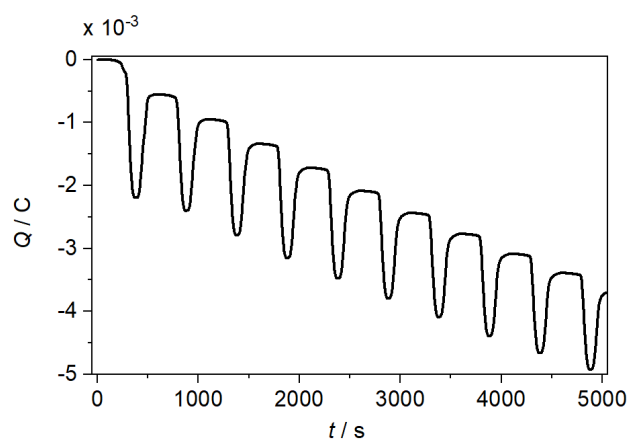
Figure F.3: First cycle of the CVs recorded on GC in Mg^{2+} - and Ca^{2+} -containing BMP-TFSI at 10 mV/s. The concentration for the Mg salts is 0.1 M, for the Ca salts 0.01 M due to its lower solubility in the IL. Reference electrodes were a Mg rod (polished in the glove box) and an Ag/AgCl wire for the Mg^{2+} -/ Ca^{2+} -containing electrolytes, respectively. All potentials were converted to Ag/AgCl (-1.55 V vs. Mg/ Mg^{2+}). As counter electrode, an Au wire was used. The salts employed for each electrolyte are indicated in each panel of the figure. The lower panel shows the first cycle of 0.1 M MgTFSI₂-containing BMP-TFSI with different 18-crown-6 ether concentrations.

Coulombic Efficiency of the Mg Deposition / Dissolution



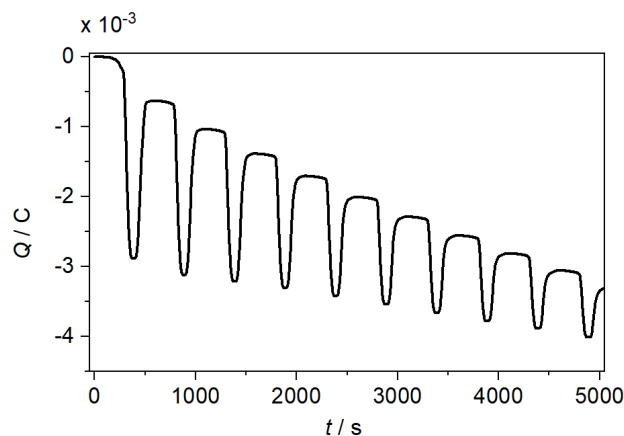
Cycle #	1	2	3	4	5	6	7	8	9	10
CE / %	17.9	23.4	29.6	34.6	39.6	36.6	41.2	33.3	38.9	36.8

Figure F.4: Charge accumulated and Coulombic efficiencies reached per cycle in the first ten cycles (5000s) of the GC substrate cycled in BMP-TFSI + 0.1 M $Mg(BH_4)_2$ at 10 mV/s.



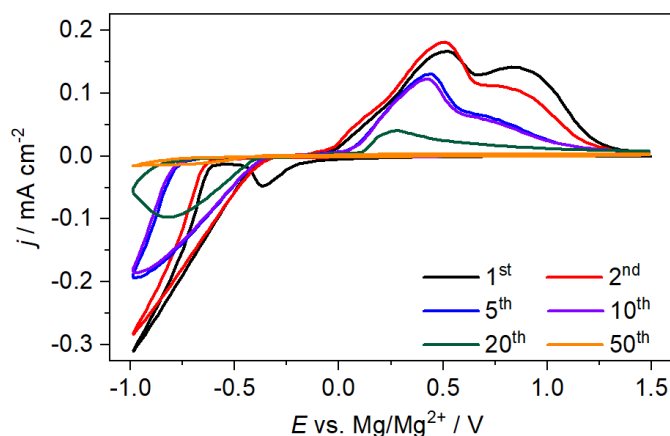
Cycle #	1	2	3	4	5	6	7	8	9	10
CE / %	17.9	23.4	29.6	34.6	39.6	36.6	41.2	33.3	38.9	36.8
Cycle #	20	30	40	50	60	70	80	90	100	
CE / %	26.7	23.4	25.1	23.9	26.4	26.3	25.7	25.0	23.5	

Figure F.5: Charge accumulated in the first ten cycles and Coulombic efficiencies reached per cycle in the first hundred cycles (5000s) of the GC substrate cycled in BMP-TFSI + 0.1 M $Mg(BH_4)_2$ + 0.1 M 18-crown-6 at 10 mV/s.



Cycle #	1	2	3	4	5	6	7	8	9	10
CE / %	78.1	84.4	83.9	83.5	82.0	81.1	80.9	80.4	76.9	75.5
Cycle #	20	30	40	50	60	70	80	90	100	
CE / %	7.6	7.2	8.8	10.6	13.5	14.6	15.4	16.1	15.6	

Figure F.6: Charge accumulated in the first ten cycles and Coulombic efficiencies reached per cycle in the first hundred cycles (5000s) of the GC substrate cycled in BMP-TFSI + 0.05 M $\text{Mg}(\text{BH}_4)_2$ + 0.1 M 18-crown-6 at 10 mV/s.



Cycle #	1	2	3	4	5	6	7	8	9	10
CE / %	74.9	81.5	80.9	80.3	79.7	78.9	78.7	78.2	77.1	75.5
Cycle #	20	30	40	50	60	70	80	90	100	
CE / %	11.7	6.6	7.1	5.4	5.9	6.2	6.8	8.0	6.8	

Figure F.7: CV recorded on GC in 0.01 M $\text{Mg}(\text{BH}_4)_2$ + 0.09 M MgTFSI_2 + 0.2 M 18-crown-6 at 10 mV/s in a beaker-type half-cell setup and Coulombic efficiencies reached per cycle in the first hundred cycles. Reference electrode is a Mg rod (polished in glove box), counter electrode an Au wire.

Simulation

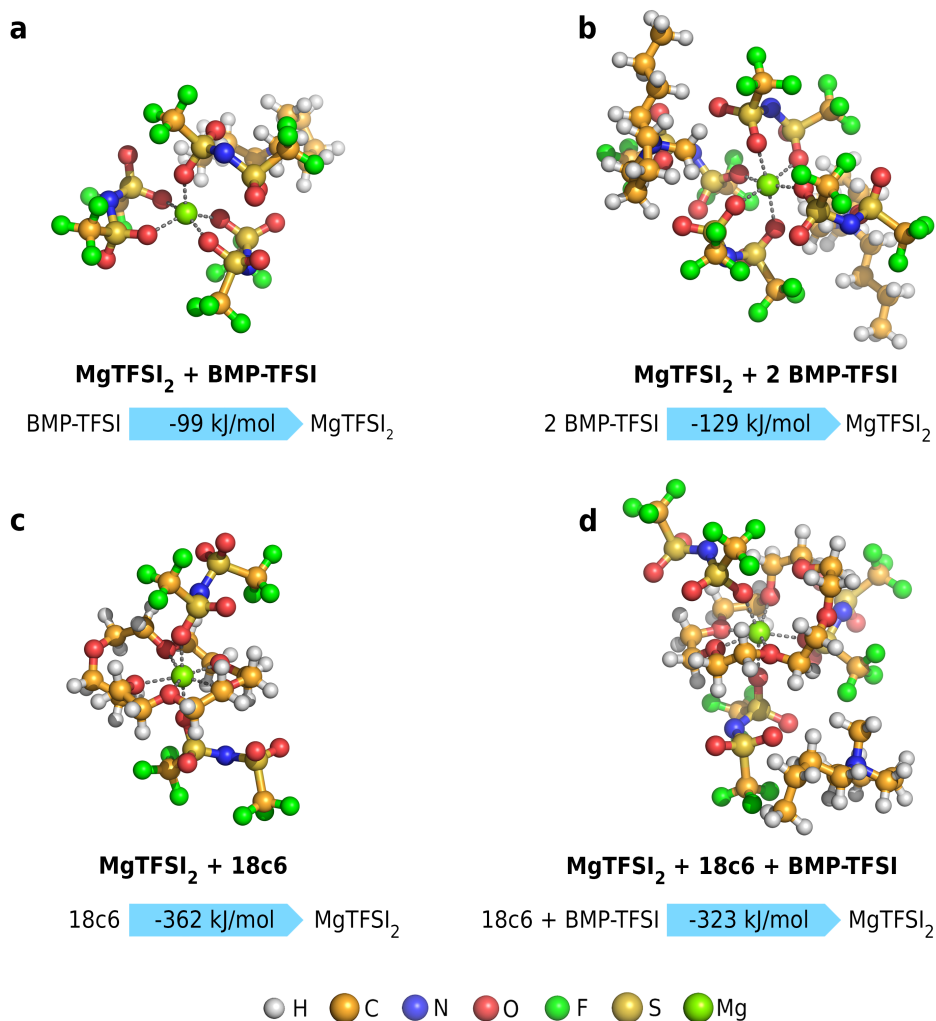


Figure F.8: Representation of a selection of clusters at different compositions cut from MD simulations and their respective coordination energies. The depicted clusters differ from the most stable configurations at their respective composition, which are shown in Fig. 9.4, and present the Mg²⁺ cation in different coordination states.

Table F.1: Calculated electron affinities and reduction potentials of BH₄⁻ and Mg(BH₄)₂.

	E_A / eV	E_{red} / V
BH ₄ ⁻	-0.36	-3.71
Mg(BH ₄) ₂	1.48	-1.87

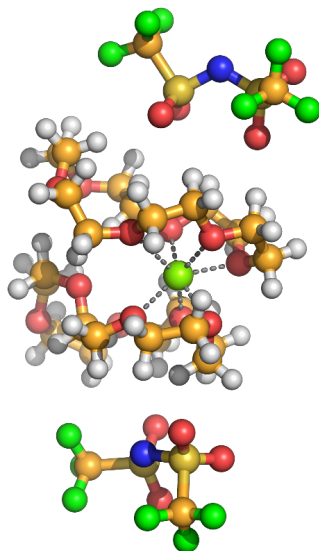


Figure F.9: Representation of the $\text{MgTFSI}_2 + 2$ 18-crown-6 cluster, in which the Mg^{2+} cation is completely surrounded by two 18-crown-6 molecules.

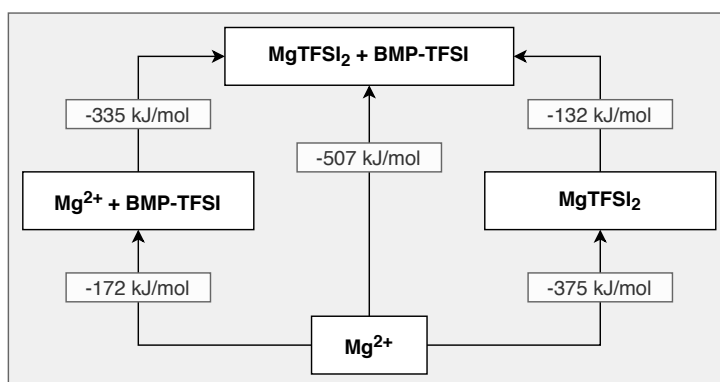


Figure F.10: Detailed scheme of the coordination energies E_c and binding energies E_b of the $\text{MgTFSI}_2 + \text{BMP-TFSI}$ cluster depicted in Fig. 9.4.

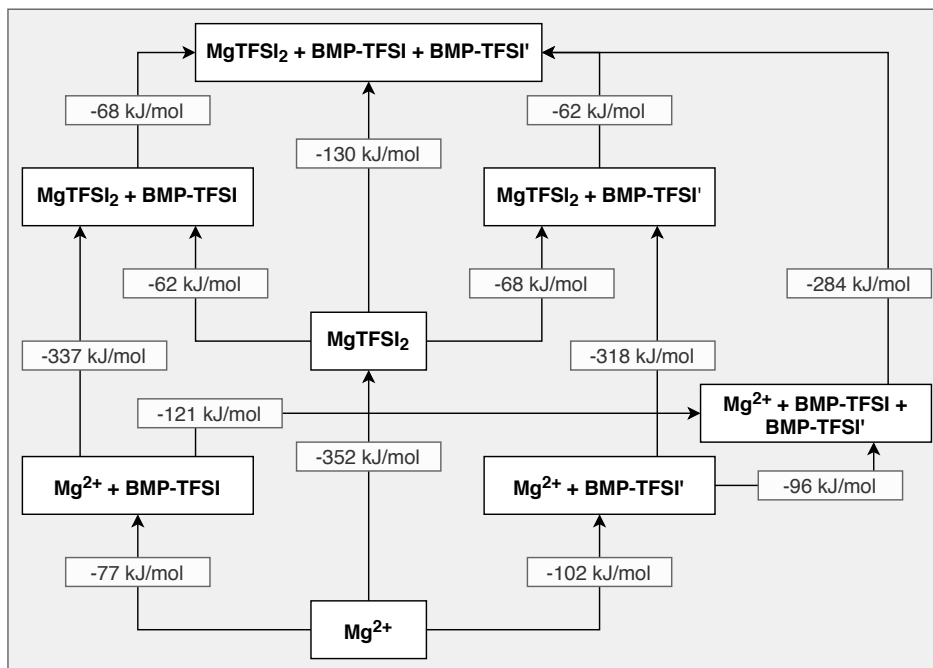


Figure F.11: Detailed scheme of the coordination energies E_c and binding energies E_b of the $MgTFSI_2 + 2$ BMP-TFSI cluster depicted in Fig. 9.4, referenced to the energy of the Mg^{2+} cation and that of the different ligands.

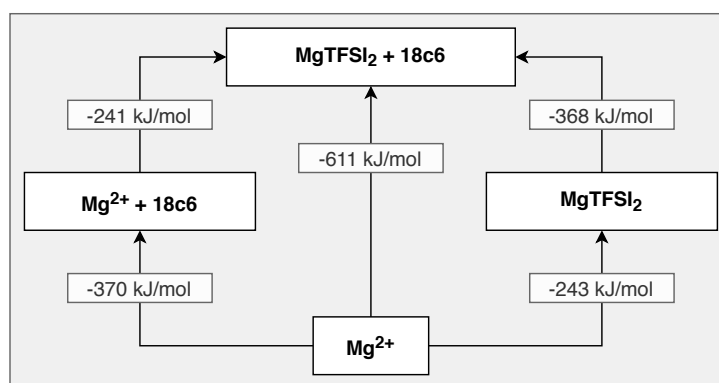


Figure F.12: Detailed scheme of the coordination energies E_c and binding energies E_b of the $MgTFSI_2 + 18c6$ cluster depicted in Fig. 9.4 referenced to the energy of the Mg^{2+} cation and that of the different ligands.

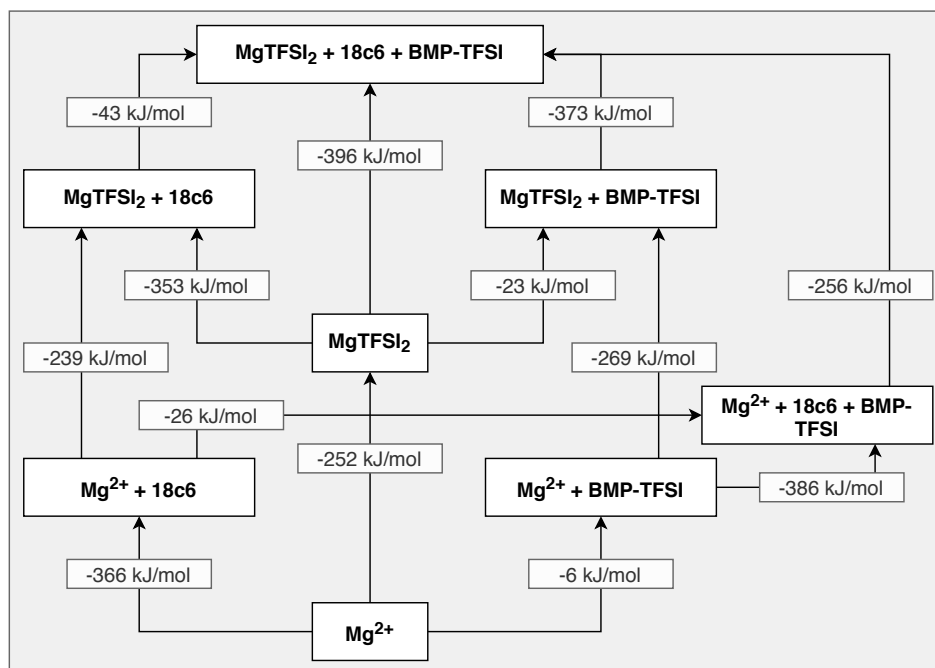


Figure F.13: Detailed scheme of the coordination energies E_c and binding energies E_b of the $\text{MgTFSI}_2 + 18\text{-crown-6} + \text{BMP-TFSI}$ cluster depicted in Fig. 9.4, referenced to the energy of the Mg^{2+} cation and that of the different ligands.

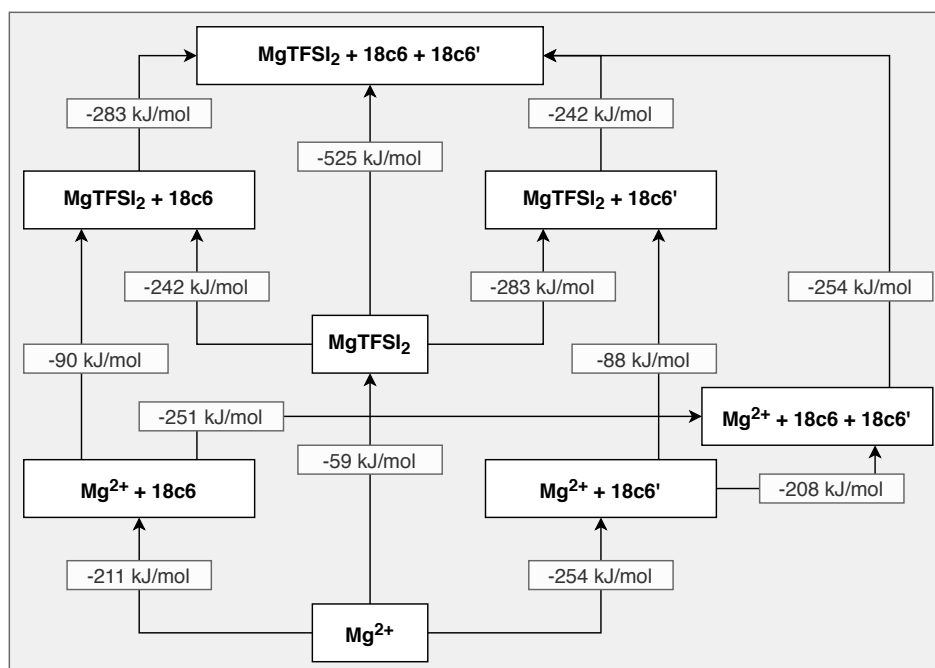


Figure F.14: Detailed scheme of the coordination energies E_c and binding energies E_b of the $\text{MgTFSI}_2 + 2 \text{ 18-crown-6}$ cluster depicted in Figure S8, referenced to the energy of the Mg^{2+} cation and that of the different ligands.

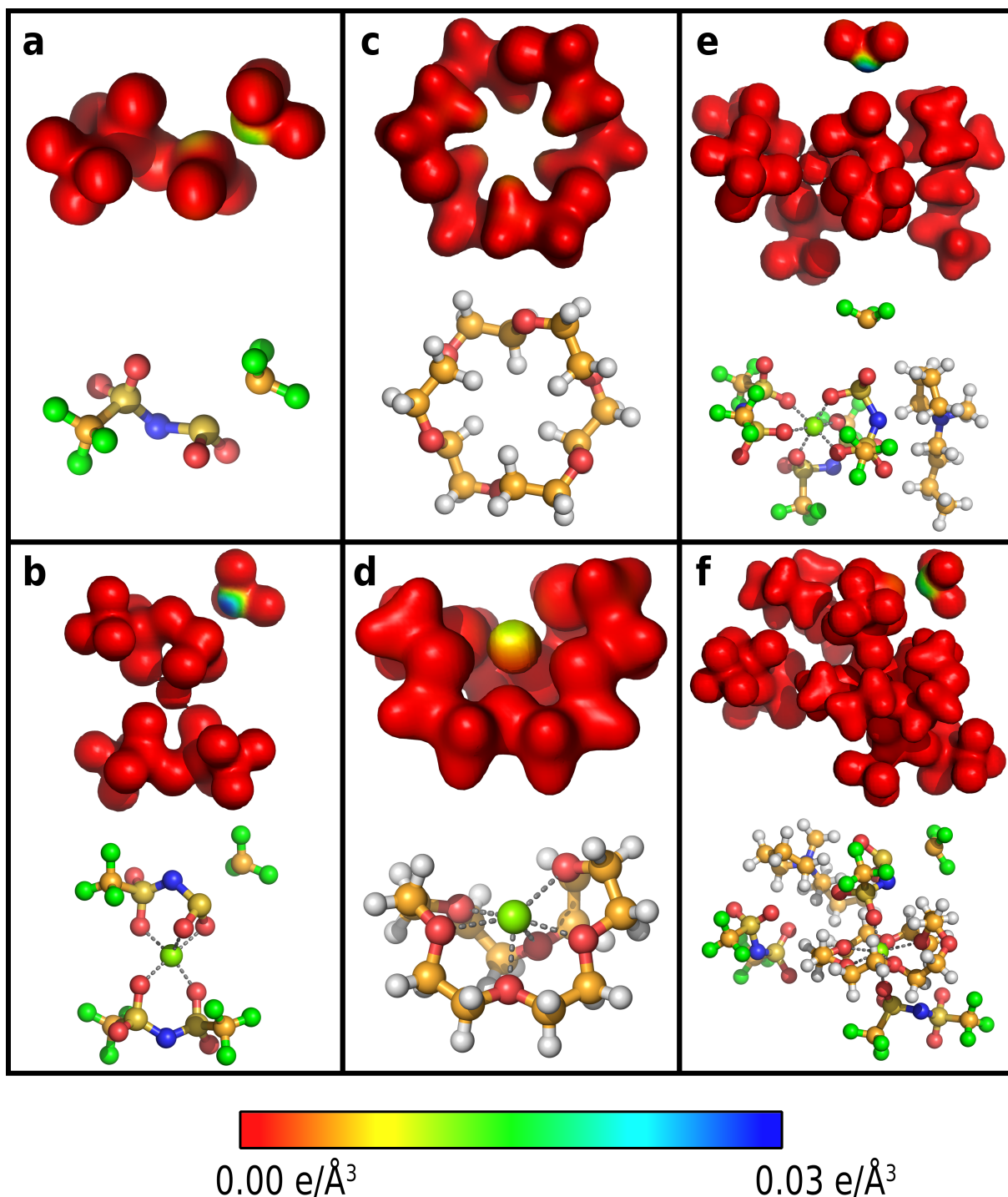


Figure F.15: Color-coded spin density distribution displayed on the electron density isosurface (value of 0.04) of the reduced clusters a) TFSI²⁻, b) [MgTFSI₂]⁻, c) [Mg²⁺ + 18c6]⁻, d) [MgTFSI₂ + BMP-TFSI]⁻, e) [MgTFSI₂ + 2 BMP-TFSI]⁻, and d) [MgTFSI₂ + 18c6 + BMP-TFSI]⁻ in their optimized geometries. Blue indicates an increased spin density, red areas are spin-free.

Bibliography

- [1] J. Ingenmey, M. von Domaros and B. Kirchner, *J. Chem. Phys.*, 2017, **146**, 154502.
- [2] J. Ingenmey, M. von Domaros, E. Perlt, S. P. Verevkin and B. Kirchner, *J. Chem. Phys.*, 2018, **148**, 193822.
- [3] J. Ingenmey, S. Gehrke and B. Kirchner, *ChemSusChem*, 2018, **11**, 1900–1910.
- [4] J. Ingenmey, J. Blasius, G. Marchelli, A. Riegel and B. Kirchner, *J. Chem. Eng. Data*, 2019, **64**, 255–261.
- [5] J. Blasius, E. Perlt, J. Ingenmey, M. von Domaros, O. Holloczki and B. Kirchner, *Angew. Chem. Int. Ed.*, 2018, **58**, 3212–3216; *Angew. Chem.*, 2018, **131**, 3245–3249.
- [6] J. Ingenmey, O. Hollóczki and B. Kirchner, in *Encyclopedia of Ionic Liquids*, ed. S. Zhang, Springer, Singapore, 2021.
- [7] I. Weber, J. Ingenmey, J. Schnaidt, B. Kirchner and R. J. Behm, *ChemElectroChem*, 2021, **8**, 390–402.
- [8] M. von Domaros, E. Perlt, J. Ingenmey, G. Marchelli and B. Kirchner, *SoftwareX*, 2018, **7**, 356–359.
- [9] R. Macchieraldo, J. Ingenmey and B. Kirchner, *Chem. Eur. J.*, 2020, **26**, 14969.
- [10] G. Marchelli, J. Ingenmey and B. Kirchner, *ChemistryOpen*, 2020, **9**, 774–785.
- [11] *Green Chemistry: Theory and Practice*, ed. P. T. Anastas and J. C. Warner, Oxford University Press, New York, 1998.
- [12] United Nations, *Transforming Our World: the 2030 Agenda for Sustainable Development*, 2015, General Assembly Resolution A/RES/70/1, http://www.un.org/ga/search/view_doc.asp?symbol=A/RES/70/1&Lang=E.
- [13] C. Flynn, E. Yamasumi, S. Fisher, D. Snow, Z. Grant, M. Kirby, P. Browning, M. Rommerskirchen and I. Russell, *Peoples' Climate Vote*, United Nations Development Programme, 2021.
- [14] C. Xu, T. A. Kohler, T. M. Lenton, J.-C. Svenning and M. Scheffer, *Proc. Natl. Acad. Sci.*, 2020, **117**, 11350–11355.
- [15] J. G. Canadell, C. Le Quéré, M. R. Raupach, C. B. Field, E. T. Buitenhuis, P. Ciais, T. J. Conway, N. P. Gillett, R. A. Houghton and G. Marland, *Proc. Natl. Acad. Sci.*, 2007, **104**, 18866–18870.
- [16] D. Fowler, P. Brimblecombe, J. Burrows, M. R. Heal, P. Grennfelt, D. S. Stevenson, A. Jowett, E. Nemitz, M. Coyle, X. Lui, Y. Chang, G. W. Fuller, M. A. Sutton, Z. Klimont, M. H. Unsworth and M. Viero, *Philos. Trans. R. Soc. A*, 2020, **378**, 20190314.

- [17] B. J. Cardinale, J. E. Duffy, A. Gonzalez, D. U. Hooper, C. Perrings, P. Venail, A. Narwani, G. M. Mace, D. Tilman, D. A. Wardle, A. P. Kinzig, G. C. Daily, M. Loreau, J. B. Grace, A. Larigauderie, D. S. Srivastava and S. Naeem, *Nature*, 2012, **486**, 59–67.
- [18] H. C. Erythropel, J. B. Zimmerman, T. M. de Winter, L. Petitjean, F. Melnikov, C. H. Lam, A. W. Lounsbury, K. E. Mellor, N. Z. Janković, Q. Tu, L. N. Pincus, M. M. Falinski, W. Shi, P. Coish, D. L. Plata and P. T. Anastas, *Green Chem.*, 2018, **20**, 1929–1961.
- [19] H. E. Murdock et al., *Renewables 2020 Global Status Report*, REN21 Secretariat, Paris, 2020.
- [20] J. B. Goodenough and Y. Kim, *Chem. Mater.*, 2010, **22**, 587–603.
- [21] J. Pallitsch, S. Reisinger and S. M. Ullreich, *Nachhaltigkeitsrecht*, 2021, **1**, 117–120.
- [22] P. P. Bawol, J. H. Thimm and H. Baltruschat, *ChemElectroChem*, 2019, **6**, 6038–6049.
- [23] A. Koellisch-Mirbach, T. Lohrmann, P. H. Reinsberg and H. Baltruschat, *J. Electroanal. Chem.*, 2020, **875**, 114560.
- [24] Y. Li and J. Lu, *ACS Energy Lett.*, 2017, **2**, 1370–1377.
- [25] V. Alizadeh, L. Esser and B. Kirchner, *J. Chem. Phys.*, 2021, **154**, 094503.
- [26] D. S. Firaha and B. Kirchner, *ChemSusChem*, 2016, **9**, 1591–1599.
- [27] B. Kirchner and B. Intemann, *Nat. Chem.*, 2016, **8**, 401–402.
- [28] A. C. Lewis, J. R. Hopkins, D. C. Carslaw, J. F. Hamilton, B. S. Nelson, G. Stewart, J. Dernie, N. Passant and T. Murrells, *Philos. Trans. R. Soc. A*, 2020, **378**, 20190328.
- [29] Ž. Knez, M. Pantić, D. Cör, Z. Novak and M. K. Hrnčič, *Chem. Eng. Process*, 2019, **141**, 107532.
- [30] F. Zheng, M. Kotobuki, S. Song, M. O. Lai and L. Lu, *J. Power Sources*, 2018, **389**, 198–213.
- [31] T. Welton, *Biophys. Rev.*, 2018, **10**, 691–706.
- [32] E. I. Izgorodina, Z. L. Seeger, D. L. A. Scarborough and S. Y. S. Tan, *Chem. Rev.*, 2017, **117**, 6696–6754.
- [33] R. Ludwig, F. Weinhold and T. C. Farrar, *J. Chem. Phys.*, 1995, **103**, 6941–6950.
- [34] R. Ludwig, F. Weinhold and T. C. Farrar, *J. Phys. Chem. A*, 1997, **101**, 8861–8870.
- [35] R. Ludwig, F. Weinhold and T. C. Farrar, *J. Chem. Phys.*, 1997, **107**, 499–507.
- [36] F. Weinhold, *J. Chem. Phys.*, 1998, **109**, 367–372.
- [37] D. Mendeleev, *Liebigs Ann.*, 1861, **119**, 1–11.

- [38] B. Kirchner, *J. Chem. Phys.*, 2005, **123**, 204116.
- [39] B. Kirchner, C. Spickermann, S. B. C. Lehmann, E. Perlt, J. Langner, M. von Domaros, P. Reuther, F. Uhlig, M. Kohagen and M. Brüssel, *Comput. Phys. Commun.*, 2011, **182**, 1428–1446.
- [40] E. Perlt, M. von Domaros, B. Kirchner, R. Ludwig and F. Weinhold, *Sci. Rep.*, 2017, **7**, 1–10.
- [41] B. Kirchner, J. Blasius, L. Esser and W. Reckien, *Adv. Theory Simul.*, 2020, 2000223.
- [42] J. Blasius and B. Kirchner, *J. Phys. Chem. B*, 2020, **124**, 7272–7283.
- [43] M. Brüssel, E. Perlt, S. B. C. Lehmann, M. von Domaros and B. Kirchner, *J. Chem. Phys.*, 2011, **135**, 194113.
- [44] G. Matisz, A.-M. Kelterer, W. M. F. Fabian and S. Kunsági-Máté, *Phys. Chem. Chem. Phys.*, 2015, **17**, 8467–8479.
- [45] M. von Domaros, S. Jähnigen, J. Friedrich and B. Kirchner, *J. Chem. Phys.*, 2016, **144**, 064305.
- [46] M. W. Chase, *J. Phys. Chem. Ref. Data Monogr.*, 1998, **9**, 1–1951.
- [47] R. Ludwig, *Angew. Chem. Int. Ed.*, 2001, **40**, 1808–1827; *Angew. Chem.*, 2001, **113**, 1856–1876.
- [48] K. Liu, J. D. Cruzan and R. J. Saykally, *Science*, 1996, **271**, 929–933.
- [49] A. G. Kalinichev and S. V. Churakov, *Chem. Phys. Lett.*, 1999, **302**, 411–417.
- [50] B. Kirchner, *Phys. Rep.*, 2007, **440**, 1–111.
- [51] B. Kirchner, F. Weinhold, J. Friedrich, E. Perlt and S. B. C. Lehmann, in *Many-Electron Approaches in Physics, Chemistry and Mathematics: A Multidisciplinary View*, ed. V. Bach and L. Delle Site, Springer, Cham, 2014, pp. 77–96.
- [52] F. Weinhold, *J. Chem. Phys.*, 1998, **109**, 373–384.
- [53] R. Ludwig and F. Weinhold, *J. Chem. Phys.*, 1999, **110**, 508–515.
- [54] R. Ludwig and F. Weinhold, *Phys. Chem. Chem. Phys.*, 2000, **2**, 1613–1619.
- [55] R. Ludwig, *ChemPhysChem*, 2007, **8**, 938–943.
- [56] A. Lenz and L. Ojamäe, *J. Chem. Phys.*, 2009, **131**, 134302.
- [57] F. Weinhold, *J. Phys. Chem. B*, 2014, **118**, 7792–7798.
- [58] S. B. C. Lehmann, C. Spickermann and B. Kirchner, *J. Chem. Theory Comput.*, 2009, **5**, 1650–1656.
- [59] M. Brüssel, E. Perlt, M. von Domaros, M. Brehm and B. Kirchner, *J. Chem. Phys.*, 2012, **137**, 164107.

- [60] R. Ludwig, *Phys. Chem. Chem. Phys.*, 2002, **4**, 5481–5487.
- [61] C. Spickermann, S. B. C. Lehmann and B. Kirchner, *J. Chem. Phys.*, 2008, **128**, 244506.
- [62] S. B. C. Lehmann, C. Spickermann and B. Kirchner, *J. Chem. Theory Comput.*, 2009, **5**, 1640–1649.
- [63] R. Ludwig, F. Weinhold and T. C. Farrar, *Mol. Phys.*, 1999, **97**, 465–477.
- [64] M. Huelsekopf and R. Ludwig, *J. Mol. Liq.*, 2000, **85**, 105–125.
- [65] M. Huelsekopf and R. Ludwig, *J. Mol. Liq.*, 2002, **98–99**, 163–171.
- [66] R. Ludwig, *ChemPhysChem*, 2005, **6**, 1369–1375.
- [67] R. Ludwig, *ChemPhysChem*, 2005, **6**, 1376–1380.
- [68] G. Matisz, W. M. F. Fabian, A.-M. Kelterer and S. Kunsági-Máté, *J. Mol. Struct. THEOCHEM*, 2010, **956**, 103–109.
- [69] G. Matisz, A.-M. Kelterer, W. M. F. Fabian and S. Kunsági-Máté, *J. Phys. Chem. B*, 2011, **115**, 3936–3941.
- [70] M. Huelsekopf and R. Ludwig, *Magn. Reson. Chem.*, 2001, **39**, S127–S134.
- [71] E. Perlt, J. Friedrich, M. von Domaros and B. Kirchner, *ChemPhysChem*, 2011, **12**, 3474–3482.
- [72] C. Spickermann, E. Perlt, M. von Domaros, M. Roatsch, J. Friedrich and B. Kirchner, *J. Chem. Theory Comput.*, 2011, **7**, 868–875.
- [73] J. Friedrich, E. Perlt, M. Roatsch, C. Spickermann and B. Kirchner, *J. Chem. Theory Comput.*, 2011, **7**, 843–851.
- [74] M. von Domaros and E. Perlt, *J. Chem. Phys.*, 2017, **146**, 124114.
- [75] R. Ludwig, F. Weinhold and T. C. Farrar, *Ber. Bunsenges. Phys. Chem.*, 1998, **102**, 197–204.
- [76] R. Ludwig, F. Weinhold and T. C. Farrar, *Ber. Bunsenges. Phys. Chem.*, 1998, **102**, 205–212.
- [77] M. A. Wendt, F. Weinhold and T. C. Farrar, *J. Chem. Phys.*, 1998, **109**, 5945–5947.
- [78] M. J. Hansen, M. A. Wendt and F. Weinhold, *Mol. Phys.*, 2003, **101**, 1147–1153.
- [79] R. Ludwig, J. Behler, B. Klink and F. Weinhold, *Angew. Chem. Int. Ed.*, 2002, **41**, 3199–3202; *Angew. Chem.*, 2002, **114**, 3331–3335.
- [80] H.-J. Song, H.-M. Xiao, H.-S. Dong and Y.-G. Huang, *J. Mol. Struct. THEOCHEM*, 2006, **767**, 67–73.
- [81] P. Borowski, J. Jaroniec, T. Janowski and K. Woliński, *Mol. Phys.*, 2003, **101**, 1413–1421.

- [82] R. Ludwig, F. Weinhold and T. C. Farrar, *Mol. Phys.*, 1999, **97**, 479–486.
- [83] R. Ludwig, O. Reis, R. Winter, F. Weinhold and T. C. Farrar, *J. Phys. Chem. B*, 1998, **102**, 9312–9318.
- [84] M. von Domaros, *Theoretical modeling of water and aqueous systems*, Ph.D. Thesis, University of Bonn, 2018.
- [85] B. Kirchner, P. J. di Dio and J. Hutter, in *Multiscale Molecular Methods in Applied Chemistry*, ed. B. Kirchner and J. Vrabc, Springer, Berlin, Heidelberg, 2011, pp. 109–153.
- [86] B. Kirchner and A. P. Seitsonen, in *High Performance Computing in Science and Engineering '07*, ed. W. E. Nagel, D. Kröner and M. Resch, Springer, Berlin, 2008, pp. 157–171.
- [87] S. Grimme, J. Antony, S. Ehrlich and H. Krieg, *J. Chem. Phys.*, 2010, **132**, 154104.
- [88] S. Gabriel, *Ber. Dtsch. Chem. Ges.*, 1888, **21**, 2664–2669.
- [89] P. Wasserscheid and T. Welton, *Ionic Liquids in Synthesis*, Wiley-VCH, Weinheim, 2008, vol. 1.
- [90] S. K. Singh and A. W. Savoy, *J. Mol. Liq.*, 2020, **297**, 112038.
- [91] *Ionic Liquids for Better Separation Processes*, ed. H. Rodríguez, Springer, Berlin, Heidelberg, 2015.
- [92] K. S. Egorova, E. G. Gordeev and V. P. Ananikov, *Chem. Rev.*, 2017, **117**, 7132–7189.
- [93] R. L. Vekariya, *J. Mol. Liq.*, 2017, **227**, 44–60.
- [94] Z. Zhu, Y. Xu, H. Li, Y. Shen, D. Meng, P. Cui, Y. Ma, Y. Wang and J. Gao, *Sep. Purif. Technol.*, 2020, **247**, 116937.
- [95] D. Corradini, F.-X. Coudert and R. Vuilleumier, *Nat. Chem*, 2016, **8**, 454–460.
- [96] M. Aghaie, N. Rezaei and S. Zendejboudi, *Renew. Sustain. Energy Rev.*, 2018, **96**, 502–525.
- [97] M. Watanabe, M. L. Thomas, S. Zhang, K. Ueno, T. Yasuda and K. Dokko, *Chem. Rev.*, 2017, **117**, 7190–7239.
- [98] H. Liu and H. Yu, *J. Mater. Sci. Technol.*, 2019, **35**, 674–686.
- [99] P. Ray, A. Balducci and B. Kirchner, *The Journal of Physical Chemistry B*, 2018, **122**, 10535–10547.
- [100] S. Denizalti, A. K. Ali, Ç. Ela, M. Ekmekci and S. Erten-Ela, *Chem. Phys. Lett.*, 2018, **691**, 373–378.
- [101] H. Weingärtner, *Angew. Chem. Int. Ed.*, 2008, **47**, 654–670; *Angew. Chem.*, 2008, **120**, 664–682.

- [102] N. V. Plechkova and K. R. Seddon, *Chem. Soc. Rev.*, 2008, **37**, 123–150.
- [103] A. S. Pensado, M. F. C. Gomes, J. N. C. Lopes, P. Malfreyt and A. A. Pádua, *Phys. Chem. Chem. Phys.*, 2011, **13**, 13518–13526.
- [104] J. K. Shah, in *Annual Reports in Computational Chemistry*, ed. D. A. Dixon, Elsevier, Amsterdam, 2018, vol. 14, pp. 95–122.
- [105] N. Byrne and C. A. Angell, *J. Mol. Biol.*, 2008, **378**, 707–714.
- [106] R. Arunkumar, C. J. Drummond and T. L. Greaves, *Front. Chem.*, 2019, **7**, 74.
- [107] P. Attri and P. Venkatesu, *Process Biochem.*, 2013, **48**, 462–470.
- [108] P. Attri, P. Venkatesu and A. Kumar, *Org. Biomol. Chem.*, 2012, **10**, 7475–7478.
- [109] J.-P. Belieres and C. A. Angell, *J. Phys. Chem. B*, 2007, **111**, 4926–4937.
- [110] T. L. Greaves and C. J. Drummond, *Chem. Rev.*, 2015, **115**, 11379–11448.
- [111] A. Mariani, M. Bonomo, X. Gao, B. Centrella, A. Nucara, R. Buscaino, A. Barge, N. Barbero, L. Gontrani and S. Passerini, *J. Mol. Liq.*, 2021, **324**, 115069.
- [112] T. L. Greaves, A. Weerawardena, C. Fong, I. Krodkiewska and C. J. Drummond, *J. Phys. Chem. B*, 2006, **110**, 22479–22487.
- [113] T. L. Greaves and C. J. Drummond, *Chem. Rev.*, 2008, **108**, 206–237.
- [114] M. Anouti, J. Jacquemin and P. Porion, *J. Phys. Chem. B*, 2012, **116**, 4228–4238.
- [115] H. Doi, X. Song, B. Minofar, R. Kanzaki, T. Takamuku and Y. Umabayashi, *Chem. Eur. J.*, 2013, **19**, 11522–11526.
- [116] M. Yoshizawa, W. Xu and C. A. Angell, *J. Am. Chem. Soc.*, 2003, **125**, 15411–15419.
- [117] S. K. Shukla and A. Kumar, *J. Phys. Chem. B*, 2013, **117**, 2456–2465.
- [118] N. Byrne, J.-P. Belieres and C. A. Angell, *Aust. J. Chem.*, 2009, **62**, 328–333.
- [119] R. Kanzaki, H. Kodamatani, T. Tomiyasu, H. Watanabe and Y. Umabayashi, *Angew. Chem. Int. Ed.*, 2016, **55**, 6266–6269; *Angew. Chem.*, 2016, **128**, 6374–6377.
- [120] K. Hashimoto, K. Fujii and M. Shibayama, *J. Mol. Liq.*, 2013, **188**, 143–147.
- [121] A. Kumar and P. Venkatesu, *Int. J. Biol. Macromol.*, 2014, **63**, 244–253.
- [122] R. Kanzaki, K. Uchida, X. Song, Y. Umabayashi and S. Ishiguro, *Anal. Sci.*, 2008, **24**, 1347–1349.
- [123] R. Kanzaki, X. Song, Y. Umabayashi and S. Ishiguro, *Chem. Lett.*, 2010, **39**, 578–579.
- [124] R. Kanzaki, H. Doi, X. Song, S. Hara, S. Ishiguro and Y. Umabayashi, *J. Phys. Chem. B*, 2012, **116**, 14146–14152.

- [125] X. Song, R. Kanzaki, S. Ishiguro and Y. Umebayashi, *Anal. Sci.*, 2012, **28**, 469–474.
- [126] J. Stoimenovski, E. I. Izgorodina and D. R. MacFarlane, *Phys. Chem. Chem. Phys.*, 2010, **12**, 10341–10347.
- [127] A. B. Patil and B. M. Bhanage, *J. Mol. Liq.*, 2018, **252**, 180–183.
- [128] I. V. Fedorova, M. A. Krestyaninov and L. P. Safonova, *J. Phys. Chem. A*, 2017, **121**, 7675–7683.
- [129] Y. Cui, J. Yin, C. Li, S. Li, A. Wang, G. Yang and Y. Jia, *Phys. Chem. Chem. Phys.*, 2016, **18**, 19731–19737.
- [130] H. Tokuda, S. Tsuzuki, M. A. B. H. Susan, K. Hayamizu and M. Watanabe, *J. Phys. Chem. B*, 2006, **110**, 19593–19600.
- [131] B. Kirchner, F. Malberg, D. S. Firaha and O. Hollóczki, *J. Phys. Condens. Matter*, 2015, **27**, 463002.
- [132] M. A. Gebbie, M. Valtiner, X. Banquy, E. T. Fox, W. A. Henderson and J. N. Israelachvili, *Proc. Natl. Acad. Sci.*, 2013, **110**, 9674–9679.
- [133] D. R. MacFarlane, M. Forsyth, E. I. Izgorodina, A. P. Abbott, G. Annat and K. Fraser, *Phys. Chem. Chem. Phys.*, 2009, **11**, 4962–4967.
- [134] P. Walden, *Z. Phys. Chem.*, 1906, **55**, 207–249.
- [135] K. E. Johnson, *Interface*, 2007, **16**, 38–41.
- [136] H. Tokuda, K. Hayamizu, K. Ishii, M. A. B. H. Susan and M. Watanabe, *J. Phys. Chem. B*, 2004, **108**, 16593–16600.
- [137] O. Hollóczki, F. Malberg, T. Welton and B. Kirchner, *Phys. Chem. Chem. Phys.*, 2014, **16**, 16880–16890.
- [138] T. Cremer, C. Kolbeck, K. R. J. Lovelock, N. Paape, R. Wölfel, P. S. Schulz, P. Wasserscheid, H. Weber, J. Thar, B. Kirchner, F. Maier and H.-P. Steinrück, *Chem. Eur. J.*, 2010, **16**, 9018–9033.
- [139] T. I. Morrow and E. J. Maginn, *J. Phys. Chem. B*, 2002, **106**, 12807–12813.
- [140] M. A. Gebbie, M. Valtiner, X. Banquy, W. A. Henderson and J. N. Israelachvili, *Proc. Natl. Acad. Sci.*, 2013, E4122.
- [141] D. A. Turton, T. Sonnleitner, A. Ortner, M. Walther, G. Hefter, K. R. Seddon, S. Stana, N. V. Plechkova, R. Buchner and K. Wynne, *Faraday Discuss.*, 2012, **154**, 145–153.
- [142] H. Weingärtner, P. Sasisanker, C. Daguene, P. J. Dyson, I. Krossing, J. M. Slattery and T. Schubert, *J. Phys. Chem. B*, 2007, **111**, 4775–4780.
- [143] Y. Zhang and E. J. Maginn, *J. Phys. Chem. Lett.*, 2015, **6**, 700–705.
- [144] M. Kohagen, M. Brehm, J. Thar, W. Zhao, F. Müller-Plathe and B. Kirchner, *J. Phys. Chem. B*, 2010, **115**, 693–702.

Bibliography

- [145] J. Thar, M. Brehm, A. P. Seitsonen and B. Kirchner, *J. Phys. Chem. B*, 2009, **113**, 15129–15132.
- [146] Q. Yang, Z. Zhang, X.-G. Sun, Y.-S. Hu, H. Xing and S. Dai, *Chem. Soc. Rev.*, 2018, **47**, 2020–2064.
- [147] A. Balducci, in *Ionic Liquids II*, ed. B. Kirchner and E. Perlt, Springer, Cham, 2017, pp. 1–27.
- [148] M. Salanne, in *Ionic Liquids II*, ed. B. Kirchner and E. Perlt, Springer, Cham, 2017, pp. 29–53.
- [149] A. Eftekhari, *Energy Storage Mater.*, 2017, **9**, 47–69.
- [150] S. Bai, P. Da, C. Li, Z. Wang, Z. Yuan, F. Fu, M. Kawecki, X. Liu, N. Sakai, J. T.-W. Wang *et al.*, *Nature*, 2019, **571**, 245–250.
- [151] K. Liu, Y. Liu, D. Lin, A. Pei and Y. Cui, *Sci. Adv.*, 2018, **4**, eaas9820.
- [152] M. A. Rahman, X. Wang and C. Wen, *J. Electrochem. Soc.*, 2013, **160**, A1759.
- [153] G. Girishkumar, B. McCloskey, A. C. Luntz, S. Swanson and W. Wilcke, *J. Phys. Chem. Lett.*, 2010, **1**, 2193–2203.
- [154] C.-S. Li, Y. Sun, F. Gebert and S.-L. Chou, *Adv. Energy Mater.*, 2017, **7**, 1700869.
- [155] P. Reinsberg, C. Bondue and H. Baltruschat, *Electrochim. Acta*, 2016, **200**, 214–221.
- [156] G. Vardar, J. G. Smith, T. Thompson, K. Inagaki, J. Naruse, H. Hiramatsu, A. E. S. Sleightholme, J. Sakamoto, D. J. Siegel and C. W. Monroe, *Chem. Mater.*, 2016, **28**, 7629–7637.
- [157] T. Khoo, A. Somers, A. A. Torriero, D. R. MacFarlane, P. C. Howlett and M. Forsyth, *Electrochim. Acta*, 2013, **87**, 701–708.
- [158] Y. Yan, T. Khoo, C. Pozo-Gonzalo, A. F. Hollenkamp, P. C. Howlett, D. R. MacFarlane and M. Forsyth, *J. Electrochem. Soc.*, 2014, **161**, A974.
- [159] C. B. Bucur, T. Gregory, A. G. Oliver and J. Muldoon, *J. Phys. Chem. Lett.*, 2015, **6**, 3578–3591.
- [160] X. Gao, A. Mariani, S. Jeong, X. Liu, X. Dou, M. Ding, A. Moretti and S. Passerini, *J. Power Sources*, 2019, **423**, 52–59.
- [161] Z. Ma, M. Forsyth, D. R. MacFarlane and M. Kar, *Green Energy Environ.*, 2019, **4**, 146–153.
- [162] M. Kar, Z. Ma, L. M. Azofra, K. Chen, M. Forsyth and D. R. MacFarlane, *Chem. Commun.*, 2016, **52**, 4033–4036.
- [163] T. Watkins, A. Kumar and D. A. Buttry, *J. Am. Chem. Soc.*, 2016, **138**, 641–650.
- [164] O. Shimamura, N. Yoshimoto, M. Matsumoto, M. Egashia and M. Morita, *J. Power Sources*, 2011, **196**, 1586–1588.

- [165] F. Sagane, K. Ogi, A. Konno and K. Kanamura, *J. Electrochem. Soc.*, 2018, **166**, A5054.
- [166] G. Vardar, A. E. S. Sleightholme, J. Naruse, H. Hiramatsu, D. J. Siegel and C. W. Monroe, *ACS Appl. Mater. Interfaces*, 2014, **6**, 18033–18039.
- [167] S. Su, Y. NuLi, N. Wang, D. Yusipu, J. Yang and J. Wang, *J. Electrochem. Soc.*, 2016, **163**, D682–D688.
- [168] J. M. Dieterich and B. Hartke, *Mol. Phys.*, 2010, **108**, 279–291.
- [169] J. M. Dieterich and B. Hartke, *J. Comp. Chem.*, 2011, **32**, 1377–1385.
- [170] J. Wang, R. M. Wolf, J. W. Caldwell, P. A. Kollman and D. A. Case, *J. Comput. Chem.*, 2004, **25**, 1157–1174.
- [171] W. L. Jorgensen, D. S. Maxwell and J. Tirado-Rives, *J. Am. Chem. Soc.*, 1996, **118**, 11225–11236.
- [172] E. Schrödinger, *Phys. Rev.*, 1926, **28**, 1049.
- [173] M. Born and R. Oppenheimer, *Ann. Phys.*, 1927, **389**, 457–484.
- [174] D. R. Hartree, *Math. Proc. Camb. Philos. Soc.*, 1928, **24**, 89–110.
- [175] V. Fock, *Z. Phys.*, 1930, **61**, 126–148.
- [176] P. Hohenberg and W. Kohn, *Phys. Rev.*, 1964, **136**, B864.
- [177] W. Kohn and L. J. Sham, *Phys. Rev.*, 1965, **140**, A1133.
- [178] J. P. Perdew, *Phys. Rev. B*, 1986, **33**, 8822; *Phys. Rev. B*, 1986, **34**, 7406.
- [179] A. D. Becke, *Phys. Rev. A*, 1988, **38**, 3098–3100.
- [180] P. J. Stephens, F. J. Devlin, C. F. Chabalowski and M. J. Frisch, *J. Phys. Chem.*, 1994, **98**, 11623–11627.
- [181] J. D. McQuarrie and D. A. Simon, *Physical Chemistry: A Molecular Approach*, University Science Books, Sausalito, 1997.
- [182] T. J. Ypma, *SIAM Rev.*, 1995, **37**, 531–551.
- [183] R. Townsend, *Implementation of an ISO/IEC 1539-2:2000 Conforming Iso_varying_string Module*, 2009, <http://www.astro.wisc.edu/~townsend/static.php?ref=iso-varying-string>.
- [184] J. Heinze, *Angew. Chem. Int. Ed.*, 1984, **23**, 831–847; *Angew. Chem.*, 1984, **96**, 823–840.
- [185] L. E. Barrosse-Antle, A. M. Bond, R. G. Compton, A. O’Mahony, E. Rogers and D. S. Silvester, *Chem. Asian J.*, 2010, **5**, 202–230.
- [186] S. Grimme, J. G. Brandenburg, C. Bannwarth and A. Hansen, *J. Chem. Phys.*, 2015, **143**, 054107.

- [187] S. Grimme, C. Bannwarth and P. Shushkov, *J. Chem. Theory Comput.*, 2017, **13**, 1989–2009.
- [188] W. Kauzmann, *Adv. Protein Chem.*, 1959, **14**, 1–63.
- [189] O. Redlich and A. T. Kister, *Ind. Eng. Chem. Res.*, 1948, **40**, 345–348.
- [190] Y. Marcus, *Solvent Mixtures: Properties and Selective Solvation*, CRC Press, Boca Raton, 2002.
- [191] G. Wypych, *Handbook of Solvents*, ChemTec Publishing, Toronto, 2001.
- [192] A. Klamt, *J. Phys. Chem.*, 1995, **99**, 2224–2235.
- [193] R. Wittig, J. Lohmann and J. Gmehling, *Ind. Eng. Chem. Res.*, 2003, **42**, 183–188.
- [194] R. Ludwig and F. Weinhold, *Phys. Chem. Chem. Phys.*, 2000, **2**, 1613–1619.
- [195] R. Ludwig and F. Weinhold, *Z. Phys. Chem.*, 2002, **216**, 659–674.
- [196] R. Ludwig, O. Reis, R. Winter, F. Weinhold and T. C. Farrar, *J. Phys. Chem. B*, 1998, **102**, 9312–9318.
- [197] W. M. Haynes, *CRC Handbook of Chemistry and Physics*, CRC Press, Boca Raton, 2014.
- [198] F. Neese, *Wiley Interdiscip. Rev. Comput. Mol. Sci.*, 2012, **2**, 73–78.
- [199] H. Kruse and S. Grimme, *J. Chem. Phys.*, 2012, **136**, 154101.
- [200] S. Grimme, S. Ehrlich and L. Goerigk, *J. Comput. Chem.*, 2011, **32**, 1456–1465.
- [201] J. L. Pascual-Ahuir, E. Silla and I. Tuñon, *J. Comput. Chem.*, 1994, **15**, 1127–1138.
- [202] A. Bondi, *J. Phys. Chem.*, 1964, **68**, 441–451.
- [203] D. A. Case, R. M. Betz, W. Botello-Smith, D. S. Cerutti, T. E. Cheatham III, T. A. Darden, R. E. Duke, T. J. Giese, H. Gohlke, A. W. Goetz, N. Homeyer, S. Izadi, P. Janowski, J. Kaus, A. Kovalenko, T. S. Lee, S. LeGrand, P. Li, C. Lin, T. Luchko, R. Luo, B. Madej, D. Mermelstein, J. M. Merz, G. Monard, H. Nguyen, H. T. Nguyen, I. Omelyan, A. Onufriev, D. R. Roe, A. Roitberg, C. Sagui, C. L. Simmerling, J. Swails, R. C. Walker, J. Wang, R. M. Wolf, X. Wu, L. Xiao, D. M. York and P. A. Kollman, *AMBER 2016*, 2016, University of California, San Francisco.
- [204] Y. Matsuda, K. Ohta, N. Mikami and A. Fujii, *Chem. Phys. Lett.*, 2009, **471**, 50–53.
- [205] D. J. Frurip, L. A. Curtiss and M. Blander, *J. Phys. Chem.*, 1978, **82**, 2555–2561.
- [206] J. E. Del Bene, *J. Am. Chem. Soc.*, 1974, **96**, 5643–5644.
- [207] D.-W. Liao, A. M. Mebel, Y.-T. Chen and S.-H. Lin, *J. Phys. Chem. A*, 1997, **101**, 9925–9934.
- [208] K. Coutinho, N. Saavedra and S. Canuto, *J. Mol. Struct. THEOCHEM*, 1999, **466**, 69–75.

- [209] Q. K. Timerghazin and G. H. Peslherbe, *J. Phys. Chem. B*, 2008, **112**, 520–528.
- [210] E. M. Cabaleiro-Lago, J. M. Hermida-Ramón, A. Peña-Gallego, E. Martínez-Núñez and A. Fernández-Ramos, *J. Mol. Struct. THEOCHEM*, 2000, **498**, 21–28.
- [211] K. Jackowski, *Chem. Phys. Lett.*, 1992, **194**, 167–171.
- [212] K. Jackowski, *J. Mol. Struct. THEOCHEM*, 1994, **303**, 239–242.
- [213] I. Nagata, K. Tamura and S. Tokuriki, *Thermochim. Acta*, 1981, **47**, 315–331.
- [214] B. W. Van de Waal, *Chem. Phys. Lett.*, 1986, **123**, 69–72.
- [215] M. Bartolomei, F. Pirani and J. M. C. Marques, *J. Comput. Chem.*, 2015, **36**, 2291–2301.
- [216] O. Engkvist, P. Hobza, H. L. Selzle and E. W. Schlag, *J. Chem. Phys.*, 1999, **110**, 5758–5762.
- [217] E. C. Lee, D. Kim, P. Jurečka, P. Tarakeshwar, P. Hobza and K. S. Kim, *J. Phys. Chem. A*, 2007, **111**, 3446–3457.
- [218] H. Takeuchi, *J. Phys. Chem. A*, 2012, **116**, 10172–10181.
- [219] R. Kusaka, Y. Inokuchi and T. Ebata, *J. Chem. Phys.*, 2012, **136**, 044304.
- [220] E. Arunan and H. S. Gutowsky, *J. Chem. Phys.*, 1993, **98**, 4294–4296.
- [221] K. O. Börnsen, S. H. Lin, H. L. Selzle and E. W. Schlag, *J. Chem. Phys.*, 1989, **90**, 1299–1306.
- [222] T. Iimori, Y. Aoki and Y. Ohshima, *J. Chem. Phys.*, 2002, **117**, 3675–3686.
- [223] L. V. Slipchenko and M. S. Gordon, *J. Phys. Chem. A*, 2008, **113**, 2092–2102.
- [224] J. Ma, D. Alfè, A. Michaelides and E. Wang, *J. Chem. Phys.*, 2009, **130**, 154303.
- [225] S. Li, V. R. Cooper, T. Thonhauser, A. Puzder and D. C. Langreth, *J. Phys. Chem. A*, 2008, **112**, 9031–9036.
- [226] R. N. Pribble and T. S. Zwier, *Science*, 1994, **265**, 75–79.
- [227] G. Graziano, *Biophys. Chem.*, 1999, **82**, 69–79.
- [228] R. C. Wilhoit, J. Chao and K. R. Hall, *J. Phys. Chem. Ref. Data*, 1985, **14**, 1–175.
- [229] J. Chao, K. R. Hall, K. N. Marsh and R. C. Wilhoit, *J. Phys. Chem. Ref. Data*, 1986, **15**, 1369–1436.
- [230] H. C. Van Ness and N. K. Kochar, *J. Chem. Eng. Data*, 1967, **12**, 38–39.
- [231] G. Marras, M. Artal, S. Otin and B. Marongiu, *Fluid Phase Equilib.*, 1994, **98**, 149–162.
- [232] I. Brown and F. Smith, *Aust. J. Chem.*, 1960, **13**, 30–37.

Bibliography

- [233] M. Góral, B. Wiśniewska-Gocłowska and A. Maćzyński, *J. Phys. Chem. Ref. Data*, 2004, **33**, 1159–1188.
- [234] A. V. Benedetti, M. Cilense, D. R. Vollet and R. C. Montone, *Thermochim. Acta*, 1983, **66**, 219–223.
- [235] D. S. Venables and C. A. Schmuttenmaer, *J. Chem. Phys.*, 2000, **113**, 11222–11236.
- [236] Y. B. Monakhova, M. V. Pozharov, T. V. Zakharova, E. K. Khvorostova, A. V. Markin, D. W. Lachenmeier, T. Kuballa and S. P. Mushtakova, *J. Solution Chem.*, 2014, **43**, 1963–1980.
- [237] S.-M. Park and W. C. Herndon, *Tetrahedron*, 1978, **34**, 3201–3205.
- [238] M. Dutkiewicz, *Chem. Phys. Lett.*, 1984, **112**, 177–181.
- [239] M. A. Villamanan and H. C. Van Ness, *J. Chem. Eng. Data*, 1984, **29**, 429–431.
- [240] A. Perera and F. Sokolić, *J. Chem. Phys.*, 2004, **121**, 11272–11282.
- [241] M. von Domaros, J. Ingenmey and B. Kirchner, In preparation.
- [242] G. Wedler and H.-J. Freund, *Lehrbuch der Physikalischen Chemie*, Wiley-VCH, Weinheim, 7th edn., 2018.
- [243] M. Kohns, S. Reiser, M. Horsch and H. Hasse, *J. Chem. Phys.*, 2016, **144**, 084112.
- [244] M. Kohns, M. Horsch and H. Hasse, *J. Chem. Phys.*, 2017, **147**, 144108.
- [245] A. Heintz, D. V. Kulikov and S. P. Verevkin, *J. Chem. Thermodyn.*, 2002, **34**, 1341–1347.
- [246] A. Heintz, S. P. Verevkin and D. Ondo, *J. Chem. Eng. Data*, 2006, **51**, 434–437.
- [247] U. Domańska and A. Marciniak, *J. Phys. Chem. B*, 2008, **112**, 11100–11105.
- [248] U. Domańska and M. Królikowska, *J. Phys. Chem. B*, 2010, **114**, 8460–8466.
- [249] M.-L. Ge, C.-Y. Lu, X.-Y. Liu, X.-B. Li, J.-Y. Chen and J.-M. Xiong, *J. Chem. Thermodyn.*, 2015, **91**, 279–285.
- [250] A. Podgorsek, J. Jacquemin, A. A. H. Pádua and M. F. Costa Gomes, *Chem. Rev.*, 2016, **116**, 6075–6106.
- [251] M. Wlazło, M. Zawadzki and U. Domańska, *J. Chem. Thermodyn.*, 2018, **116**, 316–322.
- [252] D. B. Harwood, C. J. Peters and J. I. Siepmann, *Fluid Phase Equil.*, 2016, **407**, 269–279.
- [253] T. Lazaridis and M. E. Paulaitis, *AIChE J.*, 1993, **39**, 1051–1060.
- [254] D. Frenkel and B. Smit, *Understanding Molecular Simulation*, Academic Press, Orlando, 2nd edn., 2001.

- [255] *Free Energy Calculations*, ed. C. Chipot and A. Pohorille, Springer, Berlin-Heidelberg, 2007.
- [256] G. Rutkai, A. Köster, G. Guevara-Carrion, T. Janzen, M. Schappals, C. W. Glass, M. Bernreuther, A. Wafai, S. Stephan, M. Kohns, S. Reiser, S. Deublein, M. Horsch, H. Hasse and J. Vrabec, *Comp. Phys. Commun.*, 2017, **221**, 343–351.
- [257] C. Perego, F. Giberti and M. Parrinello, *Eur. Phys. J. Spec. Top.*, 2016, **225**, 1621–1628.
- [258] C. Perego, O. Valsson and M. Parrinello, *J. Chem. Phys.*, 2018, **149**, 072305.
- [259] R. Bieshaar, A. Geiger and N. N. Medvedev, *Mol. Simul.*, 1995, **15**, 189–196.
- [260] D. Paschek, A. Geiger, J. Fischer and G. Sadowski, *Z. Phys. Chem.*, 2009, **222(4)**, 687–694.
- [261] S. Hempel, J. Fischer, D. Paschek and G. Sadowski, *Soft Mater.*, 2012, **10**, 26–41.
- [262] A. D. Cortés Morales, I. G. Economou, C. J. Peters and J. I. Siepmann, *Mol. Simul.*, 2013, **39**, 1135–1142.
- [263] J. I. Siepmann, I. R. McDonald and D. Frenkel, *J. Phys. Condens. Matter.*, 1992, **4**, 679.
- [264] H. Wang, C. Hartmann, C. Schütte and L. Delle Site, *Phys. Rev. X*, 2013, **3**, 011018.
- [265] A. Agarwal, H. Wang, C. Schütte and L. D. Site, *J. Chem. Phys.*, 2014, **141**, 034102.
- [266] T. Janzen, S. Zhang, A. Mialdun, G. Guevara-Carrion, J. Vrabec, M. He and V. Shevtsova, *Phys. Chem. Chem. Phys.*, 2017, **19**, 31856–31873.
- [267] E. C. Voutsas and D. P. Tassios, *Ind. Eng. Chem. Res.*, 1996, **35**, 1438–1445.
- [268] R. Fingerhut, W.-L. Chen, A. Schedemann, W. Cordes, J. Rarey, C.-M. Hsieh, J. Vrabec and S.-T. Lin, *Ind. Eng. Chem. Res.*, 2017, **56**, 9868–9884.
- [269] C.-K. Chang, W.-L. Chen, D. T. Wu and S.-T. Lin, *Ind. Eng. Chem. Res.*, 2018, **57**, 11229–11238.
- [270] F. Jirasek, J. Burger and H. Hasse, *Ind. Eng. Chem. Res.*, 2018, **57**, 7310–7313.
- [271] W. Acree Jr and J. S. Chickos, *J. Phys. Chem. Ref. Data*, 2016, **45**, 033101.
- [272] V. N. Emel’yanenko, G. Boeck, S. P. Verevkin and R. Ludwig, *Chem. Eur. J.*, 2014, **20**, 11640–11645.
- [273] K. Chen, Y. Wang, J. Yao and H. Li, *J. Phys. Chem. B*, 2017, **122**, 309–315.
- [274] B. Kirchner, *ChemPhysChem*, 2007, **8**, 41–43.
- [275] S. Zhang, X. Lu, Q. Zhou, X. Li, X. Zhang and S. Li, *Ionic Liquids: Physicochemical Properties*, Elsevier, Amsterdam, 2009.
- [276] R. A. Lovett and A. Ben-Naim, *J. Chem. Phys.*, 1969, **51**, 3108–3119.

Bibliography

- [277] L. Pauling, in *Hydrogen Bonding*, ed. D. Hadzi and H. W. Thompson, Pergamon Press, Oxford, 1959, pp. 1–6.
- [278] G. E. Walrafen, in *Water: A Comprehensive Treatise*, ed. F. Franks, Springer, Boston, 1971, pp. 151–214.
- [279] H. S. Frank and A. S. Quist, *J. Chem. Phys.*, 1961, **34**, 604–611.
- [280] G. Némethy and H. A. Scheraga, *J. Chem. Phys.*, 1962, **36**, 3401–3417.
- [281] G. Wada, *Bull. Chem. Soc. Jpn.*, 1961, **34**, 955–962.
- [282] S. Bouzón Capelo, T. Méndez-Morales, J. Carrete, E. López Lago, J. Vila, O. Cabeza, J. R. Rodriguez, M. Turmine and L. M. Varela, *J. Phys. Chem. B*, 2012, **116**, 11302–11312.
- [283] S. P. Verevkin, in *Experimental Thermodynamics: Measurement of the Thermodynamic Properties of Multiple Phases*, ed. R. D. Weir and T. W. De Loos, Elsevier, Amsterdam, 2005, vol. 7, pp. 6–30.
- [284] F. Malberg, O. Hollóczki, M. Thomas and B. Kirchner, *Struct. Chem.*, 2015, **26**, 1343–1349.
- [285] H. Tokuda, K. Hayamizu, K. Ishii, M. A. B. H. Susan and M. Watanabe, *J. Phys. Chem. B*, 2005, **109**, 6103–6110.
- [286] K. Ueno, H. Tokuda and M. Watanabe, *Phys. Chem. Chem. Phys.*, 2010, **12**, 1649–1658.
- [287] E. Bodo, S. Mangialardo, F. Ramondo, F. Ceccacci and P. Postorino, *J. Phys. Chem. B*, 2012, **116**, 13878–13888.
- [288] R. Ludwig, *Phys. Chem. Chem. Phys.*, 2008, **10**, 4333–4339.
- [289] W. Kurniadi and K. R. Brower, *J. Org. Chem.*, 1994, **59**, 5502–5505.
- [290] *Electrodeposition from Ionic Liquids*, ed. F. Endres, D. MacFarlane and A. Abbott, Wiley-VCH, Weinheim, 2008.
- [291] A. Stark, P. Behrend, O. Braun, A. Müller, J. Ranke, B. Ondruschka and B. Jastorff, *Green Chem.*, 2008, **10**, 1152–1161.
- [292] S. Zahn, K. Wendler, L. Delle Site and B. Kirchner, *Phys. Chem. Chem. Phys.*, 2011, **13**, 15083–15093.
- [293] R. Ludwig and U. Kragl, *Angew. Chem. Int. Ed.*, 2007, **46**, 6582–6584; *Angew. Chem.*, 2007, **119**, 6702–6704.
- [294] S. Aparicio, M. Atilhan and F. Karadas, *Ind. Eng. Chem. Res.*, 2010, **49**, 9580–9595.
- [295] D. H. Zaitsau, V. N. Emel'yanenko, P. Stange, C. Schick, S. P. Verevkin and R. Ludwig, *Angew. Chem. Int. Ed.*, 2016, **55**, 11682–11686; *Angew. Chem.*, 2016, **128**, 11856–11860.

- [296] F. M. S. Ribeiro, C. F. R. A. C. Lima, I. C. M. Vaz, A. S. M. C. Rodrigues, E. Sapei, A. Melo, A. M. S. Silva and L. M. N. B. F. Santos, *Phys. Chem. Chem. Phys.*, 2017, **19**, 16693–16701.
- [297] J. Vitorino, C. E. S. Bernardes and M. E. Minas da Piedade, *Phys. Chem. Chem. Phys.*, 2012, **14**, 4440–4446.
- [298] M. Horikawa, N. Akai, A. Kawai and K. Shibuya, *J. Phys. Chem. A*, 2014, **118**, 3280–3287.
- [299] P. Atkins and J. de Paula, *Atkins' Physical Chemistry*, Oxford University Press, Oxford, 2006.
- [300] K. Shimizu, M. Tariq, M. F. C. Gomes, L. P. N. Rebelo and J. N. C. Lopes, *J. Phys. Chem. B*, 2010, **114**, 5831–5834.
- [301] J. E. S. J. Reid, F. Agapito, C. E. S. Bernardes, F. Martins, A. J. Walker, S. Shimizu and M. E. Minas da Piedade, *Phys. Chem. Chem. Phys.*, 2017, **19**, 19928–19936.
- [302] A. B. H. Susan, A. Noda, S. Mitsushima and M. Watanabe, *Chem. Commun.*, 2003, 938–939.
- [303] T. Yasuda and M. Watanabe, *MRS Bull.*, 2013, **38**, 560–566.
- [304] W. L. Marshall and E. U. Franck, *J. Phys. Chem. Ref. Data*, 1981, **10**, 295–304.
- [305] J. H. Davis Jr and K. J. Forrester, *Tetrahedron Lett.*, 1999, **40**, 1621–1622.
- [306] J. H. Davis Jr, *Chem. Lett.*, 2004, **33**, 1072–1077.
- [307] M. S. Miran, T. Yasuda, M. A. B. H. Susan, K. Dokko and M. Watanabe, *RSC Adv.*, 2013, **3**, 4141–4144.
- [308] K. Fumino, A. Wulf and R. Ludwig, *Angew. Chem. Int. Ed.*, 2009, **48**, 3184–3186; *Angew. Chem.*, 2009, **121**, 3230–3233.
- [309] R. Hayes, G. G. Warr and R. Atkin, *Chem. Rev.*, 2015, **115**, 6357–6426.
- [310] M. Addicoat, R. Atkin, J. N. C. Lopes, M. C. Gomes, M. Firestone, R. Gardas, S. Halstead, C. Hardacre, L. J. Hardwick, J. Holbrey, P. Hunt, V. Ivaništšev, J. Jacquemin, R. Jones, B. Kirchner, R. Lynden-Bell, D. MacFarlane, G. Marlair, H. Medhi, M. Mezger, A. Pádua, I. Pantenburg, S. Perkin, J. E. S. J. Reid, M. Rutland, S. Saha, K. Shimizu, J. M. Slattery, M. Swadźba-Kwaśny, S. Tiwari, S. Tsuzuki, B. Uralcan, A. van den Bruinhorst, M. Watanabe and J. Wishart, *Faraday Discuss.*, 2017, **206**, 291–337.
- [311] B. Kirchner and A. P. Seitsonen, *Inorg. Chem.*, 2007, **46**, 2751–2754.
- [312] M. Salanne, L. J. A. Siqueira, A. P. Seitsonen, P. A. Madden and B. Kirchner, *Faraday Discuss.*, 2012, **154**, 171–188.
- [313] V. K. Thorsmølle, G. Rothenberger, D. Topgaard, J. C. Brauer, D.-B. Kuang, S. M. Zakeeruddin, B. Lindman, M. Grätzel and J.-E. Moser, *ChemPhysChem*, 2011, **12**, 145–149.

- [314] J. G. McDaniel and A. Yethiraj, *J. Phys. Chem. B*, 2017, **122**, 250–257.
- [315] H. Abe, M. Aono, T. Kiyotani and S. Tsuzuki, *Phys. Chem. Chem. Phys.*, 2016, **18**, 32337–32344.
- [316] R. Elfgen, O. Hollóczki, P. Ray, M. F. Groh, M. Ruck and B. Kirchner, *Z. Anorg. Allg. Chem.*, 2017, **643**, 41–52.
- [317] H. Haller, M. Hog, F. Scholz, H. Scherer, I. Krossing and S. Riedel, *Z. Naturforsch. B Chem. Sci.*, 2013, **68**, 1103–1107.
- [318] A. P. Abbott, S. S. M. Alabdullah, A. Y. M. Al-Murshedi and K. S. Ryder, *Faraday Discuss.*, 2018, **206**, 365–377.
- [319] S. Zahn, J. Thar and B. Kirchner, *J. Chem. Phys.*, 2010, **132**, 124506.
- [320] H.-Y. Hou, Y.-R. Huang, S.-Z. Wang and B.-F. Bai, *Acta Phys.-Chim. Sin.*, 2011, **27**, 2512–2520.
- [321] W. Qian, Y. Xu, H. Zhu and C. Yu, *J. Chem. Thermodyn.*, 2012, **49**, 87–94.
- [322] D. R. MacFarlane, J. M. Pringle, K. M. Johansson, S. A. Forsyth and M. Forsyth, *Chem. Commun.*, 2006, 1905–1917.
- [323] B. Kirchner, J. Hutter, I.-F. W. Kuo and C. J. Mundy, *Int. J. Mod. Phys. B*, 2004, **18**, 1951–1962.
- [324] A. S. Pensado, M. Brehm, J. Thar, A. P. Seitsonen and B. Kirchner, *ChemPhysChem*, 2012, **13**, 1845–1853.
- [325] I. M. Kolthoff and A. Willman, *J. Am. Chem. Soc.*, 1934, **56**, 1007–1013.
- [326] M. S. Miran, H. Kinoshita, T. Yasuda, M. A. B. H. Susan and M. Watanabe, *Phys. Chem. Chem. Phys.*, 2012, **14**, 5178–5186.
- [327] X. Sun, B. Cao, X. Zhou, S. Liu, X. Zhu and H. Fu, *J. Mol. Liq.*, 2016, **221**, 254–261.
- [328] P. Ray, S. Dohm, T. Husch, C. Schütter, K. A. Persson, A. Balducci, B. Kirchner and M. Korth, *J. Phys. Chem. C*, 2016, **120**, 12325–12336.
- [329] Z. Zhang, K. Jetsrisuparb, A. Wokaun and L. Gubler, *J. Power Sources*, 2013, **243**, 306–316.
- [330] D. S. Kim, Y. S. Kim, M. D. Guiver and B. S. Pivovar, *J. Membr. Sci.*, 2008, **321**, 199–208.
- [331] H. Haller and S. Riedel, *Z. Anorg. Allg. Chem.*, 2014, **640**, 1281–1291.
- [332] L. Mann, E. Hornberger, S. Steinhauer and S. Riedel, *Chem. Eur. J.*, 2018, **24**, 3902–3908.
- [333] J. Hutter, M. Iannuzzi, F. Schiffmann and J. VandeVondele, *Wiley Interdiscip. Rev. Comput. Mol. Sci.*, 2014, **4**, 15–25.

- [334] D. Himmel, V. Radtke, B. Butschke and I. Krossing, *Angew. Chem. Int. Ed.*, 2018, **57**, 4386–4411; *Angew. Chem.*, 2018, **130**, 4471–4498.
- [335] C. O. da Silva, E. C. da Silva and M. A. C. Nascimento, *J. Phys. Chem. A*, 1999, **103**, 11194–11199.
- [336] M. D. Liptak and G. C. Shields, *J. Am. Chem. Soc.*, 2001, **123**, 7314–7319.
- [337] I. A. Topol, G. J. Tawa, S. K. Burt and A. A. Rashin, *J. Phys. Chem. A*, 1997, **101**, 10075–10081.
- [338] I. A. Topol, G. J. Tawa, R. A. Caldwell, M. A. Eissenstat and S. K. Burt, *J. Phys. Chem. A*, 2000, **104**, 9619–9624.
- [339] Y. H. Jang, W. A. Goddard, K. T. Noyes, L. C. Sowers, S. Hwang and D. S. Chung, *J. Phys. Chem. B*, 2003, **107**, 344–357.
- [340] Y. H. Jang, L. C. Sowers, T. Çağın and W. A. Goddard, *J. Phys. Chem. A*, 2001, **105**, 274–280.
- [341] C. J. La Francois, Y. H. Jang, T. Çağın, W. A. Goddard and L. C. Sowers, *Chem. Res. Toxicol.*, 2000, **13**, 462–470.
- [342] J. Ho, *Aust. J. Chem.*, 2014, **67**, 1441–1460.
- [343] J. Ho, *Phys. Chem. Chem. Phys.*, 2015, **17**, 2859–2868.
- [344] B. Thapa and H. B. Schlegel, *J. Phys. Chem. A*, 2017, **121**, 4698–4706.
- [345] J. R. Pliego and J. M. Riveros, *J. Phys. Chem. A*, 2001, **105**, 7241–7247.
- [346] J. R. Pliego and J. M. Riveros, *J. Phys. Chem. A*, 2002, **106**, 7434–7439.
- [347] A. K. Tummanapelli and S. Vasudevan, *J. Phys. Chem. B*, 2014, **118**, 13651–13657.
- [348] A. K. Tummanapelli and S. Vasudevan, *J. Phys. Chem. B*, 2015, **119**, 12249–12255.
- [349] A. J. Ballard and C. Dellago, *J. Phys. Chem. B*, 2012, **116**, 13490–13497.
- [350] G. Kortüm, W. Vogel and K. Andrussov, *Pure Appl. Chem.*, 1960, **1**, 187–536.
- [351] N. P. Aravindakshan, K. E. Gemmell, K. E. Johnson and A. L. L. East, *J. Chem. Phys.*, 2018, **149**, 094505.
- [352] R. A. Robinson and R. H. Stokes, *Electrolyte Solutions*, Dover Publications, Mineola, 2002.
- [353] C. Schreiner, S. Zugmann, R. Hartl and H. J. Gores, *J. Chem. Eng. Data*, 2009, **55**, 1784–1788.
- [354] A. P. Abbott, K. Ryder, P. Licence and A. W. Taylor, in *Ionic Liquids Completely UnCOILed: Critical Expert Overviews*, ed. N. V. Plechkova and K. R. Seddon, John Wiley & Sons, Hoboken, 2015, pp. 1–12.
- [355] A. A. Lee, D. Vella, S. Perkin and A. Goriely, *J. Phys. Chem. Lett.*, 2014, **6**, 159–163.

- [356] S. Perkin, M. Salanne, P. Madden and R. Lynden-Bell, *Proc. Natl. Acad. Sci.*, 2013, **110**, E4121–E4121.
- [357] S. Perkin and M. Salanne, *J. Phys. Condens. Matter*, 2014, **26**, 280301.
- [358] T. Köddermann, C. Wertz, A. Heintz and R. Ludwig, *ChemPhysChem*, 2006, **7**, 1944–1949.
- [359] H. Weingärtner, A. Knocks, W. Schrader and U. Kaatze, *J. Phys. Chem. A*, 2001, **105**, 8646–8650.
- [360] C. Daguenet, P. J. Dyson, I. Krossing, A. Oleinikova, J. Slattery, C. Wakai and H. Weingärtner, *J. Phys. Chem. B*, 2006, **110**, 12682–12688.
- [361] W. Zhao, F. Leroy, B. Heggen, S. Zahn, B. Kirchner, S. Balasubramanian and F. Müller-Plathe, *J. Am. Chem. Soc.*, 2009, **131**, 15825–15833.
- [362] C. M. Breneman and K. B. Wiberg, *J. Comput. Chem.*, 1990, **11**, 361–373.
- [363] R. D. Rogers and K. R. Seddon, *Science*, 2003, **302**, 792–793.
- [364] K. R. Seddon, *Nat. Mater.*, 2003, **2**, 363–365.
- [365] A. Chaumont and G. Wipff, *J. Phys. Chem. C*, 2009, **113**, 18233–18243.
- [366] A. Chaumont and G. Wipff, *J. Phys. Chem. B*, 2008, **112**, 12014–12023.
- [367] M. Y. Lui, L. Crowhurst, J. P. Hallett, P. A. Hunt, H. Niedermeyer and T. Welton, *Chem. Sci.*, 2011, **2**, 1491–1496.
- [368] J. P. Hallett, C. L. Liotta, G. Ranieri and T. Welton, *J. Org. Chem.*, 2009, **74**, 1864–1868.
- [369] O. Kuzmina, E. Bordes, J. Schmauck, P. A. Hunt, J. P. Hallett and T. Welton, *Phys. Chem. Chem. Phys.*, 2016, **18**, 16161–16168.
- [370] C. Ma, A. Laaksonen, C. Liu, X. Lu and X. Ji, *Chem. Soc. Rev.*, 2018, **47**, 8685–8720.
- [371] E. L. Smith, A. P. Abbott and K. S. Ryder, *Chem. Rev.*, 2014, **114**, 11060–11082.
- [372] A. Korotkevich, D. S. Firaha, A. A. H. Padua and B. Kirchner, *Fluid Ph. Equilibria*, 2017, **448**, 59–68.
- [373] B. Clare, A. Sirwardana and D. R. MacFarlane, in *Ionic Liquids*, ed. B. Kirchner, Springer, Berlin, Heidelberg, 2009, pp. 1–40.
- [374] W. Xu, E. I. Cooper and C. A. Angell, *J. Phys. Chem. B*, 2003, **107**, 6170–6178.
- [375] C. Zhao, G. Burrell, A. A. J. Torriero, F. Separovic, N. F. Dunlop, D. R. MacFarlane and A. M. Bond, *J. Phys. Chem. B*, 2008, **112**, 6923–6936.
- [376] A. Rupp, N. Roznyatovskaya, H. Scherer, W. Beichel, P. Klose, C. Sturm, A. Hoffmann, J. Tübke, T. Koslowski and I. Krossing, *Chem. Eur. J.*, 2014, **20**, 9794–9804.

- [377] S. Gehrke, W. Reckien, I. Palazzo, T. Welton and O. Hollóczki, *Eur. J. Org. Chem.*, 2019, **2019**, 504–511.
- [378] B. A. D. Neto, E. C. Meurer, R. Galaverna, B. J. Bythell, J. Dupont, R. G. Cooks and M. N. Eberlin, *J. Phys. Chem. Lett.*, 2012, **3**, 3435–3441.
- [379] Y. Ma, W. Gao, H. Yu and M. Li, *J. Liq. Chromatogr. Relat. Technol.*, 2014, **37**, 73–87.
- [380] H. Chen, X. Chen, J. Deng and J. Zheng, *Chem. Sci.*, 2018, **9**, 1464–1472.
- [381] B. Kirchner, O. Hollóczki, J. N. Canongia Lopes and A. A. H. Pádua, *Wiley Interdiscip. Rev. Comput. Mol. Sci.*, 2015, **5**, 202–214.
- [382] C. Hardacre, J. D. Holbrey, C. L. Mullan, T. G. A. Youngs and D. T. Bowron, *J. Chem. Phys.*, 2010, **133**, 074510.
- [383] W. Xu and C. A. Angell, *Science*, 2003, **302**, 422–425.
- [384] R. Hayes, S. Imberti, G. G. Warr and R. Atkin, *Angew. Chem. Int. Ed.*, 2013, **52**, 4623–4627; *Angew. Chem.*, 2013, **125**, 4721–4725.
- [385] B. J. Alder and T. E. Wainwright, *Phys. Rev.*, 1970, **1**, 18–21.
- [386] J.-P. Hansen and I. R. McDonald, *Theory of Simple Liquids: with Applications to Soft Matter*, Academic Press, New York, 2013.
- [387] M. G. Del Pópolo and G. A. Voth, *J. Phys. Chem. B*, 2004, **108**, 1744–1752.
- [388] G. Kortüm and W. Vogel, *Lehrbuch der Elektrochemie*, Verlag Chemie, Weinheim, 1966.
- [389] F. Philippi, D. Rauber, M. Springborg and R. Hempelmann, *J. Phys. Chem. A*, 2019, **123**, 851–861.
- [390] U. A. Rana, M. Forsyth, D. R. MacFarlane and J. M. Pringle, *Electrochim. Acta*, 2012, **84**, 213–222.
- [391] S. Zahn, G. Bruns, J. Thar and B. Kirchner, *Phys. Chem. Chem. Phys.*, 2008, **10**, 6921–6924.
- [392] P. A. Hunt, *J. Phys. Chem. B*, 2007, **111**, 4844–4853.
- [393] O. Hollóczki, D. Gerhard, K. Massone, L. Szarvas, B. Németh, T. Veszprémi and L. Nyulászi, *New J. Chem.*, 2010, **34**, 3004–3009.
- [394] O. Hollóczki, *ACS Sustain. Chem. Eng.*, 2018, **7**, 2626–2633.
- [395] O. Holloczki, A. Wolff, J. Pallmann, R. E. Whiteside, J. Hartley, M. A. Grasser, P. Nockemann, E. Brunner, T. Doert and M. Ruck, *Chem. Eur. J.*, 2018, **24**, 16323–16331.
- [396] K. Fumino, V. Fossog, P. Stange, K. Wittler, W. Polet, R. Hempelmann and R. Ludwig, *ChemPhysChem*, 2014, **15**, 2604–2609.

- [397] J. Huang, A. Fu, H. Li, H. Li, T. Chu and Z. Wang, *Int. J. Quantum Chem.*, 2017, **117**, 170–179.
- [398] D. Z. Troter, Z. B. Todorović, D. R. Đokić-Stojanović, B. S. Đorđević, V. Todorović, S. S. Konstantinović and V. B. Veljković, *J. Serb. Chem. Soc.*, 2017, **82**, 1039–1052.
- [399] L. Bahadori, M. H. Chakrabarti, F. S. Mjalli, I. M. AlNashef, N. S. A. Manan and M. A. Hashim, *Electrochim. Acta*, 2013, **113**, 205–211.
- [400] F. Cardellini, M. Tiecco, R. Germani, G. Cardinali, L. Corte, L. Roscini and N. Spreti, *RSC Adv.*, 2014, **4**, 55990–56002.
- [401] M. A. R. Martins, S. P. Pinho and J. A. P. Coutinho, *J. Solution Chem.*, 2019, **48**, 962–982.
- [402] Y. Marcus, *Deep Eutectic Solvents*, Springer, Cham, 2019.
- [403] A. P. Abbott, D. Boothby, G. Capper, D. L. Davies and R. K. Rasheed, *J. Am. Chem. Soc.*, 2004, **126**, 9142–9147.
- [404] F. Cardellini, R. Germani, G. Cardinali, L. Corte, L. Roscini, N. Spreti and M. Tiecco, *RSC Adv.*, 2015, **5**, 31772–31786.
- [405] A. P. Abbott, C. D’Agostino, S. J. Davis, L. F. Gladden and M. D. Mantle, *Phys. Chem. Chem. Phys.*, 2016, **18**, 25528–25537.
- [406] S. Kaur, A. Gupta and H. K. Kashyap, *J. Phys. Chem. B*, 2016, **120**, 6712–6720.
- [407] P. Novák, F. Joho, R. Imhof, J.-C. Panitz and O. Haas, *J. Power Sources*, 1999, **81**, 212–216.
- [408] D. Aurbach, Y. Gofer, A. Schechter, O. Chusid, H. Gizbar, Y. Cohen, M. Moshkovich and R. Turgeman, *J. Power Sources*, 2001, **97**, 269–273.
- [409] I. Shterenberg, M. Salama, Y. Gofer, E. Levi and D. Aurbach, *MRS Bull.*, 2014, **39**, 453–460.
- [410] R. Mohtadi and F. Mizuno, *Beilstein J. Nanotechnol.*, 2014, **5**, 1291–1311.
- [411] Z. Zhao-Karger and M. Fichtner, *MRS Commun.*, 2017, **7**, 770–784.
- [412] N. N. Rajput, T. J. Seguin, B. M. Wood, X. Qu and K. A. Persson, in *Modeling Electrochemical Energy Storage at the Atomic Scale*, ed. M. Korth, Springer, Cham, 2018, pp. 79–124.
- [413] M. Fichtner, in *Magnesium Batteries: Research and Applications*, ed. M. Fichtner, Royal Society of Chemistry, 2019, pp. 1–16.
- [414] Z. Lu, A. Schechter, M. Moshkovich and D. Aurbach, *J. Electroanal. Chem.*, 1999, **466**, 203–217.
- [415] T. S. Arthur, P.-A. Glans, N. Singh, O. Tutusaus, K. Nie, Y.-S. Liu, F. Mizuno, J. Guo, D. H. Alsem, N. J. Salmon and R. Mohtadi, *Chem. Mater.*, 2017, **29**, 7183–7188.

- [416] T. Gao, S. Hou, K. Huynh, F. Wang, N. Eidson, X. Fan, F. Han, C. Luo, M. Mao, X. Li and C. Wang, *ACS Appl. Mater. Interfaces*, 2018, **10**, 14767–14776.
- [417] R. Lv, X. Guan, J. Zhang, Y. Xia and J. Luo, *Nat. Sci. Rev.*, 2020, **7**, 333–341.
- [418] J. H. Connor, W. E. Reid Jr and G. B. Wood, *J. Electrochem. Soc.*, 1957, **104**, 38–41.
- [419] R. Mohtadi, M. Matsui, T. S. Arthur and S.-J. Hwang, *Angew. Chem. Int. Ed.*, 2012, **51**, 9780–9783; *Angew. Chem.*, 2012, **124**, 9918–9921.
- [420] Y. Shao, T. Liu, G. Li, M. Gu, Z. Nie, M. Engelhard, J. Xiao, D. Lv, C. Wang, J.-G. Zhang and J. Liu, *Sci. Rep.*, 2013, **3**, 1–7.
- [421] F. Tuerxun, K. Yamamoto, M. Hattori, T. Mandai, K. Nakanishi, A. Choudhary, Y. Tateyama, K. Sodeyama, A. Nakao, T. Uchiyama, M. Matsui, K. Tsuruta, Y. Tamenori, K. Kanamura and Y. Ushimoto, *ACS Appl. Mater. Interfaces*, 2020, **12**, 25775–25785.
- [422] S.-Y. Ha, Y.-W. Lee, S. W. Woo, B. Koo, J.-S. Kim, J. Cho, K. T. Lee and N.-S. Choi, *ACS Appl. Mater. Interfaces*, 2014, **6**, 4063–4073.
- [423] C. J. Barile, R. Spatney, K. R. Zavadil and A. A. Gewirth, *J. Phys. Chem. C*, 2014, **118**, 10694–10699.
- [424] T. Fukutsuka, K. Asaka, A. Inoo, R. Yasui, K. Miyazaki, T. Abe, K. Nishio and Y. Uchimoto, *Chem. Lett.*, 2014, **43**, 1788–1790.
- [425] N. Sa, N. N. Rajput, H. Wang, B. Key, M. Ferrandon, V. Srinivasan, K. A. Persson, A. K. Burrell and J. T. Vaughey, *RSC Adv.*, 2016, **6**, 113663–113670.
- [426] S. Terada, T. Mandai, S. Suzuki, S. Tsuzuki, K. Watanabe, Y. Kamei, K. Ueno, K. Dokko and M. Watanabe, *J. Phys. Chem. C*, 2016, **120**, 1353–1365.
- [427] S. Hebié, F. Alloin, C. Iojoiu, R. Berthelot and J.-C. Leprêtre, *ACS Appl. Mater. Interfaces*, 2018, **10**, 5527–5533.
- [428] S.-J. Kang, H. Kim, S. Hwang, M. Jo, M. Jang, C. Park, S.-T. Hong and H. Lee, *ACS Appl. Mater. Interfaces*, 2018, **11**, 517–524.
- [429] N. N. Rajput, X. Qu, N. Sa, A. K. Burrell and K. A. Persson, *J. Am. Chem. Soc.*, 2015, **137**, 3411–3420.
- [430] L. Lodovico, V. L. Martins, T. M. Benedetti and R. M. Torresi, *J. Braz. Chem. Soc.*, 2014, **25**, 460–468.
- [431] Z. Ma, M. Kar, C. Xiao, M. Forsyth and D. R. MacFarlane, *Electrochem. Commun.*, 2017, **78**, 29–32.
- [432] D. Aurbach, I. Weissman, Y. Gofer and E. Levi, *Chem. Rec.*, 2003, **3**, 61–73.
- [433] N. Amir, Y. Vestfrid, O. Chusid, Y. Gofer and D. Aurbach, *J. Power Sources*, 2007, **174**, 1234–1240.

- [434] J. Muldoon, C. B. Bucur, A. G. Oliver, T. Sugimoto, M. Matsui, H. S. Kim, G. D. Allred, J. Zajicek and Y. Kotani, *Energy Environ. Sci.*, 2012, **5**, 5941–5950.
- [435] J. Muldoon, C. B. Bucur and T. Gregory, *Angew. Chem. Int. Ed.*, 2017, **56**, 12064–12084; *Angew. Chem.*, 2017, **129**, 12232–12253.
- [436] R. Deivanayagam, B. J. Ingram and R. Shahbazian-Yassar, *Energy Storage Mater.*, 2019, **21**, 136–153.
- [437] J. Zhang, X. Yao, R. K. Misra, Q. Cai and Y. Zhao, *J. Mater. Sci. Technol.*, 2020, **44**, 237–257.
- [438] A. Lewandowski and A. Świdorska-Mocek, *J. Power Sources*, 2009, **194**, 601–609.
- [439] G. A. Giffin, *J. Mater. Chem. A*, 2016, **4**, 13378–13389.
- [440] G. T. Cheek, W. E. O’Grady, S. Z. El Abedin, E. M. Moustafa and F. Endres, *J. Electrochem. Soc.*, 2008, **155**, D91–D95.
- [441] D. Alwast, J. Schnaidt, K. Hancock, G. Yetis and R. J. Behm, *ChemElectroChem*, 2019, **6**, 3009–3019.
- [442] H. Kuwata, M. Matsui and N. Imanishi, *J. Electrochem. Soc.*, 2017, **164**, A3229.
- [443] J. Z. Hu, N. R. Jaegers, Y. Chen, K. S. Han, H. Wang, V. Murugesan and K. T. Mueller, *ACS Appl. Mater. Interfaces*, 2019, **11**, 38689–38696.
- [444] T. Mandai, K. Tatesaka, K. Soh, H. Masu, A. Choudhary, Y. Tateyama, R. Ise, H. Imai, T. Takeguchi and K. Kanamura, *Phys. Chem. Chem. Phys.*, 2019, **21**, 12100–12111.
- [445] T. J. Seguin, N. T. Hahn, K. R. Zavadil and K. A. Persson, *Front. Chem.*, 2019, **7**, 175.
- [446] C. J. Pedersen and H. K. Frensdorff, *Angew. Chem. Int. Ed.*, 1972, **11**, 16–25; *Angew. Chem.*, 1971, **84**, 16–26.
- [447] F. Tuerxun, Y. Abulizi, Y. NuLi, S. Su, J. Yang and J. Wang, *J. Power Sources*, 2015, **276**, 255–261.
- [448] I. Shterenberg, M. Salama, H. D. Yoo, Y. Gofer, J.-B. Park, Y.-K. Sun and D. Aurbach, *J. Electrochem. Soc.*, 2015, **162**, A7118.
- [449] P. Canepa, G. S. Gautam, R. Malik, S. Jayaraman, Z. Rong, K. R. Zavadil, K. Persson and G. Ceder, *Chem. Mater.*, 2015, **27**, 3317–3325.
- [450] G. A. Giffin, A. Moretti, S. Jeong and S. Passerini, *J. Phys. Chem. C*, 2014, **118**, 9966–9973.
- [451] T. Watkins and D. A. Buttry, *J. Phys. Chem. B*, 2015, **119**, 7003–7014.
- [452] O. Tutusaus, R. Mohtadi, N. Singh, T. S. Arthur and F. Mizuno, *ACS Energy Lett.*, 2017, **2**, 224–229.

- [453] Y. Shao, N. N. Rajput, J. Hu, M. Hu, T. Liu, Z. Wei, M. Gu, X. Deng, S. Xu, K. S. Han, J. Wang, Z. Nie, G. Li, K. R. Zavadil, J. Xiao, C. Wang, W. A. Henderson, J.-G. Zhang, Y. Wang, K. T. Mueller, K. Persson and J. Liu, *Nano Energy*, 2015, **12**, 750–759.
- [454] F. Sagane, K. Ogi, A. Konno, M. Egashira and K. Kanamura, *J. Electrochem. Soc.*, 2016, **84**, 76–78.
- [455] A. Kitada, Y. Kang, Y. Uchimoto and K. Murase, *J. Electrochem. Soc.*, 2013, **161**, D102.
- [456] M. Matsui, *J. Power Sources*, 2011, **196**, 7048–7055.
- [457] P. Jankowski, J. M. G. Lastra and T. Vegge, *Batter. Supercaps*, 2020, **3**, 1350–1359.
- [458] D. Samuel, C. Steinhäuser, J. G. Smith, A. Kaufman, M. D. Radin, J. Naruse, H. Hiramatsu and D. J. Siegel, *ACS Appl. Mater. Interfaces*, 2017, **9**, 43755–43766.
- [459] J. D. Deetz, F. Cao, Q. Wang and H. Sun, *J. Electrochem. Soc.*, 2018, **165**, A61.
- [460] J. Z. Hu, N. N. Rajput, C. Wan, Y. Shao, X. Deng, N. R. Jaegers, M. Hu, Y. Chen, Y. Shin, J. Monk, Z. Chen, Z. Qin, K. T. Mueller, J. Liu and K. A. Persson, *Nano Energy*, 2018, **46**, 436–446.
- [461] O. Borodin, W. Behl and T. R. Jow, *J. Phys. Chem. C*, 2013, **117**, 8661–8682.
- [462] X. Qu, A. Jain, N. N. Rajput, L. Cheng, Y. Zhang, S. P. Ong, M. Brafman, E. Maginn, L. A. Curtiss and K. A. Persson, *Comput. Mater. Sci.*, 2015, **103**, 56–67.
- [463] S. Kazemiabnavi, Z. Zhang, K. Thornton and S. Banerjee, *J. Phys. Chem. B*, 2016, **120**, 5691–5702.
- [464] P. Peljo and H. H. Girault, *Energy Environ. Sci.*, 2018, **11**, 2306–2309.
- [465] Y. Yu, A. Baskin, C. Valero-Vidal, N. T. Hahn, Q. Liu, K. R. Zavadil, B. W. Eichhorn, D. Prendergast and E. J. Crumlin, *Chem. Mater.*, 2017, **29**, 8504–8512.
- [466] S. Plimpton, *J. Comput. Phys.*, 1995, **117**, 1–19.
- [467] J. N. C. Lopes and A. A. H. Pádua, *Theor. Chem. Acc.*, 2012, **131**, 1–11.
- [468] M. Brehm and B. Kirchner, *J. Chem. Inf. Model.*, 2011, **51**, 2007–2023.
- [469] M. Brehm, M. Thomas, S. Gehrke and B. Kirchner, *J. Chem. Phys.*, 2020, **152**, 164105.
- [470] F. Weigend and R. Ahlrichs, *Phys. Chem. Chem. Phys.*, 2005, **7**, 3297–3305.
- [471] V. Barone and M. Cossi, *J. Phys. Chem. A*, 1998, **102**, 1995–2001.
- [472] M.-M. Huang, Y. Jiang, P. Sasisanker, G. W. Driver and H. Weingärtner, *J. Chem. Eng. Data*, 2011, **56**, 1494–1499.
- [473] A. B. Pereiro, H. I. M. Veiga, J. M. S. S. Esperança and A. Rodríguez, *J. Chem. Thermodyn.*, 2009, **41**, 1419–1423.

- [474] P. Zaby, J. Ingenmey, B. Kirchner, S. Grimme and S. Ehlert, *Calculating an Improved Enthalpy of Vaporization by a Modified Partition Function in Quantum Cluster Equilibrium Theory*, 2021, Submitted.
- [475] C. Bannwarth, S. Ehlert and S. Grimme, *J. Chem. Theory Comput.*, 2019, **15**, 1652–1671.
- [476] S. Grimme, *Chem. Eur. J.*, 2012, **18**, 9955–9964.
- [477] Z. L. Seeger, R. Kobayashi and E. I. Izgorodina, *J. Chem. Phys.*, 2018, **148**, 193832.
- [478] H. Watanabe, N. Arai, Y. Kameda, R. Buchner and Y. Umebayashi, *J. Phys. Chem. B*, 2020, **124**, 11157–11164.
- [479] L. Goerigk and S. Grimme, *J. Chem. Theory Comput.*, 2011, **7**, 291–309.
- [480] *VLE-Calculator*, <http://vle-calc.com>, Accessed 1 July 2018.
- [481] J. W. Kang, K.-P. Yoo, H. Y. Kim, H. Lee, D. R. Yang and C. S. Lee, *Int. J. Thermophys.*, 2001, **22**, 487–494.
- [482] *Dortmund Data Bank*, <http://ddbst.com>, Accessed 1 July 2018.
- [483] J. S. Chickos and W. E. Acree Jr, *J. Phys. Chem. Ref. Data*, 2003, **32**, 519–878.
- [484] M. Allen, D. F. Evans and R. Lumry, *J. Solution Chem.*, 1985, **14**, 549–560.
- [485] V. Majer, V. Svoboda and H. V. Kehiaian, *Enthalpies of Vaporization of Organic Compounds: A Critical Review and Data Compilation*, Blackwell Scientific, Oxford, 1985, vol. 32.
- [486] S. Kapteina, K. Slowik, S. P. Verevkin and A. Heintz, *J. Chem. Eng. Data*, 2005, **50**, 398–402.
- [487] J. N. Canongia Lopes, J. M. S. S. Esperança, A. M. de Ferro, A. B. Pereira, N. V. Plechkova, L. P. N. Rebelo, K. R. Seddon and I. Vázquez-Fernández, *J. Phys. Chem. B*, 2016, **120**, 2397–2406.
- [488] G. Schaftenaar and J. H. Noordik, *J. Comput. Aided Mol. Des.*, 2000, **14**, 123–134.
- [489] J. M. Martinez and L. Martinez, *J. Comp. Chem.*, 2003, **24**, 819–825.
- [490] L. Martinez, R. Andrade, E. G. Birgin and J. M. Martinez, *J. Comp. Chem.*, 2009, **30**, 2157–2164.
- [491] J. VandeVondele, M. Krack, F. Mohamed, M. Parrinello, T. Chassaing and J. Hutter, *Comput. Phys. Commun.*, 2005, **167**, 103–128.
- [492] J. VandeVondele and J. Hutter, *J. Chem. Phys.*, 2007, **127**, 114105.
- [493] S. Goedecker, M. Teter and J. Hutter, *Phys. Rev. B*, 1996, **54**, 1703–1710.
- [494] C. Hartwigsen, S. Goedecker and J. Hutter, *Phys. Rev. B*, 1998, **58**, 3641–3662.
- [495] M. Krack, *Theor. Chem. Acc.*, 2005, **114**, 145–152.

- [496] E. Manzurola and A. Apelblat, *J. Chem. Thermodyn.*, 1985, **17**, 579–584.
- [497] J. Korpela, *Acta Chem. Scand.*, 1971, **25**, 2852–2804.
- [498] J. Chocholoušová, J. Vacek and P. Hobza, *J. Phys. Chem.*, 2003, **107**, 3086–3092.
- [499] T. Nakabayashi, H. Sato, F. Hirata and N. Nishi, *J. Phys. Chem.*, 2001, **105**, 245–250.
- [500] S. P. McCarthy, A. K. Roy, S. Kazachenko and A. J. Thakkar, *Can. J. Chem.*, 2013, **91**, 527–528.
- [501] A. K. Roy and A. J. Thakkar, *Chem. Phys. Lett.*, 2004, **393**, 347–354.
- [502] A. K. Roy and A. J. Thakkar, *Chem. Phys. Lett.*, 2004, **386**, 162–168.
- [503] A. K. Roy and A. J. Thakkar, *Chem. Phys.*, 2005, **312**, 119–126.
- [504] F. Trouton, *Philos. Mag.*, 1884, **18**, 54–57.
- [505] A. S. Coolidge, *J. Am. Chem. Soc.*, 1928, **50**, 2166–2178.
- [506] F. Ito and T. Nakanaga, *Chem. Phys. Lett.*, 2000, **318**, 571–577.
- [507] R. C. Millikan and K. S. Pitzer, *J. Am. Chem. Soc.*, 1958, **80**, 3515–3521.
- [508] K. Ta, K. A. See and A. A. Gewirth, *J. Phys. Chem. C*, 2018, **122**, 13790–13796.